# Miniaturized analytical devices for the detection of biomarkers and monitoring of metabolic hereditary diseases

**Beatriz Rebollo Calderón**

Universitat Autònoma de Barcelona

# Miniaturized analytical devices for the detection of biomarkers and monitoring of metabolic hereditary diseases

Author:

Beatriz Rebollo Calderón

Doctoral Thesis

PhD Programme in Chemistry

Supervisors:

Dr. Julián Alonso Chamarro

Dra. Mª del Mar Puyol Bosch

Department of Chemistry

Faculty of Science

2023

Memòria presentada per aspirar al Grau de Doctor per

Beatriz Rebollo Calderón

Vist i plau

Julián Alonso Chamarro Mª del Mar Puyol Bosch

Bellaterra, 27 de Setembre de 2023

“See first, think later, then test”

A Juan

A mi padre

A mi madre

# Scientific publications

B. Rebollo-Calderon, A. Calvo-López, A. Ormazabal, M. Puyol, R. Artuch and J. Alonso-Chamarro, “Point-of-care microanalyzer for potentiometric determination of ammonium in plasma” MicroTAS 2020 - 24th International Conference on Miniaturized Systems for Chemistry and Life Sciences 528-529, 2020.

B. Rebollo-Calderon, E. Alberto-Serrano, A. Calvo-López, M. Puyol and J. Alonso-Chamarro “Point-of-care microfluidic platform for the detection of key molecules in blood related to different diseases”. MicroTAS 2021 - 25th International Conference on Miniaturized Systems for Chemistry and Life Science 1517-1517, 2021.

A. Calvo-López, B. Rebollo-Calderon, A. Ormazabal, R. Artuch, J. Rosell-Ferrer, J. Alonso-Chamarro and M. Puyol. “Biomedical point-of-care microanalyzer for potentiometric determination of ammonium ion in plasma and whole blood” Anal. Chim. Acta, vol. 1205 339782, 2022 DOI: 10.1016/j.aca.2022.339782

B. Rebollo-Calderón, E. Alberto Serrano, J. Martínez Roldán, S. Véliz Illescas, C. Lozano Artigas, A. Calvo-López, M. Puyol and J. Alonso-Chamarro. “Highly versatile point-of-care potentiometric microanalyzer for home-monitoring of hereditary metabolic diseases” (in preparation)

# Conference contributions

Some aspects of this work constitute contributions to both national and international congresses, listed below:

B. Rebollo-Calderon, A. Calvo-López, M. Puyol, R. Artuch and J. Alonso-Chamarro, "Biomedical point-of-care microanalyzer for potentiometric determination of ammonium and phenylalanine in blood” *XXIVth Transfrontier Meeting on Sensor and Biosensor* (Perpignan, France). September 2019 (Poster).

B. Rebollo-Calderon, A. Calvo-López, A. Ormazabal, M. Puyol, R. Artuch and J. Alonso-Chamarro, “Point-of-care microanalyzer for potentiometric determination of ammonium in plasma” *The 24th International Conference on Miniaturized Systems for Chemistry and Life Sciences* (Virtual). October 2020 (Poster).

B. Rebollo-Calderon, A. Calvo-López, A. Ormazabal, M. Puyol, R. Artuch and J. Alonso-Chamarro, “Point-of-care microanalyzer for monitoring metabolic hereditary diseases” *XXV Transfrontier Meeting on Sensors and Biosensors* (Virtual, Sant Carles de la Ràpita, Spain). September 2021 (Oral presentation).

B. Rebollo-Calderon, E. Alberto-Serrano, A. Calvo-López, M. Puyol and J. Alonso-Chamarro, “Point-of-care microfluidic platform for the detection of key molecules in blood related to different diseases”. *The 25th International Conference on Miniaturized Systems for Chemistry and Life Science* (Virtual and Palms Springs, CA USA). October 2021 (Poster).

B. Rebollo-Calderon, “Point-of-care microanalyzer for potentiometric determination of ammonium ion in plasma and blood” *X Doctoral Workshop of the PhD program in Chemistry* (Bellaterra, Spain). May 2021 (Poster and Oral presentation).

B. Rebollo-Calderon, J. Martínez-Roldán, A. Calvo-López, J. Alonso-Chamarro and M. Puyol, “Disposable point-of-care microanalyzer for the determination of phenylalanine in patients suffering from hereditary metabolic diseases” *XXVI Transfrontier Meeting on Sensors and Biosensors* (Barcelona, Spain). September 2022 (Poster).

Conference contributions

B. Rebollo-Calderon, E. Alberto-Serrano, J. Martínez-Roldán, A. Calvo-López, M. Puyol and J. Alonso-Chamarro, “Disposable biomedical devices for at-home monitoring of different metabolic diseases” *12$^{Th}$ Ibero-American Congress on Sensors* (Aveiro, Portugal). September 2022 (Oral presentation).

# Funding

The realization of the work described in this thesis has been possible thanks to the following sources of funding:

"Convocatòria d'ajuts per donar suport a les activitats dels grups de recerca" (SGR2017 0220). *Agència de gestió d'ajusts universitaris i de recerca (AGAUR)*. 01/01/2017 - 30/09/2021.

"Lab on a chip multiparametricos para aplicaciones aeroespaciales, medioambientales, agroalimentarias y biomédicas" (CTQ2017-85011-R). *Ministerio de Economía, Indústria y Competitividad*. 01/01/2018 - 31/12/2021.

"Biosensores para la monitorización de enfermedades metabólicas hereditarias. Desarrollo y evaluación de prototipos funcionales para validación conceptual" (DTS18/00104). *Instituto de Salud Carlos III*. 01/01/2019 - 31/12/2021.

"Estrategias innovadoras de sensado basadas en la tecnología de microsistemas para las demandas analíticas actuales en medio ambiente, agroalimentario y biomedicina" (PID2020-117216RB-100). *Ministerio de Ciencia e Innovación.* 01/09/2021 - 31/08/2025.

"Analizador potenciométrico compacto como instrumento diagnostico point-of-care para la monitorización médica de enfermedades comunes y raras que causan hiperamonemia" (PDC2021-121558-100). *Ministerio de Ciencia e Innovación*. 01/12/2021 - 31/11/2023.

And the ongoing contribution by the Fundación PKU y Otros Transtornos Metabólicos Hereditarios.

# Acknowledgements

La realización de esta tesis doctoral ha sido posible gracias a la colaboración con Rafael Artuch y Aida Ormazabal y el resto del equipo del laboratorio del *Hospital de Sant Joan de Déu*, y con Javier Rosell y el grupo de Instrumentación Electrónica y Biomédica de la *Universitat Politècnica de Catalunya*. También cabe destacar el soporte económico por parte de la Fundación PKU y Otros Transtornos Metabòlicos Hereditàrios, así como por el Gobierno de España, la Generalitat de Cataluña y el Instituto de Salud Carlos III.

A nivel más personal quiero agradecer a todas aquellas personas que me han acompañado durante estos últimos años, y sin el apoyo de los cuales no hubiera podido realizar esta tesis.

Primero, a todos aquellos que han coincidido en el grupo de Sensores y Biosensores conmigo, y con los que he compartido tantos ratos en el laboratorio, a Pedro, Eva y Alex y, en particular, a Toni de quien tanto he aprendido y cuya ayuda durante estos años ha sido indispensable. También quiero agradecer a mis directores de tesis, Mar y Julián, por la oportunidad que me han brindado para desarrollar esta tesis en su grupo, y por su guía y todo lo que me han enseñado.

A mis amigos, Lidia, Manu, Ally, Cris y Aida, así como aquellas amigas que me han acompañado desde hace más de una década cuando comencé mi formación en la UAB: Raquel, Marta, Elena, Samara, Marta y Margot; quiero agradecerles todos esos buenos momentos que he disfrutado a su lado y su apoyo durante estos últimos años que me han ayudado a sobrellevar mejor las épocas más duras.

A mi padre, de quién he heredado la pasión por la investigación en ciencia, y a mi madre que siempre ha creído en mí y en mi potencial para conseguir mis objetivos.

Por ultimo quiero dar las gracias a Juan, quien ha sido mi mayor pilar durante estos últimos años, no existen palabras para expresar lo afortunada que me siento de tener alguien como él mi lado, siempre dispuesto a ayudarme, aconsejarme o, simplemente, a escucharme y entenderme. Gracias.

The work reported in this doctoral thesis has been carried out within the *Grupo de Sensores y Biosensores* of the *Universitat Autònoma de Barcelona* (Bellaterra, Spain) in collaboration with the *Hospital Sant Joan de Déu* (Esplugues de Llobregat, Spain) and the *Grupo de Instrumentación Electrónica y Biomédica* of the *Universitat Politècnica de Catalunya* (Barcelona, Spain).

It is also important to highlight the financial support by the *Fundación PKU y Otros Transtornos Metabòlicos Hereditàrios* that has allowed me to conduct this research.

# Abstract

During the last few decades there has been a marked progression towards the miniaturization and automation of analytical processes in order to reduce costs, energy, reagents and waste and to allow for point-of-care (POC) analysis. An approach is the use of microfluidic platforms that integrate all the necessary elements to carry out a complete analysis. The analytical devices presented here are a good example of this trend. They consist of miniaturized systems to allow for POC analysis in healthcare.

More specifically, this thesis focuses on the determination of biomarkers for different Inborn Errors of Metabolism (IEM). Ammonium ion, $NH_4^+$, has been selected as analyte of interest due to its marked increase in blood and its consequent serious and long-lasting neuronal affectations in patients presenting non-controlled Urea Cycle Disorders (UCDs). Currently, $NH_4^+$ determination is only carried out at the laboratories of reference centres as it requires expensive and complex equipment. However, this condition calls for immediate medical intervention and the fact that it can only be monitored in some hospitals hinders the accessibility to a swift medical treatment.

Alternatively, this work also focuses on another metabolic disease, Phenylketonuria (PKU), which also requires a close surveillance to keep Phenylalanine (Phe) levels in blood within acceptable levels. Although an increase of Phe has serious consequences for the development of the neuronal system, currently patients lack a method of self-monitoring that can be used periodically at their own homes and they must rely only on periodical controls in reference hospitals.

Therefore, there is an imperious need to procure reliable, fast and robust analytical devices for the determination of these two biomarkers, which must be cheap and easy to use in order to facilitate their implementation in all clinics and homes.

Two different approaches for the determination of these biomarkers in blood samples are described in this thesis. The first one, focused only in $NH_4^+$ determination, is the development of a high throughput analytical system for the continuous analysis of low volume blood samples in an hospital setting, based on a polymeric microfluidic platform to reduce reagents and waste volumes and costs. The second one is the development of a single-use auto-calibrating polymeric analytical platform aimed for at-home analysis of capillary blood for the determination of both biomarkers. Both these analytical approaches rely on potentiometry as the method of detection, relying on the use of solid contact ion selective electrodes (SC-ISE) for the reliable determination of $NH_4^+$. On the contrary, Phe determination is achieved indirectly by the conversion of this amino acid into ammonia by the incorporation of an enzyme into the analytical platform.

# Resumen

Durante las últimas décadas, ha habido una marcada tendencia hacia la miniaturización y la automatización de los procesos analíticos para reducir costes, energía, reactivos y residuos, y para permitir los analisis *point-of-care* (POC). Una estrategia es el uso de plataformas microfluidicas que integran todos los elementos necesarios para la realización completa de un análisis. Los sistemas analíticos presentados en este trabajo son un buen ejemplo de esta tendencia. Consisten en sistemas miniaturizados que permiten el análisis POC para el ámbito sanitario.

Más concretamente, esta tesis se centra en la determinación de biomarcadores para diferentes Errores Innatos del Metabolismo (EIM). El ion amonio, $NH_4^+$, ha sido seleccionado como ion de interés debido a su marcado incremento en sangre y sus consecuentes afectaciones neuronales, que son graves y de por vida, en pacientes que presentan Trastornos del Ciclo de la Urea (TCU) no debidamente controlados. Actualmente, el control de los niveles de $NH_4^+$ solo se hace en laboratorios de centros de referencia por la necesidad de equipamiento caro y complejo. Sin embargo, estos casos requieren intervención médica inmediata, y el hecho de que solo puedan ser diagnosticados en ciertos hospitales dificulta la accesibilidad a un rápido tratamiento médico.

Alternativamente, este trabajo también se centra en otra enfermedad metabólica, la Fenilcetonuria (PKU), en la que también es clave un control frecuente de los niveles de fenilalanina (Phe) en sangre para mantenerlos dentro de los rangos aceptables. Aunque un incremento de los niveles de Phe tiene serias consecuencias sobre el desarrollo neuronal, los pacientes no disponen de ninguna solución analítica para auto-gestionar su propia enfermedad y deben dependen únicamente de controles periódicos en hospitales de referencia.

Por lo tanto, existe una imperiosa necesidad de obtener dispositivos analíticos fiables, rápidos y robustos para estos dos analitos, y que deben ser baratos y fáciles de usar para facilitar su instalación y uso en todas las clínicas y hogares que así lo requieran.

En este trabajo se describen dos enfoques diferentes para la determinación de estos biomarcadores en sangre. El primero de ellos, que se centra solo en la determinación del $NH_4^+$, es el desarrollo de un sistema analítico de alto rendimiento para el análisis continuo de muestras de sangre de volumen reducido en hospitales y clínicas. Está basado en una plataforma microfluídica polimérica que permite reducir el uso de reactivos, muestra y los costes. El segundo enfoque se basa en una plataforma polimérica desechable y auto-calibrable para el análisis de sangre capilar en un ámbito doméstico, que sí está diseñado para la detección de ambos biomarcadores. Ambos dispositivos analíticos se basan en la potenciometria como método de detección y en el uso de electrodos selectivos de iones de estado sólido (SC-ISE) para la detección del $NH_4^+$. Por otro lado, la detección de la Phe se consigue de forma indirecta mediante la conversión de este aminoácido en amoniaco al incorporar una enzima dentro de la plataforma analítica.

# List of acronyms and abbreviations

| | |
|---|---|
| $a_\mathrm{x}$ | Ionic activity for ion X |
| BBPA | Bis(1-butylpentyl)adipate |
| BH4 | Tetrahydrobioprotein |
| CAD | Computer Aided Design |
| CAM | Computer Aided Manufacturing |
| CNC | Computer Numerical Control |
| COC | Cyclic Olefin Co-polymer |
| CS | Conductive Support |
| $D$ | Diffusivity |
| $D_\mathrm{h}$ | Hydraulic diameter |
| $E_\mathrm{cell}$ | Electrochemical cell potential |
| $E_\mathrm{cell}$ | Electrochemical cell potential |
| EDL | Electric Double Layer |
| EDTA | Ethylenediaminetetraacetic acid |
| EFGF | Electric Field Gradient Focusing |
| $E^{\circ}_{\mathrm{cell}}$ | Electrochemical cell standard potential |
| $E^{\circ}_{\mathrm{I}}$ | Indicator electrode standard potential |
| $E_\mathrm{I}$ | Indicator electrode potential |
| $E_\mathrm{ref}$ | Reference electrode potential |
| ET | Electron Transfer |
| $F$ | Faraday constant |
| FASI | Field Amplified Sample Injection |
| FASS | Field Amplified Sample Stacking |

List of acronyms and abbreviations

| | |
|---|---|
| FEP | Fluorinated ethylene-propylene |
| $f_i$ | Inertial forces |
| FIA | Flow Injection Analysis |
| FIM | Fixed Interference Method |
| Fo | Fourier number |
| $f_v$ | Viscous forces |
| GAC | Green Analytical Chemistry |
| GC | Glassy Carbon |
| GLDH | Glutamate Dehydrogenase |
| GSB | Grupo de Sensores y Biosensores |
| HEPES | 2-[4-(2-hydroxyethyl)piperazin-1-yl]ethanesulfonic acid |
| HMD | Hereditary Metabolic Diseases |
| HPA | Hyperphenylalaninemia |
| HSJD | Hospital Sant Joan de Déu |
| $I$ | Ionic strength |
| IC | Interval of Confidence |
| IEB | Grupo de Instrumentación Electrónica y Biomédica |
| IEF | Isoelectric focusing |
| IEM | Inborn Errors of Metabolism |
| IS | Internal Solution |
| ISE | Ion Selective Electrode |
| ISM | Ion Selective Membrane |
| IT | Ion Transfer |
| ITP | Isotachophoresis |
| IUPAC | International Union of Pure and Applied Chemistry |
| $K_{A,B}^{pot}$ | Potentiometric selectivity coefficient |

| | |
|---|---|
| $K_B$ | Boltzman constant |
| L | Characteristic length |
| LC-ISE | Liquid Contact Ion Selective Electrode |
| LD | Limit of detection |
| LNAA | Large Neutral Amino Acid |
| LOC | Lab-on-a-chip |
| LTCC | Low Temperature Co-fired Ceramics |
| MCFA | Multicommutated Flow Analysis System |
| MEMS | Microelectromechanical Systems |
| MW | Molecular Weight |
| MWCO | Molecular Weight Cut-Off |
| $NAD^+$ | Nicotinamide Adenine Dinucleotide |
| P | Peristaltic pump |
| PAH | Phenylalanine hydroxylase |
| PAL | Phenylalanine ammonia lyase |
| PANI | Polyaniline |
| PBS | Phosphate-Buffered Saline |
| PBSP | Poly(butyilene sebacate) plasticizer |
| PC | Polycarbonate |
| PCR | Polymerase Chain Reaction |
| PCR | Polymerase Chain Reaction |
| PDMS | Polydimethylsiloxane |
| Pe | Peclet number |
| PEDOT | Poly(3,4-ethylenedioxythiophene) |
| PES | Polyethersulfone |
| Phe | Phenylalanine |

## List of acronyms and abbreviations

| | |
|---|---|
| PKU | Phenylketonuria |
| PMMA | Poly(methyl methacrylate) |
| POC | Point-of-care |
| POT | Poly(3-octylthiophene) |
| PPy | Polypyrrole |
| PS | Polystyrene |
| PVC | Poly-vinyl chloride |
| PVDF | Polyvinyldene fluoride |
| $P_\mathrm{w}$ | Wetted perimeter |
| $R$ | Gas constant |
| $r$ | Radius |
| Re | Reynolds number |
| ROMP | Ring Opening Metathesis Polymerization |
| RSD | Relative Standard Deviation |
| S | Slope |
| SC | Solid Contact |
| SC-ISE | Solid Contact Ion Selective Electrode |
| SSM | Separate Solution Method |
| $T$ | Temperature |
| TAS | Total Analysis System |
| $\mathrm{T_g}$ | Glass transition temperature |
| TGF | Temperature Gradient Focusing |
| THF | Tetrahydrofuran |
| $T_\mathrm{m}$ | Mixing time |
| TPE | Thermoset polyester |
| $T_\mathrm{r}$ | Residence time |

| | |
|---|---|
| TRIS | 2-amino-2-(hydroxymethyl)propane-1,3-diol |
| U | Enzyme unit |
| UAB | Universitat Autònoma de Barcelona |
| UCD | Urea Cycle Disorders |
| UPC | Universitat Politècnica de Catalunya |
| UPLC-MS/MS | Ultra Performance Liquid Chromatography-tandem Mass Spectrometry |
| V | Valve |
| $v$ | Velocity |
| $\bar{X}$ | Average value |
| $z_x$ | Ionic charge for ion X |
| $\gamma$ | Activity coefficient |
| $\varepsilon$ | Interface boundary potential |
| $\eta$ | Shear viscosity |
| µPAD | Micro Paper-based Analytical Device |
| µTAS | Micro Total Analysis System |
| $\rho$ | Density |
| σ | Standard deviation |

# Table of contents

# Chapter 1

# Introduction

## 1.1. Ammonium ion and phenylalanine as biomarkers

The International Union of Pure and Applied Chemistry (IUPAC) defines biomarker as an “indicator signalling an event or condition in a biological system or sample and giving a measure of exposure, effect or susceptibility” and specifies that this biomarker “may be a measurable chemical, biochemical, physiological, behavioural or other alteration within an organism”.[1]

In this work, we have focused on ammonium ion, $NH_4^+$, and phenylalanine (Phe) as biomarkers of diseases presenting high levels of these molecules in blood. Thus, the analytical microsystems described in this dissertation focus on the potentiometric detection of these relevant biomarkers to achieve a close biochemical monitoring in a clinical setting.

### 1.1.1. Ammonium ion as biomarker for urea cycle disorders

Urea Cycle Disorders (UCDs) are only one of the over 500 different types of Hereditary Metabolic Diseases (HMD), also known as Inborn Errors of Metabolism (IEM). Individually, these diseases are rare. However, taking into account the overall incidence they can be as high as 51:100000, and in particular, UCDs have a total birth prevalence of 2.9:100000.[2]

Part of this work focuses on the UCDs, in which the congenital malfunction of any of the enzymes involved in the urea cycle (*Fig. 1.1*) leads to an impaired $NH_4^+$ detoxification, and thus, to increased levels of this molecule in blood. In healthy cases, $NH_4^+$ is found at levels lower than 50 µM in adults and children, and lower than 110 µM in newborns. Values higher than these concentrations constitute a condition known as hyperammonemia which requires immediate medical intervention to avoid hyperamonemic encephalopathy, irreversible brain damage, comma and even death. The affectations to the central nervous system are particularly severe and permanent if they occur during childhood as the nervous system is still under development and neuronal loss and defects in cell growth, migration and myelination can occur.[3]

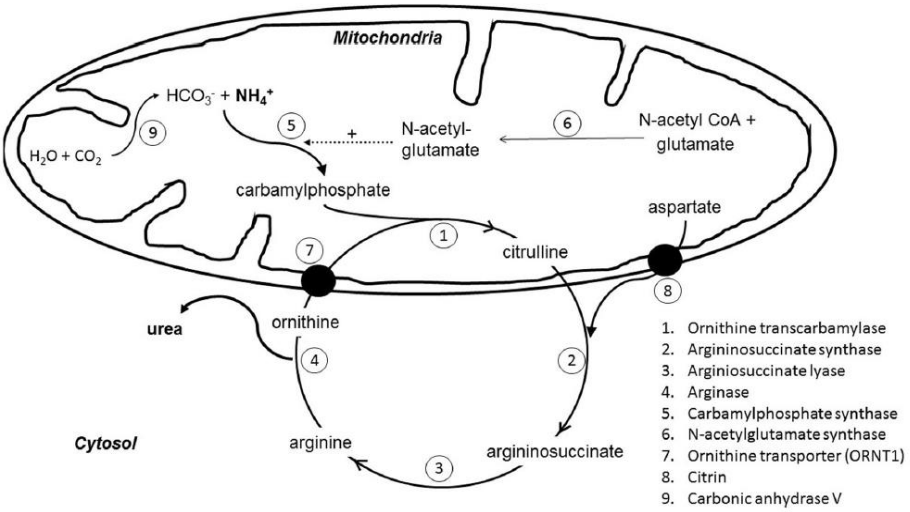

Fig. 1.1 The urea cycle disorder and enzymes involved. Adapted from (5).

Alternatively, the accumulation of $NH_4^+$ in blood can also be a consequence of either an increased production of this molecule (due to drugs, bacterial overgrowth or infection-induced catabolic states), or due to a hindering in the detoxification resulting from the loss of activity of the glutamine synthetase caused by cirrhosis and hepatic failure, as this process takes place in the periportal hepatocytes.[4,5] Indeed, cirrhosis and hepatic failure constitute the main non-congenital cause of hyperammonemia. Moreover, both cirrhosis and chronic liver disease present a high prevalence in population, with a total of 1.5 billion cases worldwide in 2017.[6]

UCDs can manifest at any point in life and there are tests for prenatal and newborn screenings. These genetic diseases cannot be cured but can be managed by the monitoring of $NH_4^+$ levels and by dietary restrictions aimed to reduce protein catabolism.[7] In cases of hyperammonemia induced acute encephalopathy, a fast medical intervention based on haemodialysis, cease of protein intake and administration of arginine and drugs for $NH_4^+$ removal is required.[5]

To ensure the best care for patients, the quantification of $NH_4^+$ levels in blood should be fast and accessible. However, $NH_4^+$ analysis is currently only carried out at laboratories of reference centres. Moreover, blood extracted from patients' needs to be taken to the laboratory and centrifuged, thus delaying the analysis process. Additionally, $NH_4^+$ levels in plasma increase dramatically with time due to cell lysis and amino acid degradation, so results obtained from the analysis of these plasma samples may not be accurate.[8]

There already exist some published works for $NH_4^+$ quantification in biological fluids. Some of them consist of wearable devices for the quantification of this analyte in sweat.[9,10] However, quantification of $NH_4^+$ levels is more reliable when the sample is whole blood. As it happens, there are other analytical microsystems reported that use blood as sample.[11–13] Moreover, there are some commercially available point-of-care (POC) for $NH_4^+$ quantification in blood, such as the Pocket Chem Ba PA-4140 by Arkray and the FUJI DRI-CHEM NX10N by Fujifilm. Both are based on optical detection, which for the analysis of blood samples is not the ideal method because the complexity of the matrix can difficult the measurement. Moreover, both present similar lineal ranges of 7 µM to 285.5 µM $NH_4^+$ and to 357 µM $NH_4^+$ respectively, which cover the pathological threshold of $NH_4^+$ concentration but are not reliable for the monitoring of very decompensated patients, as its lineal ranges do not cover very high $NH_4^+$ concentrations. Furthermore, they both require the use of a single-use consumable test strip for every analysis. This leads to the need of transporting and storing strips, which may be difficult in developing countries, and increases the cost of each analysis as well as generating more waste. Additionally, there are not commercially available $NH_4^+$ POC devices for at-home use.

### 1.1.2. Phenylalanine as biomarker for Phenylketonuria

The analytical microsystems for the potentiometric detection of $NH_4^+$ developed in this work can be modified by the inclusion of an enzyme for the indirect determination of any other biologically relevant molecule. This enzymatic concept has been employed in this thesis for the determination of Phe. This amino acid accumulates in blood in patients presenting Phenylketonuria (PKU), which is an autosomal recessive IEM where Phe cannot be appropriately metabolized in the liver, due mostly to a mutation of the phenylalanine hydroxylase (PAH) enzyme (*Fig. 1.2*), but also for a minority of cases due to a malfunction of its co-factor, tetrahydrobioprotein (BH4). Depending on the levels of Phe in blood, there are different classifications of hyperphenylalaninemia (HPA) and the clinical manifestation of PKU, which can be seen in *Table 1.I*.

Table 1.I Classifications of HPA and PKU diseases according to the Phe concentration in blood.

| Classification | [Phe] (µM) |
|---|---|
| Mild HPA | 120 – 600 |
| HPA | 600 – 1200 |
| Classical PKU | > 1200 |

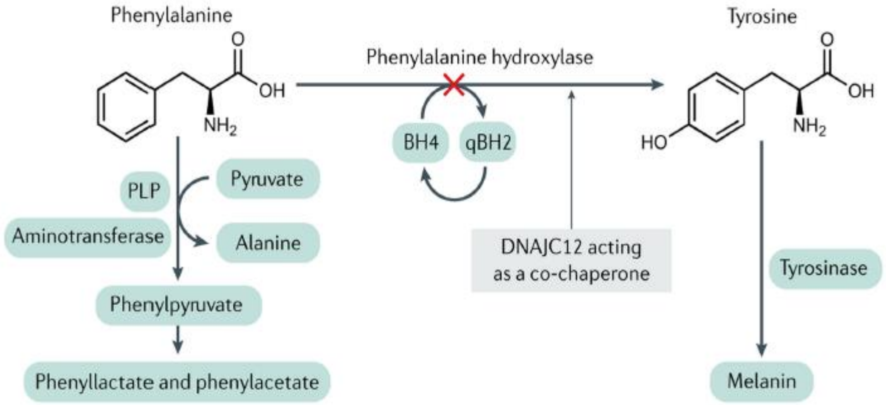

Fig. 1.2 Phe metabolism affected by the inactivity of PAH in PKU cases (14).

This disease has an average incidence of 6.5:100000 worldwide.[2] If left untreated, PKU leads to severe intellectual impairment and behavioural issues due to affectations in the central nervous system related to disturbances in dendritic growth, synaptic connectivity, reduction of cerebral glucose metabolism, large neutral amino acid (LNAA) and neurotransmitter deficiencies.[14] However, thanks to neonatal screening, early detection is possible and, with adequate management, the prognosis is good. The main treatment consists of the adherence to a Phe-restricted diet for life which, on its own, is enough to prevent neurological decline. However, due to the difficulties in maintaining this Phe-restricted diet, alternative treatments are under development, such as enzyme replacement therapy, gene therapy, liver transplantation, BH4 therapy, the use of LNAA to compete with Phe at the blood brain barrier and the use of glycomacropeptide as an adjunt to the Phe-restricted diet.[15]

Periodic controls, weekly, fortnightly or monthly depending on the age of the patient, of the Phe levels in blood are routinely carried out at reference hospitals to ensure that they are kept at acceptable levels. Nowadays, amino acids determination in hospital laboratories is performed by ultra-performance liquid chromatography-tandem mass spectrometry (UPLC-MS/MS) and different biological fluids can be analysed (such as plasma, blood, urine and cerebrospinal fluid). Regarding Phe in particular, analysis can be carried out using dried blood spots, which can be easily shipped to the hospital without requiring the presence of the patient. However, currently patients lack the possibility to keep a closer control of their pathology from their own homes, as there are not commercially available POC devices to be used at home. Nonetheless, work towards the development of a POC device for Phe determination at home is undergoing, and some reports about Phe determination in different biological fluids, such as urine, plasma and sweat, by different methods of detection have already been published.[16–19] Nevertheless, very few reported devices use blood as sample, and those that do present different drawbacks, such as the need for sample pre-treatment in the form of dilution[20] and lack of robustness and need for storage under-vacuum conditions.[21]

## 1.2. Analytical chemistry: towards miniaturization of analytical systems

Analytical chemistry may be broadly defined as a metrology science focused on obtaining quantitative and qualitative information about the nature of matter, as well as the development and improvement of analytical tools and methods to answer scientific and socials needs related to the determination of the matter composition. These social needs have evolved during time, demanding better, faster and more affordable solutions to analytical issues. Therefore, analytical chemistry has evolved from a science confined at laboratories and performed by qualified personnel to a real time and *in situ* discipline, and ubiquitously found in every area of interest, such as healthcare and diagnostics,[22–25] culturing and analysis,[26–29] nucleic acid assays,[30–32] drug screening and discovery,[33] omics,[34–36] environmental analysis,[37–43] food analysis[44–46] and space exploration.[47–51]

The publication in 1990 by Manz *et al.*[52] was an inflection point in the field of analytical chemistry, and constitutes a milestone in the miniaturization trend that was occurring at the time. It stablished the concept of a Micro Total Analysis System (µTAS) as a miniaturized version of Total Analysis System (TAS) that had arisen during the 80s. The development of TAS responded to the need to assemble and automate the different steps involved in a given analytical process. The µTAS, or lab-on-a-chip (LOC) takes this concept a step forward by downscaling the size to a chip-like device and reducing the volumes of sample, reagents and waste, which in turn leads to lower times of analysis. The decrease in size also enables its transportation making POC devices a reality. This evolution was possible largely thanks to the technology already developed in the field of Microelectronic Mechanical Systems (MEMS).[53]

As a consequence of the miniaturized nature of µTAS, progressively portable devices are being developed for *in situ* measurements. An additional trend within the µTAS field is the development of multiplexed POC devices which can quantify various analytes simultaneously in a fast, reliable and low cost manner.[54] This is particularly important for healthcare analysis, as the determination of a single biomarker may not be reliable for a proper diagnosis or monitoring of a disease.

In parallel to the miniaturization trend, since the early 2000s there has been a shift towards Green Analytical Chemistry (GAC) that derives from Green Chemistry, and its 12 principles that arose in the 1998.[55] GAC strives to make analytical processes more environmentally friendly by means of miniaturization in order to downscale the volumes of reagents, wastes and samples, the avoidance of harmful chemicals, avoidance of derivatization and sample pre-treatment processes, the promotion of the use of renewable sourced reagents, the reduction of energy consumption and cost and the increase of safety for the operators.[56–58]

Likewise, in 2003, the World Health Organization released the ASSURED criteria that requires POC devices to be Affordable, Sensitive, Specific, User-friendly, Rapid and Robust, Equipment-free and Delivered.[59] Later, in 2019, these criteria were extended to include three more characteristics: Real-time connectivity, Ease of specimen collection and Environmental friendliness, thus forming the new acronym REASSURED.[60]

## 1.3. Microfluidics in miniaturized analytical platforms

The miniaturization trend that led to the development of µTAS involved the downscaling of the microfluidic platforms dimensions, a reduction in the channel size and a diminishment of the sample and reagents volume used. The reduction of the scale of the channels and compartments where liquids flow leads to an increase in the surface to volume ratio, which causes the fluids at the microscale displaying a different behaviour and characteristics than in the macroscale. As a consequence, surface interactions dominate and surface tension becomes the dominant force in these type of systems.[61] Laminar flow is a distinctive feature of miniaturized microfluidic platforms.[62]

This type of behaviour can be characterized using the dimensionless Reynolds number (Re), which relates the inertial ($f_\mathrm{i}$) and viscous forces ($f_\mathrm{v}$) of a fluid and results from the expression indicated in *Eq. 1.1*:

$$\mathrm{Re} = \frac{f_\mathrm{i}}{f_\mathrm{v}} = \frac{\rho v D_\mathrm{h}}{\eta} \qquad \text{Eq. 1.1}$$

in which $\rho$ ($\mathrm{kg{\cdot}m^{-3}}$) is the density of the fluid, $v$ ($\mathrm{m{\cdot}s^{-1}}$) is the velocity of the fluid, $D_\mathrm{h}$ (m) is the hydraulic diameter of the channel and $\eta$ ($\mathrm{N{\cdot}s{\cdot}m^{-2}}$) is the shear viscosity of the fluid. $D_\mathrm{h}$ is in turn defined by *Eq. 1.2* as:[63]

$$D_h = \frac{4\,Area}{P_\mathrm{w}} \qquad \text{Eq. 1.2}$$

where the area corresponds to the cross-section area and $P_\mathrm{w}$ is the wetted perimeter of the channel.

From Eq. 1.1, we can see that when the Re is high (over 10000), the inertial forces are dominant which corresponds to a turbulent flow (*Fig. 1.3A*) which is characterize d by random movement and chaotic mixing. When the Re is low (less than 2000), the prevailing forces are the viscous ones. Thus, the fluid displays a laminar flow *(Fig. 1.3B)*, in which parallel fluids streams form, and mixing is minimal and caused only by molecular diffusion. This fluidic behaviour allows a close spatiotemporal control of the fluids, which can be used to our advantage in relation to different applications such as separation techniques, cell screening, protein positioning and membrane assembly.[64–68]

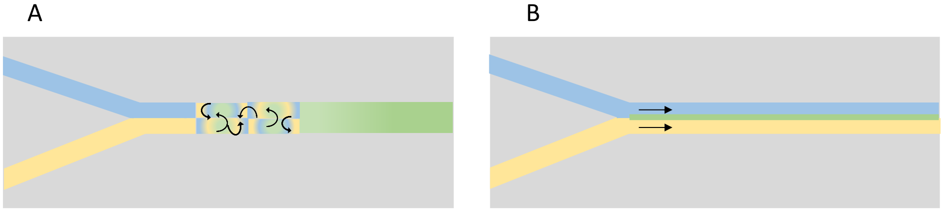

Fig. 1.3 Schematic representations of the turbulent flow (A) and the laminar flow (B) of fluid one (blue) and fluid two (yellow) injected from two different inlets converging in the same microchannel, and the resulting mixing (green).

Nevertheless, for the applicability of some µTAS, it is important to accomplish an optimum mixing of the different reagents involved in the analytical process. Because the laminar flow relies on diffusion as the driving force to achieve mixing, the times for this process to occur are unacceptably long, particularly for larger molecules.

Another two relevant dimensionless numbers to define fluid dynamics are the Peclet numer (Pe) and the Fourier number (Fo).[62,69] The first one expresses the relative importance of convection to diffusion (*Eq. 1.3*):

$$\mathrm{Pe} = \frac{v\,L}{D} \qquad \text{Eq. 1.3}$$

in which $L$ (m) is the characteristic length of the channel and $D$ ($\mathrm{m}^2{\cdot}\mathrm{s}^{-1}$) is the diffusivity for a spherical molecule of radius $a$ (m). $D$ can be defined according to the Stokes-Einstein relationship defined in *Eq. 1.4:*

$$D \sim \frac{K_\mathrm{B} T}{6\pi\eta a} \qquad \text{Eq. 1.4}$$

in which $K_\mathrm{B}$ is the Boltzman constant and $T$ (in K) is the temperature. According to the Pe, we can calculate the channel width necessary for a given particle flowing at a given velocity to completely mix.

The Fo (*Eq. 1.5*) expresses the ratio between the residence time ($T_r$) and the mixing time ($T_m$).

$$\mathrm{Fo} = \frac{T_\mathrm{r}}{T_\mathrm{m}} = \frac{L\,D}{{D_h}^2\,v} \qquad \text{Eq. 1.5}$$

Therefore, if Fo > 1, $T_\mathrm{r}$ is enough for mixing to occur, and it can be achieved by decreasing the flow rate or the diameter of the channel, or by increasing the length of the channel.

To avoid the previously mentioned problem of exclusively diffusion-driven mixing and achieve fluidic mixing at short times it is necessary to introduce active or passive micromixers in the microfluidic platforms, which will be discussed more in depth in a later section of this chapter.

## 1.4. Microfluidic analytical platforms: integration of the basic unitary operations

One main characteristic of the TAS and µTAS is the ability to integrate all the different functional elements necessary to carry out the basic unitary operations that constitute a complete analytical process.[70] Therefore, the final configuration of the analytical platform needs to be designed and tailored taking into consideration the particular purpose for a given analytical microsystem. We can classify the different functional elements in various categories such as fluid management (including the introduction of the fluids into the platform and its transport), pre-treatment of the sample, detection, and data treatment and signal processing (*Fig. 1.4*).

Fig. 1.4 Basic unitary operations for a given analytical process integrated in a µTAS.

### 1.4.1. Fluid management

A µTAS should have a reliable fluidic interface between the microfluidic platform and the external elements. Hence, fluidic connections should be low cost, easy to assemble and reuse, withstand high pressures and conditions, be chemically inert, avoid cross-contamination, have a minimal dead volume, and allow a high density of connections if necessary.[71,72] Ideally, these connections should be standardized in order for µTAS and LOCs to be commercially successful, but this has yet to be achieved. Instead, the fluidic connexions are usually designed depending on the particular use for a given device. There have been several types of connections developed during the last years. There are works reporting adhesive-free reversible connections which can be just simple insertions of a tube on an opening in the surface of a microfluidic platform[73–75] or rely on the use of an additional compression mechanism such as screws,[76,77] vacuum[78] or magnetic forces.[79] Alternatively, there are also adhesive-based permanent fluidic connections[80] which stand out by their robustness (although the use of adhesive entails the possibility of clogging and chemical incompatibilities), and connections that are integrated monolithically on the microfluidic platform itself by different methods, such as injection moulding,[81,82] welding[83,84] and 3D-printing.[85–88]

The microanalyzers developed in this work rely on flow injection analysis (FIA): a continuous flow methodology based on the discrete injection of a determinate volume of a sample into the microchannels of the analytical platform, where a carrier solution is already flowing. This way, the sample is carried through each of the elements of the microfluidic platform and eventually, to the detector (*Fig. 1.5*).

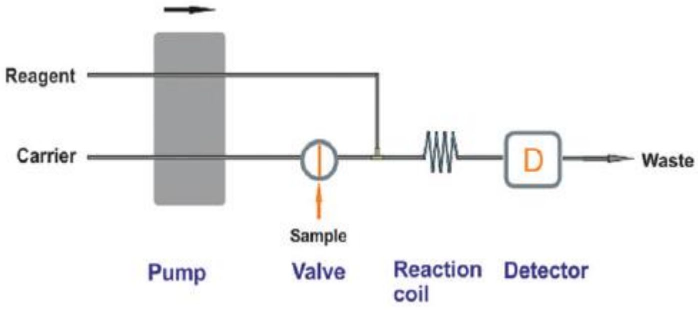

Fig. 1.5 Schematic representation of a basic FIA system (89).

A FIA system, unlike a discrete analysis, allows a continuous measurement of the signal. When the sample is injected, a transitory analytical signal in form of a peak instead of a plateau-like signal in chemical equilibrium is obtained.[89] The height of this peak can be related to the concentration of the analyte. Once the sample plug has left the detection chamber, the signal returns to a baseline, allowing for the correction of possible signal drifts.

FIA systems are easily adapted by the inclusion of computer-controlled commutation elements to obtain multicommutated flow analysis systems (MCFA) that display a high level of versatility and automation.[90]

Once liquids are inside the microfluidic platform, there are different approaches to manage them through the microchannels, and control flow rate, direction and duration. According to the main strategy employed for fluidic propulsion we can differentiate those that rely in capillary forces such as the case of lateral flow based devices, pressure-driven devices, centrifuge-based platforms, and electrokinetic and acoustically driven devices.[91]

The analytical systems developed in this work fall within the group of the pressure-driven devices, which allows a close control of the flow rate. There are works in the literature that integrate the elements responsible for the liquid control and transport into the analytical microsystem itself, and the increased portability makes them great as POC devices. However, this integration is in most cases difficult and increases the complexity of the analytical platform. Therefore, hybrid systems in which these elements are outside the microfluidic platform are also common. The *Grupo de Sensores y Biosensores* (GSB) of the *Universitat Autònoma de Barcelona* (UAB) (Bellaterra, Spain) group has experience in this hybrid systems, particularly with the use of peristaltic pumps and solenoid valves as active actuators for fluidics.

#### 1.4.1.1. Peristaltic pumps

Most pumps can be classified into two different categories: mechanical or non-mechanical pumps. Peristaltic pumps fall into the former group as they use peristaltic movements to propel fluids, and this can be achieved by the use of different energy sources, such as motors, piezoelectric elements, temperature or pneumatic of electrostatic actuation. [92]

The most popular one is the use of motors due to its simplicity and high throughput, and also because it is possible to use only one motor to propel fluids through different channels. Therefore, these peristaltic pumps have been extensively used, commercialized and miniaturized, and this will be the type of pump mainly used in this work. A schematic representation of this peristaltic pumps and its components can be seen in *Fig. 1.6.*[93]

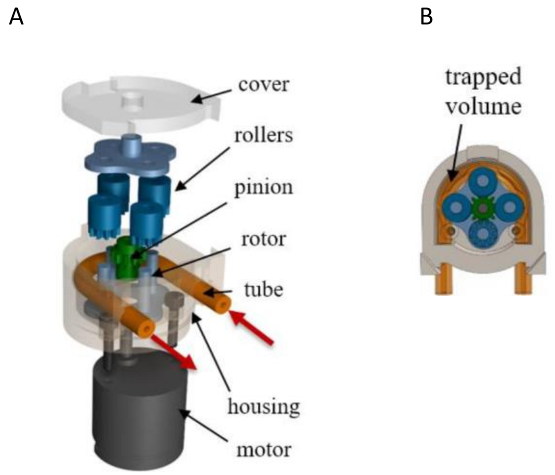

Fig. 1.6 Schematic representations of a 4 roller rotary peristaltic micropump components (A) and top view (B). Adapted from (93).

### 1.4.1.2. Valves

Like in the case of pumps, valves can also be classified into active or passive depending on whether they require an external energy input or not. Valves are the elements responsible for the control of the direction of the fluids and they can be miniaturized to be integrated into microfluidic platforms.[94]

In this work we will use mainly two types of valves, a 6-way injection valve and a 3-way solenoid valve.[90] The mechanism for both valves can be seen in *Fig. 1.7* and *Fig. 1.8* respectively.

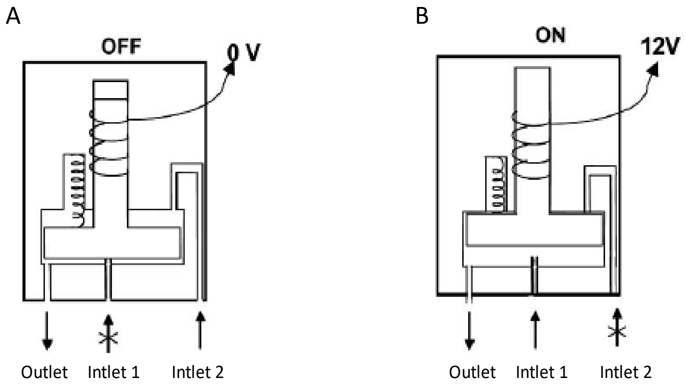

Fig. 1.7 Schematic representations of a 3-way solenoid valve, on the OFF (A) and ON position (B). Adapted from (90).

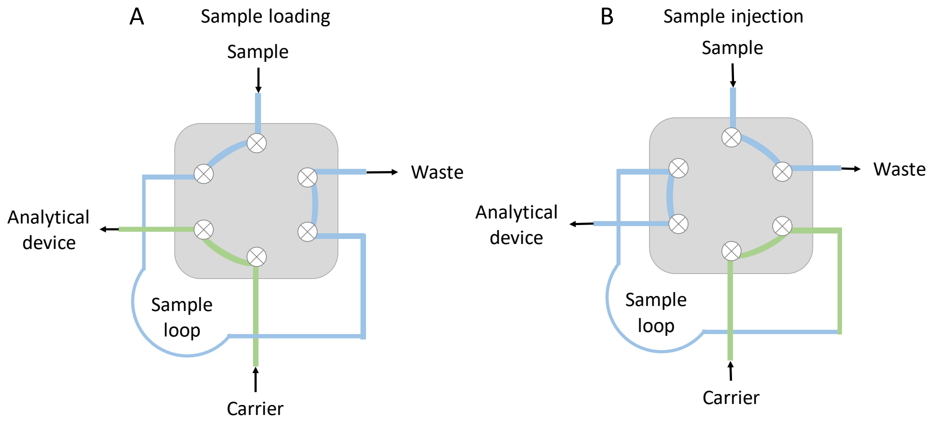

Fig. 1.8 Schematic representations of a 6-way injection valve working mechanism steps: A) sample loading and B) sample injection.

### 1.4.2. Sample pre-treatment

Depending on the particular analytical process carried out by the µTAS or the detection system used it may be necessary to treat the sample prior to the detection of the analyte of interest. Traditionally, most of these steps took place outside the µTAS platform, but efforts in the last years have been undertaken in order to incorporate them into the analytical microsystem in order to fully consolidate the complete analytical process on the same platform.[95] Several pre-treatment steps have been already incorporated into µTAS, such as:

- Separation: used in order to isolate the analyte of interest from the rest of the sample matrix by means of different approaches such as the use of microfilters or taking advantage of the diffusion of the target analyte across a laminar boundary while the rest of the particles are retained in the original flow, among others.[96–99]

- Pre-concentration: useful for samples that contain low concentrations of the analyte of interest, with the intention of increasing the sensitivity of the detection method. These methods can be broadly divided into static and dynamic techniques.[100] The static ones are solvent extraction techniques, surface binding approaches and the use of porous and nanochannels, whereas the latter group can be further subdivided in those techniques that are based on changes in the analyte velocity across a sample and buffer boundary (such as field-amplified sample stacking (FASS), field-amplified sample injection (FASI), pH-mediated stacking, isotachophoresis (ITP) and sweeping) and those that rely on the velocity of the analyte approaching zero at some point of the channel (isoelectric focusing (IEF), temperature gradient focusing (TGF) and electric field gradient focusing (EFGF)). Additionally, on-chip Polymerase Chain Reaction (PCR) processes can be used to increase the DNA available for analysis.[32,101]

- Cell lysis: is necessary for the analysis of intracellular material and it involves the rupturing of the cell membrane by various means,[102] such as mechanical,[103,104] chemical,[101,105] enzymatic,[106] thermal,[107] acoustic[108–110] or electrical.[111–113]

- Derivatization: consists of obtaining an alternative chemical species that is more suitable for an efficient detection.[114]

- Labelling: in the case of biochemical analysis, analytes may be specifically or unspecifically labelled for separation or detection.[115]

### 1.4.3. Reaction

In the cases that a reaction is necessary for the analysis to take place is necessary to ensure an optimum mixing of the reagents. As has been previously mentioned, the laminar flow that dominates at the microfluidic scale hinder this mixing, and the inclusion of micromixers in the microfluidic platform is necessary in order to promote it. There are two main groups of micromixers, passive or active, according to the source of the energy to drive the mixing process.[69,116]

The active mixers use different external energy sources such as pressure,[117,118] temperature,[119,120] acoustics,[121–124] electric[125–128] and magnetic fields.[129–133] These active mixers involve the incorporation of additional actuators to the microfluidic platform, contributing to an increase of its complexity and cost.

On the contrary, passive mixers rely only on the energy coming from the element driving the fluid at a determined flow rate. This flow is restructured by the microfluidic channels arrangement to speed the mixing, owing to the increase of the interface between the different fluids and the decrease of the diffusion path. The simplest designs for this type of micromixers are the T-mixer (*Fig. 1.9A*) and the Y-mixers (*Fig. 1.9B*), which consist of two inlets that converge in the same channel in a T-type or Y-type union respectively. This type of micromixers rely only on diffusion happening in a laminar flow, so the channels need to be long enough to ensure total mixing. In order to reduce this length, other approaches for mixing rely on the reduction of width of the channels or the streams, by using multiple parallel streams (*Fig. 1.9C*) or by hydrodynamic focusing (*Fig. 1.9D*). More complex micromixers are serial lamination micromixers, which split and recombine the streams to increase mixing, and can have multiple configurations, as seen in *Fig. 1.9E-H*. Similarly, another group of micromixers are based on the creation of chaotic mixing by the introduction of different geometries in the channel that split, stretch, fold or break the flow stream. These geometries can be obstacles in the walls or channels, zig-zag designs, and different types of rips and grooves on the channels surfaces.

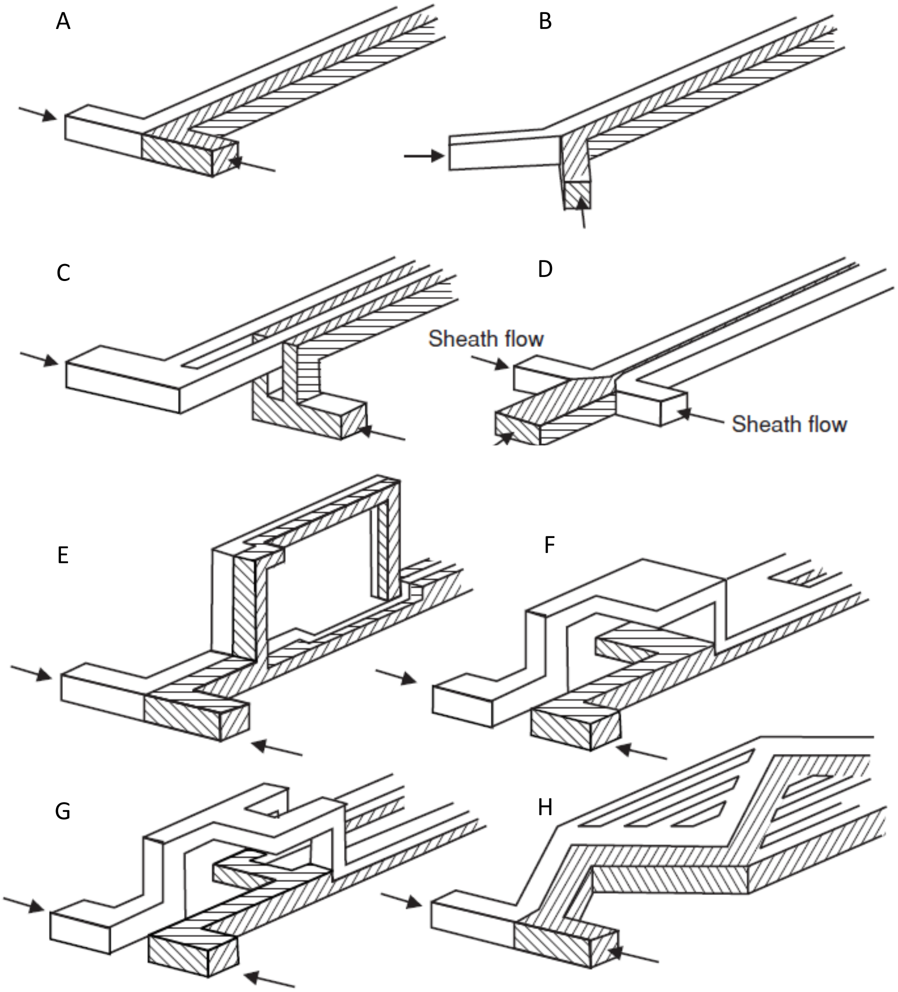

Fig. 1.9 Schematic representations of the main passive micromixer structures: A) T-mixer, B) Y-mixer, C) parallel lamination, D) hydrodynamic focusing and E-H) different configurations for serial lamination micromixers . Adapted from (116).

### 1.4.4. Detection

The detection is the most important unit operation of the analytical microsystem as it is the responsible for the detection and quantification of the target analyte. When selecting a suitable detection method for an analytical microsystem for a particular application it is important to take into account whether an easy and cost-effective integration into a small device is possible. Moreover, the level of sensitivity, selectivity and limit of detection (LD) that a detection method offers is also a determining factor.

Several different methods of detection exist. The two most common detection groups are optical and electrochemical methods. Within the first group, there are several optical approaches such as absorbance,[134–136] fluorescence,[30,137–139] chemiluminescence,[47,140,141] surface plasmon resonance[142–145] and surface enhanced Raman spectroscopy.[146–150] Electrochemical detection includes potentiometry,[151–153] conductivity,[154] amperometry,[155–157] impedance[158] and voltammetry.[159–161] There are also microsystems that use mass spectrometry as detection method.[162–165]

The GSB group has extended experience and knowledge in the development of microsystems based on both electrochemical[51,166–169] and optical[170–173] methods of detection. The devices presented in this dissertation all rely on electrochemical detection, specifically, potentiometry.

## 1.5.Electrochemical detection methods

Electrochemical detection is commonly used for POC devices due to their selectivity, low cost, fast response, simplicity and the possibility to use miniaturized electrodes.

### 1.5.1. Amperometry

Traditionally, most electrochemical biomedical POCs are based on amperometric detection, from which the glucometer is the most well-known.[174] This method of detection consists of the measurement of a current produced by the reduction or oxidation of electroactive species, which is linearly dependent on the target analyte activity, under a constant potential conditions. This amperometric cell involves the use of an indicator electrode, at the surface of which the electroactive species can be found, a reference electrode, which maintains the fixed potential, and optionally, an auxiliary electrode which helps measuring the current at a constant potential.[175]

### 1.5.2. Potentiometry

Potentiometry consists of measuring a difference in potential between two electrochemical half-cells at near-zero current conditions (*Eq. 1.6*). One of these half-cells acts as the indicator electrode whereas the other acts as the reference electrode, and they are electrically connected via a salt bridge.

$$E_{\mathrm{cell}} = E_{\mathrm{I}} - E_{\mathrm{ref}} \qquad \text{Eq. 1.6}$$

Where $E_I$ is the potential of the indicator electrode, $E_{ref}$ is the potential of the reference electrode and the $E_{cell}$ is the resultant potential of the electrochemical cell.

According to the phase-boundary potential model (*Fig. 1.10*), the total potential measured in the electrochemical cell corresponds to the sum of all the interface boundary potentials ($\varepsilon$) within this electrochemical cell.[176] Of all these interphase potentials, the one arising at the interface between the sample solution and the indicator electrode ($\varepsilon_6$ in *Fig. 1.10*) depends on the activity of the ion of interest present in the sample for which the membrane is selective, as defined by the Nernst equation (*Eq. 1.7*):[177]

$$E_{\mathrm{I}} = E_{\mathrm{I}}^{\circ} + \frac{RT}{z_{\mathrm{A}}F} \cdot ln\, a_{\mathrm{A}}^{z_{\mathrm{A}}} \qquad \text{Eq. 1.7}$$

in which $E_{\mathrm{I}}$ is the electrode potential (mV), $E_{\mathrm{I}}^{\circ}$ is the standard potential of the electrode, $R$ is the gas constant (8.314 J $K^{-1}$ $mol^{-1}$), $T$ is the absolute temperature, $F$ is the Faraday constant (96487 C $mol^{-1}$), $z_A$ is the charge of the ion A and $a_A$ is the activity of the ion A. The relation between ion activity and ion concentration is seen in *Eq. 1.8*:

$$a_A \ = \ \gamma \ \cdot \ [A] \qquad \text{Eq. 1.8}$$

where $a_{\mathrm{A}}$ is ion activity, γ is the activity coefficient and [A] is the concentration of the ion. In turn, $\gamma$ is defined by the Debye-Hükel limiting law (*Eq. 1.9*) as a function of the ionic strength of the solution:[178]

$$\log \gamma \ = \ -0.509|z_{+}z_{-}|I^{1/2} \qquad \text{Eq. 1.9}$$

for an aqueous solution at 25 °C and $I$ is the ionic strength. Therefore, under certain conditions of low stable $I$ values, the value of $\gamma$ is close to 1, hence, $a_A$ can be considered to be equal to the concentration of A.

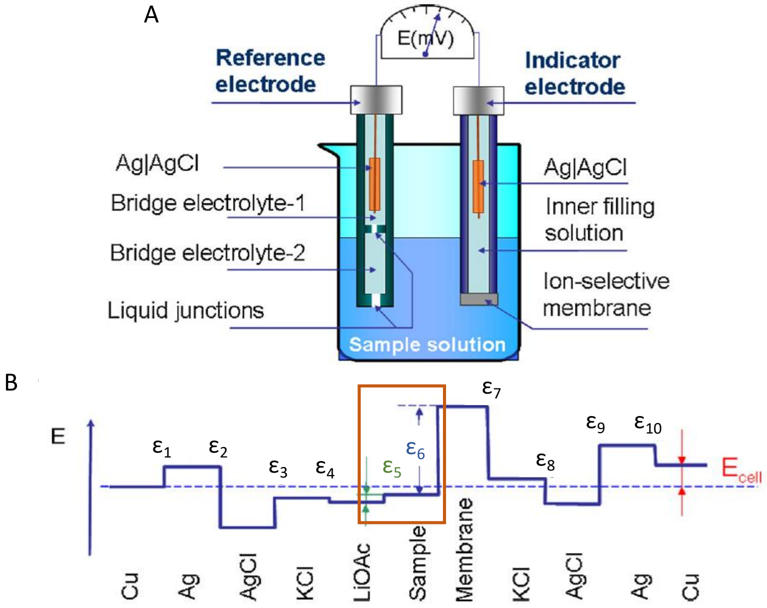

Fig. 1.10 A) Representation of a potentiometric cell assembly. B) Representation of the boundaries potentials ($\varepsilon_1$ to $\varepsilon_{10}$) that conform the final potentiometric cell potential ($E_{cell}$). Interphase potentials dependent on the ion of interest concentration of the sample indicated in orange. Adapted from (176).

## 1.6. Ion selective electrodes

Chemical sensors transform chemical information into an analytical signal.[179] They require a receptor or recognition element, which can specifically bind to the analyte of interest, and a transducer, to transform the signal resulting from the analyte-receptor interaction into a useful signal, which can in turn be amplified and processed. A subgroup of chemical sensors is potentiometric sensors. This type of sensors commonly uses Ion selective electrodes (ISE) as indicator electrodes, as is the case of the microanalyzers described in this thesis. In potentiometric sensors the reference electrode is, usually, a Ag/AgCl electrode.

Prior to use, potentiometric sensors must be calibrated by measuring the potential when in contact with standard solutions of a given analyte. From this, the values corresponding to the linear regression such as the one in *Eq. 1.10* can be determined experimentally:

$$E_{\mathrm{cell}} = E^{\circ}_{\mathrm{cell}} + S \cdot log\, a_{\mathrm{A}} \qquad \text{Eq. 1.10}$$

where $E^{\circ}_{\mathrm{cell}}$ is the potential difference between the indicator and reference electrodes when $a_{\mathrm{A}} = 1$ and $S$ is the slope of the lineal function.[176] This $S$ value corresponds to the sensitivity and theoretically must be +59.2 mV·dec$^{-1}$ and +29 mV·dec$^{-1}$ for monovalent and divalent cations respectively. In the case of monovalent and divalent anions the sensitivities are the same but in negative values.

Despite some disadvantages (such as a fixed sensitivity limited to 59 mV·dec$^{-1}$ for monovalent ions and the need for a stable signal during long measurements and between calibration and measurements) ISEs have been extensively used due to the simplicity of its use and setup, its low cost and energy consumption, high efficiency and reliability and its small size and portability.

The development of ISEs can be traced back to 1906, when Cremer[180] related changes in the potential of a glass membrane with changes in pH of a solution in contact with this membrane. During the following years the classic liquid-contact ISEs (LC-ISEs) were stablished (*Fig. 1.11A*). These ISEs relied on an internal solution (IS) which is separated from the sample by an ion selective membrane (ISM). The presence of the IS presents several drawbacks, such as the need of refills and the need to keep a vertical position, the risk of leakage and the difficulty to reduce the size and integrate this sensor in a miniaturized platform.[181]

In order to overcome these disadvantages, the first solid-contact ISE (SC-ISE) was created in 1971 and consisted of a metal wire coated with a $Ca^{2+}$ selective polymeric membrane.[182] This ISE performance was not satisfactory due to a high potential drift caused by the blockage of charge transfer between the ISM and the metal caused by the lack of a proper fast and reversible ion-to-electrode transduction. This brings about, in 1992, the development of a novel SC-ISE (*Fig. 1.11B*) incorporating a polypyrrole (PPy) based ion-to-electron transducer layer to achieve a stable and reproducible potential, which is referred here as a solid contact (SC) layer.[183]

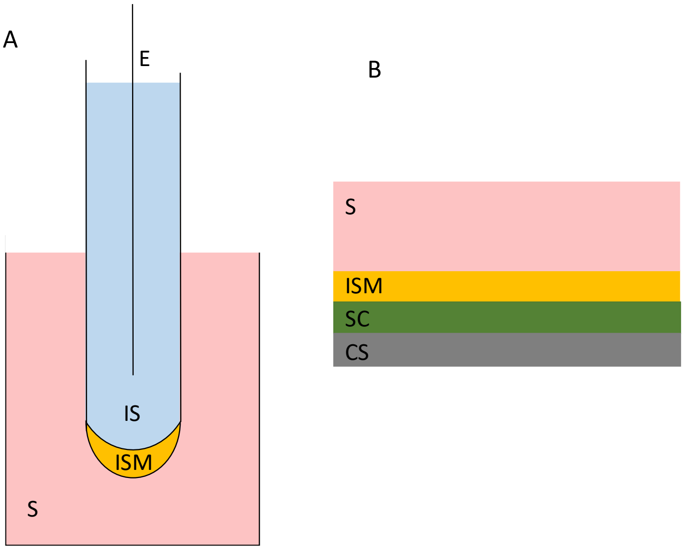

Fig. 1.11 Schematic representations of a classic LC-ISE (A) and a SC-ISE (B). E: electrode, IS: internal solution, ISM: ion selective membrane, S: liquid sample, SC: solid contact layer, CS: conductive support.

As stated previously in this chapter, the resulting measured potential for a sample containing a given target analyte concentration is the sum of all interface potentials of the system. The response mechanism for the interface potential between the ISM and the SC layer is different depending on the type of material used, and according to this, we can differentiate two different groups.[184]

The first group of materials corresponds to conducting polymers, such as PPy,[185–187] poly(3,4-ethylenedioxythiophene) (PEDOT),[188–191] poly(3-octylthiophene) (POT),[192–194] and polyaniline (PANI).[195–198] The response mechanism of SC-ISEs containing these polymers is known as redox capacitance mechanism[199] and is based on the reversible and fast redox capacity of these molecules, which is used for the ion-to-electron conversion. In *Fig. 1.12A* we can see a depiction of this response mechanism for the determination of potassium ions ($K^+$) using an $Y^-$ anion-doped PEDOT as polymer on top of a glassy carbon (GC) support, with the ion transfer (IT) and electron transfer (ET) processes detailed. Conductive polymers have been intensively used to fabricate well performing ISEs with a stable potential. However, the use of these conductive polymer also presents challenges. Significantly, their hydrophilic nature allows the formation of a water layer between the ISM and the SC layer and this in turn hinders the ion-to-electron transduction and deteriorates the adhesion between the ISM and the SC layer, leading to mechanical failure. These effect has been identified even in the case of water repellent polymers, particularly at the contact defect points between the ISM and the SC layer. Additionally, these conductive polymers can be sensitive to light or reactive to chemical species (ex. $O_2$ and $CO_2$) leading to undesired chemical side reactions that can interfere with the redox capacity of the system.

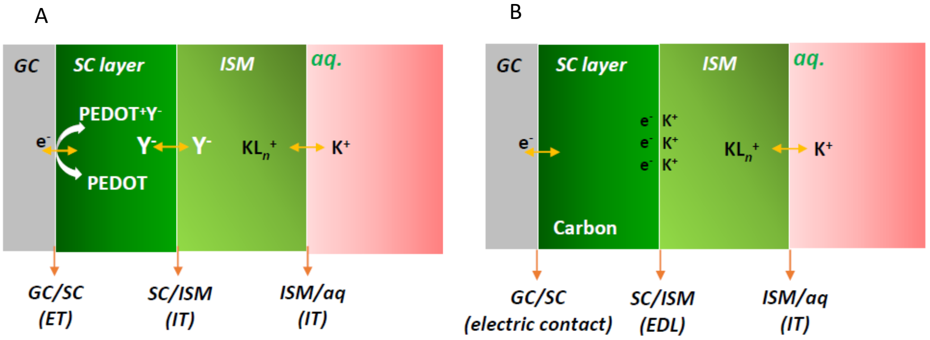

Fig. 1.12 Schematic representations of the redox capacitance mechanism (A) and the electric double layer mechanism (B) for SC-ISEs. ISM: ion selective membrane, SC: solid contact, IT: ion transfer, ET: electron transfer, GC: glassy carbon electrode substrate, aq: aqueous solution. The three different interfaces are indicated with orange arrows. Adapted from (199).

The second group of materials for the SC layer corresponds to carbon materials, which present a desirable high conductivity, chemical inertness and are not sensitive to light. Carbon single-walled[200–202] and multi-walled nanotubes,[188,203,204] graphene,[205–209] fullerens,[210] 3D microporous carbon[211,212] and colloid-imprinted mesoporous carbon[213,214] have all been used as transducers for SC-ISEs. This ISEs response is based on the electric double layer (EDL) mechanism[199] which consists on the formation of an asymmetrical capacitor on the ISM-SC layer interface, with the ion of interest on the ISM side and the electron on the SC side. In *Fig. 1.12B* we can see the representation of this response mechanism for the detection of the ion $K^+$ using a carbon based transducer.

The ISM is the element of the ISE that makes it selective for a particular ion. Most ISM are composed of three main constituents: a polymer, a plasticizer and a ionophore, and may or may not contain an additive.

- The polymer constitutes a stable interface which serves as a matrix to retain the rest of the elements. This material must have a good mechanical strength, film-forming ability, be immiscible and undergo minimal swelling with water.[215] The most commonly used polymer for ISE fabrication that fulfils these requirements is poly-vinyl chloride (PVC) due to its cheap cost.

- The plasticizer is employed because the glass transition temperature ($T_g$) of most polymers is higher than the ambient temperature at which this ISEs are used. Therefore, a plasticizer is used at a high percentage for the matrix to display a viscous state that increases ionic mobility and it constitutes the solvent for the rest of components.[216]

- The ionophore complexes the ion of interest and is the responsible for the selectivity of the ISM. Currently, ionophores have been used for the potentiometric detection of more than 70 different analytes, comprising ions, surfactants and some non-ionic molecules.[217] Must be adequately soluble in the plasticizer.

- The additive increases the selectivity of the ISM as it ensures the extraction of the ion of interest without the extraction of the counter-ion. When the ionophore used is not charged, the additive used is of opposite charge from the ion of interest as it avoids the extraction of counter ions and this charged sites also help stabilize the ion-ionophore complex and reduce electrical resistance thus promoting ionic mobility. If the ionophore is charged, an additive of opposite sign from the ionophore (that is, the same as the ion of interest) is not required but may be used, as its presence may optimize selectivity.[216]

The main problems that a ISM may present is the poor mechanical adhesion to the electrode substrate by part of the PVC, and eventually lead to a separation of the ISM from the subjacent substrate, and the leaching of the plasticizer into the sample, which may result in a loss of selectivity and potential stability respectively.

Another aspect to take into account is the fact that the performance of some ISEs is improved and the potential drift is reduced when a conditioning step is carried out prior to use.[218] In this step, the ISEs are submerged into a solution of a determinate concentration of the ion of interest overnight in order to condition the ISE membrane and, thus, allow a better contact between the solution and the ionophore present in the membrane.[219]

### 1.6.1. Increasing stability and reproducibility: towards free calibration and auto-calibrating ISEs

There are two aspects to take into account regarding the use of ISEs without a prior calibration.[184] The first aspect is related to the stability of the potential, which correlates to the frequency of calibration procedures needed for a particular individual electrode in order to obtain reliable measurements. With high stability and low potential drift the frequency of calibration procedures needed is reduced, and this may be accomplished primarily by optimizing the SC layer to achieve an unpolarised interface and a high exchange current density.

The second aspect is the $E^{\circ}_{\mathrm{cell}}$ reproducibility between ISEs. This parameter corresponds to the Y-intercept value of the lineal regression of the calibration curve. If this parameter is stable between different ISEs from the same batch, these means that they will all behave identically and it would not be necessary to calibrate each one of them individually prior to use. This $E^{\circ}_{\mathrm{cell}}$ is defined by all the ISE structure and is influenced by the potential of each individual interface.[218] Therefore, for the $E^{\circ}_{\mathrm{cell}}$ to be reproducible it is required a high degree of control of all interfaces of the system and, thus, a well-mastered and reproducible fabrication process is a must.

Currently, free-calibration electrochemical sensors are based on the intra-batch reproducibility of the analytical devices. Therefore, only a few of them need to be calibrated at the factory and the rest can be used without a previous calibration assuming that they will behave in the same manner as the calibrated ones.[220] Nonetheless, potentiometric ISEs present a low reproducibility between devices. For this reason, the GSB has developed a new approach based on an auto-calibrating step prior to use for every individual devices.[221]

This auto-calibration procedure consists of the use of two identical ISE. The one in contact with the sample acts as an indicator electrode and the other acts as the reference electrode. Prior to the analysis of the sample the auto-calibration procedure takes place. During this process, each ISE comes into contact with a solution of a given concentration of the ion of interest which must be within the ISE working linear range.

Two different concentrations are used, the lower one is in contact with the indicator electrode, whereas the higher one is in contact with the reference electrode. When the microanalyzer is connected to the reader, the resulting potential between both electrodes is measured. If both concentrations have a difference of a decade, for example, when using $10^{-5}$ and $10^{-4}$ M concentrations of a given analyte, the resulting calibration curve obtained for a monovalent ion must have a slope of –59.2 mV·dec$^{-1}$. But even if the ISEs are not identical and the resulting calibration curve differs from this theoretical value, a reliable quantification of the analyte would still be obtained from the interpolation in this calibration curve. The definition of this calibration curves is done according to the following calculations (*Eq. 1.11*), assuming a measured potential of 55.8 mV:

$$\begin{gathered}
-55.8 = a + b \cdot \ log[10^{-5}] - (b \cdot \ log[10^{-4}] + a) \\
-55.8 = \ b \cdot (log[10^{-5}] - log[10^{-4}]) \\
b = 55.8\, mV \\
-55.8 = \ 55.8 \cdot log[10^{-5}] + a \\
a = 223.2 \\
E = 55.8 \cdot log[A] + 223.2
\end{gathered} \tag{Eq. 1.11}$$

Then, the indicator electrode comes into contact with the sample, leading to a change in the measured potential. This new potential value can be interpolated into the calibration curve to obtain the total concentration of ion A in the indicator electrode. This can be easily calculated, as the volume of the detection chamber and the sample are known. This auto-calibration approach has already been evaluated using chloride (Cl$^-$) electrodes showing very promising results.[222]

### 1.6.2. Calibration curve

All analytic system need to be calibrated to characterize its analytical features. The calibration curve, in potentiometry, consists of the representation of the measured electrode potential E (mV) versus the logarithmic value of the $a_A$, which is used to interpolate the potential obtained when analysing a given sample to determine the unknown concentration of an analyte.

In a calibration curve we can identify three different regions depending on the type of response for a given $a_A$. These three regions can be differentiated in *Fig. 1.13:* a no response, a non-linear response and a Nernstian response region. The no response area occurs at very low $a_A$, when the sensor does not respond to the presence of the ion of interest and there is not a measurable change in the potential. The Nernstian response region is found at higher $a_A$, when the sensor presents a change in the measured potential that correlates lineally to the $a_A$, following the Nernst equation. In between these two regions, the non-linear response is found, when there is a change in the measured potential but that does not correlate lineally with the Nernst equation.

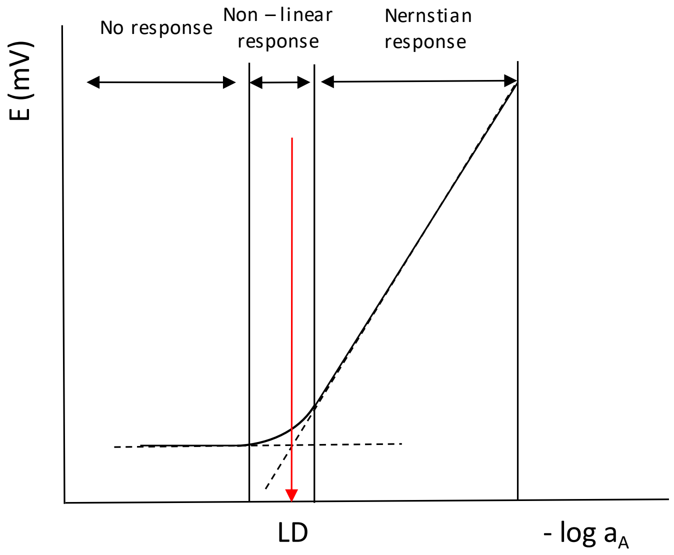

Fig. 1.13 Example of a calibration curve for a cation A. LD: limit of detection marked in red.

Regarding the Nernstian response, the slope of this calibration curve corresponds to the sensitivity of the analytical sensor. According to the Nernst equation this sensitivity at 25 °C equals to +59.2 mV·dec$^{-1}$ and +29 mV·dec$^{-1}$ for monovalent and divalent cations respectively. In the case of monovalent and divalent anions the sensitivities are the same but in negative values.

### 1.6.3. Limit of detection and linear range

The LD can be defined as the $a_{\underline{A}}$ at the point of intersection of the extrapolated lines resulting from the Nernstian response and the no response region.[177] This value is depicted in *Fig. 1.13* as LD, and this parameter indicates the lower $a_A$ that can be reliable measured by the analytical system. Alternatively, the linear range or working range of the analytic system is defined as the range of $a_A$ within which we can obtain a Nernstian response, and indicates the $a_A$ range where the sensor can give a reliable quantification of the analyte of interest.

Both the LD and the linear range are parameters of upmost importance that need to be taken into account when considering the suitability of a particular analytical system for a specific application.

### 1.6.4. Selectivity coefficients

In some cases, the potential measured by the analytical system may be altered due the presence of interfering substances in the sample. These substances can be either electrode/electrochemical interferences or chemical interferences. The first group include other ions that can also be detected by the ISE, giving a similar response to that of the ion of interest, therefore producing an apparent increase in the $a_A$. The second class include species that interact with the target ion and hence, decreases its activity, or substances that react with the ISE membrane, leading to changes in its chemical composition or blocking its surface, thus decreasing the ISE response to the presence of the target ion.

Considering complex sample matrixes, it is common to find interfering ions. Therefore, it is necessary to be able determine the ability of the ISE to distinguish the ion of interest, A from another interfering ion, B, that may be present in the sample. For this aim, the potentiometric selectivity coefficient ($K_{A,B}^{pot}$) must be determined. The smaller this parameter is, the higher the ISE preference for the target ion A. To determine the $K_{A,B}^{pot}$ there are two different methods: the Fixed Interference Method (FIM) and the Separate Solution Method (SSM).[223] The method used in this thesis has been the FIM, which consist on analysing standard solutions that mix varying concentrations of the ion *A* with a constant concentration of the interfering ion *B*, as opposed to having these two ions in different solutions, as would be the case of the SSM.

At very low $a_A$, the potential measured is mainly caused by the presence of the ion B. So, this measured potential corresponds the activity of ion B ($a_B$) and is independent from $a_A$. On the contrary, at higher $a_A$, the measured potential is dependent of $a_A$. Thus, $a_A$ can be obtained from the intersection between the extrapolated lines resulting from these two differentiated response regions, as represented in *Fig. 1.14*. The potentiometric selectivity coefficient can be calculated from the Nikolsky – Eisenman (*Eq. 1.12*) equation as seen in *Eq. 1.13*:

$$E = E^0 + \frac{RT}{z_A F} \ln\left(a_A + \sum K_{A,B}^{pot} a_B^{z_A/z_B}\right) \qquad \text{Eq. 1.12}$$

$$K_{A,B}^{pot} = \frac{a_A}{a_B^{\frac{z_A}{z_B}}} \qquad \text{Eq. 1.13}$$

where $z_A$ and $z_B$ are the charges of the ions *A* and *B* respectively.

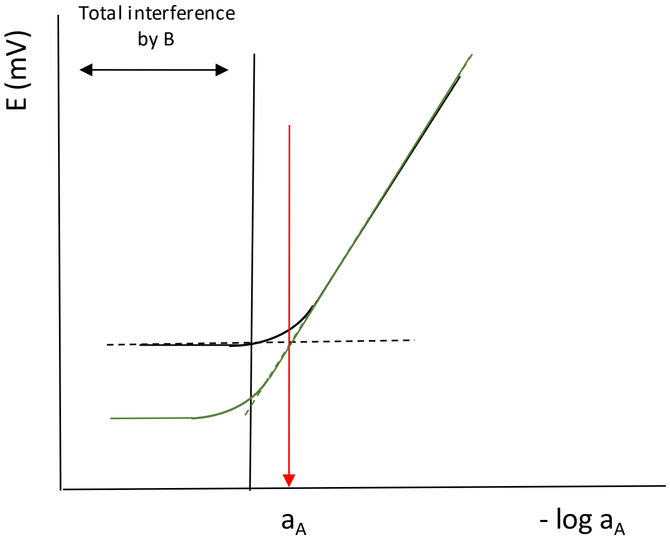

Fig. 1.14 Example of a calibration curve for a cation A in the presence of a fixed concentration of interfering ion B. $a_A$: activity of A marked in red. Calibration curve for cation A without the interfering ion B represented in green.

## 1.7. Materials for the fabrication of microfluidic platforms

During the design of a microfluidic analytical system there are several concerns to take into account when choosing a particular material to fabricate the analytical platform. The selected material has to be compatible with all the chemical substances and temperatures used during the operation of the device, as well as the functional components that need to be integrated into the platform for the analytical process. The material should also be cheap in case that the device is meant to be manufactured at large-scale, to reduce costs.

The main materials currently used for the fabrication of microfluidic platforms can be classified in three categories: inorganic materials, paper and polymers.

### 1.7.1. Inorganic materials

Inorganic materials were the first substrates used for the fabrication of microfluidic systems, mainly silicon and glass. Nowadays, other inorganic materials, such as low-temperature co-fired ceramics (LTCC) and vitroceramics are also commonly used.

Silicon was the first material used for microfluidics fabrication,[224] as methods for microfabrication using this material were well-known due to its extensive use in microelectronics. This material presents advantages such as an easily achieved surface modification, based on silanol group (-Si-OH) chemistry, and a decent biocompatibility.[225] However, the use of silicon has other drawbacks, like the difficulty to make active fluidic elements due to its high elastic modulus and the impracticability of its use in optical applications due to its opaque nature in the visible region.[226] Moreover, fabrication of silicon devices is, in most cases, complex as it requires clean room facilities and skilled personnel.

After some time, glass substituted silicon as the material of choice for fabricating microfluidics devices.[227–229] Similar to silicon, glass surface can be modified via silanes. Nevertheless, glass is biocompatible, has a relatively low nonspecific absorption, and has a high chemical and temperature resistance. In addition, glass is transparent and, therefore, suitable for optical applications.[226]

LTCC is a glass-ceramic composite material that usually presents alumina as a ceramic filler. It has been extensively used as packaging material in the integrated circuits field. In recent times, it has gained popularity as an alternative material for fabrication of microfluidics devices due to its chemical inertness, biocompatibility, stability at high temperatures, mechanical strength, packaging properties and easy integration of electronic circuits.[166,230–233] Moreover, its laminar commercialization is useful, as different layers can be patterned with different designs and then assembled, laminated and fired at high temperatures. This allows the design and fabrication of complex 3D microfluidic structures than can be difficult to achieve by other methods of fabrication.

### 1.7.2. Paper

Paper emerged as a novel candidate material for the fabrication of microfluidic devices when *Whitesides et al.* published the first microfluidic paper-based analytical device (µPAD).[234] From then on, there has been an exponential increase in µPAD reported in the literature. This is due to paper being inexpensive and abundant, biocompatible, easily modified and safely disposed. It is also a suitable material for the fabrication of flexible and wearable devices, and for large scale manufacturing. Furthermore, it does not require external pumping sources as capillary forces can be used as a passive mechanism to move solutions through the previously defined hydrophilic channels created by several techniques, such as wax screen, inject printing, photolithography, ink jet etching and plasma or laser treatment.[235,236]

### 1.7.3. Polymers

Polymers are organic long-chain materials that have gained a lot of relevance in microfluidics due to its inexpensive cost, easy manufacturing at large-scale by different processes, and its adaptability to specific applications through changes in formulation and chemical modifications. Polymers can be classified in duroplastics, elastomers and thermoplastics according to the level of interlinking of the polymer chains.[225]

Duroplastics undergo a chemical crosslinking that results in a tight and stable 3D network. Once cured, these materials are temperature stable, and if heated they will decompose, but not melt. An example of this type of polymer is SU-8, an epoxy based resin. [225,237]

Elastomers are flexible and stretchable polymers and these properties can be tailored by their crosslinking content. The main elastomer used in microfluidics and µTAS fabrication is polydimethylsiloxane (PDMS). PDMS has long chains, low melting and $T_g$, and has high flexibility and elasticity. It is also durable, gas permeable and easily bonded to other substrates. Nevertheless, this material suffers from issues such as hydrophobicity and incompatibility to some solvents. PDMS started to be used in the late 1990s. Even though it has been extensively used in academic laboratories due to its fast prototyping, it has not reached the same level of popularity commercially.[226] PDMS is particularly useful in biological applications, where it can be used as a structural material for *in vitro* and *in vivo* experiments, in biomimetic applications to replicate biological surfaces and as a substrate material for flexible and wearable sensors.[238] Other elastomers used for the fabrication of microfluidics have been thermoset polyester (TPE)[239] and polyfluoropolyethers.[240,241]

Thermoplastics are densely cross-linked polymers that are mouldable when heated to their $T_g$ but that retain their shape at lower temperatures. Polystyrene (PS),[242] polycarbonate (PC),[243–245] polymethylcethacrylate (PMMA),[246–248] fluorinated ethylene-propylene (FEP)[249–251] and cyclic olefin co-polymer (COC)[173,252–254] have all been used for the fabrication of microfluidic platforms.

#### 1.7.3.1. Cyclic Olefin Co-polymer

All microfluidic analytical platforms described in this thesis have been fabricated using a class of thermoplastic polymers, COC.

COC is a fitting material for the fabrication of these analytical microsystems since it displays a high chemical resistance, low water absorption, high $T_g$, good optical features and low shrinkage. It is also a suitable material for microfabrication as it is commercially available, inexpensive, can be easily and fast prototyped and other elements can be integrated into the device platform. [255]

There are several types of COCs depending on the type of cyclic monomers and polymerization methods. Obviously, the physical and chemical properties vary depending on the specific chemical structure. Regarding the polymerization methods, COC can be produced by chain copolymerization of cyclic monomers such as norbornene or tetracyclododecene with ethylene or by Ring Opening Metathesis Polymerization (ROMP) of various cyclic monomers followed by hydrogenation. Both methods can be seen in *Fig. 1.15*.

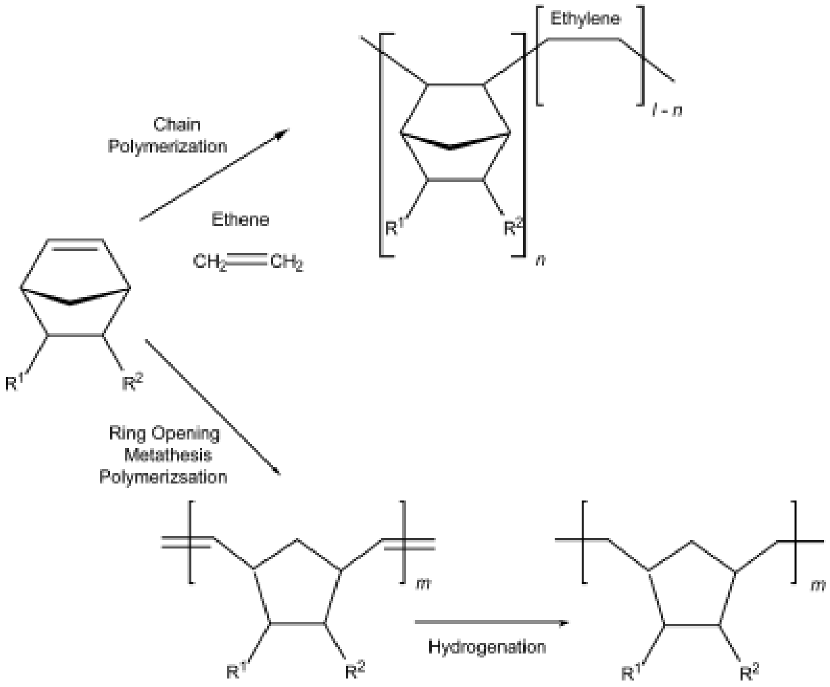

Fig. 1.15 Polymerization process for COC (255).

The COC material used for the fabrication of the microanalytical devices presented in this thesis is composed of monomeric units of ethylene and norbornene[256] in different proportions and its structure is found in *Fig. 1.16*.

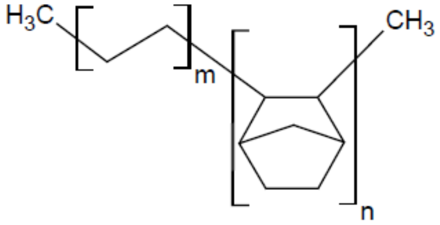

Fig. 1.16 Chemical structure of COC constituted by ethylene and norbornene monomers (256).

COC consists of an amorphous, transparent co-polymer with high chemical resistance to hydrolysis, acids, alkalis and polar solvents and presents high hydrophobicity and negligible swelling and water uptake. It displays high strength and rigidity and good insulating properties. It also presents very good optical features, with high light transmission in the visible and near ultraviolet range, which make it a promising candidate for analytical systems based on an optical method of detection. However, the most outstanding feature is that $T_g$ can be modified to cover a wide range of temperatures, from 80 °C to 180 °C, by the adjustment of the ethylene and norbornene percentage composition. This characteristic is depicted in *Fig. 1.17* where it can be seen that an increase in norbornene content is correlated with a linear rise in $T_g$.[257]

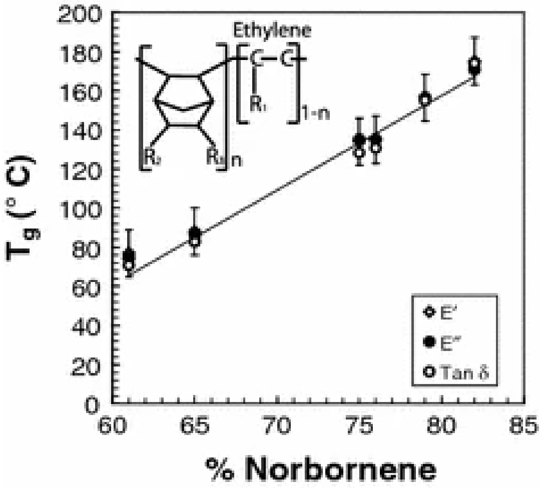

Fig. 1.17 Variation of $T_g$ in relation to norbornene percentage composition (257).

The fact that COC layers with a wide range of different $T_g$ are commercially available gives us the possibility to exploit this property to assemble the final 3D structure of the microfluidic platform using two different COC materials with distinctive $T_g$. The COC layers with a higher $T_g$ will act as the structural layers, whereas those COC layers with a lower $T_g$ will act as the sealing layers. Hence, it is possible to use temperature to melt the sealing layers while the structural ones remain solid, resulting in the sealing of the device to obtain a final monolithic microanalyzer. This approach eliminates the need to introduce additional materials as adhesives, thus avoiding the possible resultant obstructions in the microchannels.

## 1.8. Microfabrication of miniaturized analytical platforms

Regarding polymers, which will be the focus of this section, there is a wide range of microstructuring techniques available. In addition, there also exist different approaches for back end processing in order to integrate electrodes, and sealing strategies for the encapsulation of the final microfluidic platform.[258] Here, there is a summary of these technologies, emphasizing those that have been employed for the fabrication of the analytical microanalyzers developed during this work.

### 1.8.1. Design

The first step in the fabrication process of the analytical microsystems is the design, through a Computer Aided Design (CAD) software, of the patterns for each of the layers that will constitute the final device. The design approach used in this thesis is a layer-by-layer design (*Fig. 1.18*), which consist of the formation of the final 3D structure of the analytical platform by the superposition of previously individually microstructured layers.

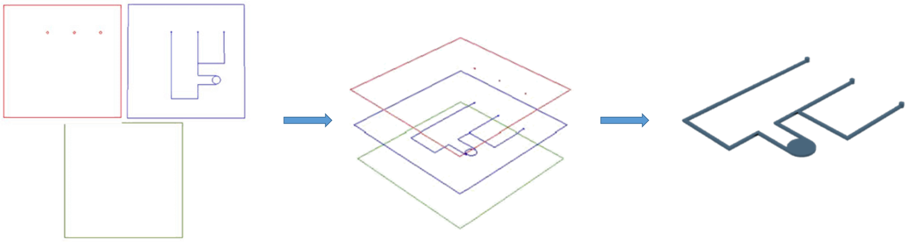

Fig. 1.18 Schematic representation of the layer-by-layer design process. Three different layers (red, purple and green) with different motives can be superposed in the correct order to form the desired three dimensional final design (blue).

During the design step, the material for the fabrication needs to be selected. For the fabrication of all the platforms described in this work COC has been chosen as substrate material, due to some of its properties, mainly the easiness to integrate electrodes and the commercial availability of COC with different $T_g$, which allows an adhesive-free fabrication of 3D microfluidic platforms.

### 1.8.2. Microstructuring techniques for polymeric analytical platforms

After the design of the analytical platform structure has been completed, the selected substrate material must be microstructured into the desired motives. For the microstructuring of COC, this can be achieved following different approaches, which can be divided into replication methods and material removing techniques.

### 1.8.2.1. Replication methods

These methods are based on the replication of a master structure that is the geometrical inverse of the desired structure. Hot embossing is widely used due to its high replication accuracy, for low to medium volume of production. This method consists on pressing a heated master into a melted polymer under vacuum conditions.[259,260] Injection moulding[261] plays a predominant role in the commercial success of microfluidic platforms. In this technique the polymer material is heated, melted and transported by a screw to be injected into the mould at high pressure.

### 1.8.2.2. Material removing techniques

Material removing techniques create a design by removing material from the bulk of the substrate. The two main techniques are laser ablation and micromachinning, which is the one used during the fabrication process of the microanalyzers described in this work.

Laser ablation consists on focussing a high intensity laser beam on the material to melt, evaporate or vaporize the material at the focal point. This takes place above a certain threshold that is dependent on the material, the wavelength and the pulse duration.[262] This process can be carried out using a mask to expose only the material to be eliminated or by moving the laser beam or the substrate itself in order to generate the desired pattern. This method has some drawbacks derived from the surfaces' characteristic roughness and the possibility of surface chemistry alteration due to the intense laser light.[258]

Micromilling uses a machine with computer numerical control (CNC). This technique consists of using rotating cutting tools to remove the bulk material resulting on the creation of a microscale pattern. CNC machines are used to fabricate a device from a 3D CAD, increasing repeatability and precision and decreasing human error and time of fabrication. This is a fast method for prototyping, and is the microstructuring approach employed for the structuring of the analytical platforms used in this work.

It is important to note that the final thickness of the motives does not depend on the design itself. In fact, the thickness will be determined by the specific tool used in the micromachining process. Thus, the minimum resolution that can be achieved depends on the smallest tool diameter available. Likewise, the length of the tool determines the maximum cutting depth possible. There are a wide range of milling and drilling tools of different shapes, sizes and materials (usually made of high speed steel and carbide) commercially available.[263] End mill tools remove materials by cutting along any axis and have helical grooves that curl from the tip towards the shaft, whereas drill mills only cut in the Z axis and are used to cut holes. The state of the tool is of high importance, as dull tools cause more friction, and this leads to an increase in temperature. Considering that the material used is COC, which is a thermoplastic, this heat can cause the localized melting of the polymer and the breakage of the tool.

### 1.8.3. Back end processes

Microstructuring processes alone do not produce a functioning microfluidic device. Further steps are imperative to achieve a complete analytical platform suitable for a certain purpose. These further steps are known as back-end processing and englobe the cutting and dicing of the device out of the polymeric substrate, the fabrication and integration of electrodes and the encapsulation to obtain a final monolithic hermetic analytical platform.

#### 1.8.3.1. Integration of electrodes

Regarding electrode fabrication there are two main groups of technologies to integrate conducting elements into the polymeric platform: thin-film technologies and thick-film technologies. Thin-film technologies (for 50 – 250 nm films) include sputtering and evaporation, which rely on the vaporization of a material to be deposited on top of the substrate by means of a shadow mask under vacuum conditions.[264,265]

The main exponent of the thick-film technologies is the screen-printing method, which is the one used in the fabrication of the polymeric devices described in this work and is depicted in *Fig. 1.19*. This process consists of the use of a blade or a squeegee to push a conductive paste through a mesh screen structured into the desired pattern for the electrode. Finally, the screen is removed and the paste is dried to evaporate the solvent.[258,266] The electrodes obtained by this method are thicker than the ones obtained by thin-film technologies, in the order of some tens of micrometres. But the process is simple and fast, no vacuum is required and the paste composition can be altered by the addition of metals, polymers and organic particles, such as enzymes depending on the application.[267]

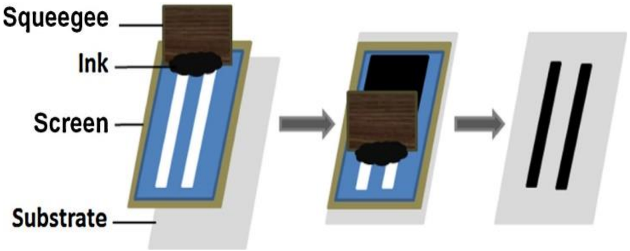

Fig. 1.19 Schematic representation of the screen-printing process adapted from (266).

### 1.8.3.2. Encapsulation

After the microstructuring of the design, it is necessary a bonding step to seal the microfluidic channels, without deforming them and without affecting the functionality of the device. For this purpose, there are several methods, such as relying on the surface adhesion of the polymer itself to create a thigh seal (which is particularly useful in the case of PDMS), the use of adhesives and glues, solvent bonding, ultrasonic or laser welding and thermal pressure bonding.

Adhesives are one of the most common sealing techniques, due to its simplicity and low cost. The main drawback of adhesive based methods is that it can cause structural damage by clogging or melting of the microchannels, particularly in the case of complex designs or very small channels.[71,255,258] Solvent bonding is another frequent method for bonding in which an organic solvent is used to break the polymer chains at the surface of the polymer and then they diffuse and re-crosslink to bond together two polymer layers when the solvent evaporates.[268] However, if an excess of solvent is applied the microchannels can also be damaged.[258]

Laser and ultrasonic welding allow localised bonding by the induction of heat to soften the interface between the polymer layers.[258] However, the use of a laser requires the top polymer to be transparent in order to reach the absorbing bottom layer, and for this purpose an absorbing pigment may be needed at the interface.[269] Ultrasonic welding has a limited depth resolution and microfluidic structure needs to include energy director elements to achieve a localized and reproducible welding.[270]

Alternatively, the analytical microsystems described in this dissertation all have been fabricated using thermal pressure bonding for the sealing process. This method uses a temperature above the $T_g$ and pressure to bond together thermoplastic polymers by the interlinking of the polymer chains.[260,271] Pressure and temperature need to be closely controlled, and high enough to allow the bonding but not so much as to cause the deformation of the microstructure. A way to prevent the deformation is to use materials with two different $T_g$, so only one of them softens while the other remains solid.

### 1.8.4. Final microanalytical devices

After the complete fabrication process the final monolithic analytical platforms are obtained. These microanalyzers must be suitable for connection to the necessary external elements in order to carry out the analytical process of interest. *Chapter 3* will focus more on the particular designs of the microanalyzers described in this thesis and the fabrication processes employed in their manufacturing.

## 1.9. References

(1) Nordberg, M.; Duffus, J.; Templeton, D. M. Glossary of Terms Used in Toxicokinetics (IUPAC Recommendations 2003). *Pure Appl. Chem.* **2004**, *76* (5), 1033–1082. https://doi.org/10.1351/pac200476051033.

(2) Waters, D.; Adeloye, D.; Woolham, D.; Wastnedge, E.; Patel, S.; Rudan, I. Global Birth Prevalence and Mortality from Inborn Errors of Metabolism: A Systematic Analysis of the Evidence. *J. Glob. Health* **2018**, *8* (2), 021102. https://doi.org/10.7189/jogh.08.021102.

(3) Maines, E.; Piccoli, G.; Pascarella, A.; Colucci, F.; Burlina, A. B. Inherited Hyperammonemias: A Contemporary View on Pathogenesis and Diagnosis. *Expert Opin. Orphan Drugs* **2018**, *6* (2), 105–116. https://doi.org/10.1080/21678707.2018.1409108.

(4) Häberle, J. Clinical and Biochemical Aspects of Primary and Secondary Hyperammonemic Disorders. *Arch. Biochem. Biophys.* **2013**, *536* (2), 101–108. https://doi.org/10.1016/j.abb.2013.04.009.

(5) Tchan, M. Hyperammonemia and Lactic Acidosis in Adults:

Differential Diagnoses with a Focus on Inborn Errors of Metabolism. *Rev. Endocr. Metab. Disord.* **2018**, *19*, 69–79. https://doi.org/10.1007/s11154-018-9444-5.

(6) Cheemerla, S.; Balakrishnan, M. Global Epidemiology of Chronic Liver Disease. *Clin. Liver Dis.* **2021**, *17* (5), 365–370. https://doi.org/10.1002/cld.1061.

(7) Häberle, J.; Boddaert, N.; Burlina, A.; Chakrapani, A.; Dixon, M.; Huemer, M.; Karall, D.; Martinelli, D.; Crespo, P.; Santer, R.; Servais, A.; Valayannopoulos, V.; Lindner, M.; Rubio, V.; Dionisi-Vici, C. Suggested Guidelines for the Diagnosis and Management of Urea Cycle Disorders. *Orphanet J. Rare Dis.* **2012**, *7*, 32. https://doi.org/10.1186/1750-1172-7-32.

(8) Cojocaru, K.-A.; Oprea, O. R.; Dobreanu, M. The Influence of Transport Condition and Processing Time on Plasma Ammonia Results. *Acta Marisiensis - Ser. Medica* **2022**, *68* (1), 24–27. https://doi.org/10.2478/amma-2022-0005.

(9) Zamarayeva, A. M.; Yamamoto, N. A. D.; Toor, A.; Payne, M. E.; Woods, C.; Pister, V. I.; Khan, Y.; Evans, J. W.; Arias, A. C. Optimization of Printed Sensors to Monitor Sodium, Ammonium, and Lactate in Sweat. *APL Mater.* **2020**, *8*, 100905. https://doi.org/10.1063/5.0014836.

(10) Keene, S. T.; Fogarty, D.; Cooke, R.; Casadevall, C. D.; Salleo, A.; Parlak, O. Wearable Organic Electrochemical Transistor Patch for Multiplexed Sensing of Calcium and Ammonium Ions from Human Perspiration. *Adv. Healthc. Mater.* **2019**, *8* (24), 1901321. https://doi.org/10.1002/adhm.201901321.

(11) Veltman, T. R.; Tsai, C. J.; Gomez-Ospina, N.; Kanan, M. W.; Chu, G. Point-of-Care Analysis of Blood Ammonia with a Gas-Phase Sensor. *ACS Sensors* **2020**, *5* (8), 2415–2421. https://doi.org/10.1021/acssensors.0c00480.

(12) Brannelly, N. T.; Killard, A. J. An Electrochemical Sensor Device for Measuring Blood Ammonia at the Point of Care. *Talanta* **2017**, *167*, 296–301. https://doi.org/10.1016/j.talanta.2017.02.025.

(13) Ayyub, O. B.; Behrens, A. M.; Heligman, B. T.; Natoli, M. E.; Ayoub, J. J.; Cunningham, G.; Summar, M.; Kofinas, P. Simple and

Inexpensive Quantification of Ammonia in Whole Blood. *Mol. Genet. Metab.* **2015**, *115* (2–3), 95–100. https://doi.org/10.1016/j.ymgme.2015.04.004.

(14) van Spronsen, F. J.; Blau, N.; Harding, C.; Burlina, A.; Longo, N.; Bosch, A. M. Phenylketonuria. *Nat. Rev. Dis. Prim.* **2021**, *7*, 36. https://doi.org/10.1038/s41572-021-00267-0.

(15) Cleary, M. A.; Skeath, R. Phenylketonuria. *Paediatr. Child Health (Oxford).* **2019**, *29* (3), 111–115. https://doi.org/10.1016/j.paed.2019.01.001.

(16) Messina, M. A.; Meli, C.; Conoci, S.; Petralia, S. A Facile Method for Urinary Phenylalanine Measurement on Paper-Based Lab-on-Chip for PKU Therapy Monitoring. *Analyst* **2017**, *142* (24), 4629–4632. https://doi.org/10.1039/C7AN01115F.

(17) Cheung, K. M.; Yang, K.-A.; Nakatsuka, N.; Zhao, C.; Ye, M.; Jung, M. E.; Yang, H.; Weiss, P. S.; Stojanović, M. N.; Andrews, A. M. Phenylalanine Monitoring via Aptamer-Field-Effect Transistor Sensors. *ACS Sensors* **2019**, *4* (12), 3308–3317. https://doi.org/10.1021/acssensors.9b01963.

(18) Çimen, D.; Bereli, N.; Denizli, A. Surface Plasmon Resonance Based on Molecularly Imprinted Polymeric Film for L-Phenylalanine Detection. *Biosensors* **2021**, *11* (1), 21. https://doi.org/10.3390/bios11010021.

(19) Parrilla, M.; Vanhooydonck, A.; Watts, R.; De Wael, K. Wearable Wristband-Based Electrochemical Sensor for the Detection of Phenylalanine in Biofluids. *Biosens. Bioelectron.* **2022**, *197*, 113764. https://doi.org/10.1016/j.bios.2021.113764.

(20) Idili, A.; Parolo, C.; Ortega, G.; Plaxco, K. W. Calibration-Free Measurement of Phenylalanine Levels in the Blood Using an Electrochemical Aptamer-Based Sensor Suitable for Point-of-Care Applications. *ACS Sensors* **2019**, *4* (12), 3227–3233. https://doi.org/10.1021/acssensors.9b01703.

(21) Robinson, R.; Wong, L.; Monnat, R. J.; Fu, E. Development of a Whole Blood Paper-Based Device for Phenylalanine Detection in the Context of PKU Therapy Monitoring. *Micromachines* **2016**, *7* (2), 28. https://doi.org/10.3390/mi7020028.

(22) Jung, W.; Han, J.; Choi, J. W.; Ahn, C. H. Point-of-Care Testing (POCT) Diagnostic Systems Using Microfluidic Lab-on-a-Chip Technologies. *Microelectronic Engineering*. Elsevier B.V. January 25, 2015, pp 46–57. https://doi.org/10.1016/j.mee.2014.09.024.

(23) Foudeh, A. M.; Fatanat Didar, T.; Veres, T.; Tabrizian, M. Microfluidic Designs and Techniques Using Lab-on-a-Chip Devices for Pathogen Detection for Point-of-Care Diagnostics. *Lab on a Chip*. Royal Society of Chemistry September 21, 2012, pp 3249–3266. https://doi.org/10.1039/c2lc40630f.

(24) Ceylan, O.; Mishra, G. K.; Yazici, M.; Qureshi, A.; Niazi, J. H.; Gurbuz, Y. A Hand-Held Point-of-Care Biosensor Device for Detection of Multiple Cancer and Cardiac Disease Biomarkers Using Interdigitated Capacitive Arrays. *IEEE Trans. Biomed. Circuits Syst.* **2018**, *12* (6), 1440–1449. https://doi.org/10.1109/TBCAS.2018.2870297.

(25) Kolluri, N.; Klapperich, C. M.; Cabodi, M. Towards Lab-on-a-Chip Diagnostics for Malaria Elimination. *Lab Chip* **2018**, *18* (1), 75–94. https://doi.org/10.1039/c7lc00758b.

(26) Ertl, P.; Sticker, D.; Charwat, V.; Kasper, C.; Lepperdinger, G. Lab-on-a-Chip Technologies for Stem Cell Analysis. *Trends Biotechnol.* **2014**, *32* (5), 245–253. https://doi.org/10.1016/j.tibtech.2014.03.004.

(27) Podwin, A.; Lizanets, D.; Przystupski, D.; Kubicki, W.; Śniadek, P.; Kulbacka, J.; Wymysłowski, A.; Walczak, R.; Dziuban, J. A. Lab-on-Chip Platform for Culturing and Dynamic Evaluation of Cells Development. *Micromachines* **2020**, *11* (2), 196. https://doi.org/10.3390/mi11020196.

(28) Perozziello, G.; Møllenbach, J.; Laursen, S.; Di Fabrizio, E.; Gernaey, K.; Krühne, U. Lab on a Chip Automates in Vitro Cell Culturing. *Microelectron. Eng.* **2012**, *98*, 655–658. https://doi.org/10.1016/j.mee.2012.07.027.

(29) Bunge, F.; Driesche, S.; Vellekoop, M. Microfluidic Platform for the Long-Term On-Chip Cultivation of Mammalian Cells for Lab-On-A-Chip Applications. *Sensors* **2017**, *17* (7), 1603. https://doi.org/10.3390/s17071603.

(30) Hung, T. Q.; Chin, W. H.; Sun, Y.; Wolff, A.; Bang, D. D. A Novel Lab-on-Chip Platform with Integrated Solid Phase PCR and Supercritical Angle Fluorescence (SAF) Microlens Array for Highly Sensitive and Multiplexed Pathogen Detection. *Biosens. Bioelectron.* **2017**, *90*, 217–223. https://doi.org/10.1016/j.bios.2016.11.028.

(31) Ben-Yoav, H.; Dykstra, P. H.; Bentley, W. E.; Ghodssi, R. A Controlled Microfluidic Electrochemical Lab-on-a-Chip for Label-Free Diffusion-Restricted DNA Hybridization Analysis. *Biosens. Bioelectron.* **2015**, *64*, 579–585. https://doi.org/10.1016/j.bios.2014.09.069.

(32) Geissler, M.; Brassard, D.; Clime, L.; Pilar, A. V. C.; Malic, L.; Daoud, J.; Barrère, V.; Luebbert, C.; Blais, B. W.; Corneau, N.; Veres, T. Centrifugal Microfluidic Lab-on-a-Chip System with Automated Sample Lysis, DNA Amplification and Microarray Hybridization for Identification of Enterohemorrhagic Escherichia Coli Culture Isolates. *Analyst* **2020**, *145* (21), 6831–6845. https://doi.org/10.1039/D0AN01232G.

(33) Vladisavljević, G. T.; Khalid, N.; Neves, M. A.; Kuroiwa, T.; Nakajima, M.; Uemura, K.; Ichikawa, S.; Kobayashi, I. Industrial Lab-on-a-Chip: Design, Applications and Scale-up for Drug Discovery and Delivery. *Adv. Drug Deliv. Rev.* **2013**, *65* (11–12), 1626–1663. https://doi.org/10.1016/j.addr.2013.07.017.

(34) Choucha Snouber, L.; Bunescu, A.; Naudot, M.; Legallais, C.; Brochot, C.; Dumas, M. E.; Elena-Herrmann, B.; Leclerc, E. Metabolomics-on-a-Chip of Hepatotoxicity Induced by Anticancer Drug Flutamide and Its Active Metabolite Hydroxyflutamide Using HepG2/C3a Microfluidic Biochips. *Toxicol. Sci.* **2013**, *132* (1), 8–20. https://doi.org/10.1093/toxsci/kfs230.

(35) Jellali, R.; Gilard, F.; Pandolfi, V.; Legendre, A.; Fleury, M.-J.; Paullier, P.; Legallais, C.; Leclerc, E. Metabolomics-on-a-Chip Approach to Study Hepatotoxicity of DDT, Permethrin and Their Mixtures. *J. Appl. Toxicol.* **2018**, *38* (8), 1121–1134. https://doi.org/10.1002/jat.3624.

(36) Krivitsky, V.; Zverzhinetsky, M.; Krivitsky, A.; Hsiung, L.-C.; Naddaka, V.; Gabriel, I.; Lefler, S.; Conroy, J.; Burstein, L.; Patolsky, F. Cellular Metabolomics by a Universal Redox-Reactive

Nanosensors Array: From the Cell Level to Tumor-on-a-Chip Analysis. *Nano Lett.* **2019**, *19* (4), 2478–2488. https://doi.org/10.1021/acs.nanolett.9b00052.

(37) Yea, K.; Lee, S.; Kyong, J. B.; Choo, J.; Lee, E. K.; Joo, S.-W.; Lee, S. Ultra-Sensitive Trace Analysis of Cyanide Water Pollutant in a PDMS Microfluidic Channel Using Surface-Enhanced Raman Spectroscopy. *Analyst* **2005**, *130* (7), 1009. https://doi.org/10.1039/b501980j.

(38) Sun, H.; Jia, Y.; Dong, H.; Fan, L.; Zheng, J. Multiplex Quantification of Metals in Airborne Particulate Matter via Smartphone and Paper-Based Microfluidics. *Anal. Chim. Acta* **2018**, *1044*, 110–118. https://doi.org/10.1016/j.aca.2018.07.053.

(39) Liu, F.; Nordin, A. N.; Li, F.; Voiculescu, I. A Lab-on-Chip Cell-Based Biosensor for Label-Free Sensing of Water Toxicants. *Lab Chip* **2014**, *14* (7), 1270–1280. https://doi.org/10.1039/C3LC51085A.

(40) Inpota, P.; Strzelak, K.; Koncki, R.; Sripumkhai, W.; Jeamsaksiri, W.; Ratanawimarnwong, N.; Wilairat, P.; Choengchan, N.; Chantiwas, R.; Nacapricha, D. Microfluidic Analysis with Front-Face Fluorometric Detection for the Determination of Total Inorganic Iodine in Drinking Water. *Anal. Sci.* **2018**, *34*, 161–167. https://doi.org/10.2116/analsci.34.161.

(41) Fornells, E.; Murray, E.; Waheed, S.; Morrin, A.; Diamond, D.; Paull, B.; Breadmore, M. Integrated 3D Printed Heaters for Microfluidic Applications: Ammonium Analysis within Environmental Water. *Anal. Chim. Acta* **2020**, *1098*, 94–101. https://doi.org/10.1016/j.aca.2019.11.025.

(42) Kung, C.-T.; Hou, C.-Y.; Wang, Y.-N.; Fu, L.-M. Microfluidic Paper-Based Analytical Devices for Environmental Analysis of Soil, Air, Ecology and River Water. *Sensors Actuators B Chem.* **2019**, *301*, 126855. https://doi.org/10.1016/j.snb.2019.126855.

(43) Pol, R.; Céspedes, F.; Gabriel, D.; Baeza, M. Microfluidic Lab-on-a-Chip Platforms for Environmental Monitoring. *TrAC Trends Anal. Chem.* **2017**, *95*, 62–68. https://doi.org/10.1016/j.trac.2017.08.001.

(44) Al Mughairy, B.; Al-Lawati, H. A. J. Recent Analytical Advancements

in Microfluidics Using Chemiluminescence Detection Systems for Food Analysis. *TrAC Trends Anal. Chem.* **2020**, *124*, 115802. https://doi.org/10.1016/j.trac.2019.115802.

(45) Trofimchuk, E.; Hu, Y.; Nilghaz, A.; Hua, M. Z.; Sun, S.; Lu, X. Development of Paper-Based Microfluidic Device for the Determination of Nitrite in Meat. *Food Chem.* **2020**, *316*, 126396. https://doi.org/10.1016/j.foodchem.2020.126396.

(46) Wang, S.; Liu, N.; Zheng, L.; Cai, G.; Lin, J. A Lab-on-Chip Device for the Sample-in-Result-out Detection of Viable Salmonella Using Loop-Mediated Isothermal Amplification and Real-Time Turbidity Monitoring. *Lab Chip* **2020**, *20* (13), 2296–2305. https://doi.org/10.1039/D0LC00290A.

(47) Nascetti, A.; Mirasoli, M.; Marchegiani, E.; Zangheri, M.; Costantini, F.; Porchetta, A.; Iannascoli, L.; Lovecchio, N.; Caputo, D.; de Cesare, G.; Pirrotta, S.; Roda, A. Integrated Chemiluminescence-Based Lab-on-Chip for Detection of Life Markers in Extraterrestrial Environments. *Biosens. Bioelectron.* **2019**, *123*, 195–203. https://doi.org/10.1016/j.bios.2018.08.056.

(48) Mora, M. F.; Greer, F.; Stockton, A. M.; Bryant, S.; Willis, P. A. Toward Total Automation of Microfluidics for Extraterrestial In Situ Analysis. *Anal. Chem.* **2011**, *83* (22), 8636–8641. https://doi.org/10.1021/ac202095k.

(49) Pietrogrande, M. C. Enantioselective Separation of Amino Acids as Biomarkers Indicating Life in Extraterrestrial Environments Amino Acid Analysis. *Analytical and Bioanalytical Chemistry*. Springer October 29, 2013, pp 7931–7940. https://doi.org/10.1007/s00216-013-6915-0.

(50) Calvo-López, A.; Ymbern, O.; Puyol, M.; Casalta, J. M.; Alonso-Chamarro, J. Potentiometric Analytical Microsystem Based on the Integration of a Gas-Diffusion Step for on-Line Ammonium Determination in Water Recycling Processes in Manned Space Missions. *Anal. Chim. Acta* **2015**, *874*, 26–32. https://doi.org/10.1016/j.aca.2014.12.038.

(51) Calvo-López, A.; Arasa-Puig, E.; Puyol, M.; Casalta, J. M.; Alonso-Chamarro, J. Biparametric Potentiometric Analytical Microsystem for Nitrate and Potassium Monitoring in Water Recycling Processes

for Manned Space Missions. *Anal. Chim. Acta* **2013**, *804*, 190–196. https://doi.org/10.1016/j.aca.2013.10.013.

(52) Manz, A.; Graber, N.; Widmer, H. M. Miniaturized Total Chemical Analysis Systems: A Novel Concept for Chemical Sensing. *Sensors Actuators B. Chem.* **1990**, *1* (1–6), 244–248. https://doi.org/10.1016/0925-4005(90)80209-I.

(53) Verpoorte, E.; De Rooij, N. F. Microfluidics Meets MEMS. *Proc. IEEE* **2003**, *91* (6), 930–953. https://doi.org/10.1109/JPROC.2003.813570.

(54) Dincer, C.; Bruch, R.; Kling, A.; Dittrich, P. S.; Urban, G. A. Multiplexed Point-of-Care Testing – XPOCT. *Trends Biotechnol.* **2017**, *35* (8), 728–742. https://doi.org/10.1016/j.tibtech.2017.03.013.

(55) Anastas, P.; Eghbali, N. Green Chemistry: Principles and Practice. *Chem. Soc. Rev.* **2010**, *39* (1), 301–312. https://doi.org/10.1039/B918763B.

(56) Tobiszewski, M.; Marć, M.; Gałuszka, A.; Namieśnik, J. Green Chemistry Metrics with Special Reference to Green Analytical Chemistry. *Molecules* **2015**, *20* (6), 10928–10946. https://doi.org/10.3390/molecules200610928.

(57) Agrawal, A.; Keçili, R.; Ghorbani-Bidkorbeh, F.; Hussain, C. M. Green Miniaturized Technologies in Analytical and Bioanalytical Chemistry. *TrAC Trends Anal. Chem.* **2021**, *143*, 116383. https://doi.org/10.1016/j.trac.2021.116383.

(58) Gałuszka, A.; Migaszewski, Z.; Namieśnik, J. The 12 Principles of Green Analytical Chemistry and the SIGNIFICANCE Mnemonic of Green Analytical Practices. *TrAC Trends Anal. Chem.* **2013**, *50*, 78–84. https://doi.org/10.1016/j.trac.2013.04.010.

(59) Hannah Kettler, Karen White, S. H.; UNDP/World Bank/WHO Special Programme for Research and Training in Tropical Diseases. Mapping the Landscape of Diagnostics for Sexually Transmitted Infections : Key Findings and Recommendations. *World Heal. Organ.* **2004**.

(60) Land, K. J.; Boeras, D. I.; Chen, X.-S.; Ramsay, A. R.; Peeling, R. W.

REASSURED Diagnostics to Inform Disease Control Strategies, Strengthen Health Systems and Improve Patient Outcomes. *Nat. Microbiol.* **2019**, *4*, 46–54. https://doi.org/10.1038/s41564-018-0295-3.

(61) Azizipour, N.; Avazpour, R.; Rosenzweig, D. H.; Sawan, M.; Ajji, A. Evolution of Biochip Technology: A Review from Lab-on-a-Chip to Organ-on-a-Chip. *Micromachines* **2020**, *11* (6), 599. https://doi.org/10.3390/mi11060599.

(62) Squires, T. M.; Quake, S. R. Microfluidics: Fluid Physics at the Nanoliter Scale. *Rev. Mod. Phys.* **2005**, *77* (3), 977–1026. https://doi.org/10.1103/RevModPhys.77.977.

(63) Ward, K.; Fan, Z. H. Mixing in Microfluidic Devices and Enhancement Methods. *J. Micromechanics Microengineering* **2015**, *25* (9), 094001. https://doi.org/10.1088/0960-1317/25/9/094001.

(64) Dusseiller, M. R.; Niederberger, B.; Städler, B.; Falconnet, D.; Textor, M.; Vörös, J. A Novel Crossed Microfluidic Device for the Precise Positioning of Proteins and Vesicles. *Lab Chip* **2005**, *5* (12), 1387. https://doi.org/10.1039/b509957a.

(65) Wei, Z.; Zhao, D.; Li, X.; Wu, M.; Wang, W.; Huang, H.; Wang, X.; Du, Q.; Liang, Z.; Li, Z. A Laminar Flow Electroporation System for Efficient DNA and SiRNA Delivery. *Anal. Chem.* **2011**, *83* (15), 5881–5887. https://doi.org/10.1021/ac200625b.

(66) Tong, Z.; Ivask, A.; Guo, K.; McCormick, S.; Lombi, E.; Priest, C.; Voelcker, N. H. Crossed Flow Microfluidics for High Throughput Screening of Bioactive Chemical–Cell Interactions. *Lab Chip* **2017**, *17* (3), 501–510. https://doi.org/10.1039/C6LC01261B.

(67) Cai, Q.; Meng, J.; Ge, Y.; Gao, Y.; Zeng, Y.; Li, H.; Sun, Y. Fishing Antitumor Ingredients by G-Quadruplex Affinity from Herbal Extract on a Three-Phase-Laminar-Flow Microfluidic Chip. *Talanta* **2020**, *220*, 121368. https://doi.org/10.1016/J.TALANTA.2020.121368.

(68) Ly, K. L.; Hu, P.; Pham, L. H. P.; Luo, X. Flow-Assembled Chitosan Membranes in Microfluidics: Recent Advances and Applications. *J. Mater. Chem. B* **2021**, *9* (15), 3258–3283.

https://doi.org/10.1039/d1tb00045d.

(69) Bayareh, M.; Ashani, M. N.; Usefian, A. Active and Passive Micromixers: A Comprehensive Review. *Chem. Eng. Process. - Process Intensif.* **2020**, *147*, 107771. https://doi.org/10.1016/j.cep.2019.107771.

(70) Lim, Y. C.; Kouzani, A. Z.; Duan, W. Lab-on-a-Chip: A Component View. *Microsyst. Technol.* **2010**, *16*, 1995–2015. https://doi.org/10.1007/s00542-010-1141-6.

(71) Temiz, Y.; Lovchik, R. D.; Kaigala, G. V.; Delamarche, E. Lab-on-a-Chip Devices: How to Close and Plug the Lab? *Microelectron. Eng.* **2015**, *132*, 156–175. https://doi.org/10.1016/j.mee.2014.10.013.

(72) Fredrickson, C. K.; Fan, Z. H. Macro-to-Micro Interfaces for Microfluidic Devices. *Lab Chip* **2004**, *4* (6), 526–533. https://doi.org/10.1039/b410720a.

(73) Christensen, A. M.; Chang-Yen, D. A.; Gale, B. K. Characterization of Interconnects Used in PDMS Microfluidic Systems. *J. Micromechanics Microengineering* **2005**, *15*, 928–934. https://doi.org/10.1088/0960-1317/15/5/005.

(74) Saarela, V.; Franssila, S.; Tuomikoski, S.; Marttila, S.; Östman, P.; Sikanen, T.; Kotiaho, T.; Kostiainen, R. Re-Usable Multi-Inlet PDMS Fluidic Connector. *Sensors Actuators B Chem.* **2006**, *114* (1), 552–557. https://doi.org/10.1016/j.snb.2005.06.009.

(75) Chen, A.; Pan, T. Fit-to-Flow (F2F) Interconnects: Universal Reversible Adhesive-Free Microfluidic Adaptors for Lab-on-a-Chip Systems. *Lab Chip* **2011**, *11* (4), 727–732. https://doi.org/10.1039/C0LC00384K.

(76) Yang, Z.; Maeda, R. Socket with Built-in Valves for the Interconnection of Microfluidic Chips to Macro Constituents. *J. Chromatogr. A* **2003**, *1013* (1–2), 29–33. https://doi.org/10.1016/S0021-9673(03)01125-7.

(77) Wilhelm, E.; Neumann, C.; Duttenhofer, T.; Pires, L.; Rapp, B. E. Connecting Microfluidic Chips Using a Chemically Inert, Reversible, Multichannel Chip-to-World-Interface. *Lab Chip* **2013**, *13* (22), 4343. https://doi.org/10.1039/c3lc50861g.

(78) Cooksey, G. A.; Plant, A. L.; Atencia, J. A Vacuum Manifold for Rapid World-to-Chip Connectivity of Complex PDMS Microdevices. *Lab Chip* **2009**, *9* (9), 1298. https://doi.org/10.1039/b820683j.

(79) Atencia, J.; Cooksey, G. A.; Jahn, A.; Zook, J. M.; Vreeland, W. N.; Locascio, L. E. Magnetic Connectors for Microfluidic Applications. *Lab Chip* **2010**, *10* (2), 246–249. https://doi.org/10.1039/B913331C.

(80) Szabo, E.; Hess-dunning, A. Irreversible, Self-Aligned Microfluidic Packaging for Chronic Implant Applications. *J. Micromechanics Microengineering* **2021**, *31* (9), 1–10. https://doi.org/1010.1088/1361-6439/ac1994.

(81) Mair, D. A.; Geiger, E.; Pisano, A. P.; Fréchet, J. M. J.; Svec, F. Injection Molded Microfluidic Chips Featuring Integrated Interconnects. *Lab Chip* **2006**, *6* (10), 1346–1354. https://doi.org/10.1039/B605911B.

(82) Xu, Z.; Cao, D.; Zhao, W.; Song, M.; Liu, J. Investigation of Injection Molding of Orthogonal Fluidic Connector for Microfluidic Devices. *AIP Adv.* **2017**, *7* (2), 025205. https://doi.org/10.1063/1.4976618.

(83) Finkbeiner, T.; Soergel, H. L.; Koschitzky, M. P.; Ahrens, R.; Guber, A. E. Ultrasonic Welding for the Rapid Integration of Fluidic Connectors into Microfluidic Chips. *J. Micromechanics Microengineering* **2019**, *29*, 065011. https://doi.org/10.1088/1361-6439/ab10d2.

(84) Ng, S. H.; Wang, Z. F.; de Rooij, N. F. Microfluidic Connectors by Ultrasonic Welding. *Microelectron. Eng.* **2009**, *86* (4–6), 1354–1357. https://doi.org/10.1016/j.mee.2009.01.048.

(85) Beckwith, A. L.; Borenstein, J. T.; Velasquez-Garcia, L. F. Monolithic, 3D-Printed Microfluidic Platform for Recapitulation of Dynamic Tumor Microenvironments. *J. Microelectromechanical Syst.* **2018**, *27* (6), 1009–1022. https://doi.org/10.1109/JMEMS.2018.2869327.

(86) Gong, H.; Woolley, A. T.; Nordin, G. P. 3D Printed High Density, Reversible, Chip-to-Chip Microfluidic Interconnects. *Lab Chip* **2018**, *18* (4), 639–647. https://doi.org/10.1039/C7LC01113J.

(87) van den Driesche, S.; Lucklum, F.; Bunge, F.; Vellekoop, M. 3D Printing Solutions for Microfluidic Chip-To-World Connections. *Micromachines* **2018**, *9* (2), 71. https://doi.org/10.3390/mi9020071.

(88) Xu, Q.; Lo, J.; Lee, S.-W. Characterization and Evaluation of 3D-Printed Connectors for Microfluidics. *Micromachines* **2021**, *12* (8), 874. https://doi.org/10.3390/mi12080874.

(89) Trojanowicz, M.; Kołacińska, K. Recent Advances in Flow Injection Analysis. *Analyst* **2016**, *141* (7), 2085–2139. https://doi.org/10.1039/C5AN02522B.

(90) Llorent-Martinez, E.; Barrales, P.; Fernandez-de Cordova, M.; Ruiz-Medina, A. Multicommutation in Flow Systems: A Useful Tool for Pharmaceutical and Clinical Analysis. *Curr. Pharm. Anal.* **2010**, *6* (1), 53–65. https://doi.org/10.2174/157341210790780195.

(91) Mark, D.; Haeberle, S.; Roth, G.; Von Stetten, F.; Zengerle, R. Microfluidic Lab-on-a-Chip Platforms: Requirements, Characteristics and Applications. *Chem. Soc. Rev.* **2010**, *39* (3), 1153–1182. https://doi.org/https://doi.org/10.1039/B820557B.

(92) Forouzandeh, F.; Arevalo, A.; Alfadhel, A.; Borkholder, D. A. A Review of Peristaltic Micropumps. *Sensors Actuators A Phys.* **2021**, *326*, 112602. https://doi.org/10.1016/j.sna.2021.112602.

(93) Tamadon, I.; Simoni, V.; Iacovacci, V.; Vistoli, F.; Ricotti, L.; Menciassi, A. Miniaturized Peristaltic Rotary Pump for Non-Continuous Drug Dosing. In *2019 41st Annual International Conference of the IEEE Engineering in Medicine and Biology Society (EMBC).* Berlin, Germany; IEEE, 2019; pp 5522–5526. https://doi.org/10.1109/EMBC.2019.8857811.

(94) Zhang, C.; Xing, D.; Li, Y. Micropumps, Microvalves, and Micromixers within PCR Microfluidic Chips: Advances and Trends. *Biotechnol. Adv.* **2007**, *25* (5), 483–514. https://doi.org/10.1016/j.biotechadv.2007.05.003.

(95) Ríos, Á.; Ríos, Á.; Zougagh, M.; Zougagh, M. Sample Preparation for Micro Total Analytical Systems (µ-TASs). *TrAC Trends Anal. Chem.* **2013**, *43*, 174–188. https://doi.org/10.1016/j.trac.2012.12.009.

(96) Çetin, B.; Kang, Y.; Wu, Z.; Li, D. Continuous Particle Separation by Size via AC-Dielectrophoresis Using a Lab-on-a-Chip Device with 3-D Electrodes. *Electrophoresis* **2009**, *30* (5), 766–772. https://doi.org/10.1002/elps.200800464.

(97) Krivitsky, V.; Hsiung, L.-C.; Lichtenstein, A.; Brudnik, B.; Kantaev, R.; Elnathan, R.; Pevzner, A.; Khatchtourints, A.; Patolsky, F. Si Nanowires Forest-Based On-Chip Biomolecular Filtering, Separation and Preconcentration Devices: Nanowires Do It All. *Nano Lett.* **2012**, *12* (9), 4748–4756. https://doi.org/10.1021/nl3021889.

(98) Hejazian, M.; Li, W.; Nguyen, N.-T. Lab on a Chip for Continuous-Flow Magnetic Cell Separation. *Lab Chip* **2015**, *15* (4), 959–970. https://doi.org/10.1039/C4LC01422G.

(99) Crowley, T. A.; Pizziconi, V. Isolation of Plasma from Whole Blood Using Planar Microfilters for Lab-on-a-Chip Applications. *Lab Chip* **2005**, *5* (9), 922. https://doi.org/10.1039/b502930a.

(100) Lin, C.-C.; Hsu, J.-L.; Lee, G.-B. Sample Preconcentration in Microfluidic Devices. *Microfluid. Nanofluidics* **2011**, *10*, 481–511. https://doi.org/10.1007/s10404-010-0661-9.

(101) Kim, S. C.; Clark, I. C.; Shahi, P.; Abate, A. R. Single-Cell RT-PCR in Microfluidic Droplets with Integrated Chemical Lysis. *Anal. Chem.* **2018**, *90* (2), 1273–1279. https://doi.org/10.1021/acs.analchem.7b04050.

(102) Shehadul Islam, M.; Aryasomayajula, A.; Selvaganapathy, P. A Review on Macroscale and Microscale Cell Lysis Methods. *Micromachines* **2017**, *8* (3), 83. https://doi.org/10.3390/mi8030083.

(103) Kido, H.; Micic, M.; Smith, D.; Zoval, J.; Norton, J.; Madou, M. A Novel, Compact Disk-like Centrifugal Microfluidics System for Cell Lysis and Sample Homogenization. *Colloids Surfaces B Biointerfaces* **2007**, *58* (1), 44–51. https://doi.org/10.1016/j.colsurfb.2007.03.015.

(104) Yasui, T.; Yanagida, T.; Shimada, T.; Otsuka, K.; Takeuchi, M.; Nagashima, K.; Rahong, S.; Naito, T.; Takeshita, D.; Yonese, A.; Magofuku, R.; Zhu, Z.; Kaji, N.; Kanai, M.; Kawai, T.; Baba, Y.

Engineering Nanowire-Mediated Cell Lysis for Microbial Cell Identification. *ACS Nano* **2019**, *13* (2), 2262–2273. https://doi.org/10.1021/acsnano.8b08959.

(105) Nasiri, R.; Shamloo, A.; Akbari, J.; Tebon, P.; R. Dokmeci, M.; Ahadian, S. Design and Simulation of an Integrated Centrifugal Microfluidic Device for CTCs Separation and Cell Lysis. *Micromachines* **2020**, *11* (7), 699. https://doi.org/10.3390/mi11070699.

(106) Liu, Y.; Schulze-Makuch, D.; de Vera, J.-P.; Cockell, C.; Leya, T.; Baqué, M.; Walther-Antonio, M. The Development of an Effective Bacterial Single-Cell Lysis Method Suitable for Whole Genome Amplification in Microfluidic Platforms. *Micromachines* **2018**, *9* (8), 367. https://doi.org/10.3390/mi9080367.

(107) Packard, M.; Wheeler, E.; Alocilja, E.; Shusteff, M. Performance Evaluation of Fast Microfluidic Thermal Lysis of Bacteria for Diagnostic Sample Preparation. *Diagnostics* **2013**, *3* (1), 105–116. https://doi.org/10.3390/diagnostics3010105.

(108) Taller, D.; Richards, K.; Slouka, Z.; Senapati, S.; Hill, R.; Go, D. B.; Chang, H.-C. On-Chip Surface Acoustic Wave Lysis and Ion-Exchange Nanomembrane Detection of Exosomal RNA for Pancreatic Cancer Study and Diagnosis. *Lab Chip* **2015**, *15* (7), 1656–1666. https://doi.org/10.1039/C5LC00036J.

(109) Salehi-Reyhani, A.; Gesellchen, F.; Mampallil, D.; Wilson, R.; Reboud, J.; Ces, O.; Willison, K. R.; Cooper, J. M.; Klug, D. R. Chemical-Free Lysis and Fractionation of Cells by Use of Surface Acoustic Waves for Sensitive Protein Assays. *Anal. Chem.* **2015**, *87* (4), 2161–2169. https://doi.org/10.1021/ac5033758.

(110) Farooq, U.; Liu, X.; Zhou, W.; Hassan, M.; Niu, L.; Meng, L. Cell Lysis Induced by Nanowire Collision Based on Acoustic Streaming Using Surface Acoustic Waves. *Sensors Actuators B Chem.* **2021**, *345*, 130335. https://doi.org/10.1016/j.snb.2021.130335.

(111) Won, E.-J.; Thai, D. A.; Duong, D. D.; Lee, N. Y.; Song, Y.-J. Microfluidic Electrical Cell Lysis for High-Throughput and Continuous Production of Cell-Free Varicella-Zoster Virus. *J. Biotechnol.* **2021**, *335*, 19–26. https://doi.org/10.1016/j.jbiotec.2021.06.006.

(112) Ameri, S. K.; Singh, P. K.; Dokmeci, M. R.; Khademhosseini, A.; Xu, Q.; Sonkusale, S. R. All Electronic Approach for High-Throughput Cell Trapping and Lysis with Electrical Impedance Monitoring. *Biosens. Bioelectron.* **2014**, *54*, 462–467. https://doi.org/10.1016/j.bios.2013.11.031.

(113) de Lange, N.; Tran, T. M.; Abate, A. R. Electrical Lysis of Cells for Detergent-Free Droplet Assays. *Biomicrofluidics* **2016**, *10* (2), 024114. https://doi.org/10.1063/1.4944742.

(114) Pang, X.; Lewis, A. C.; Ródenas-García, M. Microfluidic Lab-on-a-Chip Derivatization for Gaseous Carbonyl Analysis. *J. Chromatogr. A* **2013**, *1296*, 93–103. https://doi.org/10.1016/j.chroma.2013.04.066.

(115) Park, B.; Choi, S.-J. Sensitive Immunoassay-Based Detection of Vibrio Parahaemolyticus Using Capture and Labeling Particles in a Stationary Liquid Phase Lab-on-a-Chip. *Biosens. Bioelectron.* **2017**, *90*, 269–275. https://doi.org/10.1016/j.bios.2016.11.071.

(116) Nguyen, N.-T.; Wu, Z. Micromixers—a Review. *J. Micromechanics Microengineering* **2005**, *15* (2), 1–16. https://doi.org/10.1088/0960-1317/15/2/R01.

(117) Oh, K. W.; Lee, K.; Ahn, B.; Furlani, E. P. Design of Pressure-Driven Microfluidic Networks Using Electric Circuit Analogy. *Lab Chip* **2012**, *12* (3), 515–545. https://doi.org/10.1039/C2LC20799K.

(118) Wu, J. W.; Xia, H. M.; Zhang, Y. Y.; Zhao, S. F.; Zhu, P.; Wang, Z. P. An Efficient Micromixer Combining Oscillatory Flow and Divergent Circular Chambers. *Microsyst. Technol.* **2019**, *25*, 2741–2750. https://doi.org/10.1007/s00542-018-4193-7.

(119) Huang, C.; Tsou, C. The Implementation of a Thermal Bubble Actuated Microfluidic Chip with Microvalve, Micropump and Micromixer. *Sensors Actuators A Phys.* **2014**, *210*, 147–156. https://doi.org/10.1016/j.sna.2014.02.015.

(120) Kunti, G.; Bhattacharya, A.; Chakraborty, S. Electrothermally Actuated Moving Contact Line Dynamics over Chemically Patterned Surfaces with Resistive Heaters. *Phys. Fluids* **2018**, *30* (6), 062004. https://doi.org/10.1063/1.5028172.

(121) Liu, R. H.; Yang, J.; Pindera, M. Z.; Athavale, M.; Grodzinski, P. Bubble-Induced Acoustic Micromixing. *Lab Chip* **2002**, *2* (3), 151–157. https://doi.org/10.1039/b201952c.

(122) Orbay, S.; Ozcelik, A.; Lata, J.; Kaynak, M.; Wu, M.; Huang, T. J. Mixing High-Viscosity Fluids via Acoustically Driven Bubbles. *J. Micromechanics Microengineering* **2017**, *27* (1), 015008. https://doi.org/10.1088/0960-1317/27/1/015008.

(123) Yaralioglu, G. G.; Wygant, I. O.; Marentis, T. C.; Khuri-Yakub, B. T. Ultrasonic Mixing in Microfluidic Channels Using Integrated Transducers. *Anal. Chem.* **2004**, *76* (13), 3694–3698. https://doi.org/10.1021/ac035220k.

(124) Luong, T.-D.; Phan, V.-N.; Nguyen, N.-T. High-Throughput Micromixers Based on Acoustic Streaming Induced by Surface Acoustic Wave. *Microfluid. Nanofluidics* **2011**, *10*, 619–625. https://doi.org/10.1007/s10404-010-0694-0.

(125) Deval, J.; Tabeling, P.; Chih-Ming Ho. A Dielectrophoretic Chaotic Mixer. In *Tech. Dig. MEMS 2002 IEEE Int. Conf. Fifteenth IEEE Int. Conf. Micro Electro Mech. Syst. (Cat. No.02CH37266),* Las Vegas, NV, USA 2002, 36–39. https://doi.org/10.1109/MEMSYS.2002.984074.

(126) Daghighi, Y.; Li, D. Numerical Study of a Novel Induced-Charge Electrokinetic Micro-Mixer. *Anal. Chim. Acta* **2013**, *763*, 28–37. https://doi.org/10.1016/j.aca.2012.12.010.

(127) Matsubara, K.; Narumi, T. Microfluidic Mixing Using Unsteady Electroosmotic Vortices Produced by a Staggered Array of Electrodes. *Chem. Eng. J.* **2016**, *288*, 638–647. https://doi.org/10.1016/j.cej.2015.12.013.

(128) Zhang, K.; Ren, Y.; Hou, L.; Feng, X.; Chen, X.; Jiang, H. An Efficient Micromixer Actuated by Induced-Charge Electroosmosis Using Asymmetrical Floating Electrodes. *Microfluid. Nanofluidics* **2018**, *22*, 130. https://doi.org/10.1007/s10404-018-2153-2.

(129) Hejazian, M.; Nguyen, N.-T. A Rapid Magnetofluidic Micromixer Using Diluted Ferrofluid. *Micromachines* **2017**, *8* (2), 37. https://doi.org/10.3390/mi8020037.

(130) Nouri, D.; Zabihi-Hesari, A.; Passandideh-Fard, M. Rapid Mixing in Micromixers Using Magnetic Field. *Sensors Actuators A Phys.* **2017**, *255*, 79–86. https://doi.org/10.1016/j.sna.2017.01.005.

(131) Owen, D.; Ballard, M.; Alexeev, A.; Hesketh, P. J. Rapid Microfluidic Mixing via Rotating Magnetic Microbeads. *Sensors Actuators A Phys.* **2016**, *251*, 84–91. https://doi.org/10.1016/j.sna.2016.09.040.

(132) Kang, T. G.; Hulsen, M. A.; Anderson, P. D.; den Toonder, J. M. J.; Meijer, H. E. H. Chaotic Mixing Induced by a Magnetic Chain in a Rotating Magnetic Field. *Phys. Rev. E* **2007**, *76* (6), 066303. https://doi.org/10.1103/PhysRevE.76.066303.

(133) Fu, L. M.; Tsai, C. H.; Leong, K. P.; Wen, C. Y. Rapid Micromixer via Ferrofluids. *Phys. Procedia* **2010**, *9*, 270–273. https://doi.org/10.1016/j.phpro.2010.11.060.

(134) Date, Y.; Terakado, S.; Sasaki, K.; Aota, A.; Matsumoto, N.; Shiku, H.; Ino, K.; Watanabe, Y.; Matsue, T.; Ohmura, N. Microfluidic Heavy Metal Immunoassay Based on Absorbance Measurement. *Biosens. Bioelectron.* **2012**, *33* (1), 106–112. https://doi.org/10.1016/j.bios.2011.12.030.

(135) Usuba, R.; Yokokawa, M.; Ackermann, T. N.; Llobera, A.; Fukunaga, K.; Murata, S.; Ohkohchi, N.; Suzuki, H. Photonic Lab-on-a-Chip for Rapid Cytokine Detection. *ACS Sensors* **2016**, *1* (8), 979–986. https://doi.org/10.1021/acssensors.6b00193.

(136) Jung, D. G.; Jung, D.; Kong, S. H. A Lab-on-a-Chip-Based Non-Invasive Optical Sensor for Measuring Glucose in Saliva. *Sensors* **2017**, *17* (11), 2607. https://doi.org/10.3390/s17112607.

(137) Mainz, E. R.; Gunasekara, D. B.; Caruso, G.; Jensen, D. T.; Hulvey, M. K.; Fracassi da Silva, J. A.; Metto, E. C.; Culbertson, A. H.; Culbertson, C. T.; Lunte, S. M. Monitoring Intracellular Nitric Oxide Production Using Microchip Electrophoresis and Laser-Induced Fluorescence Detection. *Anal. Methods* **2012**, *4* (2), 414–420. https://doi.org/10.1039/c2ay05542b.

(138) Zhang, W.; Tullier, M. P.; Patel, K.; Carranza, A.; Pojman, J. A.; Radadia, A. D. Microfluidics Using a Thiol–Acrylate Resin for Fluorescence-Based Pathogen Detection Assays. *Lab Chip* **2015**, *15*

(21), 4227–4231. https://doi.org/10.1039/C5LC00971E.

(139) Guo, L.; Shi, Y.; Liu, X.; Han, Z.; Zhao, Z.; Chen, Y.; Xie, W.; Li, X. Enhanced Fluorescence Detection of Proteins Using ZnO Nanowires Integrated inside Microfluidic Chips. *Biosens. Bioelectron.* **2018**, *99*, 368–374. https://doi.org/10.1016/j.bios.2017.08.003.

(140) Hu, B.; Li, J.; Mou, L.; Liu, Y.; Deng, J.; Qian, W.; Sun, J.; Cha, R.; Jiang, X. An Automated and Portable Microfluidic Chemiluminescence Immunoassay for Quantitative Detection of Biomarkers. *Lab Chip* **2017**, *17* (13), 2225–2234. https://doi.org/10.1039/c7lc00249a.

(141) Huang, Y.; Zhao, S.; Shi, M.; Liu, J.; Liang, H. Microchip Electrophoresis Coupled with On-Line Magnetic Separation and Chemiluminescence Detection for Multiplexed Immunoassay. *Electrophoresis* **2012**, *33* (7), 1198–1204. https://doi.org/10.1002/elps.201100543.

(142) Yavas, O.; Aćimović, S. S.; Garcia-Guirado, J.; Berthelot, J.; Dobosz, P.; Sanz, V.; Quidant, R. Self-Calibrating On-Chip Localized Surface Plasmon Resonance Sensing for Quantitative and Multiplexed Detection of Cancer Markers in Human Serum. *ACS Sensors* **2018**, *3* (7), 1376–1384. https://doi.org/10.1021/acssensors.8b00305.

(143) Pan, M.-Y.; Lee, K.-L.; Wang, L.; Wei, P.-K. Chip-Based Digital Surface Plasmon Resonance Sensing Platform for Ultrasensitive Biomolecular Detection. *Biosens. Bioelectron.* **2017**, *91*, 580–587. https://doi.org/10.1016/j.bios.2017.01.003.

(144) Aćimović, S. S.; Ortega, M. A.; Sanz, V.; Berthelot, J.; Garcia-Cordero, J. L.; Renger, J.; Maerkl, S. J.; Kreuzer, M. P.; Quidant, R. LSPR Chip for Parallel, Rapid, and Sensitive Detection of Cancer Markers in Serum. *Nano Lett.* **2014**, *14* (5), 2636–2641. https://doi.org/10.1021/nl500574n.

(145) Austin Suthanthiraraj, P. P.; Sen, A. K. Localized Surface Plasmon Resonance (LSPR) Biosensor Based on Thermally Annealed Silver Nanostructures with on-Chip Blood-Plasma Separation for the Detection of Dengue Non-Structural Protein NS1 Antigen. *Biosens. Bioelectron.* **2019**, *132*, 38–46. https://doi.org/10.1016/j.bios.2019.02.036.

(146) Zheng, Z.; Wu, L.; Li, L.; Zong, S.; Wang, Z.; Cui, Y. Simultaneous and Highly Sensitive Detection of Multiple Breast Cancer Biomarkers in Real Samples Using a SERS Microfluidic Chip. *Talanta* **2018**, *188*, 507–515. https://doi.org/10.1016/j.talanta.2018.06.013.

(147) Qi, J.; Zeng, J.; Zhao, F.; Lin, S. H.; Raja, B.; Strych, U.; Willson, R. C.; Shih, W. C. Label-Free, in Situ SERS Monitoring of Individual DNA Hybridization in Microfluidics. *Nanoscale* **2014**, *6* (15), 8521–8526. https://doi.org/10.1039/c4nr01951b.

(148) Kline, N. D.; Tripathi, A.; Mirsafavi, R.; Pardoe, I.; Moskovits, M.; Meinhart, C.; Guicheteau, J. A.; Christesen, S. D.; Fountain, A. W. Optimization of Surface-Enhanced Raman Spectroscopy Conditions for Implementation into a Microfluidic Device for Drug Detection. *Anal. Chem.* **2016**, *88* (21), 10513–10522. https://doi.org/10.1021/acs.analchem.6b02573.

(149) Meier, T.-A.; Poehler, E.; Kemper, F.; Pabst, O.; Jahnke, H.-G.; Beckert, E.; Robitzki, A.; Belder, D. Fast Electrically Assisted Regeneration of On-Chip SERS Substrates. *Lab Chip* **2015**, *15* (14), 2923–2927. https://doi.org/10.1039/c5lc00397k.

(150) Bizzarri, A. R.; Moscetti, I.; Cannistraro, S. Surface Enhanced Raman Spectroscopy Based Immunosensor for Ultrasensitive and Selective Detection of Wild Type P53 and Mutant P53R175H. *Anal. Chim. Acta* **2018**, *1029*, 86–96. https://doi.org/10.1016/j.aca.2018.04.049.

(151) Pijanowska, D. G.; Sprenkels, A. J.; van der Linden, H.; Olthuis, W.; Bergveld, P.; van den Berg, A. A Flow-through Potentiometric Sensor for an Integrated Microdialysis System. *Sensors Actuators B Chem.* **2004**, *103* (1–2), 350–355. https://doi.org/10.1016/j.snb.2004.04.108.

(152) Ricotta, V.; Yu, Y.; Clayton, N.; Chuang, Y.-C.; Wang, Y.; Mueller, S.; Levon, K.; Simon, M.; Rafailovich, M. A Chip-Based Potentiometric Sensor for a Zika Virus Diagnostic Using 3D Surface Molecular Imprinting. *Analyst* **2019**, *144* (14), 4266–4280. https://doi.org/10.1039/C9AN00580C.

(153) Gallardo-Gonzalez, J.; Baraket, A.; Boudjaoui, S.; Metzner, T.; Hauser, F.; Rößler, T.; Krause, S.; Zine, N.; Streklas, A.; Alcácer, A.; Bausells, J.; Errachid, A. A Fully Integrated Passive Microfluidic Lab-

on-a-Chip for Real-Time Electrochemical Detection of Ammonium: Sewage Applications. *Sci. Total Environ.* **2019**, *653*, 1223–1230. https://doi.org/10.1016/j.scitotenv.2018.11.002.

(154) Guijt, R. M.; Armstrong, J. P.; Candish, E.; Lefleur, V.; Percey, W. J.; Shabala, S.; Hauser, P. C.; Breadmore, M. C. Microfluidic Chips for Capillary Electrophoresis with Integrated Electrodes for Capacitively Coupled Conductivity Detection Based on Printed Circuit Board Technology. *Sensors Actuators B Chem.* **2011**, *159* (1), 307–313. https://doi.org/10.1016/j.snb.2011.06.023.

(155) Moschou, D.; Greathead, L.; Pantelidis, P.; Kelleher, P.; Morgan, H.; Prodromakis, T. Amperometric IFN-γ Immunosensors with Commercially Fabricated PCB Sensing Electrodes. *Biosens. Bioelectron.* **2016**, *86*, 805–810. https://doi.org/10.1016/j.bios.2016.07.075.

(156) Gunasekara, D. B.; Hulvey, M. K.; Lunte, S. M. In-Channel Amperometric Detection for Microchip Electrophoresis Using a Wireless Isolated Potentiostat. *Electrophoresis* **2011**, *32* (8), 832–837. https://doi.org/10.1002/elps.201000681.

(157) Ordeig, O.; Ortiz, P.; Muñoz-Berbel, X.; Demming, S.; Büttgenbach, S.; Fernández-Sánchez, C.; Llobera, A. Dual Photonic-Electrochemical Lab on a Chip for Online Simultaneous Absorbance and Amperometric Measurements. *Anal. Chem.* **2012**, *84* (8), 3546–3553. https://doi.org/10.1021/ac203106x.

(158) Guo, J.; Li, C. M.; Kang, Y. PDMS-Film Coated on PCB for AC Impedance Sensing of Biological Cells. *Biomed. Microdevices* **2014**, *16*, 681–686. https://doi.org/10.1007/s10544-014-9872-2.

(159) Jung, W.; Jang, A.; Bishop, P. L.; Ahn, C. H. A Polymer Lab Chip Sensor with Microfabricated Planar Silver Electrode for Continuous and On-Site Heavy Metal Measurement. *Sensors Actuators B Chem.* **2011**, *155* (1), 145–153. https://doi.org/10.1016/j.snb.2010.11.039.

(160) Jothimuthu, P.; Wilson, R. A.; Herren, J.; Haynes, E. N.; Heineman, W. R.; Papautsky, I. Lab-on-a-Chip Sensor for Detection of Highly Electronegative Heavy Metals by Anodic Stripping Voltammetry. *Biomed. Microdevices* **2011**, *13*, 695–703. https://doi.org/10.1007/s10544-011-9539-1.

(161) Kokkinos, C.; Economou, A.; Raptis, I. Microfabricated Disposable Lab-on-a-Chip Sensors with Integrated Bismuth Microelectrode Arrays for Voltammetric Determination of Trace Metals. *Anal. Chim. Acta* **2012**, *710*, 1–8. https://doi.org/10.1016/j.aca.2011.10.048.

(162) Condina, M. R.; Dilmetz, B. A.; Razavi Bazaz, S.; Meneses, J.; Ebrahimi Warkiani, M.; Hoffmann, P. Rapid Separation and Identification of Beer Spoilage Bacteria by Inertial Microfluidics and MALDI-TOF Mass Spectrometry. *Lab Chip* **2019**, *19* (11), 1961–1970. https://doi.org/10.1039/c9lc00152b.

(163) Yang, J.; Zhu, J.; Pei, R.; Oliver, J. A.; Landry, D. W.; Stojanovic, M. N.; Lin, Q. Integrated Microfluidic Aptasensor for Mass Spectrometric Detection of Vasopressin in Human Plasma Ultrafiltrate. *Anal. Methods* **2016**, *8* (26), 5190–5196. https://doi.org/10.1039/C5AY02979A.

(164) Baker, C. A.; Roper, M. G. Online Coupling of Digital Microfluidic Devices with Mass Spectrometry Detection Using an Eductor with Electrospray Ionization. *Anal. Chem.* **2012**, *84* (6), 2955–2960. https://doi.org/10.1021/ac300100b.

(165) Tsao, C. W.; Tao, S.; Chen, C. F.; Liu, J.; Devoe, D. L. Interfacing Microfluidics to LDI-MS by Automatic Robotic Spotting. *Microfluid. Nanofluidics* **2010**, *8*, 777–787. https://doi.org/10.1007/s10404-009-0510-x.

(166) Ibáñez-García, N.; Alonso, J.; Martínez-Cisneros, C. S.; Valdés, F. Green-Tape Ceramics. New Technological Approach for Integrating Electronics and Fluidics in Microsystems. *TrAC Trends Anal. Chem.* **2008**, *27* (1), 24–33. https://doi.org/10.1016/j.trac.2007.11.002.

(167) Ibáñez-García, N.; Baeza, M.; Puyol, M.; Gómez, R.; Batlle, M.; Alonso-Chamarro, J. Biparametric Potentiometric Analytical Microsystem Based on the Green Tape Technology. *Electroanalysis* **2010**, *22* (20), 2376–2382. https://doi.org/10.1002/elan.201000133.

(168) Ibanez-Garcia, N.; Mercader, M. B.; Mendes da Rocha, Z.; Seabra, C. A.; Góngora-Rubio, M. R.; Chamarro, J. A. Continuous Flow Analytical Microsystems Based on Low-Temperature Co-Fired Ceramic Technology. Integrated Potentiometric Detection Based

on Solvent Polymeric Ion-Selective Electrodes. *Anal. Chem.* **2006**, *78* (9), 2985–2992. https://doi.org/10.1021/ac051994k.

(169) Calvo-López, A.; Puyol, M.; Casalta, J. M.; Alonso-Chamarro, J. Multi-Parametric Polymer-Based Potentiometric Analytical Microsystem for Future Manned Space Missions. *Anal. Chim. Acta* **2017**, *995*, 77–84. https://doi.org/10.1016/j.aca.2017.08.043.

(170) Ymbern, O.; Berenguel-Alonso, M.; Calvo-López, A.; Gómez-de Pedro, S.; Izquierdo, D.; Alonso-Chamarro, J. Versatile Lock and Key Assembly for Optical Measurements with Microfluidic Platforms and Cartridges. *Anal. Chem.* **2015**, *87* (3), 1503–1508. https://doi.org/10.1021/ac504255t.

(171) Ymbern, O.; Sández, N.; Calvo-López, A.; Puyol, M.; Alonso-Chamarro, J. Gas Diffusion as a New Fluidic Unit Operation for Centrifugal Microfluidic Platforms. *Lab Chip* **2014**, *14* (5), 1014–1022. https://doi.org/10.1039/c3lc51114f.

(172) da Rocha, Z. M.; Martinez-Cisneros, C. S.; Seabra, A. C.; Valdés, F.; Gongora-Rubio, M. R.; Alonso-Chamarro, J. Compact and Autonomous Multiwavelength Microanalyzer for In-Line and in Situ Colorimetric Determinations. *Lab Chip* **2012**, *12* (1), 109–117. https://doi.org/10.1039/C1LC20747D.

(173) Sández, N.; Calvo-López, A.; Vidigal, S. S. M. P.; Rangel, A. O. S. S.; Alonso-Chamarro, J. Automated Analytical Microsystem for the Spectrophotometric Monitoring of Titratable Acidity in White, Rosé and Red Wines. *Anal. Chim. Acta* **2019**, *1091*, 50–58. https://doi.org/10.1016/j.aca.2019.09.052.

(174) Chen, C.; Xie, Q.; Yang, D.; Xiao, H.; Fu, Y.; Tan, Y.; Yao, S. Recent Advances in Electrochemical Glucose Biosensors: A Review. *RSC Adv.* **2013**, *3* (14), 4473–4491. https://doi.org/10.1039/c2ra22351a.

(175) Wang, Y.; Xu, H.; Zhang, J.; Li, G. Electrochemical Sensors for Clinic Analysis. *Sensors* **2008**, *8* (4), 2043–2081. https://doi.org/10.3390/s8042043.

(176) Lindner, E.; Pendley, B. D. A Tutorial on the Application of Ion-Selective Electrode Potentiometry: An Analytical Method with Unique Qualities, Unexplored Opportunities and Potential Pitfalls;

Tutorial. *Anal. Chim. Acta* **2013**, *762*, 1–13. https://doi.org/10.1016/j.aca.2012.11.022.

(177) Lindner, E.; Umezawa, Y. Performance Evaluation Criteria for Preparation and Measurement of Macro- and Microfabricated Ion-Selective Electrodes (IUPAC Technical Report). *Pure Appl. Chem.* **2008**, *80* (1), 85–104. https://doi.org/10.1351/pac200880010085.

(178) Atkins, P and De Paula, J. *Physical Chemistry, Eighth Edition*; Oxford University Press, 2018.

(179) Hulanicki, A.; Glab, S.; Ingman, F. Chemical Sensors Definitions and Classification. *Pure Appl. Chem* **1991**, *63* (9), 1247–1250. https://doi.org/10.1351/pac199163091247.

(180) Cremer, M. Über Die Ursache Der Elektromotorischen Eigenschaften Der Gewebe, Zugleich Ein Beitrag Zur Lehre von Den Polyphasischen Elektrolytketten. *z. Biol* **1906**, *47*, 542.

(181) Kałuża, D.; Michalska, A.; Maksymiuk, K. Solid-Contact Ion-Selective Electrodes Paving the Way for Improved Non-Zero Current Sensors: A Minireview. *ChemElectroChem* **2022**, *9* (1), e202100892. https://doi.org/10.1002/celc.202100892.

(182) Cattrall, R. W.; Freiser, H. Coated Wire Ion-Selective Electrodes. *Anal. Chem.* **1971**, *43* (13), 1905–1906. https://doi.org/10.1021/ac60307a032.

(183) Cadogan, A.; Gao, Z.; Lewenstam, A.; Ivaska, A.; Diamond, D. All-Solid-State Sodium-Selective Electrode Based on a Calixarene Ionophore in a Poly(Vinyl Chloride) Membrane with a Polypyrrole Solid Contact. *Anal. Chem.* **1992**, *64* (21), 2496–2501. https://doi.org/10.1021/ac00045a007.

(184) Shao, Y.; Ying, Y.; Ping, J. Recent Advances in Solid-Contact Ion-Selective Electrodes: Functional Materials, Transduction Mechanisms, and Development Trends. *Chem. Soc. Rev.* **2020**, *49* (13), 4405–4465. https://doi.org/10.1039/C9CS00587K.

(185) Kisiel, A.; Mazur, M.; Kuśnieruk, S.; Kijewska, K.; Krysiński, P.; Michalska, A. Polypyrrole Microcapsules as a Transducer for Ion-Selective Electrodes. *Electrochem. commun.* **2010**, *12* (11), 1568–1571. https://doi.org/10.1016/j.elecom.2010.08.035.

(186) Jaworska, E.; Michalska, A.; Maksymiuk, K. Polypyrrole Nanospheres - Electrochemical Properties and Application as a Solid Contact in Ion-Selective Electrodes. *Electroanalysis* **2017**, *29* (1), 123–130. https://doi.org/10.1002/elan.201600554.

(187) He, N.; Papp, S.; Lindfors, T.; Höfler, L.; Latonen, R.-M.; Gyurcsányi, R. E. Pre-Polarized Hydrophobic Conducting Polymer Solid-Contact Ion-Selective Electrodes with Improved Potential Reproducibility. *Anal. Chem.* **2017**, *89* (4), 2598–2605. https://doi.org/10.1021/acs.analchem.6b04885.

(188) Mousavi, Z.; Bobacka, J.; Lewenstam, A.; Ivaska, A. Poly(3,4-Ethylenedioxythiophene) (PEDOT) Doped with Carbon Nanotubes as Ion-to-Electron Transducer in Polymer Membrane-Based Potassium Ion-Selective Electrodes. *J. Electroanal. Chem.* **2009**, *633* (1), 246–252. https://doi.org/10.1016/j.jelechem.2009.06.005.

(189) Guzinski, M.; Jarvis, J. M.; Perez, F.; Pendley, B. D.; Lindner, E.; De Marco, R.; Crespo, G. A.; Acres, R. G.; Walker, R.; Bishop, J. PEDOT(PSS) as Solid Contact for Ion-Selective Electrodes: The Influence of the PEDOT(PSS) Film Thickness on the Equilibration Times. *Anal. Chem.* **2017**, *89* (6), 3508–3516. https://doi.org/10.1021/acs.analchem.6b04625.

(190) Vanamo, U.; Hupa, E.; Yrjänä, V.; Bobacka, J. New Signal Readout Principle for Solid-Contact Ion-Selective Electrodes. *Anal. Chem.* **2016**, *88* (8), 4369–4374. https://doi.org/10.1021/acs.analchem.5b04800.

(191) Han, T.; Mousavi, Z.; Mattinen, U.; Bobacka, J. Coulometric Response Characteristics of Solid Contact Ion-Selective Electrodes for Divalent Cations. *J. Solid State Electrochem.* **2020**, *24*, 2975–2983. https://doi.org/10.1007/s10008-020-04718-8.

(192) Veder, J.-P.; De Marco, R.; Patel, K.; Si, P.; Grygolowicz-Pawlak, E.; James, M.; Alam, M. T.; Sohail, M.; Lee, J.; Pretsch, E.; Bakker, E. Evidence for a Surface Confined Ion-to-Electron Transduction Reaction in Solid-Contact Ion-Selective Electrodes Based on Poly(3-Octylthiophene). *Anal. Chem.* **2013**, *85* (21), 10495–10502. https://doi.org/10.1021/ac4024999.

(193) Jarvis, J. M.; Guzinski, M.; Pendley, B. D.; Lindner, E. Poly(3-

Octylthiophene) as Solid Contact for Ion-Selective Electrodes: Contradictions and Possibilities. *J. Solid State Electrochem.* **2016**, *20*, 3033–3041. https://doi.org/10.1007/s10008-016-3340-2.

(194) Zdrachek, E.; Bakker, E. Electrochemically Switchable Polymeric Membrane Ion-Selective Electrodes. *Anal. Chem.* **2018**, *90* (12), 7591–7599. https://doi.org/10.1021/acs.analchem.8b01282.

(195) Shishkanova, T. V.; Sapurina, I.; Stejskal, J.; Král, V.; Volf, R. Ion-Selective Electrodes: Polyaniline Modification and Anion Recognition. *Anal. Chim. Acta* **2005**, *553*, 160–168. https://doi.org/10.1016/j.aca.2005.08.018.

(196) Zeng, X.; Liu, Y.; Jiang, X.; Waterhouse, G. I. N.; Zhang, Z.; Yu, L. Improving the Stability of Pb2+ Ion-Selective Electrodes by Using 3D Polyaniline Nanowire Arrays as the Inner Solid-Contact Transducer. *Electrochim. Acta* **2021**, *384*, 138414. https://doi.org/10.1016/j.electacta.2021.138414.

(197) Liu, C.; Jiang, X.; Zhao, Y.; Jiang, W.; Zhang, Z.; Yu, L. A Solid-Contact Pb2+ - Selective Electrode Based on Electrospun Polyaniline Microfibers Film as Ion-to-Electron Transducer. *Electrochim. Acta* **2017**, *231*, 53–60. https://doi.org/10.1016/j.electacta.2017.01.162.

(198) El-Rahman, M. K. A.; Rezk, M. R.; Mahmoud, A. M.; Elghobashy, M. R. Design of a Stable Solid-Contact Ion-Selective Electrode Based on Polyaniline Nanoparticles as Ion-to-Electron Transducer for Application in Process Analytical Technology as a Real-Time Analyzer. *Sensors Actuators B Chem.* **2015**, *208*, 14–21. https://doi.org/10.1016/j.snb.2014.11.009.

(199) Lyu, Y.; Gan, S.; Bao, Y.; Zhong, L.; Xu, J.; Wang, W.; Liu, Z.; Ma, Y.; Yang, G.; Niu, L. Solid-Contact Ion-Selective Electrodes: Response Mechanisms, Transducer Materials and Wearable Sensors. *Membranes (Basel).* **2020**, *10* (6), 128. https://doi.org/10.3390/membranes10060128.

(200) Crespo, G. A.; Macho, S.; Rius, F. X. Ion-Selective Electrodes Using Carbon Nanotubes as Ion-to-Electron Transducers. *Anal. Chem.* **2008**, *80* (4), 1316–1322. https://doi.org/10.1021/ac071156l.

(201) Mensah, S. T.; Gonzalez, Y.; Calvo-Marzal, P.; Chumbimuni-Torres,

K. Y. Nanomolar Detection Limits of Cd2+ , Ag+ , and K+ Using Paper-Strip Ion-Selective Electrodes. *Anal. Chem.* **2014**, *86* (15), 7269–7273. https://doi.org/10.1021/ac501470p.

(202) Ampurdanés, J.; Crespo, G. A.; Maroto, A.; Sarmentero, M. A.; Ballester, P.; Rius, F. X. Determination of Choline and Derivatives with a Solid-Contact Ion-Selective Electrode Based on Octaamide Cavitand and Carbon Nanotubes. *Biosens. Bioelectron.* **2009**, *25* (2), 344–349. https://doi.org/10.1016/j.bios.2009.07.006.

(203) Pietrzak, K.; Wardak, C. Comparative Study of Nitrate All Solid State Ion-Selective Electrode Based on Multiwalled Carbon Nanotubes-Ionic Liquid Nanocomposite. *Sensors Actuators B Chem.* **2021**, *348*, 130720. https://doi.org/10.1016/j.snb.2021.130720.

(204) Zhu, J.; Li, X.; Qin, Y.; Zhang, Y. Single-Piece Solid-Contact Ion-Selective Electrodes with Polymer–Carbon Nanotube Composites. *Sensors Actuators B Chem.* **2010**, *148* (1), 166–172. https://doi.org/10.1016/j.snb.2010.04.041.

(205) He, Q.; Das, S. R.; Garland, N. T.; Jing, D.; Hondred, J. A.; Cargill, A. A.; Ding, S.; Karunakaran, C.; Claussen, J. C. Enabling Inkjet Printed Graphene for Ion Selective Electrodes with Postprint Thermal Annealing. *ACS Appl. Mater. Interfaces* **2017**, *9* (14), 12719–12727. https://doi.org/10.1021/acsami.7b00092.

(206) Ping, J.; Wang, Y.; Ying, Y.; Wu, J. Application of Electrochemically Reduced Graphene Oxide on Screen-Printed Ion-Selective Electrode. *Anal. Chem.* **2012**, *84* (7), 3473–3479. https://doi.org/10.1021/ac203480z.

(207) Mahmoud, A. M.; Ragab, M. T.; Ramadan, N. K.; El-Ragehy, N. A.; El-Zeany, B. A. Design of Solid-contact Ion-selective Electrode with Graphene Transducer Layer for the Determination of Flavoxate Hydrochloride in Dosage Form and in Spiked Human Plasma. *Electroanalysis* **2020**, *32* (12), 2803–2811. https://doi.org/10.1002/elan.202060377.

(208) Zhang, R.; Gu, Y.; Wang, Z.; Li, Y.; Fan, Q.; Jia, Y. Aptamer Cell Sensor Based on Porous Graphene Oxide Decorated Ion-Selective-Electrode: Double Sensing Platform for Cell and Ion. *Biosens. Bioelectron.* **2018**, *117*, 303–311. https://doi.org/10.1016/j.bios.2018.06.021.

(209) Boeva, Z. A.; Lindfors, T. Few-Layer Graphene and Polyaniline Composite as Ion-to-Electron Transducer in Silicone Rubber Solid-Contact Ion-Selective Electrodes. *Sensors Actuators B Chem.* **2016**, *224*, 624–631. https://doi.org/10.1016/j.snb.2015.10.054.

(210) Fouskaki, M.; Chaniotakis, N. Fullerene-Based Electrochemical Buffer Layer for Ion-Selective Electrodes. *Analyst* **2008**, *133* (8), 1072–1075. https://doi.org/10.1039/b719759d.

(211) Lai, C.-Z.; Fierke, M. A.; Stein, A.; Bühlmann, P. Ion-Selective Electrodes with Three-Dimensionally Ordered Macroporous Carbon as the Solid Contact. *Anal. Chem.* **2007**, *79* (12), 4621–4626. https://doi.org/10.1021/ac070132b.

(212) Fierke, M. A.; Lai, C.-Z.; Bühlmann, P.; Stein, A. Effects of Architecture and Surface Chemistry of Three-Dimensionally Ordered Macroporous Carbon Solid Contacts on Performance of Ion-Selective Electrodes. *Anal. Chem.* **2010**, *82* (2), 680–688. https://doi.org/10.1021/ac902222n.

(213) Hu, J.; Zou, X. U.; Stein, A.; Bühlmann, P. Ion-Selective Electrodes with Colloid-Imprinted Mesoporous Carbon as Solid Contact. *Anal. Chem.* **2014**, *86* (14), 7111–7118. https://doi.org/10.1021/ac501633r.

(214) Hu, J.; Zhao, W.; Bühlmann, P.; Stein, A. Paper-Based All-Solid-State Ion-Sensing Platform with a Solid Contact Comprising Colloid-Imprinted Mesoporous Carbon and a Redox Buffer. *ACS Appl. Nano Mater.* **2018**, *1* (1), 293–301. https://doi.org/10.1021/acsanm.7b00151.

(215) Bieg, C.; Fuchsberger, K.; Stelzle, M. Introduction to Polymer-Based Solid-Contact Ion-Selective Electrodes—Basic Concepts, Practical Considerations, and Current Research Topics. *Anal. Bioanal. Chem.* **2017**, *409*, 45–61. https://doi.org/10.1007/s00216-016-9945-6.

(216) Johnson, R. D.; Bachas, L. G. Ionophore-Based Ion-Selective Potentiometric and Optical Sensors. *Anal. Bioanal. Chem.* **2003**, *376*, 328–341. https://doi.org/10.1007/s00216-003-1931-0.

(217) Pechenkina, I. A.; Mikhelson, K. N. Materials for the Ionophore-Based Membranes for Ion-Selective Electrodes: Problems and Achievements (Review Paper). *Russ. J. Electrochem.* **2015**, *51* (2),

93–102. https://doi.org/10.1134/S1023193515020111.

(218) Rousseau, C. R.; Bühlmann, P. Calibration-Free Potentiometric Sensing with Solid-Contact Ion-Selective Electrodes. *TrAC Trends Anal. Chem.* **2021**, *140*, 116277. https://doi.org/10.1016/j.trac.2021.116277.

(219) Lazo Fraga, A. R.; Calvo Quintana, J.; Li Destri, G.; Giamblanco, N.; Toro, R. G.; Punzo, F. Polymeric Membranes Conditioning for Sensors Applications: Mechanism and Influence on Analytes Detection. *J. Solid State Electrochem.* **2012**, *16*, 901–909. https://doi.org/10.1007/s10008-011-1456-y.

(220) Hoss, U.; Budiman, E. S. Factory-Calibrated Continuous Glucose Sensors: The Science Behind the Technology. *Diabetes Technol. Ther.* **2017**, *19* (2), 44–50. https://doi.org/10.1089/dia.2017.0025.

(221) Calvo-Lopez, A.; Puyol, M.; Alonso-Chamarro, J. New Strategy of Autocalibration for Disposable Potentiometric Point-of-Care Analyzers. In *XXII Transfront. Meet. Sensors Biosensors. Barcelona, Spain* 2018.

(222) Carretero, L. G. Dispositiu Point of Care (POC) per a La Determinació de Clorur En Suor per Al Diagnòstic de Fibrosi Quística. Bachelor's Thesis, Universitat Autònoma de Barcelona, Spain, 2022.

(223) Umezawa, Y.; Bühlmann, P.; Umezawa, K.; Tohda, K.; Amemiya, S. Potentiometric Selectivity Coefficients of Ion-Selective Electrodes. Part I. Inorganic Cations (Technical Report). *Pure Appl. Chem.* **2000**, *72* (10), 1851–2082. https://doi.org/10.1351/pac200072101851.

(224) Terry, S. C.; Jerman, J. H.; Angell, J. B. A Gas Chromatographic Air Analyzer Fabricated on a Silicon Wafer. *IEEE Trans. Electron Devices* **1979**, *26* (12), 1880–1886. https://doi.org/10.1109/T-ED.1979.19791.

(225) Waldbaur, A.; Rapp, H.; Länge, K.; Rapp, B. E. Let There Be Chip—towards Rapid Prototyping of Microfluidic Devices: One-Step Manufacturing Processes. *Anal. Methods* **2011**, *3* (12), 2681–2716. https://doi.org/10.1039/c1ay05253e.

(226) Nge, P. N.; Rogers, C. I.; Woolley, A. T. Advances in Microfluidic

Materials, Functions, Integration, and Applications. *Chem. Rev.* **2013**, *113* (4), 2550–2583. https://doi.org/10.1021/cr300337x.

(227) Zhao, S.; Li, X.; Liu, Y.-M. Integrated Microfluidic System with Chemiluminescence Detection for Single Cell Analysis after Intracellular Labeling. *Anal. Chem.* **2009**, *81* (10), 3873–3878. https://doi.org/10.1021/ac900391u.

(228) Mellors, J. S.; Gorbounov, V.; Ramsey, R. S.; Ramsey, J. M. Fully Integrated Glass Microfluidic Device for Performing High-Efficiency Capillary Electrophoresis and Electrospray Ionization Mass Spectrometry. *Anal. Chem.* **2008**, *80* (18), 6881–6887. https://doi.org/10.1021/ac800428w.

(229) Mellors, J. S.; Jorabchi, K.; Smith, L. M.; Ramsey, J. M. Integrated Microfluidic Device for Automated Single Cell Analysis Using Electrophoretic Separation and Electrospray Ionization Mass Spectrometry. *Anal. Chem.* **2010**, *82* (3), 967–973. https://doi.org/10.1021/ac902218y.

(230) Martínez-Cisneros, C. S.; Ibáñez-García, N.; Valdés, F.; Alonso, J. Miniaturized Total Analysis Systems: Integration of Electronics and Fluidics Using Low-Temperature Co-Fired Ceramics. *Anal. Chem.* **2007**, *79* (21), 8376–8380. https://doi.org/10.1021/ac0713398.

(231) Ibanez-Garcia, N.; Mercader, M. B.; Mendes da Rocha, Z.; Seabra, C. A.; Góngora-Rubio, M. R.; Chamarro, J. A. Continuous Flow Analytical Microsystems Based on Low-Temperature Co-Fired Ceramic Technology. Integrated Potentiometric Detection Based on Solvent Polymeric Ion-Selective Electrodes. *Anal. Chem.* **2006**, *78* (9), 2985–2992. https://doi.org/10.1021/ac051994k.

(232) Gongora-Rubio, M. R.; Espinoza-Vallejos, P.; Sola-Laguna, L.; Santiago-Avilés, J. J. Overview of Low Temperature Co-Fired Ceramics Tape Technology for Meso-System Technology (MsST). *Sensors Actuators A Phys.* **2001**, *89* (3), 222–241. https://doi.org/10.1016/S0924-4247(00)00554-9.

(233) Vasudev, A.; Kaushik, A.; Jones, K.; Bhansali, S. Prospects of Low Temperature Co-Fired Ceramic (LTCC) Based Microfluidic Systems for Point-of-Care Biosensing and Environmental Sensing. *Microfluid. Nanofluidics* **2013**, *14*, 683–702. https://doi.org/10.1007/s10404-012-1087-3.

(234) Martinez, A. W.; Phillips, S. T.; Butte, M. J.; Whitesides, G. M. Patterned Paper as a Platform for Inexpensive, Low-Volume, Portable Bioassays. *Angew. Chemie Int. Ed.* **2007**, *46* (8), 1318–1320. https://doi.org/10.1002/anie.200603817.

(235) Li, X.; Ballerini, D. R.; Shen, W. A Perspective on Paper-Based Microfluidics: Current Status and Future Trends. *Biomicrofluidics* **2012**, *6* (1), 11301–1130113. https://doi.org/10.1063/1.3687398.

(236) Qamar, A. Z.; Shamsi, M. H. Desktop Fabrication of Lab-On-Chip Devices on Flexible Substrates: A Brief Review. *Micromachines* **2020**, *11* (2), 126. https://doi.org/10.3390/mi11020126.

(237) Al-Shehri, S.; Palitsin, V.; Webb, R. P.; Grime, G. W. Fabrication of Three-Dimensional SU-8 Microchannels by Proton Beam Writing for Microfluidics Applications: Fluid Flow Characterisation. *Nucl. Instruments Methods Phys. Res. Sect. B Beam Interact. with Mater. Atoms* **2015**, *348*, 223–228. https://doi.org/10.1016/j.nimb.2014.12.014.

(238) Raj M, K.; Chakraborty, S. PDMS Microfluidics: A Mini Review. *J. Appl. Polym. Sci.* **2020**, *137* (27), 48958. https://doi.org/10.1002/app.48958.

(239) Kim, J.; DeMello, A. J.; Chang, S.-I.; Hong, J.; O'Hare, D. Thermoset Polyester Droplet-Based Microfluidic Devices for High Frequency Generation. *Lab Chip* **2011**, *11* (23), 4108–4112. https://doi.org/10.1039/c1lc20603f.

(240) Liao, S.; He, Y.; Chu, Y.; Liao, H.; Wang, Y. Solvent-Resistant and Fully Recyclable Perfluoropolyether-Based Elastomer for Microfluidic Chip Fabrication. *J. Mater. Chem. A* **2019**, *7* (27), 16249–16256. https://doi.org/10.1039/C9TA03661J.

(241) Kotz, F.; Risch, P.; Helmer, D.; Rapp, B. Highly Fluorinated Methacrylates for Optical 3D Printing of Microfluidic Devices. *Micromachines* **2018**, *9* (3), 115. https://doi.org/10.3390/mi9030115.

(242) Oliveira, B.; Veigas, B.; Fernandes, A. R.; Águas, H.; Martins, R.; Fortunato, E.; Baptista, P. V. Fast Prototyping Microfluidics: Integrating Droplet Digital Lamp for Absolute Quantification of Cancer Biomarkers. *Sensors* **2020**, *20* (6), 1624.

https://doi.org/10.3390/s20061624.

(243) Salman, A.; Carney, H.; Bateson, S.; Ali, Z. Shunting Microfluidic PCR Device for Rapid Bacterial Detection. *Talanta* **2020**, *207*, 120303. https://doi.org/10.1016/j.talanta.2019.120303.

(244) Li, F.; Zheng, Y.; Wu, J.; Zhao, L.; Shui, L.; Pu, Q.; Liu, S. Smartphone Assisted Immunodetection of HIV P24 Antigen Using Reusable, Centrifugal Microchannel Array Chip. *Talanta* **2019**, *203*, 83–89. https://doi.org/10.1016/j.talanta.2019.05.042.

(245) La, H. C.; Lee, N. Y. Fabrication of a Polycarbonate Microdevice and Boronic Acid-Mediated Surface Modification for on-Chip Sample Purification and Amplification of Foodborne Pathogens. *Biomed. Microdevices* **2019**, *21*, 72. https://doi.org/10.1007/s10544-019-0420-y.

(246) Fan, Y.; Gao, K.; Chen, J.; Li, W.; Zhang, Y. Low-Cost PMMA-Based Microfluidics for the Visualization of Enhanced Oil Recovery. *Oil Gas Sci. Technol. – Rev. d'IFP Energies Nouv.* **2018**, *73*, 26. https://doi.org/10.2516/ogst/2018026.

(247) Trinh, K. T. L.; Zhang, H.; Kang, D.-J.; Kahng, S.-H.; Tall, B. D.; Lee, N. Y. Fabrication of Polymerase Chain Reaction Plastic Lab-on-a-Chip Device for Rapid Molecular Diagnoses. *Int. Neurourol. J.* **2016**, *20* (1), S38-48. https://doi.org/10.5213/inj.1632602.301.

(248) Wu, Y.-T.; Yang, C.-E.; Ko, C.-H.; Wang, Y.-N.; Liu, C.-C.; Fu, L.-M. Microfluidic Detection Platform with Integrated Micro-Spectrometer System. *Chem. Eng. J.* **2020**, *393*, 124700. https://doi.org/10.1016/j.cej.2020.124700.

(249) Debski, P.; Sklodowska, K.; Michalski, J.; Korczyk, P.; Dolata, M.; Jakiela, S. Continuous Recirculation of Microdroplets in a Closed Loop Tailored for Screening of Bacteria Cultures. *Micromachines* **2018**, *9* (9), 469. https://doi.org/10.3390/mi9090469.

(250) Alves, I. P.; Reis, N. M. Immunocapture of Escherichia Coli in a Fluoropolymer Microcapillary Array. *J. Chromatogr. A* **2019**, *1585*, 46–55. https://doi.org/10.1016/j.chroma.2018.11.067.

(251) Pivetal, J.; Pereira, F. M.; Barbosa, A. I.; Castanheira, A. P.; Reis, N. M.; Edwards, A. D. Covalent Immobilisation of Antibodies in Teflon-

FEP Microfluidic Devices for the Sensitive Quantification of Clinically Relevant Protein Biomarkers. *Analyst* **2017**, *142* (6), 959–968. https://doi.org/10.1039/C6AN02622B.

(252) Do, J.; Ahn, C. H. A Polymer Lab-on-a-Chip for Magnetic Immunoassay with on-Chip Sampling and Detection Capabilities. *Lab Chip* **2008**, *8* (4), 542–549. https://doi.org/10.1039/b715569g.

(253) Berenguel-Alonso, M.; Sabés-Alsina, M.; Morató, R.; Ymbern, O.; Rodríguez-Vázquez, L.; Talló-Parra, O.; Alonso-Chamarro, J.; Puyol, M.; López-Béjar, M. Rapid Prototyping of a Cyclic Olefin Copolymer Microfluidic Device for Automated Oocyte Culturing. *SLAS Technol. Transl. Life Sci. Innov.* **2017**, *22* (5), 507–517. https://doi.org/10.1177/2472555216684625.

(254) Calvo-López, A.; Ymbern, O.; Puyol, M.; Casalta, J. M.; Alonso-Chamarro, J. Potentiometric Analytical Microsystem Based on the Integration of a Gas-Diffusion Step for on-Line Ammonium Determination in Water Recycling Processes in Manned Space Missions. *Anal. Chim. Acta* **2015**, *874*, 26–32. https://doi.org/10.1016/j.aca.2014.12.038.

(255) Nunes, P. S.; Ohlsson, P. D.; Ordeig, O.; Kutter, J. P. Cyclic Olefin Polymers: Emerging Materials for Lab-on-a-Chip Applications. *Microfluid. Nanofluidics* **2010**, *9*, 145–161. https://doi.org/10.1007/s10404-010-0605-4.

(256) Blochowiak, M. Structure and Properties of Norbornene-Ethylene Copolymers. PhD Thesis, Technical University of Lódiz, Poland, 2006.

(257) Leech, P. W.; Zhang, X.; Zhu, Y. Effect of Norbornene Content on Deformation Properties and Hot Embossing of Cyclic Olefin Copolymers. *J. Mater. Sci.* **2010**, *45*, 5364–5369. https://doi.org/10.1007/s10853-010-4585-2.

(258) Becker, H.; Gärtner, C. Polymer Microfabrication Technologies for Microfluidic Systems. *Anal. Bioanal. Chem.* **2008**, *390* (1), 89–111. https://doi.org/10.1007/s00216-007-1692-2.

(259) Kolew, A.; Münch, D.; Sikora, K.; Worgull, M. Hot Embossing of Micro and Sub-Micro Structured Inserts for Polymer Replication. *Microsyst. Technol.* **2011**, *17*, 609–618.

https://doi.org/10.1007/s00542-010-1182-x.

(260) Jena, R. K.; Chester, S. A.; Srivastava, V.; Yue, C. Y.; Anand, L.; Lam, Y. C. Large-Strain Thermo-Mechanical Behavior of Cyclic Olefin Copolymers: Application to Hot Embossing and Thermal Bonding for the Fabrication of Microfluidic Devices. *Sensors Actuators B Chem.* **2011**, *155* (1), 93–105. https://doi.org/10.1016/j.snb.2010.11.031.

(261) Maghsoudi, K.; Jafari, R.; Momen, G.; Farzaneh, M. Micro-Nanostructured Polymer Surfaces Using Injection Molding: A Review. *Mater. Today Commun.* **2017**, *13*, 126–143. https://doi.org/10.1016/j.mtcomm.2017.09.013.

(262) Khan Malek, C. G. Laser Processing for Bio-Microfluidics Applications (Part I). *Anal. Bioanal. Chem.* **2006**, *385*, 1351–1361. https://doi.org/10.1007/s00216-006-0514-2.

(263) Guckenberger, D. J.; de Groot, T. E.; Wan, A. M. D.; Beebe, D. J.; Young, E. W. K. Micromilling: A Method for Ultra-Rapid Prototyping of Plastic Microfluidic Devices. *Lab Chip* **2015**, *15* (11), 2364–2378. https://doi.org/10.1039/C5LC00234F.

(264) Benelmekki, M.; Erbe, A. Nanostructured Thin Films–Background, Preparation and Relation to the Technological Revolution of the 21st Century. *Front. Nanosci.* **2019**, *14*, 1–34. https://doi.org/10.1016/B978-0-08-102572-7.00001-5.

(265) Simon, A. H. *Chapter 7 - Sputter Processing*, 4th ed.; William Andrew Publishing, 2018. https://doi.org/10.1016/B978-0-12-812311-9.00007-4.

(266) Chu, Z.; Peng, J.; Jin, W. Advanced Nanomaterial Inks for Screen-Printed Chemical Sensors. *Sensors Actuators B Chem.* **2017**, *243*, 919–926. https://doi.org/10.1016/j.snb.2016.12.022.

(267) Renedo, O. D.; Alonso-Lomillo, M. A.; Martínez, M. J. A. Recent Developments in the Field of Screen-Printed Electrodes and Their Related Applications. *Talanta* **2007**, *73* (2), 202–219. https://doi.org/10.1016/j.talanta.2007.03.050.

(268) Chen, P.-C.; Duong, L. H. Novel Solvent Bonding Method for Thermoplastic Microfluidic Chips. *Sensors Actuators B Chem.* **2016**,

*237*, 556–562. https://doi.org/10.1016/j.snb.2016.06.135.

(269) Amanat, N.; James, N. L.; McKenzie, D. R. Welding Methods for Joining Thermoplastic Polymers for the Hermetic Enclosure of Medical Devices. *Med. Eng. Phys.* **2010**, *32* (7), 690–699. https://doi.org/10.1016/j.medengphy.2010.04.011.

(270) Kistrup, K.; Poulsen, C. E.; Hansen, M. F.; Wolff, A. Ultrasonic Welding for Fast Bonding of Self-Aligned Structures in Lab-on-a-Chip Systems. *Lab Chip* **2015**, *15* (9), 1998–2001. https://doi.org/10.1039/C5LC00174A.

(271) Steigert, J.; Haeberle, S.; Brenner, T.; Müller, C.; Steinert, C. P.; Koltay, P.; Gottschlich, N.; Reinecke, H.; Rühe, J.; Zengerle, R.; Ducrée, J. Rapid Prototyping of Microfluidic Chips in COC. *J. Micromechanics Microengineering* **2007**, *17* (2), 333–341. https://doi.org/10.1088/0960-1317/17/2/020.

# Chapter 2

# Objectives

The main objective of this doctoral thesis is the development and validation of functional prototypes of POC potentiometric platforms for the biochemical management of different IEMs. This work focuses mainly on the management of IEMs presenting hyperammonemia as their main physiopathological trait, and also, on the modification of these analytical microsystems by the incorporation of an enzyme for the indirect measurement of other metabolites by their conversion into $NH_4^+$. Thus, allowing the application of these µTAS for the management of a wide range of diseases. The central goal of this doctoral thesis can be further subdivided into two fundamental points:

1) The development and validation with real samples of a FIA reusable microsystem for the potentiometric detection of $NH_4^+$ in blood for hospital use, aimed to the detection of hiperammonemic states and the subsequent follow-up. Moreover, the further automation of this complete analytical system as a POC device for continuous and autonomous functioning in a clinical setting.

2) The development of a disposable auto-calibrating microanalytical device for the potentiometric measurement of $NH_4^+$ in blood for use at home. Furthermore, the modification of this device by the incorporation of an enzyme for the indirect measurement of other biologically relevant metabolites in blood, biomarkers of some IEM, for use at home.

Both these analytical devices to be developed must fulfil some features such as a high degree of miniaturization, robustness, reliability, low sample and reagent volume, low cost to allow further industrialization and commercialization, high degree of automation, ease of use, short analysis times and, in the case of the reusable microsystem, a high throughput. In addition, they must present satisfactory analytical characteristics suitable for the application of interest.

In order to achieve these main objectives, several other additional goals have to be met. Regarding the FIA analytical system for continuous and autonomous functioning in a clinical setting, these are:

1) Design and fabrication of microfluidic platforms based on COC-technology and the integration of the elements required for the potentiometric determination of $NH_4^+$ by flow injection technique.

2) Selection of the appropriate material for the separation of $NH_4^+$ from the sample matrix.

3) Optimization of the hydrodynamic and chemical variables of the analytical microsystem in order to obtain the best analytical features that allow the discrimination between healthy and pathological $NH_4^+$ levels.

4) Validation of the analytical microsystem by the analysis of real plasma and blood samples from healthy individuals and patients presenting hyperammonemia, and comparison of the obtained results with the stablished reference method.

5) Full automation of the developed FIA system to develop a POC analyzer and its implementation in a hospital setting for continued use, and further validation with blood samples.

Regarding the disposable auto-calibrating microanalytical device, the goals are:

1) Design and fabrication of analytical platforms based on COC-technology devoted to the control of IEM at the home of the patients. Integration of the elements required for the potentiometric measurement of $NH_4^+$ and for the separation of $NH_4^+$ from the sample matrix.

2) Optimization of chemical variables in order to obtain the best analytical characteristics suitable for the measurement of $NH_4^+$ in blood at home.

3) Modification of these disposable microanalytical devices with urease, as a model enzyme, for indirect determination of urea in

blood in order to validate theindirect determination of a biomarker by the enzymatic analytical system concept.

4) Optimization of the chemical variables in order to obtain the best analytical characteristics for the discrimination of urea in healthy and pathological working ranges.

5) Modification of these disposable microanalytical devices with the addition of Phenylalanine ammonia lyase (PAL) for the indirect detection of Phe.

6) Optimization of the chemical variables in order to obtain the best analytical characteristics for the detection of healthy and pathological concentrations of Phe.

# Chapter 3

# Experimental

The following chapter details the materials and reagents used during the experimental work carried out during the realization of this thesis. It also describes the designs and fabrication processes for every developed analytical prototype.

## 3.1. Materials and reagents

The analytical platforms were fabricated using COC 8007 (of 25 µm thickness) and COC 6013 (of 400 µm and 130 µm thickness) obtained from Tekni-Plex (Erembodegem, Belgium). The electric connectors were constituted by a conductive epoxy (CircuitWorks, Chemtronics, The Netherlands).

For the fabrication of the reference electrode, the Ag/AgCl C2030812D3 paste (Gwent, Pontypool, United Kingdom) was used. Regarding the ISE conductive support, two materials were used: an epoxy-graphite resin constituted by 50 % powdered graphite of 50 µm particle size (Merk, Germany), 36 % epoxy Araldite-M (Ciba Geigy, Spain) and 14 % hardener HR (Ciba Geigy, Spain), and a screen-printed carbon paste, Electrodag PF-407A (Henkel, Germany). Likewise, two ISM compositions were employed: the first was composed of 1 % nonactin (Sigma-Aldrich, Spain) as a recognition element, 33.5 % PCV (Sigma-Aldrich, Spain) as polymer matrix and 65.5 % bis(1-butylpentyl)adipate (BBPA) (Sigma-Aldrich, Spain) as plasticizer. The second ISM composition used was constituted by 2 % nonactin (Sigma-Aldrich, Spain), 33.5 % PVC (Sigma-Aldrich, Spain), 65.5 % of a poly(butylene sebacate) plasticizer (PBSP) commercialized as Paraplex G-25 (Hallstar, Illinois, US) and 0.5 % Potassium tetrakis(4-chlorophenyl)borate (Sigma-Aldrich, Spain) as an additive. Both ISM formulations used tetrahydrofuran (THF) (Sigma-Aldrich, Spain) as solvent. Prototypes that included the ISM formulation with BBPA must undergo an overnight conditioning step in contact with $10^{-4}$ M ammonium chloride ($NH_4Cl$) for 4 hours and with 0.1 M $NH_4Cl$ for 16 hours prior to use.

The reagents used in this work included $NH_4Cl$ (Acros Organics, Belgium) for the preparation of standard solutions of $NH_4^+$ and potassium chloride (KCl) (Sigma-Aldrich, Spain) to keep stable the potential of the reference electrode and for the interference study. For the conversion of $NH_4^+$ to gaseous $NH_3$, sodium hydroxide (NaOH) (Sigma-Aldrich, Spain) was used, together with $10^{-3}$ M ethylenediaminetetraacetic acid (EDTA) (Panreac, Spain). Additionally, two different buffers, 2-amino-2-(hydroxymethyl)propane-1,3-diol (TRIS) (Thermo Fisher Scientific, Spain) and 2-[4-(2-hydroxyethyl)piperazin-1-yl]ethanesulfonic acid (HEPES) (Sigma-Aldrich, Spain) were used to adjust the pH and the ionic strength. To fix the pH of these two buffers, hydrochloric acid (HCl) (Sigma-Aldrich, Spain) was used for the TRIS buffer and barium hydroxide ($Ba(OH)_2$) (Thermo Fisher Scientific, Spain) was used for the HEPES buffer. Reagents employed for the interference effect experiments included sodium chloride (NaCl) and lithium chloride (LiCl), both from Sigma-Aldrich, (Spain). For the preparation of Phosphate Buffered Saline (PBS), di-sodium hydrogen phosphate ($Na_2HPO_4$) was purchased from Sigma-Aldrich (Spain). Enzyme Urease was purchased from Sigma-Aldrich (Spain) and Phenylalanine ammonia lyase (PAL) was donated from Gecco Biotech (The Netherlands). For the preparation of the standard solutions, urea and L-phenylalanine from Sigma-Aldrich (Spain) were employed. For the automated POC analyzer for hospital use, the same calibration solution of the Ammonia Ultra kit that is used by the reference method from ABBOT (Illinois, US) was employed as control solution.

All solutions were prepared using Milli-Q water and were degassed previous to use to avoid the formation of air bubbles inside the channels of the microfluidic platform.

A hydrophobic polyvinyldene fluoride (PVDF) membrane of 125 µm thickness and 0.45 µm porous size obtained from Millipore (US) was used for the separation of $NH_4^+$ from the matrix sample by a gas diffusion process. Different membranes of varied composition and porous sizes were tested as protective membranes to avoid direct contact between the blood matrix and the PVDF membrane. The particular providers, materials and structure of these protective membranes can be seen in *Table 3.I*. Values of pore size (µm) and molecular weight cut-off (MWCO) were compared by conversion following *Eq. 3.1*:

$$r = 0.066 \cdot MW^{1/3} \qquad \text{Eq. 3.1}$$

where r (nm) is the minimum radius and MW is the molecular weight (Da).

Table 3.I Summary of materials, pore size, molecular weight cut-off and manufacturer of the different membranes evaluated to be used as protective membranes.

| **Membrane** | **Material** | **Pore size (µm)** | **MWCO (kDa)** | **Manufacturer** |
|---|---|---|---|---|
| **1** | Polycarbonate | 0.05 | $5.4 \cdot 10^{+4}$* | Whatman Nucleopore |
| **2** | Polycarbonate | 0.015 | $9.4 \cdot 10^{+3}$* | Whatman Nucleopore |
| **3** | Hydrophilic PVDF | 0.65 | $7.6 \cdot 10^{+8}$* | Millipore |
| **4** | Regenerated cellulose | $4.86 \cdot 10^{-3}$* | 50 | Spectra/Por |
| **5** | Cellulose | $3.02 \cdot 10^{-3}$* | 12 | Sigma-Aldrich |
| **6** | Regenerated cellulose | $1.32 \cdot 10^{-3}$* | 1 | Sigma-Aldrich |
| **7** | Polyethersulfone | $4.86 \cdot 10^{-3}$* | 50 | Merk Millipore |
| **8** | Ester cellulose | $2.84 \cdot 10^{-3}$* | 10 | Spectra Por |

*MWCO values calculated as indicated in reference[1].

## 3.2. Microsystem for the detection of ammonium ion in blood for hospital use

All the designs and fabrication processes for the microfluidic platforms evaluated during the development of the FIA microanalyzer for hospital use aimed at $NH_4^+$ determination in blood are detailed hereunder.

### 3.2.1. Design

During the course of this doctoral thesis three different prototypes were developed for the FIA microsystem destined for the detection of $NH_4^+$ in blood at a hospital or a clinic. They will be referred as prototype I (PI), prototype II (PII) and prototype III (PIII).

In the case of the PI, the design of the microfluidic platform was customized for the determination of $NH_4^+$ by means of the direct contact between the sample and the ISM, and it is shown in *Fig. 3.1*. This design includes a micromixer to facilitate the mixing of a buffer solution at a neutral pH with a carrier solution containing the $NH_4Cl$ standard solution or the sample to be analyzed. The $NH_4^+$ present in the standard solution or sample reaches a detection chamber of 1.8 mm or 3.5 mm diameter where the ISE is located. The microfluidic channels were 400 µm wide and 300 µm deep, and the micromixer had a total length of 21.1 cm. To keep the reference electrode at a stable potential, a 0.1 M KCl solution constantly flows through a separate channel that joins the buffer solution after the ISE, thus creating a free-diffusion liquid junction.[2]

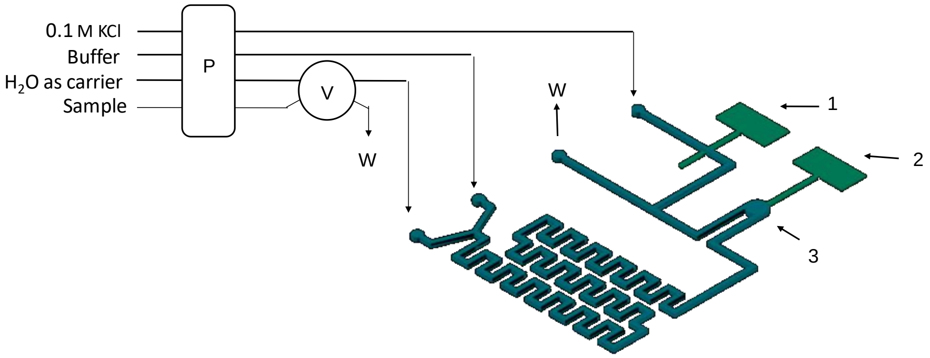

Fig. 3.1 Schematic representation of the design for PI: 1) reference electrode, 2) indicator electrode, 3) detection chamber, P) peristaltic pump, V) six-way injection valve and W) waste.

In addition to all the elements previously described in PI, the PII design, which is shown in *Fig. 3.2*, also includes a gas diffusion membrane (a PDVF membrane) located between two overlapped serpentine channels. On one side of this membrane, the carrier solution containing the standard solutions or the samples is mixed with a NaOH 0.1 M solution with $10^{-3}$ M EDTA in the micromixer and this constitutes the donor solution. EDTA was used to avoid the precipitation inside the microchannels of hydroxides resulting from the metals in the blood matrix. $NH_4^+$, in the presence of NaOH, converts into $NH_3$ soluble gas, which can diffuse through the gas diffusion membrane and reach the channels on the other side of the gas diffusion membrane. There, an acceptor buffer solution at a neutral pH flows, $NH_3$ converts back into $NH_4^+$, and is directed towards the detection chamber, where it is detected by the ISE.

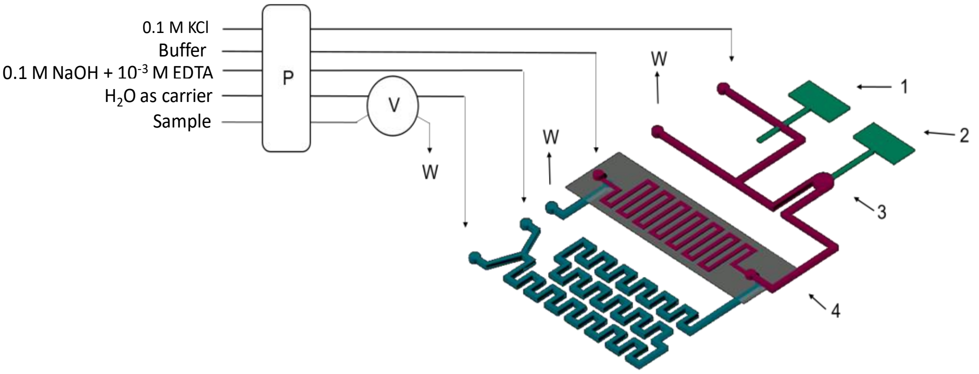

Fig. 3.2 Schematic representation of the design for PII: 1) reference electrode, 2) indicator electrode, 3) detection chamber, 4) gas diffusion membrane, P) peristaltic pump, V) six-way injection valve and W) waste.

Regarding PIII, its design can be seen in *Fig. 3.3* and is very similar to that of PII. The single difference is the addition of a second membrane, located between the gas diffusion membrane and the donor solution. The purpose of this extra membrane was to avoid direct contact between the gas diffusion membrane and the blood matrix. In this way, we can protect it from compounds present in blood, such as blood proteins, and prevent pore clogging, therefore, lengthening the membrane lifetime.

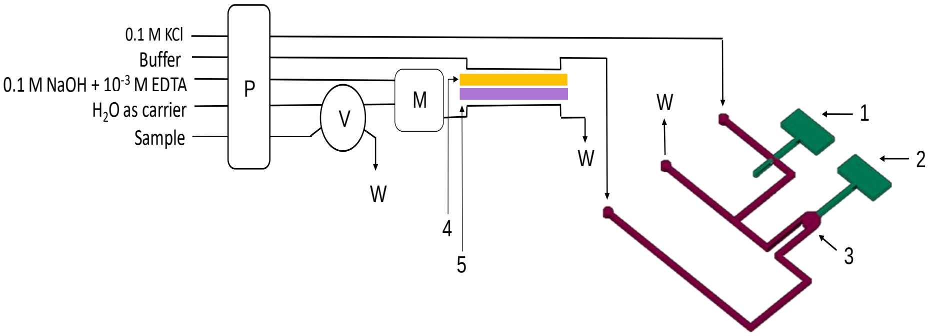

Fig. 3.3 Schematic representation of the design for PIII: 1) reference electrode, 2) indicator electrode, 3) detection chamber, 4) gas diffusion membrane in orange, 5) protective membrane in purple, P) peristaltic pump, V) six-way injection valve and W) waste.

The design of the channels at both sides of the gas diffusion membrane are represented in *Fig. 3.4* and its dimensions are of 1 mm width, 11 cm length and 100 µm depth. Inlets and outlets do not overlap at the same point to avoid excessive pressure over the gas diffusion membrane at the inlets points. The design of this analytical platform ensured the successful isolation of $NH_4^+$ from the rest of the compounds of the complex sample matrix, avoiding undesired interferences in potentiometric detection.

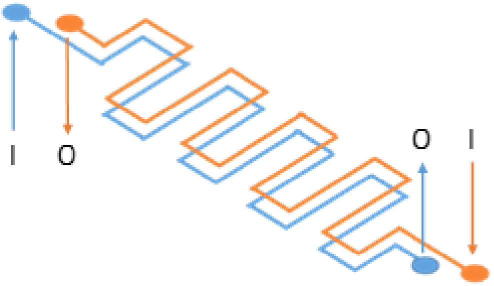

Fig. 3.4 Schematic representation of the microchannels on both sides of the gas diffusion membrane, with the inlets (I) and the outlets (O) indicated.

An alternative configuration of this microfluidic configuration was also developed, the main difference of which is the structure of both inlets, which are designed in a step-like configuration (*Fig. 3.5*). Moreover, in order to facilitate fabrication and to avoid overpressure, channels of this alternative gas diffusion module have the same width and length but the depth is of 200 µm instead of 100 µm.

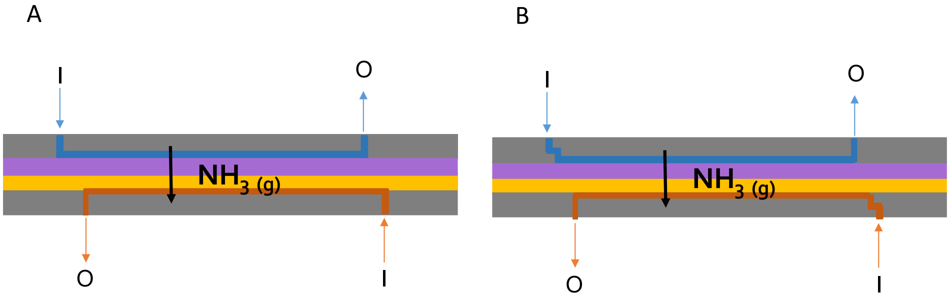

Fig. 3.5 Schematic representation of the lateral view for the microchannels at both sides of the gas diffusion membrane (A) and the alternative configuration (B), showing the protective membrane (purple) and the gas diffusion membrane (yellow) and the inlets (I) and outlets (O) of the donor side (blue) and the acceptor side (orange).

### 3.2.2. Microfabrication

All the microfluidic platforms described in the previous section were obtained following the same fabrication processes which are depicted in *Fig. 3.6*. The GSB group owns the necessary infrastructure to carry out this microfabrication procedure and has extensive experience in thermoplastic polymer-technology, which has already been described in previous works of the group.[3–7]

In this dissertation, in order to facilitate the optimization of the different elements of the analytical system, PI, PII and PIII were fabricated as modular devices, in which we have three different constituents: the mixing module, the gas diffusion module and the detection module.

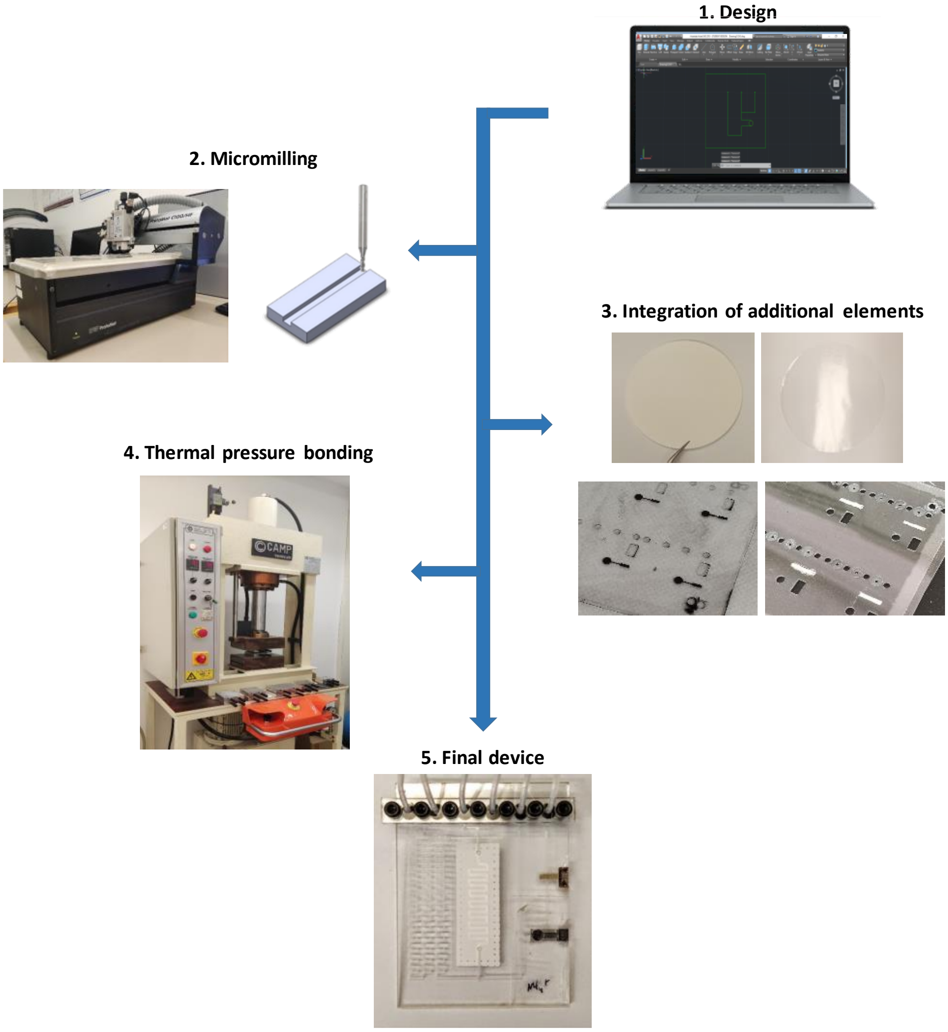

Fig. 3.6 Overview of the different steps for the fabrication of the analytical microsystems using thermoplastics multilayer technology: 1) Design 2) Micromilling 3) Integration of additional elements 4) Thermal pressure bonding 5) Final devices.

The fabrication process begins with the selection of the substrate material and the design of the patterns for each layer that constitute the final 3D structure. For the fabrication of all prototypes, the selected substrate material for the mixing and detection modules was COC. In particular, two different COC sheets of two different thicknesses and composition were used. This way, we have two different COC substrates of different $T_g$. One of the COC has a thickness of 25 µm and a $T_g$ of 78 °C, and serves as sealant during the thermal-pressure bonding process. The other COC sheets have a thickness of 400 µm and a $T_g$ of 138 °C, and are used as structural layers containing the micromachined motifs. The mixing module was constituted by five structural layers intercalated with four sealing layers. For the detection module, a total of six structural layers and five sealing layers were used.

On the other hand, the first configuration of the gas diffusion module consisted of a steel structure, which contained two 3.6 x 6 x 0.29 cm PMMA layers, previously micromilled with the corresponding microchannels. Both the gas diffusion and the protective membranes were positioned between the two PMMA layers so that donor and acceptor channels overlapped when hermetically closed by a screw thread. For ease of fabrication, the alternative gas diffusion configuration was fabricated using six 25 µm COC layers and seven 400 µm COC layers, and the overall dimensions were also of 3.6 x 6 x 0.29 for each side, to fit the same steel structure.

As mentioned in *Chapter 1*, the design of each structural layer was carried out through a CAD software and the superposition of all these motives constitutes the final 3D structure of the analytical platform. Afterwards, individual designs were processed using a computer aided manufacturing (CAM) processing software to obtain a CAM file that can be read by the micromilling machine software.

The following step in the fabrication process was microstructuring each COC layer. The technology chosen for the microfabrication was micromilling of polymer surface. For this purpose, a ProtoMat C/HF mill/drill unit (LPKF Laser & Electronics, Garbsen, Germany) with a working area of 200 x 300 mm was used (*Fig. 3.7A*). Most parameters, including the drill position in the XY plane and its rotational and displacement speeds are controlled by the CircuitMaster software. However, the drill position in the Z plane is manually controlled via a micrometre of a 10 µm resolution. Although this results in a less automated fabrication process, it allows a more precise and continuous control of the patterns depth, which is significantly important when prototyping complex designs as these ones. The employed tools in the micromilling process were end milling tools of 0.4, 0.8, 1 and 2 mm diameter and are depicted in *Fig. 3.7B*.

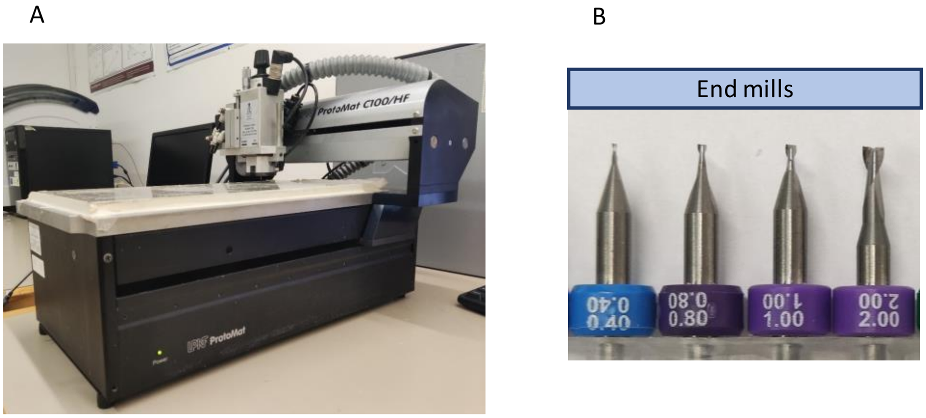

Fig. 3.7 Real image of the micromilling machine, B) Real image of the end mills employed during the micromilling process.

After that, the additional elements required for the analytic microsystem operation are added. In this case, the epoxy-graphite is placed to act as conductive support of the ISE and left to cure overnight at 40 °C (and sanded afterwards). The Ag/AgCl paste is screen printed to constitute the reference electrodes (*Fig. 3.8*). The ISM is also deposited by drop-casting with a micropipette in intervals of 5 minutes to allow the slowly evaporation of the organic solvent without the formation of bubbles within the membrane.

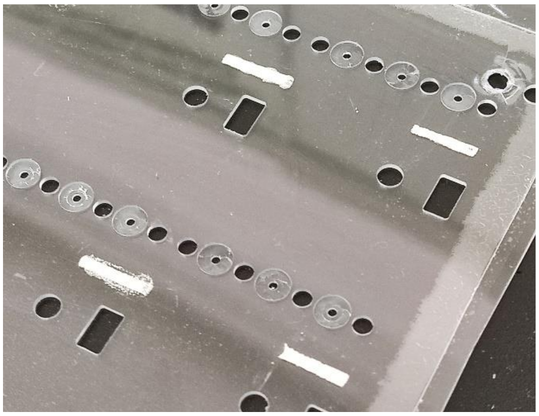

Fig. 3.8 Real image of the Ag/AgCl screen-printed paste for the reference electrodes.

The next step is to carry out a thermal-pressure bonding with all the layers stacked and aligned in the correct order. This seals all the COC layers in an irreversible way, hence, obtaining a monolithic device with the desired 3D design. For this purpose, a hydraulic press (Talleres Francisco Camps SA, Granollers, Spain) was used (*Fig. 3.9A)*. A metallic plate with a working area of 100 x 100 cm was used to obtain an optimum alignment between the different layers by means of four 2 mm diameter fiducial holes (*Fig. 3.9B*). Between the outside COC layers and the metallic plaque, a silicon sheet was placed to homogenize pressure to the entire surface, a PMMA plate was used to avoid deformation of the micromachinned structures, and an anti-adherent polymer sheet was used to keep the COC surface clean (*Fig. 3.9C*).

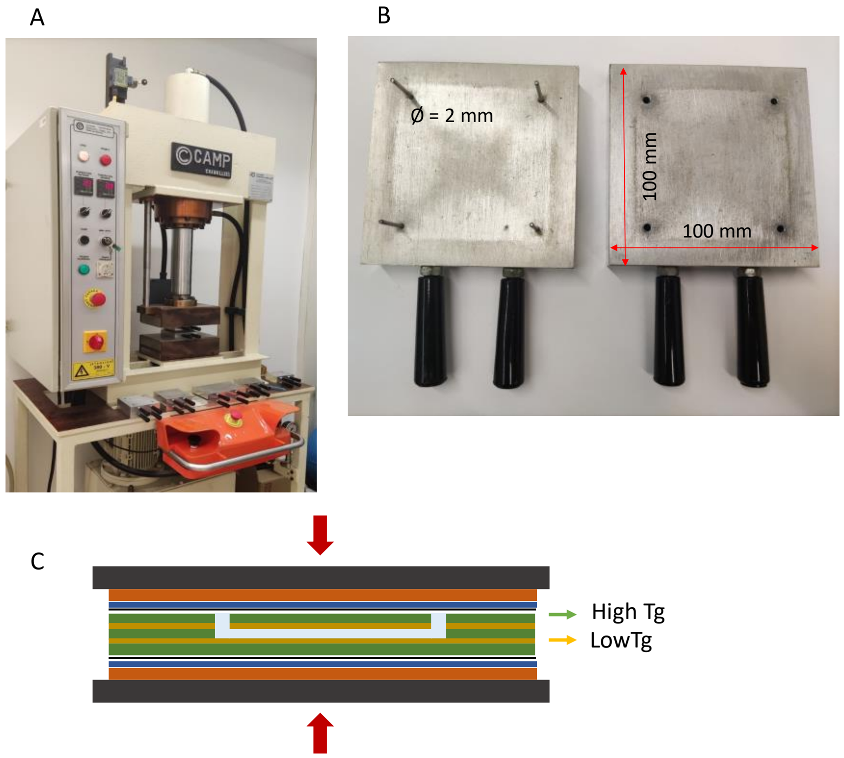

Fig. 3.9 A) Real image of the hydraulic press used for the thermal-pressure bonding, B) Real image of the metallic plates used for alignment of the COC layers, C) Schematic depiction of the arrangement for the thermal pressure bonding process of a basic schematic microfluidic system constituted of an inlet, a channel and an outlet. The silicon sheet (orange), PMMA plate (blue), anti-adherent polymer (black line) and COC layers of high $T_g$ (green) and low $T_g$ (yellow) and metallic plates (dark grey) are depicted. Pressure direction is indicated by the red arrows.

The thermal pressure bonding procedure consisted in increasing and decreasing the temperature under a constant pressure conditions of 4 bar. The maximum temperature achieved during this process was 102 °C, which is above the $T_g$ for the sealing COC layers and lower than the $T_g$ for the COC structural layers. This way, all layers are irreversibly sealed together, without the need to use any adhesives and without the risk of deformation of the micromilled patterns.

Finally, elements that are not compatible with the thermal pressure bonding process are incorporated. These elements are electric connectors (*Fig. 3.10A*), as well as fluidic connectors, used to attach devices to external components. These fluidic connectors consist of a PMMA piece that presses a Teflon tube with an O-ring against the microfluidic device ports with the aid of screws (*Fig. 3.10B*).

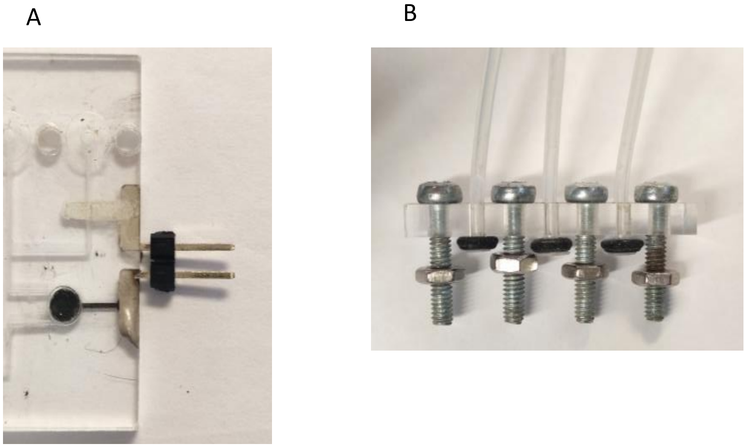

Fig. 3.10 A) Real images of the electric connectors and B) Real image of the fluidic connectors.

### 3.2.3. Final device

Three different constituents can be distinguished: the mixing module (*Fig. 3.11*A), the detection module (*Fig. 3.11*B) and the gas diffusion module (*Fig. 3.11C-F*). The two former modules both have dimensions of 3.4 x 2.7 x 0.2 cm, whereas the later module has dimensions of 8 x 3.2 x 5 cm when closed. Both gas diffusion module configurations have glued flanges in inlets and outlets for fluidic connection.

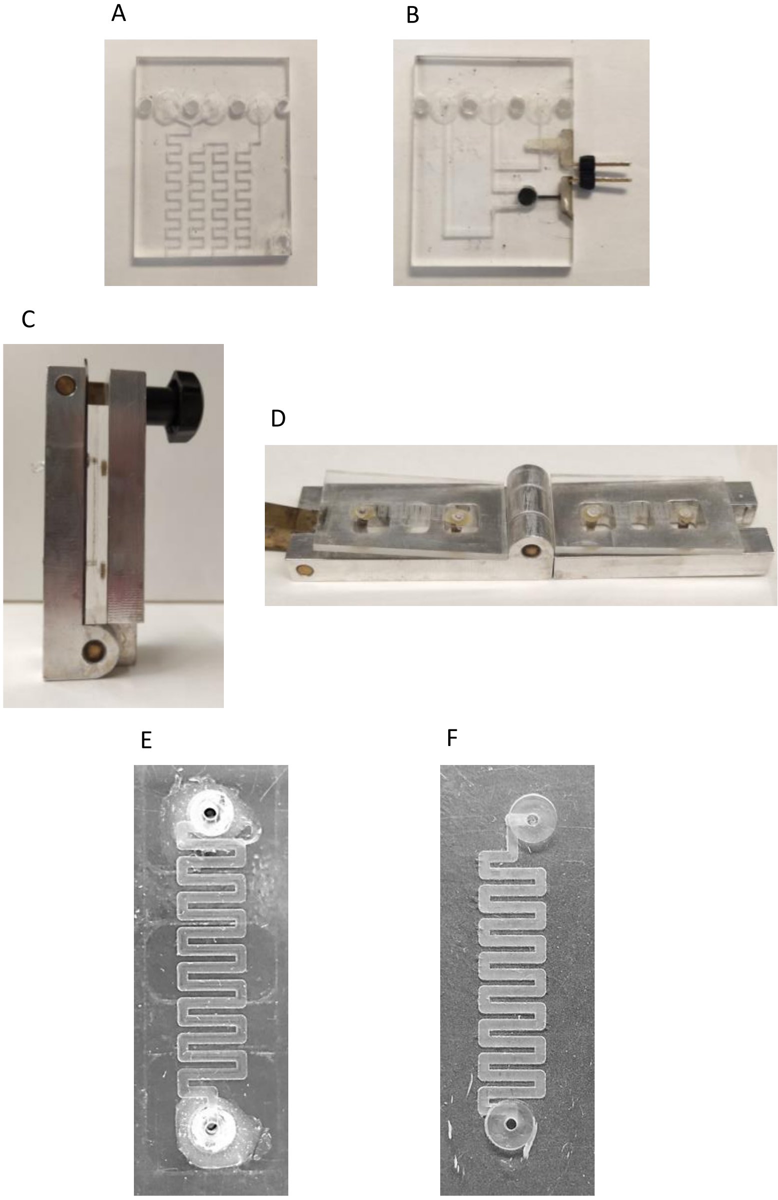

Fig. 3.11 Real images of the different modules: A) mixing module, B) the detection module, C) gas diffusion module closed, D) gas diffusion module opened, E) microchannels of the original configuration of the gas diffusion module (F) and alternative gas diffusion module configuration (G).

### 3.2.4. Experimental set-ups

The experimental set-up for PI (*Fig. 3.12A*) and PII and PIII (*Fig. 3.12B*) consisted of a four channel peristaltic pump (Minipuls 3, Gilson, WI, US) equipped with Tygon tubes (Ismatec, Wertheim, Germany) of 1.14 mm of internal diameter for the liquid propulsion of all channels with the exception of the auxiliary 0.1 M KCl solution, for which Tygon tubes of 0.64 mm of internal diameter ( Ismatec, Wertheim, Germany) were used. Moreover, a six-way injection valve (Hamilton, MVP, Reno, EEUU) was used for the sample injection. Teflon tubes of 0.8 mm of diameter (Scharlab, S.L., Cambridge, England) were used to connect the analytical microsystem to the external elements. Signal acquisition was carried out by a potentiometer (TMI, Barcelona, Spain).

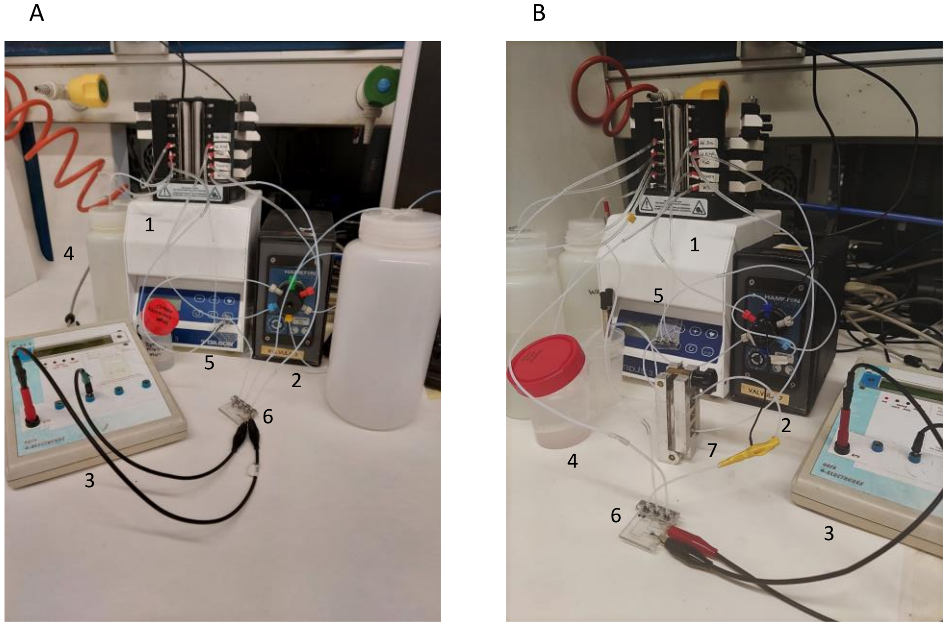

Fig. 3.12 Real images of the experimental set-up for PI (A) and PII and PIII (B). 1) peristaltic pump, 2) six-way injection valve, 3) potentiometer, 4) reagents, 5) micromixer, 6) detection module and 7) gas diffusion module.

A second set-up was designed and fabricated aimed at the automation of the analytical process using PIII. It consists of a 4-channel peristaltic pump (Spetec, Germany), five 3-way injection valves (NResearch, NJ, US), a microfluidic bubble trap (Elveflow, France), and a potentiometric reader developed by the *Grupo de Instrumentación Electrónica y Biomédica* (IEB) of the *Universitat Politécnica de Catalunya* (UPC) (Barcelona, Spain). In *Fig. 3.13* it can be seen a schematic diagram of all elements (*Fig. 3.13A*) and a real image of the top (*Fig. 3.13B*) and lateral view (*Fig. 3.13C*) of developed automated POC and a close-up of the miniaturized potentiometric reader (*Fig. 3.13D*).

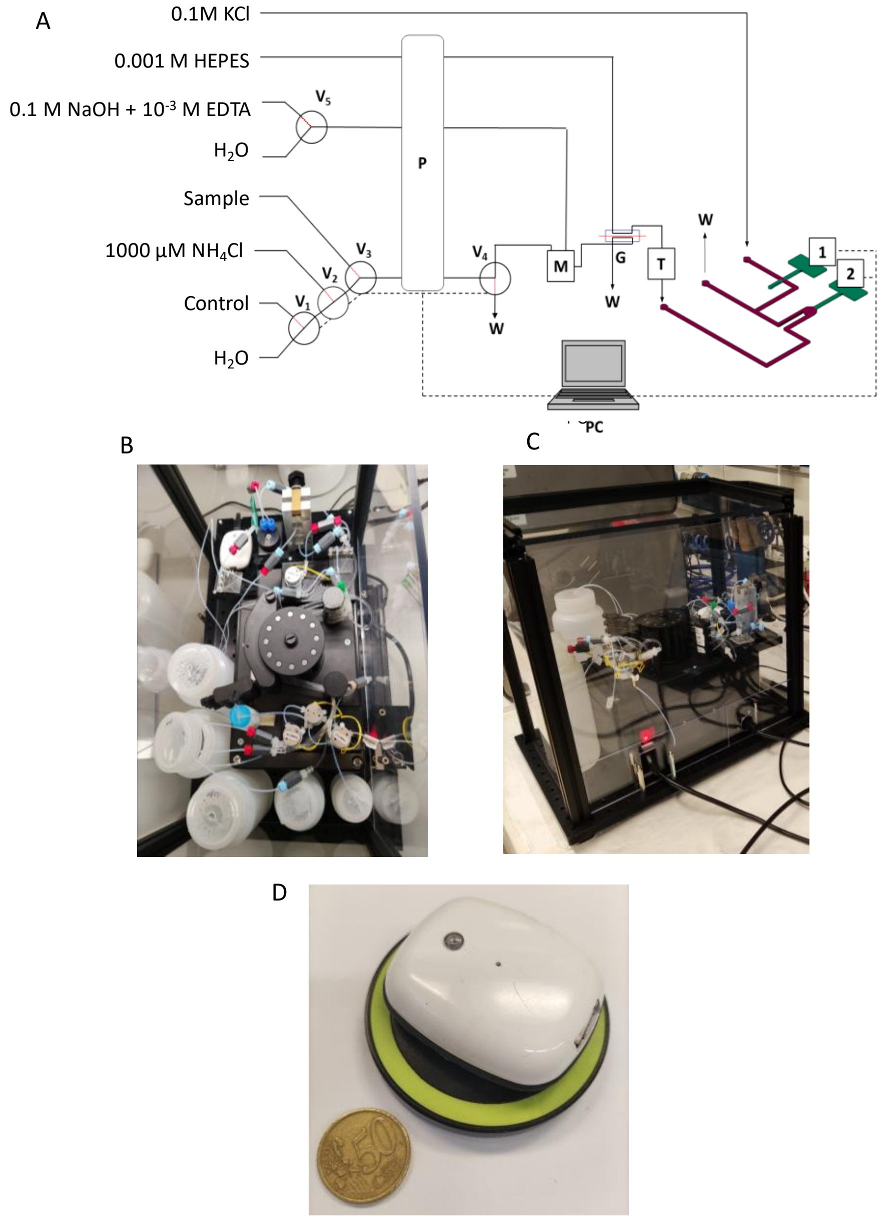

Fig. 3.13 A) Schematic representation of the automated experimental set-up for PIII: 1) reference electrode, 2) indicator electrode, T) bubble trap, V) 3-way injection valve, P) peristaltic pump, M) micromixer, G) gas diffusion module, PC) computer, W) waste. B) Real image of the top-view of the automated POC, C) lateral view of the automated POC and D) real image of the miniaturized potentiometric reader.

Tygon tubes of 1.14 mm and 0.64 mm internal diameter (Ismatec, Wertheim, Germany) and Teflon tubes of 0.8 mm internal diameter were used for the fluid propulsion. For fluidic connections between the 3-way injection valves and the Teflon tubes, two-piece inert fitting sets were used (NResearch, NJ, US). For fluidic connections between Teflon tubes and between Teflon tubes and Tygon tubes, flangeless fittings from IDEX Health and Science (WA, US) were employed to build a more robust system. This automated POC system was controlled by a Labview program, also developed by the IEB group, which handles the control of the different elements for the fluidic management, the data acquisition via Bluetooth and the treatment of this data. Components are contained within a methacrylate support.

## 3.3. Disposable device for the determination of ammonium ion in blood at home

All designs and fabrication process for the analytical platforms evaluated during the development of the disposable device for $NH_4^+$ determination in blood at home are detailed next.

### 3.3.1. Design

The concept for the disposable microanalytical device for the determination of $NH_4^+$ in blood at home is entirely different from the previous described prototypes, and it will be referred as disposable prototype (DP). A schematic representation of its design is shown in *Fig. 3.14*.

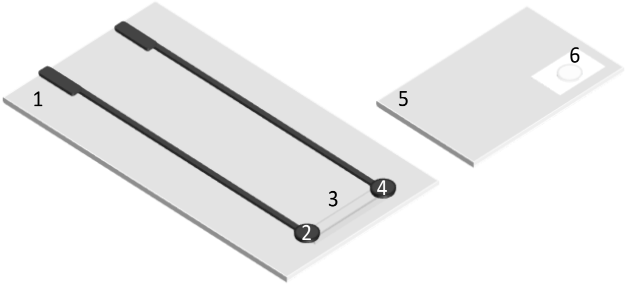

Fig. 3.14 Schematic representation of the DP design, constituted by a detection module (1) containing a reference electrode (2), a salt bridge (3) and an indicator electrode (4), and a gas diffusion module (5) containing a gas diffusion membrane (6) and sampling area.

It is composed by two different modules: a detection module and a gas diffusion module. The first one contains two identical ISEs, one acting as reference electrode and the other one acting as indicator electrode. They are connected by a channel of 0.8 mm width, that once filled with a specific reagent serves as salt bridge. Two different detection modules for the DP were fabricated with two different ISE sizes: 3.5 mm and 1.8

mm of diameter and a salt bridge of 6.1 mm and 4.4 mm length, respectively.

On the other hand, the second module contains a gas diffusion membrane of 3.5 mm diameter. For a functional $NH_4^+$ detection, the gas diffusion module is placed over the detection module, so that the gas diffusion membrane lays over the indicator electrode.

This device only contained the gas diffusion membrane because it is meant to be a single-use analytical device, so there is no need to protect this membrane from the blood matrix.

The operational protocol is as follows: blood sample is deposited on top of the gas diffusion membrane, where a NaOH 0.1 M solution converts the $NH_4^+$ present in the sample into volatile $NH_3$. It diffuses through the PVDF membrane and reaches a buffer solution at a neutral pH underneath. There, $NH_3$ converts back into $NH_4^+$, and is detected by the ISE. During sample measurement, as both electrodes are in contact through a salt bridge composed by the buffer, $NH_4^+$ from the sample diffuses to the reference electrode. However, this process is slow enough to ensure that reference electrode maintains its potential constant during the time of analysis. The need to have two identical ISE arised from the approach selected to achieve an autocalibration,[8,9] which has already been previously described in *Chapter 1*.

### 3.3.2. Microfabrication

The microfabrication of the DP follows the same procedure employed for the previous prototypes described in *Fig. 3.6.* COC sheets were the same as for PI, PII and PIII, but also an additional 130 µm COC sheet with a $T_g$ of 138 °C was employed. The 25 µm thickness COC with a lower $T_g$ was selected as a sealing layer whereas the 130 µm and 400 µm thick COC with a higher $T_g$ were used as structural layers. The detection module has three 400 µm COC structural layers plus one 130 µm COC layer and three 25 µm sealing layers. On the other hand, the gas diffusion module is constituted by two structural layers: one of 130 µm and another of 400 µm; and two 25 µm sealing layers. Between both structural layers, a gas diffusion membrane is located. During use, both modules are bound together with a reversible double-side adhesive.

These COC substrates are micromilled using the same equipment and tools as previously described to create the desired patterns. Then, the screen-printed carbon paste is placed and cured at 80 °C for 30 minutes to form the conductive support of the ISEs. Afterwards, the thermal pressure bonding process is performed. For the gas diffusion module, the gas diffusion membrane is located between the COC sheets and then, the whole is thermo-laminated. Finally, the ISM is deposited by drop casting on top of the conductive supports.

### 3.3.3. Final device

A real image of the detection and gas diffusion modules of the disposable microanalytical device can be seen in *Fig. 3.15.* The detection module with small ISE has a size of 2.5 x 1.5 x 0.2 cm whereas the detection module with the big ISEs has a size of 2.5 x 1.7 x 0.2 cm. The gas diffusion module size is 1.5 x 2 x 0.1 cm.

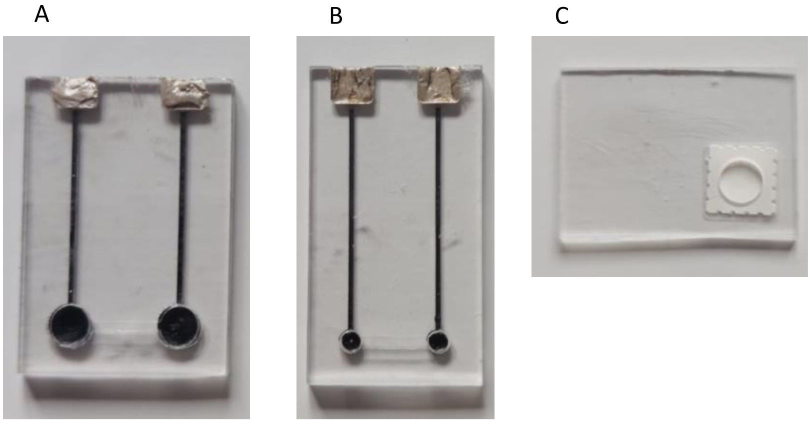

Fig. 3.15 Real image of the DP: A) detection module with 3.5 mm diameter ISEs, B) detection module with 1.8 mm diameter ISEs and C) gas diffusion module.

### 3.3.4. Experimental set-ups

Two different experimental set-ups were used during the optimization and analytical characterization of these DP. The first one is referred as batch set-up and a real image and a schematic representation can be seen in *Fig. 3.16A* and *Fig. 3.16B* respectively.

In this batch set-up all the ISEs in the DP act as indicator electrodes and a commercial reference electrode (Orion 900200 Sure-Flow, Thermo Scientific) was used. All the electrodes were submerged on a given volume of the buffer solution under continuous agitation conditions by means of a magnetic stirrer and the gas diffusion membrane was not present. A potentiometer was used to measure the resulting potential and a 16-channel multiswitch (TMI, Barcelona, Spain) was used to be able to calibrate several ISEs at the same time.

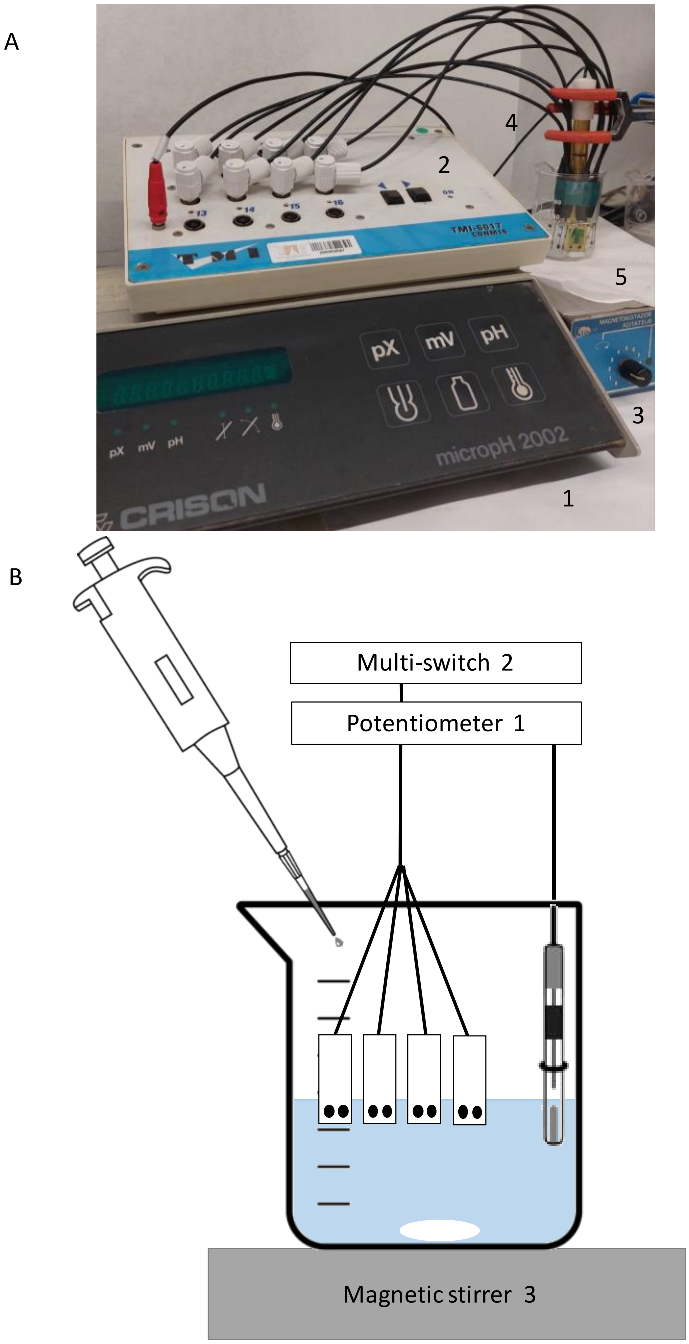

Fig. 3.16 A) Real image of the batch set up and B) schematic representation of the batch set-up. 1) potentiometer, 2) multi-switch, 3) magnetic stirrer, 4) reference electrode and 5) microanalytical devices.

The second set-up employed was the dual set-up, in which the device is used in the same manner as it will be used for the home device: one of the ISE acting as an indicator electrode and the other one acting as a reference electrode. In this case, a potentiometer (TMI, Barcelona, Spain) was employed for the measurement of the potential and a motor was used to incorporate a vibration to mimic the magnetic stirring. Real images and a schematic representation of the dual set-up are depicted in *Fig. 3.17A-C*.

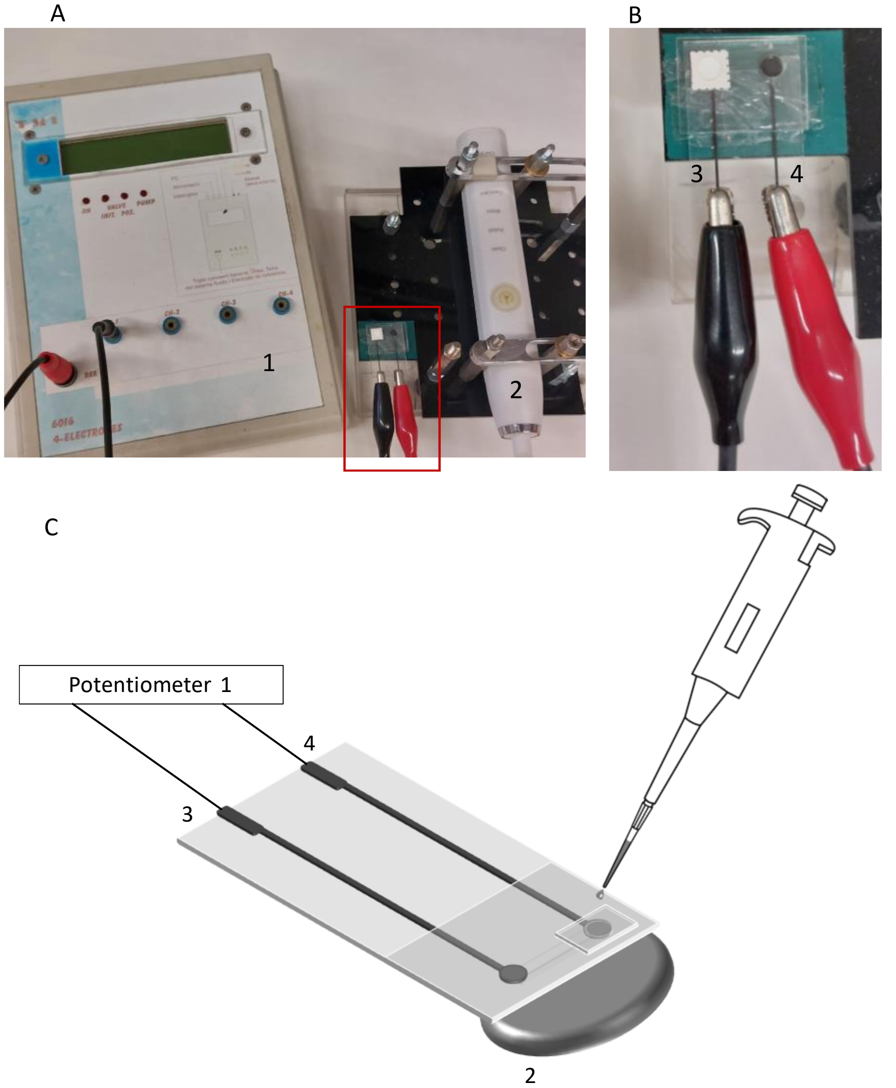

Fig. 3.17 A) Real image of the dual set up, B) close-up of the area in red and C) schematic representation of the dual set-up. 1) potentiometer, 2) vibrating motor, 3) reference electrode, 4) indicator electrode.

## 3.4.References

(1) Erickson, H. P. Size and Shape of Protein Molecules at the Nanometer Level Determined by Sedimentation, Gel Filtration, and Electron Microscopy. *Biol. Proced. Online* **2009**, *11* (1), 32–51. https://doi.org/10.1007/s12575-009-9008-x.

(2) Dohner, R. E.; Wegmann, D.; Morf, W. E.; Simon, W. Reference Electrode with Free-Flowing Free-Diffusion Liquid Junction. *Anal. Chem.* **1986**, *58* (12), 2585–2589. https://doi.org/10.1021/ac00125a053.

(3) Sández, N.; Calvo-López, A.; Vidigal, S. S. M. P.; Rangel, A. O. S. S.; Alonso-Chamarro, J. Automated Analytical Microsystem for the Spectrophotometric Monitoring of Titratable Acidity in White, Rosé and Red Wines. *Anal. Chim. Acta* **2019**, *1091*, 50–58. https://doi.org/10.1016/j.aca.2019.09.052.

(4) Berenguel-Alonso, M.; Sabés-Alsina, M.; Morató, R.; Ymbern, O.; Rodríguez-Vázquez, L.; Talló-Parra, O.; Alonso-Chamarro, J.; Puyol, M.; López-Béjar, M. Rapid Prototyping of a Cyclic Olefin Copolymer Microfluidic Device for Automated Oocyte Culturing. *SLAS Technol. Transl. Life Sci. Innov.* **2017**, *22* (5), 507–517. https://doi.org/10.1177/2472555216684625.

(5) Calvo-López, A.; Puyol, M.; Casalta, J. M.; Alonso-Chamarro, J. Multi-Parametric Polymer-Based Potentiometric Analytical Microsystem for Future Manned Space Missions. *Anal. Chim. Acta* **2017**, *995*, 77–84. https://doi.org/10.1016/j.aca.2017.08.043.

(6) Calvo-López, A.; Arasa-Puig, E.; Puyol, M.; Casalta, J. M.; Alonso-Chamarro, J. Biparametric Potentiometric Analytical Microsystem for Nitrate and Potassium Monitoring in Water Recycling Processes for Manned Space Missions. *Anal. Chim. Acta* **2013**, *804*, 190–196. https://doi.org/10.1016/j.aca.2013.10.013.

(7) Calvo-López, A.; Ymbern, O.; Puyol, M.; Casalta, J. M.; Alonso-Chamarro, J. Potentiometric Analytical Microsystem Based on the Integration of a Gas-Diffusion Step for on-Line Ammonium Determination in Water Recycling Processes in Manned Space Missions. *Anal. Chim. Acta* **2015**, *874*, 26–32. https://doi.org/10.1016/j.aca.2014.12.038.

(8) Carretero, L. G. Dispositiu Point of Care (POC) per a La Determinació de Clorur En Suor per Al Diagnòstic de Fibrosi Quística. Bachelor’s Thesis, Universitat Autònoma de Barcelona, Spain, 2022.

(9) Calvo-Lopez, A.; Puyol, M.; Alonso-Chamarro, J. New Strategy of Autocalibration for Disposable Potentiometric Point-of-Care Analyzers. In *XXII Transfront. Meet. Sensors Biosensors. Barcelona, Spain* 2018.

# Chapter 4

# Prototypes for determination of ammonium ion for hospital use

This chapter focuses on the results obtained regarding the development of a FIA prototype for the high-throughput analysis of blood samples in a clinical setting. This prototype was designed to be suitable for its implementation in any kind of medical centre, from small clinics to reference hospitals, owing to its projected low cost and ease of use, which does not require expert personnel. Due its small dimensions and the fact that it is meant to analyse blood samples, it could be stationed close to patients, such as in Emergency Rooms or in Intensive Care Units to ensure a fast and constant monitoring of patients. The development of such POC device would constitute a huge improvement in comparison to the current approach for $NH_4^+$ quantification at hospitals, which is carried out at the laboratories of reference centres with expensive and complex equipment.

This section discusses the optimization of the hydrodynamic and chemical variables, as well as the characterization of the analytical response of the FIA system for hospital use, previously described in *Chapter 3*. The aim was to achieve a suitable sensitivity, LD and linear working range for the determination of $NH_4^+$ at healthy and pathological levels as well as to obtain acceptable repeatability and reproducibility in order to develop a robust POC device.

Of utmost importance was the application of the prototype to the analysis of whole blood samples instead of plasma samples. To assess the suitability of the proposed microanalyzer as a reliable tool for the diagnostic and monitoring of hyperammonemia states, its analytical performance compared to that of the current method employed at hospitals by analysis of real plasma and blood samples. This was done in collaboration with the Hospital Sant Joan de Déu (HSJD) (Espugles de Llobregat, Spain) which is the reference centre of the region for IEM. They provided the plasma and blood samples and carried out the $NH_4^+$

quantification by the standard method that was used as a reference method.

## 4.1.Experimental

All optimizations were carried out by the analysis, in triplicate, of two different concentrations of a decade of difference. As mentioned previously in *Chapter 1*, according to the Nernst equation, the theoretical difference between these two concentrations should be –59.2 mV. For the optimization of the hydrodynamic and chemical parameters the concentration and flow rate of the auxiliary KCl solution were kept at 0.1 M and 300 µl/min respectively. Likewise, the analytical characteristics of the optimized analytical systems were obtained from a calibration procedure consisting of the analysis of a series of $NH_4Cl$ standard solutions by triplicates.

Furthermore, repeatability studies of this analytical system were carried out by either 10 or 20 consecutively analysis of $NH_4Cl$ standards solutions. The relative standard deviation (RSD) was calculated as RSD (%) = $(\sigma/\overline{X}) \cdot 100$, where $\bar{X}$ is the average value and σ is the standard deviation.

Reproducibility studies of these analytical systems were assessed by the calibration curves, resulting from a single analysis of different concentrations of $NH_4Cl$ standard solutions, obtained at different days. The selection of the protective membrane was done in the same way, obtaining a calibration curve for each membrane candidate.

The $\log K_{A,B}^{pot}$ for all interfering cations were calculated following the Fixed Interference Method, by using a fixed concentration of 0.01 M of the interfering ion in the $NH_4Cl$ standard solution.

The suitability of the optimized microanalytical device for the determination of $NH_4^+$ in real plasma and blood samples was evaluated in parallel using the proposed microsystem and the current method used at reference centres. These analyses were carried out at the HSJD. The reference method is a spectrophotometric enzymatic method carried out by the Architect ci8200 analyser (ABBOT, IL, US).[1] This analyser is an automated and expensive equipment designed for the multiparametric routine analysis of plasma samples. This $NH_4^+$ detection method is based on the reaction of the analyte with glutamate dehydrogenase (GLDH) and the subsequent decrease in absorbance at 340 nm due to the production of the oxidized form of nicotinamide adenine dinucleotide ($NAD^+$).

$$\mathrm{NH_4^+} + \mathrm{NADH} + \alpha - \mathrm{ketoglutarate} \xrightarrow{\mathrm{GLDH}} \mathrm{NAD^+} + \mathrm{glutamate}$$

This spectrophotometric enzymatic method is suitable for plasma samples only, not blood. Thus, plasma was obtained from the centrifugation of blood samples during 10 minutes at 3000 rpm and 10 °C. For comparison purposes plasma samples, and blood samples and their corresponding plasmas, were analysed in parallel with both methods and results were evaluated with a paired t-test and the graphical representation of the results with each method.

One factor to take into account is that there are no available reference methods for $NH_4^+$ quantification in blood samples. This is what makes the proposed FIA microanalyzer for hospital use a great alternative for the currently used method, that uses plasma. However, the fact that both systems use different samples matrix increases the difficulty for the validation procedure. Moreover, when analysing plasma samples there is a delay in time, due to the required centrifugation step, which may increase the $NH_4^+$ levels.[2]

## 4.2. Prototype I for ammonium ion detection

The PI configuration has been used for the evaluation of the degradation effect of the assessed buffer solutions and the reproducibility study. PI was used because it allowed to correlate the analytical characteristics of the system only to the degradation of the buffer or the state of the ISE. Hence, the state of the gas diffusion membranes is not taken into account. Moreover, an interference study was also carried out to assess the possible interferences for the ISE by other ions normally found in the matrix sample.

### 4.2.1. Evaluation of the buffer solution

TRIS is a well-known buffer solution that has been extensively used in previous works related to the potentiometric analysis of $NH_4^+$ in the GSB. Nevertheless, TRIS contains a primary amine group which could lead to the production of $NH_3$ in case of degradation, and to the consequently interference in the potentiometric detection by the ISE of the desired analyte. Therefore, an alternative buffer, HEPES, which has a $pK_a$ of 7.48 (at 25 ºC) and its buffer capacity ranges from 6.8 to 8.2,[3] was also tested to avoid this possible complication. The disassociation reactions for both TRIS and HEPES can be seen in *Fig. 4.1A* and *Fig. 4.1B.*[4]

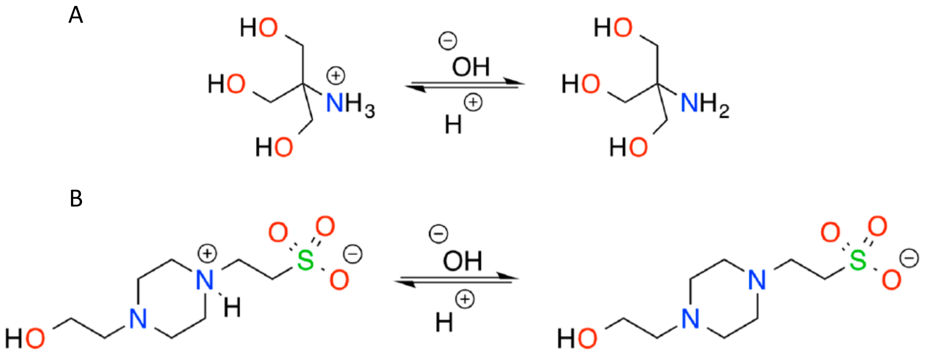

Fig. 4.1 Equilibrium reactions for TRIS (A) and HEPES buffer (B) from (4).

In this sense, reproducibility study was carried out using both buffer solutions. For this purpose, the calibration curves on days 1, 7 and 14 were obtained using 0.001 M TRIS (*Fig. 4.2A*) and 0.001 M HEPES (*Fig. 4.2B*) respectively, to assess if the degradation of the buffer affected the sensitivity and linear working range of the analytical microsystem. The flow rate for the carrier and the buffer solutions was 800 µl/min and the injection volume was 100 µl. The pH values for both buffers were set at 7.

Results of this calibration procedures appears in *Table 4.I*. In this table, it can be seen that despite the fact that the linear range and an acceptable LD are maintained for both buffers there is a clear decrease in sensitivity at day 14 as well as a decrease in the signal heights using TRIS compared to HEPES. This is most likely related to the degradation of TRIS into $NH_4^+$.

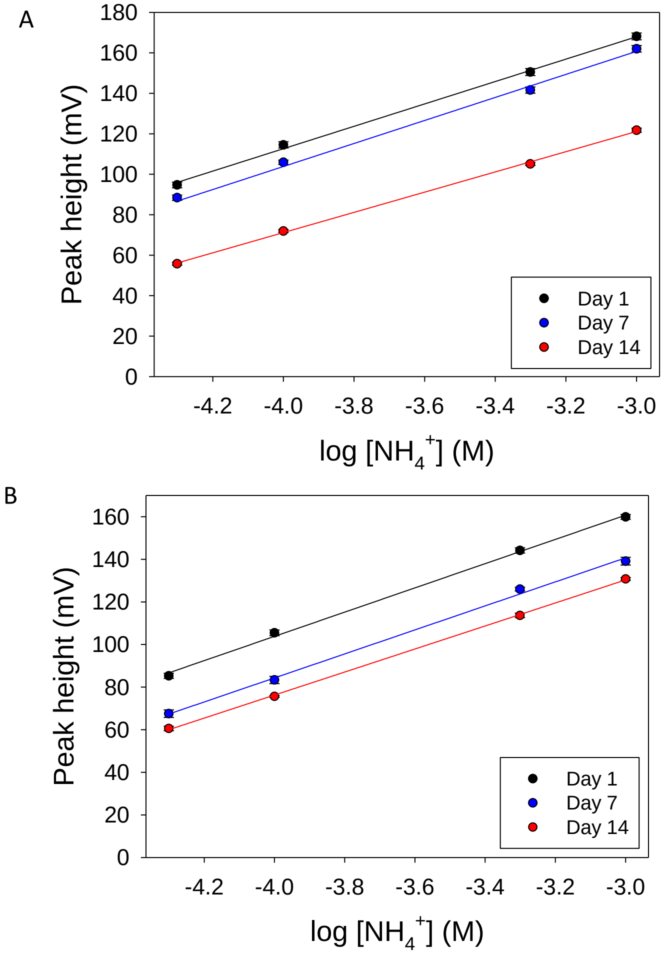

Fig. 4.2 Calibration curves obtained using 0.001 M TRIS (A) and 0.001 M HEPES (B) for day 1 (black), day 7 (blue) and day 14 (red).

Table 4.I Analytical characteristics obtained using TRIS (top) and HEPES (down) as buffer for days 1, 7 and 14.

**0.001 M TRIS**

| Day | Slope | Y-intercept | Linear range (µM) | LD (µM) | $R^2$ |
|---|---|---|---|---|---|
| **1** | 55.3 | 334.0 | 50 – 1000 | 0.9 | 0.9962 |
| **7** | 55.3 | 326.5 | 50 – 1000 | 1.3 | 0.9961 |
| **14** | 49.9 | 271.0 | 50 – 1000 | 3.8 | 0.9860 |

**0.001 M HEPES**

| Day | Slope | Y-intercept | Linear range (µM) | LD (µM) | $R^2$ |
|---|---|---|---|---|---|
| **1** | 56.9 | 333.4 | 50 – 1000 | 1.5 | 0.9972 |
| **7** | 56.4 | 309.8 | 50 – 1000 | 3.2 | 0.9956 |
| **14** | 54.1 | 292.5 | 50 – 1000 | 3.9 | 0.9991 |

### 4.2.2. Reproducibility study

To assess the lifetime of the ISEs used with 0.001M HEPES at pH 7 as buffer, the calibration curves for days 1, 7, 14, 21 and 28 for PI were obtained (*Fig. 4.3*). The flow rate for the buffer and carrier were 800 µl/min and the injection volume was 100 µl. The resulting analytical characteristics are detailed in *Table 4.II*.

Results showed that at day 1 there was an acceptable sensitivity, a working linear range of 50 to 1000 µM $NH_4^+$ and low LD. These good analytical characteristics were maintained during the following days. As a matter of fact, there was an increase of the signal peaks, which reached a maximum on day 21, most likely due to the prolonged wetting and exposure to the analyte. At day 28, the sensitivity decreased to sub-nernstian levels, even though the lineal range was maintained and the LD remained very low, at 1.8 µM $NH_4^+$.

These results indicate that the ISE could be used up to 28 days with acceptable analytical performance using HEPES as buffer.

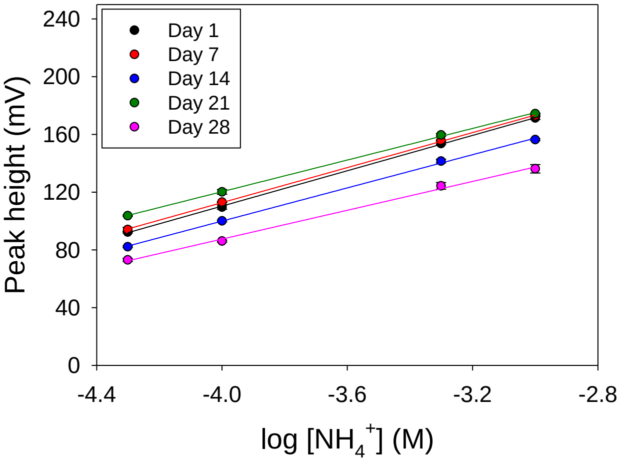

Fig. 4.3 Calibration curves for microanalytical devices for day 1 (black), 7 (red), 14 (blue), 21 (green) and 28 (pink) with HEPES.

Table 4.II Analytical characteristics for calibration curves obtained during a 28 day period using HEPES as buffer.

| Day | Slope | Y-intercept | Linear range | LD (µm) | $R^2$ |
|---|---|---|---|---|---|
| **1** | 61.3 | 355.3 | 50 – 1000 | 1.6 | 0.9991 |
| **7** | 60.6 | 355.4 | 50 – 1000 | 1.4 | 0.9993 |
| **14** | 57.5 | 330.0 | 50 – 1000 | 1.8 | 0.9985 |
| **21** | 54.8 | 339.5 | 50 – 1000 | 0.6 | 0.9988 |
| **28** | 49.9 | 287.2 | 50 – 1000 | 1.8 | 0.9935 |

### 4.2.3. Interference study

The ISM used in this analytical microsystem includes nonactin as ionophore, which is selective for $NH_4^+$ but can also be sensitive to other monovalent cations. Therefore, the level of interference was assessed by the calculation of the $\log K_{A,B}^{pot}$ for $K^+$, $Na^+$, $Li^+$ and $Ba^{+2}$. The first two ions are the main interfering ions present in blood samples and in serum. Their concentrations range from 3 to 5.5 mM and from 130 to 150 mM respectively.[5] On the other hand, despite $Li^+$ not being present in blood, it is a well stablished mood stabilizer, which can be used for the treatment of psychiatric presentations of UCDs. In this cases, $Li^+$ therapeutic concentrations in plasma range from 0.6 to 0.8 mM, and must be closely monitored to avoid toxicity issues, which have been reported at levels as low as 1 to 1.5 mM.[6] Furthermore, the $\log K_{A,B}^{pot}$ for

$Ba^{+2}$ was also evaluated because $Ba(OH)_2$ is used for the pH adjustment of the HEPES buffer.

Experimental conditions employed were 0.01 M HEPES buffer at pH 7.1, 800 µl/min flow rate and a 100 µl sample volume. The resulting $\log K_{A,B}^{pot}$ are included in *Table 4.III* and reveal that the main interfering ion of the ISM used is $K^+$. Regarding $Na^+$, it displays less interference, whereas $Li^+$ and $Ba^{+2}$ present a much lower level of interference than the other two cations evaluated.

Table 4.III Potentiometric selectivity coefficients for the different cations evaluated.

| **Interfering Cation (B)** | $\log K_{A,B}^{pot}$ |
|---|---|
| **$Na^+$** | −2.6 |
| **$K^+$** | −1.1 |
| **$Li^+$** | −3.3 |
| **$Ba^{+2}$** | −3.7 |

## 4.3. Prototype II for ammonium ion detection

Considering the high interferences of $K^+$ and $Na^+$ and their presence at high concentrations in plasma and blood, it was not possible to use PI for the determination of $NH_4^+$ in real plasma and blood samples. Therefore, it was necessary to isolate the target analyte from the rest of the complex biological sample matrix. For this purpose, a gas diffusion membrane was employed. This separation system was already used in the GSB in previous works[7–9] and is schematically represented in *Fig. 4.4.*

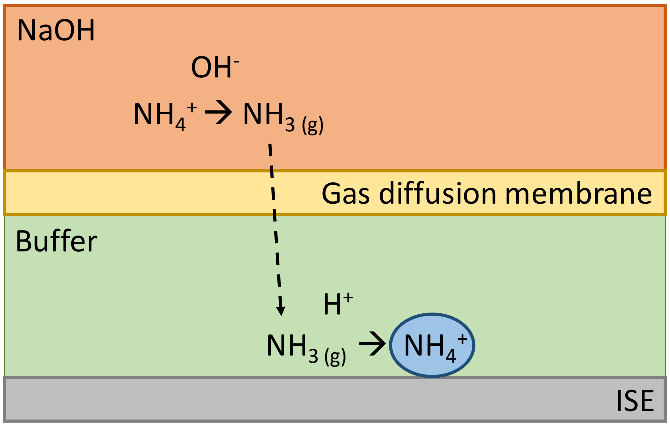

Fig. 4.4 Schematic representation of the gas diffusion process for $NH_4^+$ detection using PII.

### 4.3.1. Optimization of chemical and hydrodynamic variables

One hydrodynamic variable evaluated was the size of the detection chamber, with the intention of speeding up the emptying of the sample plug from the detection chamber, thus, reducing the analysis time. The optimization of the variables was carried out with an analytical platform containing a detection chamber of 3.5 mm (*Fig. 4.5A*) of diameter, which was the same as the ones used with PI, but also with a smaller detection chamber, of 1.8 mm of diameter (*Fig. 4.5B*). By using a smaller chamber, the surface of the ion selective electrode is reduced as well as the residence time in the detection chamber. Hence, there is a decrease in the peak heights of the potentiometric signals obtained and a consequent reduction of the analysis time.

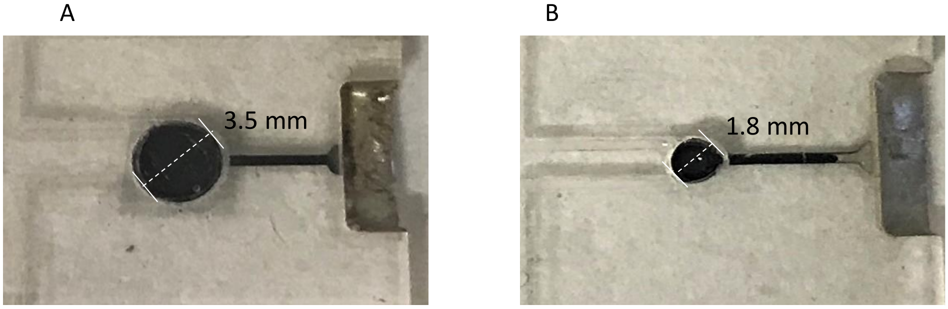

Fig. 4.5 Two different detection chamber sizes evaluated: A) 3.5 mm and B) 1.8 mm of diameter.

This effect can be seen in *Fig. 4.6,* which shows the signal recordings of an 100 µl injection of a standard solution of 20 µM $NH_4Cl$ with each one of the detection chambers, and a 22 % reduction in the signal peak.

Despite the fact that HEPES demonstrated a better stability than TRIS in a previous section, the concentration and pH of TRIS for the PII were also evalutated, in order to assess if there were differences regarding the capacity to convert $NH_3$ to $NH_4^+$.

Furthermore, it is important to note that the complete optimization process lasted for several days. So, slightly discrepancies between signal peak heights may occur due to small changes in the ISE response with time of use.

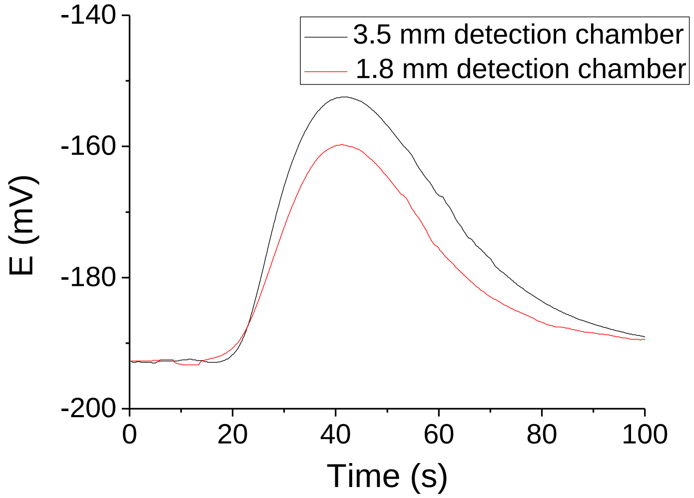

Fig. 4.6 Two signal peaks corresponding to a 100 µl injection of a standard solution of a 20 µM $NH_4Cl$ standard solution with PII containing a detection chamber of 3.5 mm diameter (black) and of 1.8 mm diameter (red).

The optimization begun with the 3.5 mm detection chamber and a summary of this optimization can be seen in *Table 4.IV*.

Table 4.IV Optimization of the hydrodynamic and chemical variables of PII with the 3.5 mm diameter detection chamber.

| Variable | Volume (µl) | Flow rate (µl/min) | [Buffer] (M) | [Buffer] pH | [NaOH] (M) | Optimized value |
|---|---|---|---|---|---|---|
| **Sample volume** | 25 – 500 | 650 | 0.005 | 7.1 | 0.1 | 225 |
| **Flow rate** | 225 | 300 – 800 | 0.005 | 7.1 | 0.1 | 650 |
| **[TRIS]** | 225 | 650 | 0.001 – 0.05 | 7.1 | 0.1 | 0.001 |
| **TRIS pH** | 225 | 650 | 0.001 | 7.1 – 8.2 | 0.1 | 7.1 |
| **[NaOH]** | 225 | 650 | 0.001 | 7.1 | $10^{-4}$ – 0.1 | 0.1 |
| **[HEPES]** | 100 | 650 | 0.001 – 0.05 | 7.1 | 0.1 | 0.001 |
| **HEPES pH** | 100 | 650 | 0.001 | 7 – 8 | 0.1 | 7 |

The first variable to be evaluated was the sample volume. The flow rate of the channels for carrier, sample, buffer solution and NaOH solution were each set to an arbitrary value of 650 µl/min to avoid high pressure onto the gas diffusion membrane, and TRIS was set at 0.005 M. The NaOH concentration for the donor solution was set at 0.1 M, as a more basic solution ensured the total conversion of $NH_4^+$ into volatile $NH_3$. Likewise, the buffer pH of the acceptor solution used was set at 7.1, as a more acidic pH promotes the total conversion of the $NH_3$ back into $NH_4^+$. A wide range of different sample volumes from 25 to 500µl were tested. The lowest volume that provided a Nernstian behaviour (a potential of –59 mV between two concentrations of a decade of difference) was 225 µl (*Fig. 4.7*). It is important to select the lower volume possible as the prospective use of this microsystem is the analysis of blood samples, which in most cases are from newborns and young children. Furthermore, using reduced injection volumes produces lower peak heights, leading to shorter times of analysis and a higher throughput of the analytical system. This is particularly important, as an hyperammonemic case constitutes a medical emergency, which requires a fast diagnosis for a prompt treatment.

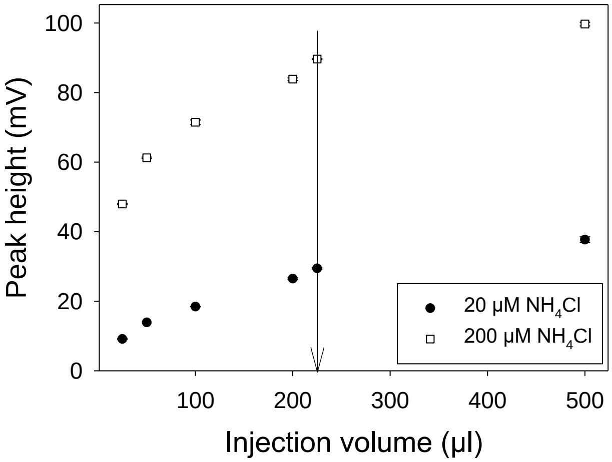

Fig. 4.7 Optimization of the volume injection for PII with the 3.5 mm detection chamber, using standard solutions of 20 µM $NH_4Cl$ (black circles) and 200 µM $NH_4Cl$ (white squares). Arrow indicates the optimized value.

Next, the flow rate of the buffer, NaOH solution, carrier and sample was optimized. All variables were kept at the same arbitrary values as before and the previously optimized value of 225 µl for the sample volume was used. As can be seen in *Fig. 4.8* flow rates ranging from 300 to 800 µl/min were tested and as it can be seen, lower flow rates cause slightly higher signals because the available diffusion time is extended. Nevertheless, these lower flow rates also led to a lengthening of the analysis time. Thus, 650 µl/min was chosen as the optimimum, as it allows us to have a reduced time of analysis while keeping a Nernstian behaviour, and avoiding very high flow rates that could damage the gas diffusion membrane.

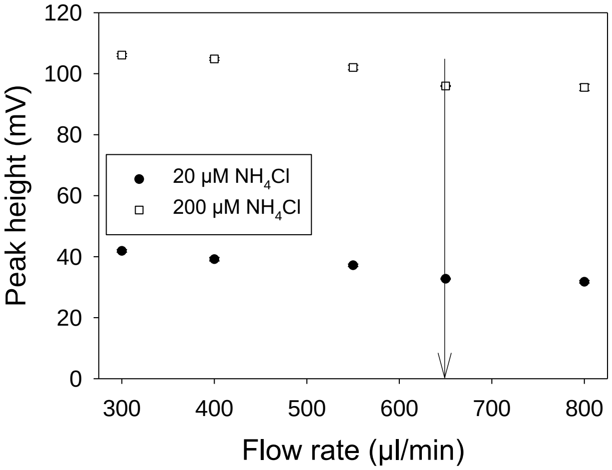

Fig. 4.8 Optimization of the flow rate for PII with 3.5 mm detection chamber, using standard solutions of 20 µM $NH_4Cl$ (black circles) and 200 µM $NH_4Cl$ (white squares). Arrow indicates the optimized value.

The following parameter to be evaluated was the concentration of TRIS buffer. A sample volume of 225 µl and a flow rate of 650 µl/min were employed and the rest of the parameters were maintained to their initial arbitrary values. A wide range of concentrations from 0.001 M to 0.05 M were tested, and it can be seen in *Fig. 4.9* that a concentration of 0.001 M gave the higher peak height, so this was the buffer concentration selected as the optimum. At higher buffer concentrations, the peak heights decreased. As mentioned in *Chapter 1*, ISEs measure ionic activity, rather than ionic concentration. According to the Debye-Hükel equation, at a high ionic strength (i.e. when using a high buffer concentration), $\gamma$ decreases. For lower $\gamma$, the measured ionic activity for a given ionic concentration is reduced.

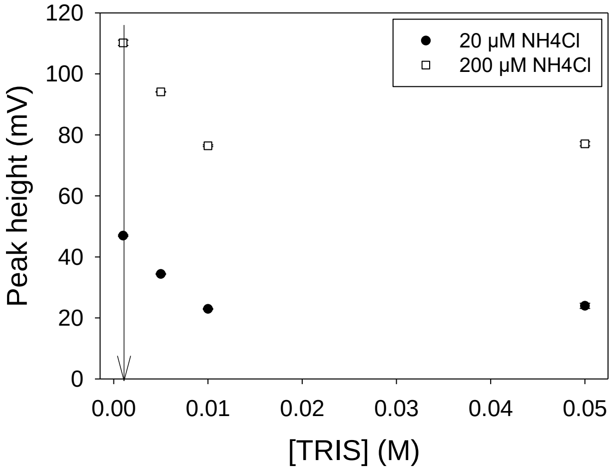

Fig. 4.9 Optimization of the TRIS concentration for PII with 3.5 mm detection chamber, using standard solutions of 20 µM $NH_4Cl$ (black circles) and 200 µM $NH_4Cl$ (white squares). Arrow indicates the optimized value.

Because this concentration is quite low, baselines recordings with the different buffer concentrations were evaluated to ensure baseline stability. Indeed, baselines are stable for all concentration as can be seen in *Fig. 4.10*. On the other hand, buffer concentration did affect the baseline value, which increased as the buffer concentration rised. This fact explains why higher signal peaks were obtained when using lower buffer concentrations.

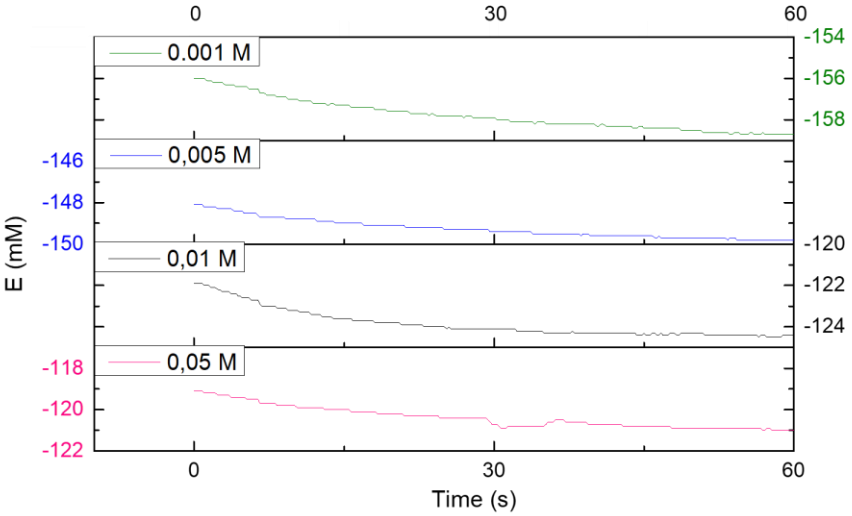

Fig. 4.10 Baselines of the signal recordings obtained using different TRIS concentrations: 0.05 M (pink), 0.01 M (black), 0.05 M (blue) and 0.001 M (green).

The following step was the buffer pH optimization. The sample volume used was 225 µl, the flow rate was 650 µl/min and the TRIS concentration was 0.001 M. The NaOH concentration was kept at 0.1 M as in the previous cases. Different pH, ranging from 7 to 8.2 were evaluated. As can be seen in *Fig. 4.11*, the most acidic pH assessed, 7.1, did seem to give slightly higher signals. Thus, this pH was chosen to be used as the optimum buffer pH for PII, as a more acidic pH promoted the conversion of $NH_3$ to $NH_4^+$.

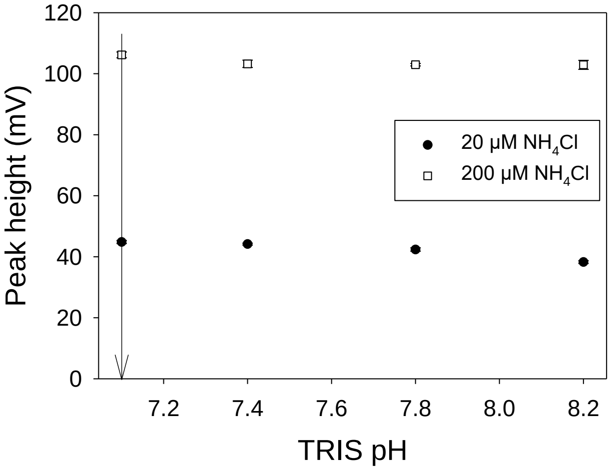

Fig. 4.11 Optimization of the TRIS pH for PII with 3.5 mm detection chamber, using standard solutions of 20 µM $NH_4Cl$ (black circles) and 200 µM $NH_4Cl$ (white squares). Arrow indicates the optimized value.

Finally, NaOH concentration was evaluated. Different concentrations ranging from 0.0001 M to 0.1 M were evaluated. As can be seen in *Fig. 4.12*, concentrations higher than 0.001 M produced signals of similar heights. Hence, the highest NaOH concentration was chosen to achieve the higher degree of $NH_4^+$ to $NH_3$ conversion, ensuring the total diffusion of the ion of interest even at highly concentrated samples.

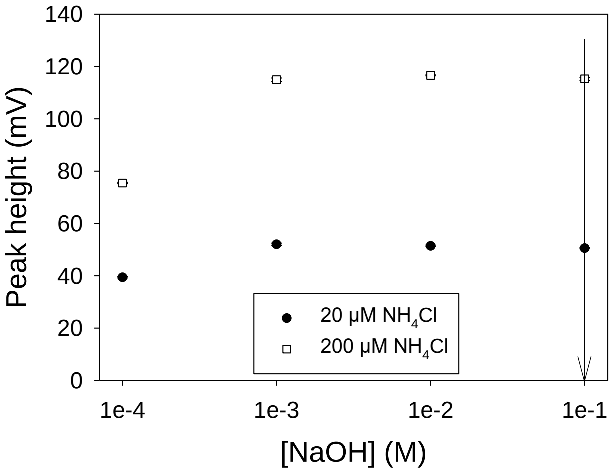

Fig. 4.12 Optimization of the NaOH concentration for PII with 3.5 mm detection chamber, using standard solutions of 20 µM $NH_4Cl$ (black circles) and 200 µM $NH_4Cl$ (white squares). Arrow indicates the optimized value.

Once the optimization of the different hydrodynamic and chemical parameters was finished, signals were high enough to further reduce the sample volume from 225 µl to only 100 µl, while maintaining the same the analytical characteristics. These high signals were, to a large extent the result of using a buffer concentration of 0.001 M instead of 0.005 M. The reduction of sample volume also led to a reduction of the analysis time, while maintaining a suitable linear working range and LD.

The use of HEPES, instead of TRIS was also considered for PII. The optimization of HEPES concentration was carried out using a sample volume of 100 µl and the rest of the parameters set to the previous values selected during the optimization done using TRIS. Resembling the example of the TRIS concentration optimization, the highest signals were obtained with a concentration of 0.001 M (*Fig. 4.13*). Thus, this concentration was selected for further optimization of the process. In this particular case, at a high buffer concentration of 0.05 M, higher signal peaks were obtained than for 0.01 M and 0.005 M. This went against the trend appreciated in the previous buffer concentration optimization (*Fig. 4.9*). However, this results shown in *Fig. 4.13* for the 0.05 M concentration were considered an anomaly, likely due to lack of stability of the ISE potential, due the continued usage during the optimization process.

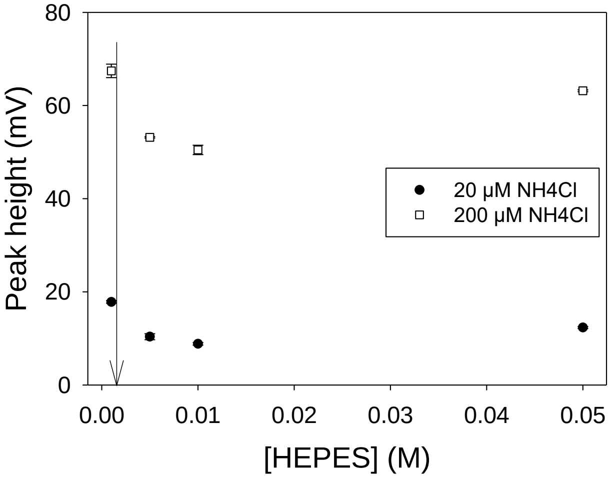

Fig. 4.13 Optimization of the HEPES concentrations for PII with 3.5 mm detection chamber, using standard solutions of 20 µM $NH_4Cl$ (black circles) and 200 µM $NH_4Cl$ (white squares). Arrow indicates the optimized value.

Lastly, the HEPES pH was evaluated. All parameters were set at their optimized values, and a range of pH from 7 to 8.2 was tested. In *Fig. 4.14,* it can be seen that the height of the signals obtained seem to be independent from the pH used. Consequently, a pH of 7 was selected based on the fact that a more acidic pH favours the conversion of $NH_4^+$ into $NH_3$.

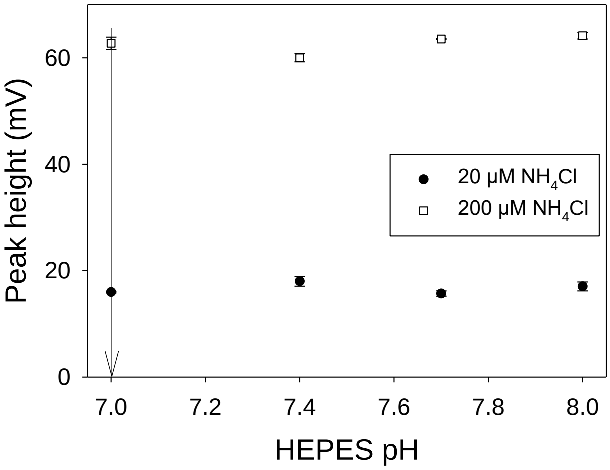

Fig. 4.14 Optimization of the HEPES pH for PII with 3.5 mm detection chamber, using standard solutions of 20 µM $NH_4Cl$ (black circles) and 200 µM $NH_4Cl$ (white squares). Arrow indicates the optimized value.

Once the optimization process for PII with the 3.5 mm detection chamber was finalized, the optimization of the hydrodynamic and chemical variables for PII with 1.8 mm detection chamber took place and a summary can be seen in *Table 4.V*.

Table 4.V Optimization of the hydrodynamic and chemical variables for PII with the 1.8 mm diameter detection chamber.

| Variable | [Buffer] (M) | Volume (µl) | Flow rate (µl/min) | [Buffer] pH | [NaOH] (M) | Optimized value |
|---|---|---|---|---|---|---|
| **[TRIS]** | 0.001 – 0.05 | 500 | 650 | 7.1 | 0.1 | 0.001 |
| **Sample volume** | 0.001 | 25 – 500 | 650 | 7.1 | 0.1 | 200 |
| **Flow rate** | 0.001 | 200 | 400 – 800 | 7.1 | 0.1 | 650 |
| **TRIS pH** | 0.001 | 200 | 650 | 7.1 – 8 | 0.1 | 7.1 |
| **[NaOH]** | 0.001 | 200 | 650 | 7.1 | $10^{-4}$ – 0.1 | 0.1 |
| **[HEPES]** | 0.001 – 0.05 | 200 | 650 | 7.1 | 0.1 | 0.001 |
| **HEPES pH** | 0.001 | 200 | 650 | 7 – 8 | 0.1 | 7 |

Due to the fact that for the optimization process using the 3.5 mm detection chamber the buffer concentration largely influenced the signal height obtained, it was determined that this parameter would be the first to be assessed. In this instance, the sample volume was randomly set to 500 µl, the flow rate was 650 µl/min, TRIS pH was 7.1 and the NaOH concentration used was 0.1 M. Different TRIS concentrations ranging from 0.001 to 0.05 M were evaluated and, as can be seen in *Fig. 4.15*, the highest signals resulted from the use of a concentration of 0.001 M, whereas the signals diminished when employing higher TRIS concentrations. Therefore, this 0.001 M concentration was selected as the optimum for the TRIS buffer.

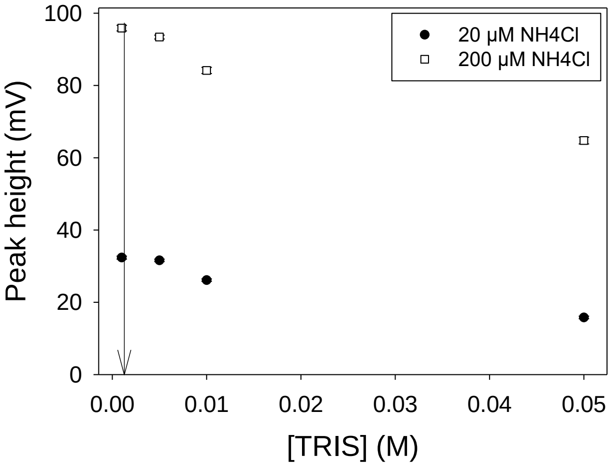

Fig. 4.15 Optimization of the TRIS concentration for PII with 1.8 mm detection chamber, using standard solutions of 20 µM $NH_4Cl$ (black circles) and 200 µM $NH_4Cl$ (white squares). Arrow indicates the optimized value.

Afterwards, the sample volume was evaluated. TRIS concentration was kept at the already optimized value of 0.001 M, whereas the flow rate was set at 650 µl/min, TRIS pH at 7.1, and the NaOH concentration at 0.1 M. Several sample volumes ranging from 25 µl to 500 µl were used under this conditions and, the smallest volume that allowed us to keep a Nernstian behaviour was 200 µl (*Fig. 4.16*).

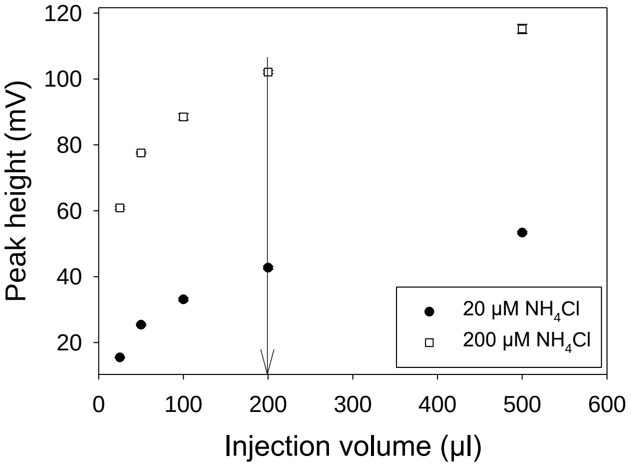

Fig. 4.16 Optimization of the sample volume for PII with the 1.8 mm detection chamber, using standard solutions of 20 µM $NH_4Cl$ (black circles) and 200 µM $NH_4Cl$ (white squares). Arrow indicates the optimized value.

The following step was the assessment of the flow rate. For this, the previously optimized values of TRIS concentration of 0.001 M and a sample volume of 200 µl were used. The buffer pH was kept at 7.1 and the NaOH concentration used was 0.1 M. The flow rates tested for buffer, NaOH solution, carrier and sample ranged from 400 µl/min to 800 µl/min. Similarly to the optimization with the 3.5 mm diameter detection chamber, faster flow rates caused a slightly lower signal heights (*Fig. 4.17).* A 650 µl/min flow rate was chosen as it was the best value that balanced signal height and fast analysis time.

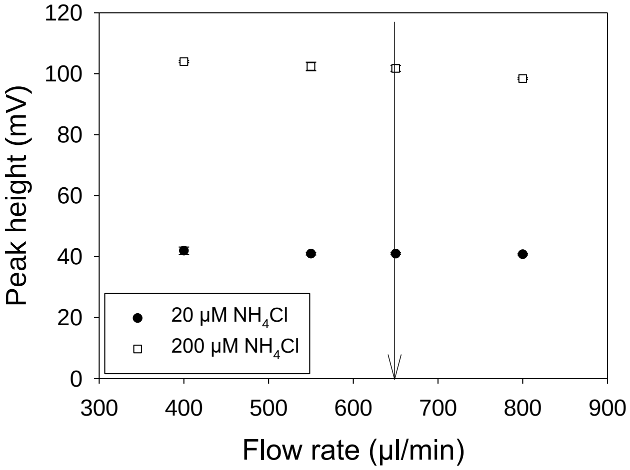

Fig. 4.17 Optimization of the flow rate for PII with 1.8 mm detection chamber, using standard solutions of 20 µM $NH_4Cl$ (black circles) and 200 µM $NH_4Cl$ (white squares). Arrow indicates the optimized value.

TRIS pH was optimised as follows: the previously optimized values for the TRIS concentration, sample volume and flow rate 0.001 M, 200 µl and 650 µl/min were used respectively, and the NaOH concentration was kept at 0.1 M. The different pH for the TRIS buffer assessed range from 7 to 8.2. As can be seen in *Fig. 4.18*, a more acidic pH provoked slightly higher signal heights, because this lower pH caused the conversion of a higher percentage of $NH_3$ to $NH_4^+$ to be detected by the ISE. Therefore, the lower pH, 7.1 was selected as the optimum.

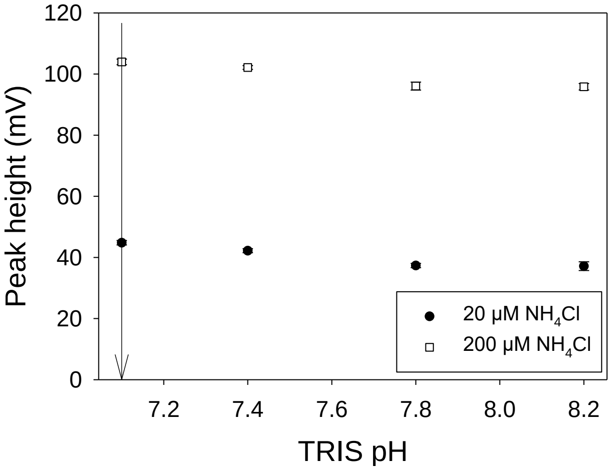

Fig. 4.18 Optimization of the TRIS pH for PII with 1.8 mm detection chamber, using standard solutions of 20 µM $NH_4Cl$ (black circles) and 200 µM $NH_4Cl$ (white squares). Arrow indicates the optimized value.

Finally, NaOH concentration was evaluated. For this, all the previously optimized values of the hydrodynamic and chemical parameters were employed: 0.001 M TRIS at 7.1 pH, sample volume of 200 µl and a flow rate of 650 µl/min. Concentrations for the NaOH solution ranged from 0.0001 M to 0.1 M. In the same way as the optimization of the 3.5 mm diameter detection chamber, NaOH concentrations below $10^{-4}$ M were not enough to convert all the $NH_4^+$ into volatile $NH_3$. However, as shown in *Fig. 4.19* concentrations over $10^{-4}$ M did give a Nernstian behaviour, and he highest one, 0.1 M, was selected as optimum to ensure total $NH_3$ conversion even at high concentrations.

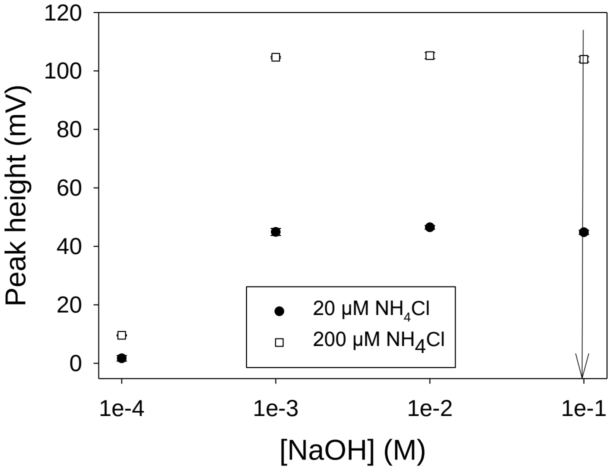

Fig. 4.19 Optimization of the NaOH concentration for PII with a 1.8 mm detection chamber, using standard solutions of 20 µM $NH_4Cl$ (black circles) and 200 µM $NH_4Cl$ (white squares).

For the PII containing the 1.8 mm detection chamber, HEPES was also appraised to be used as buffer of choice. For this purpose, the optimization of the buffer concentration and pH was repeated using HEPES instead of TRIS. In the first case, a sample volume of 200 µl, a flow rate of 650 µl/min and a NaOH concentration of 0.1M were used as were previously optimized, whereas the pH buffer was kept at 7.1. In the same manner as the prior optimization with TRIS, the concentration that produced higher signals heights was 0.001 M (*Fig. 4.20*) and, thus, this was the one selected.

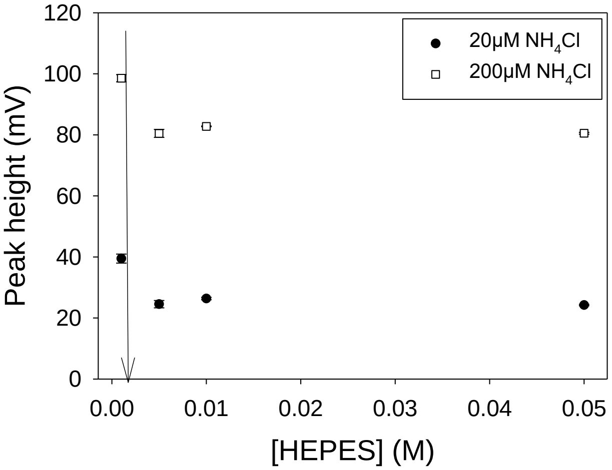

Fig. 4.20 Optimization of the HEPES concentration for PII with 1.8 mm detection chamber, using standard solutions of 20 µM $NH_4Cl$ (black circles) and 200 µM $NH_4Cl$ (white squares). Arrow indicates the optimized value.

At last, the optimization of HEPES pH was done, using all the previously optimized values for the rest of the parameters: an HEPES concentration of 0.001 M, a sample volume of 200 µl, a flow rate of 650 µl/min and a NaOH concentration of 0.1M. Different pH ranging from 7 to 8 were evaluated, and found that, unlike the case of TRIS, the signals heights obtained were similar for all pH tested (*Fig. 4.21*). In this case, the lowest pH, 7, was selected as the optimized value to ensure the total conversion of $NH_3$ into $NH_4^+$, even at higher concentrations.

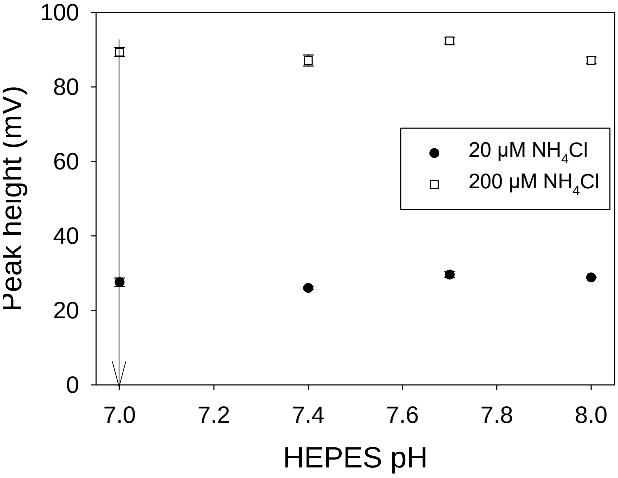

Fig. 4.21 Optimization of the HEPES pH for PII with 1.8 mm detection chamber, using standard solutions of 20 µM $NH_4Cl$ (black circles) and 200 µM $NH_4Cl$ (white squares). Arrow indicates the optimized value.

### 4.3.2. Analytical characteristics of prototype II

Once the optimization of the hydrodynamic and chemical parameters was completed, the signal recording of a calibration procedure was obtained and the calibration curve resulting of the adjustment of the Nernst equation was represented.

For the analytical platforms with 3.5 mm diameter detection chamber, this signal recording and the resulting calibration curve can be seen in *Fig. 4.22A* and *Fig. 4.22B,* using TRIS and HEPES respectively. The corresponding analytical characteristics can be seen in *Table 4.VI.*

Table 4.VI Analytical characteristics for PII with a 3.5 mm detection chamber using TRIS and HEPES as buffer.

| Buffer | Slope | Y-intercept | Linear range (µM) | LD (µM) | $R^2$ |
|---|---|---|---|---|---|
| **TRIS** | 56.6 ± 0.7 | 310 ± 3 | 10 – 1000 | 3.3 | 0.999 |
| **HEPES** | 51 ± 1 | 267 ± 6 | 10 – 1000 | 5.7 | 0.997 |

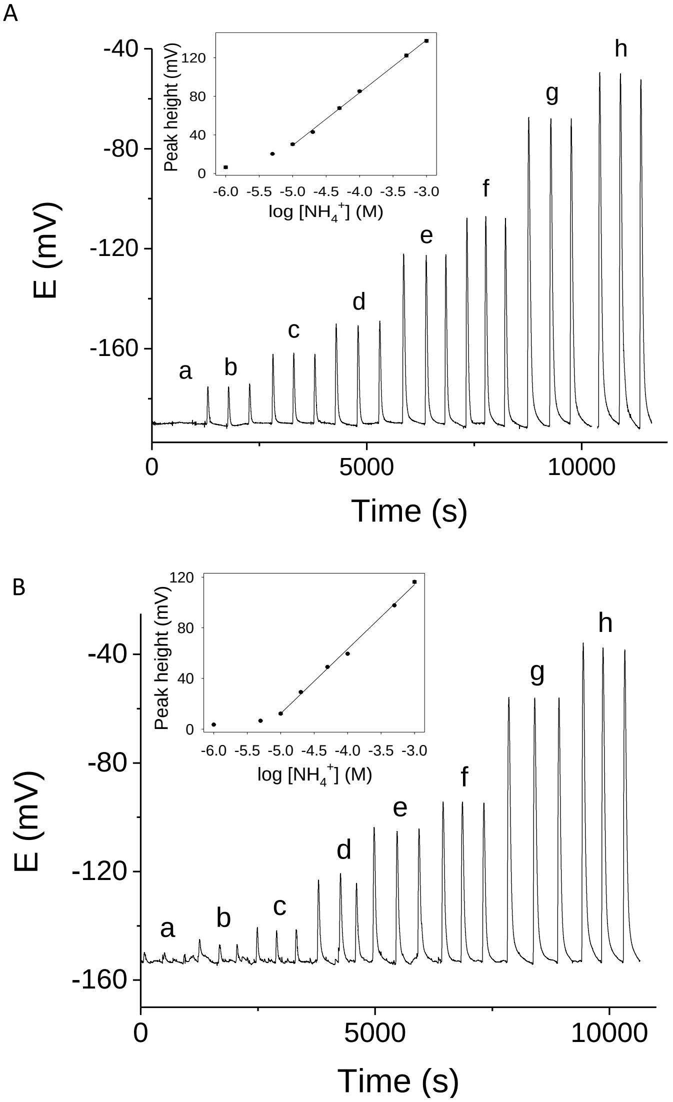

Fig. 4.22 Signal recording and calibration curves for PII with the 3.5 mm diameter detection chamber using $NH_4Cl$ standard solutions of 1 µM (a), 5 µM (b), 10 µM (c), 20 µM (d), 50 µM (e) and 100 µM (f), 500 µM (g), and 1000 µM using TRIS (A) and HEPES (B) as buffer.

The analytical characteristics when using PII with the 1.8 mm diameter detection chamber with TRIS (*Fig. 4.23A*) and HEPES (*Fig. 4.23B*) as buffer can be seen in *Table 4.VII*.

Table 4.VII Analytical characteristics for PII with a 1.8 mm detection chamber using TRIS and HEPES as buffer.

| Buffer | Slope | Y-intercept | Linear range (µM) | LD (µM) | $R^2$ |
|---|---|---|---|---|---|
| **TRIS** | 55 ± 1 | 302 ± 5 | 10 – 1000 | 2.9 | 0.998 |
| **HEPES** | 60.0 ± 0.7 | 313 ± 3 | 10 – 1000 | 6.2 | 0.999 |

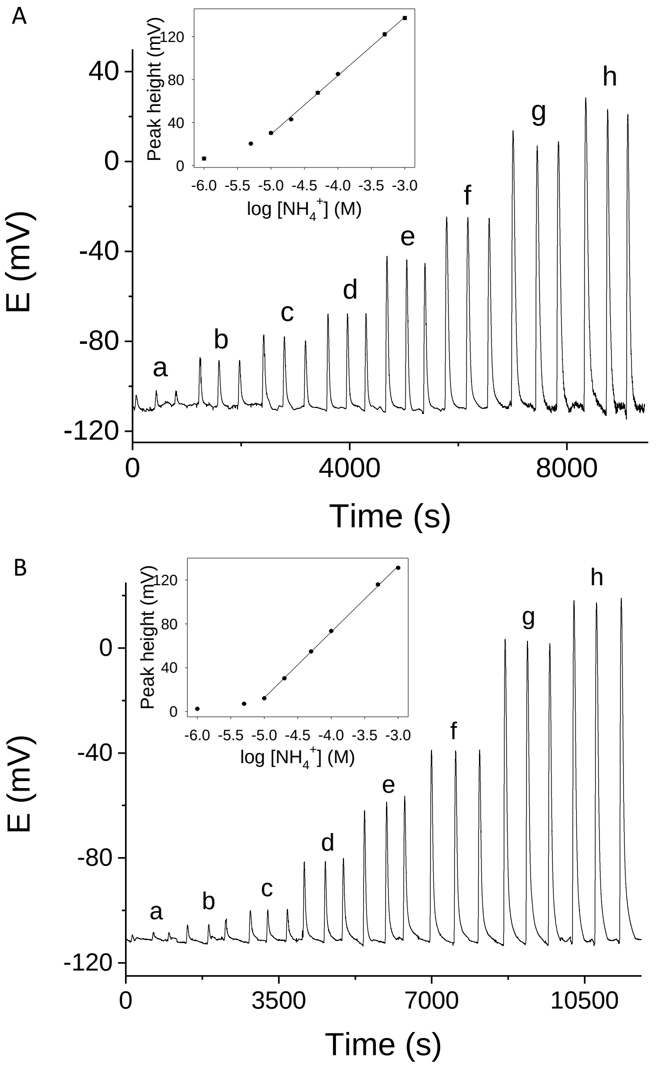

Fig. 4.23 Signal recording and calibration curves for PII containing a 1.8 mm diameter detection chamber using $NH_4Cl$ standard solutions of 1 µM (a), 5 µM (b), 10 µM (c), 20 µM (d), 50 µM (e) and 100 µM (f), 500 µM (g), and 1000 µM using TRIS (A) and HEPES (B) as buffer.

In both *Fig. 4.22* and *Fig. 4.23*, it can be seen that signal peaks for both detection chamber sizes were slightly lower when using HEPES instead of TRIS as buffer. Nevertheless, for all combinations of detection chamber size and buffer, the same linear working range, a Nernstian behaviour and a satisfactory sensitivity were obtained, as well as a low enough LD. However, using a 1.8 mm detection chamber involved consuming the double of the injection volume (200 µl instead of 100 µl). For this reason, the 3.5 mm detection chamber was finally selected to continue with the repeatability of the analytical microsystem study.

Repeatability of the microsystem was assessed by 20 consecutive analysis of $NH_4Cl$ standards solutions of 30 µM and 100 µM $NH_4Cl$, which is the range of $NH_4^+$concentrations for most non-pathological samples. These analyses were carried out under the previously optimized variables using both TRIS (*Fig. 4.24*) and HEPES (*Fig. 4.25*). For both buffer solutions, the RSD obtained for the two concentrations were acceptable, well below 5 %, as can be seen in *Table 4.VIII*.

Table 4.VIII RSD values and signal peaks for consecutive analysis of 30 µM and 100 µM $NH_4Cl$ using TRIS and HEPES as buffer for PII with a 3.5 mm detection chamber.

| Buffer | [$NH_4Cl$] | RSD (%) | E (mV) |
|---|---|---|---|
| **TRIS** | 30 | 2 | 42.1 ± 0.9 |
|  | 100 | 3 | 81 ± 2 |
| **HEPES** | 30 | 3 | 31.4 ± 0.8 |
|  | 100 | 1 | 84 ± 1 |

According to the previous results, both TRIS and HEPES buffer gave satisfactory sensitivity and linear working range for the reliably quantification of physio-pathological $NH_4^+$. Therefore, HEPES was selected to be used owing to the fact that it does not present the same issues with degradation as TRIS and the consequent loss of sensitivity of the ISE.

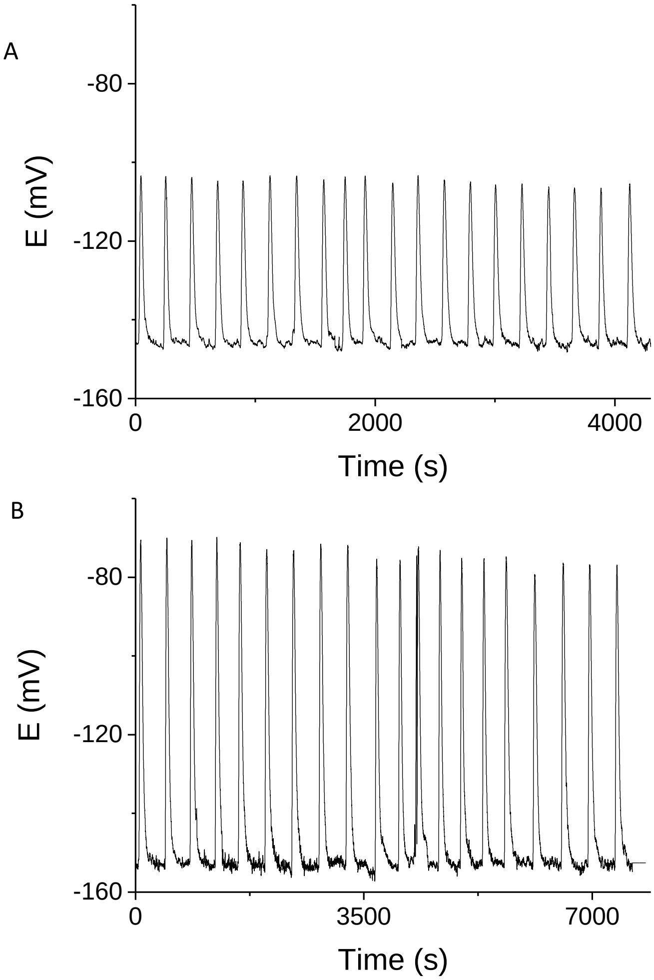

Fig. 4.24 Consecutive analysis of standard solutions of 30 µM $NH_4Cl$ (A) and 100 µM $NH_4Cl$ (B) when using TRIS as buffer.

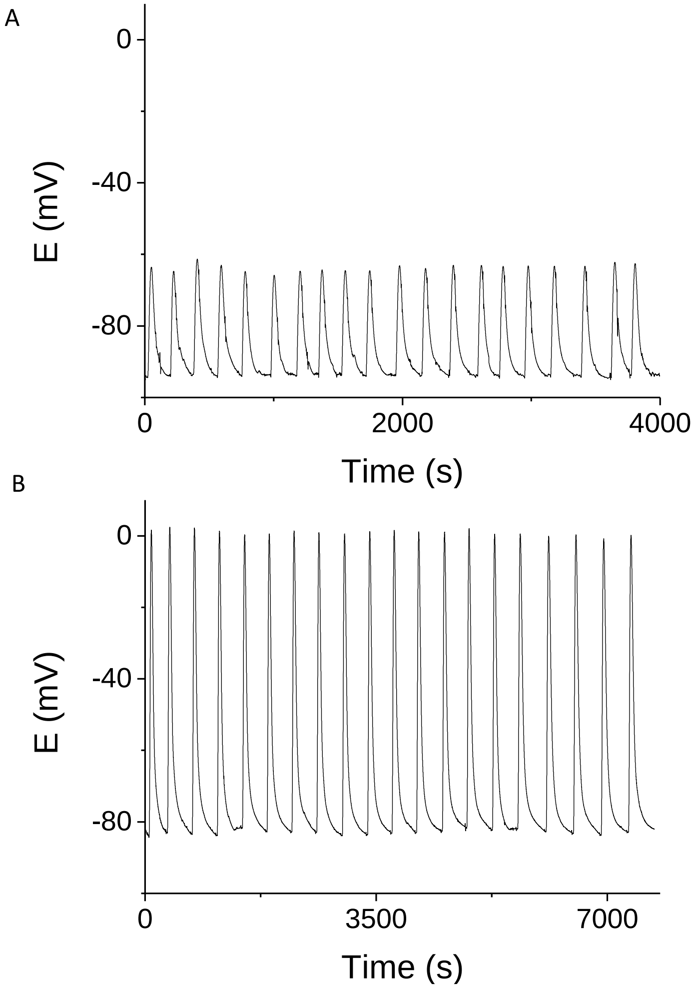

Fig. 4.25 Consecutive analysis of standard solutions of 30 µM $NH_4Cl$ (A) and 100 µM $NH_4Cl$ (B) when using HEPES as buffer.

### 4.3.3. Evaluation of a gas diffusion membrane to avoid interfering cations

The signal recording obtained by the injection of 100 µl of 0.1 M KCl solution (in the absence of $NH_4Cl$) with both PI and PII, that is, with and without the presence of a gas diffusion membrane, can be seen in *Fig. 4.26*. From this graph, it is clear that the presence of the PVDF gas diffusion membrane was successful in avoiding the interfering effect of other cations that may be present in the sample, even at high concentrations. The use of the gas diffusion membrane would not be useful to avoid the interference by other volatile elements, which would also be able to cross the membrane. Nevertheless, there are not any volatile elements expected in the blood matrix that could interfere in the detection of $NH_4^+$ by the ISE.

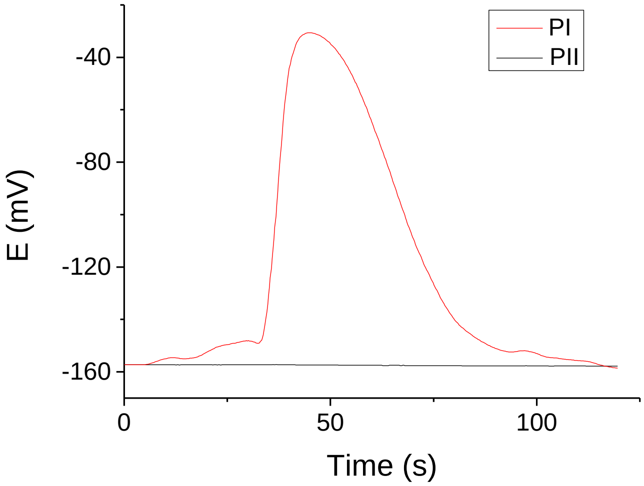

Fig. 4.26 Signal recording obtained for an injection of 100 µl 0.1M KCl with PI (red) and with PII (red).

### 4.3.4. Analysis of plasma samples

A total of 22 plasma samples were analysed in parallel using the proposed PII microanalyzer and the enzymatic reference method. Results indicated that there were not significant differences between the two data groups according to the paired t-test ($t_{calc} = 1.405$, $t_{tab} = 2.08$, $t_{calc} < t_{tab}$) and the graphical representation of the results with each method (*Fig. 4.27*), which yield a regression equation of $Y = 1.01 (\pm 0.05) \cdot \log [NH4+] + 1 (\pm 10)$ ($n = 22$; 95 % confidence) and a $R^2$ of 0.9875. Therefore, it could be concluded that the proposed analytical device was suitable to be used in the determination of $NH_4^+$ in plasma.

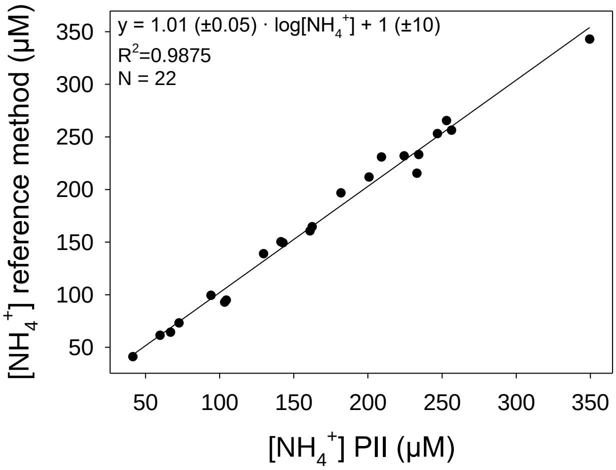

Fig. 4.27 Comparative study of the results for the analysis of plasma samples with PII containing the 3.5 mm detection chamber and the enzymatic reference method (n=22).

Until here it was demonstrated that the gas diffusion membrane avoided the effect of the interfering elements present in plasma samples. However, the much more complex blood matrix was a challenge and the use of PII for the analysis of these types of samples was not possible. When attempting to analyse the first blood sample, the gas diffusion membrane was damaged as shown in *Fig. 4.28*. There was a clear change in the surface of the gas diffusion membrane, particularly in the NaOH inlet and nearby areas (where the blood sample enters the gas diffusion module). This was most likely related to the adhesion of proteins on the membrane surface, a process known as fouling. This damage in the membrane allowed the NaOH solution to cross the membrane and reach the ISE, preventing further analysis to take place due to the interfering effect of Na$^+$.

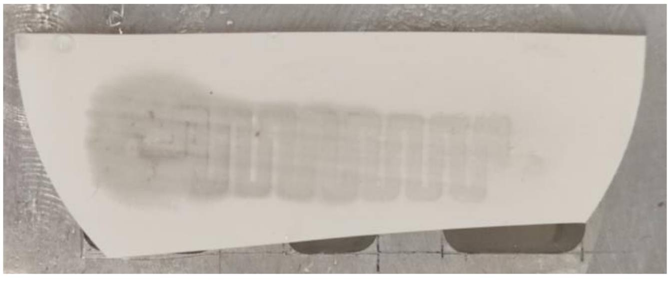

Fig. 4.28 Real image of the PVDF gas diffusion membrane after direct contact with a blood sample.

To avoid the deterioration of the membrane due to its direct contact with the blood matrix it was necessary to modify the design of the proposed microanalyzer in order to protect the gas diffusion membrane and allow consecutive blood analysis.

## 4.4. Prototype III for ammonium ion detection

In order to develop a reusable and high-throughput analytical system for the potentiometric determination of $NH_4^+$ in blood, the design of PII was modified by the inclusion of an additional barrier with protective purposes to avoid fouling on the gas diffusion membrane and allow the reuse of the analytical system after an analysis of a blood sample.

In *Fig. 4.29* appears a representation of the gas diffusion process with a protective membrane for PIII. Owing to the fact that previous results showed that the use of TRIS or HEPES as buffer solution did not lead to different analytical characteristics, and that the TRIS degradation could be counterproductive for the potentiometric determination, it was decided to use HEPES for the rest of the work.

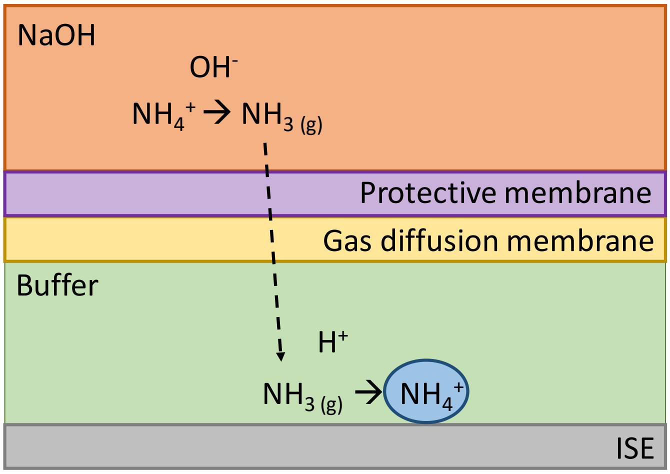

Fig. 4.29 Schematic representation of the gas diffusion process for $NH_4^+$ detection with PIII.

### 4.4.1. Selection of the protective membrane

The first step for the inclusion of this protective membrane was to select the appropriate membrane material and porous size to be used; that allowed the diffusion of the $NH_3$ generated but prevented the pass of the different biomolecules and blood cells present in the blood matrix to avoid fouling on the gas diffusion membrane.

Several membranes meant for haemodialysis purposes were evaluated and a summary of the characteristics of all the candidate membranes can be seen in *Chapter 3*. All these membranes displayed a great variability of materials and porous sizes. Dialysis membranes are traditionally divided into cellulose-based membranes and synthetic membranes. Cellulose based membranes have a denser and symmetrical structure and a more hydrophilic nature. However, natural cellulose exposes hydroxyl groups and this leads to the activation of pathways of the complement system, which is a part of the immune system. This effect can be avoided by the substitutions of these hydroxyl groups with other moieties, as is the case with different types of cellulose ester membranes. On the other hand, synthetic membranes can have a larger pore size, have a high chemical and thermal resistance and may be symmetric or asymmetric, which is useful to confer them with a higher mechanical strength. Nevertheless, some of these types of membranes, such as those composed by polyethersulfone (PES), tend to be more hydrophobic and this is associated with fouling on the membrane by adhesion of the proteins to the surface.[10–12]

This selection process was carried out by the evaluation of the analytical characteristics of PIII containing the gas diffusion membrane by the incorporation of different protective membranes, of several materials and various porous sizes. Calibration procedures were carried out using the optimized conditions achieved in the previous section: 100 µl injection volume, 650 µl/min flow rate, a buffer concentration of 0.001 M HEPES at a pH 7.1 and 0.1 M NaOH. The resulting calibration curves can be seen in *Fig. 4.30* and a summary of the resulting analytical characteristics can be seen in *Table 4.IX*. Only results for membranes 1 to 6 are shown, as membranes 7 and 8 were too thick to allow the perfect sealing of the gas diffusion module structure; resulting in leaking that prevented the correct functioning of the microfluidic system. Therefore, these two membranes were discarded from the evaluation process.

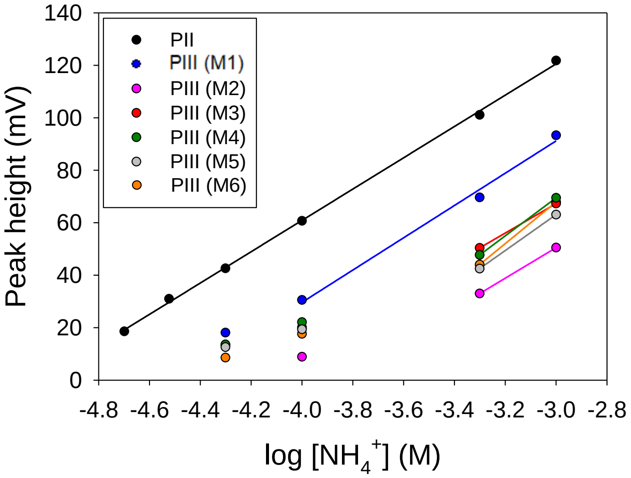

Fig. 4.30 Calibrations obtained using PII and PIII with each of the protective membrane candidates M1 – M6.

Table 4.IX Analytical characteristics obtained using PII and PIII with each of the protective membrane candidates.

| Injection volume: 100 µl | | | | | |
|---|---|---|---|---|---|
| **Protective membrane** | **Slope** | **Y-intercept** | **Linear range (µM)** | **LD (µM)** | **R$^2$** |
| **None** | 59.7 | 299.6 | 20 – 1000 | 9.4 | 0.9993 |
| **M1** | 55.2 | 254.2 | 50 – 1000 | 24.8 | 0.9944 |
| **M2** | 58.1 | 224.1 | 500 – 1000 | 139.6 | – |
| **M3** | 54.1 | 235.7 | 500 – 1000 | 63.3 | – |
| **M4** | 56.1 | 234.7 | 500 – 1000 | 66.0 | – |
| **M5** | 52.1 | 216.3 | 500 – 1000 | 71.1 | – |
| **M6** | 65.8 | 262.2 | 500 – 1000 | 295.3 | – |
| **M7** | | | No data | | |
| **M8** | | | No data | | |

From *Fig. 4.30* it is evident that the highest signal peaks were obtained when only the gas diffusion membrane was used. The incorporation of any of the appraised protective membrane produced a reduction of these signal heights, in a manner that was dependent on the specific membrane employed. The representation of the signal percentage decrease is shown in *Fig. 4.31* for each one of the protective membranes 1 to 6 for 100 µ M $NH_4Cl$.

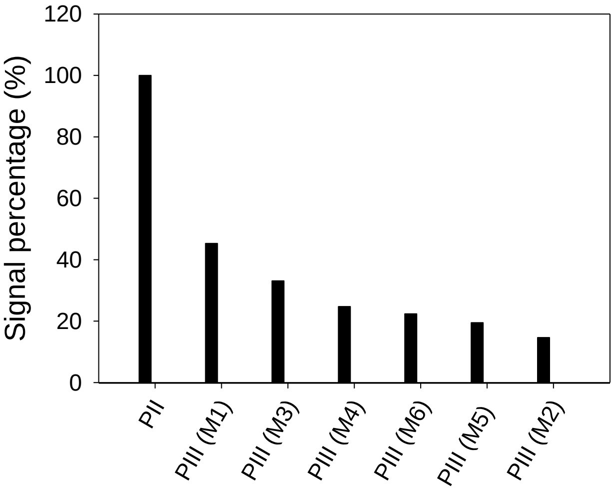

Fig. 4.31 Signal percentage decrease (%) when using PII and PIII with the different protective membranes (M1-M6) for 100 µM $NH_4Cl$.

The decrease in the signal led to a reduction of the linear working range from 20 to 1000 µM $NH_4Cl$ (with only the gas diffusion membrane) to a linear working range from 500 to 1000 µM $NH_4Cl$ (for all of the protective membranes tested), with the exception of membrane 1 (M1).

M1 was the single membrane that showed an acceptable sensitivity and linear working range from 50 to 1000 µM $NH_4Cl$ and constituted a promising candidate as a barrier membrane for PIII. Additionally, M3 and M4 both caused an acceptable loss of signal percentage. However, M3 provoked a slow leaking in the gas diffusion module which prevented its use for a prolonged time. Regarding M4, the linear working range from 500 – 1000 µM $NH_4Cl$ rendered the analytical microsystem unsuitable to be used for discrimination of healthy and pathological levels of $NH_4^+$ in plasma and blood. However, it could be possible to optimize the working conditions to achieve satisfactory analytical characteristics using M4.

These two membranes were further evaluated. M1 and M4 are very different materials. The former is a synthetic membrane made of hydrophilic polycarbonate whereas the latter is made of regenerated cellulose. There are also differences in the porous size, as M1 has larger pore size (0.05 µm) than M4 ($4.86 \cdot 10^{-3}$ µm). This may influence the diffusion of $NH_3$ through the membrane and explains why the use of M1 did not cause such a signal loss as the use of M4. However, it had to be assessed if the pore size of M1 and M4 were suitable for the protection of the gas diffusion membrane from the blood matrix.

### 4.4.2. Optimization of c for the use of M4

In order to reach an acceptable linear working range with M4 it was necessary to increase the quantity of $NH_3$ diffused through the gas diffusion membrane. The first approach was to increase the injection volume to 225 µl. The resulting calibration curve is shown in *Fig. 4.32* together with the calibration curve obtained with an injection volume of 100 µl. When increasing the injection volume to 225 µl the signal heights increase, the linear regression is E = 58.8 log $[NH_4^+]$ + 255.3 and the LD is 66 µM. However, the linear working range is from 500 to 1000 µM $NH_4Cl$ for both injection volumes.

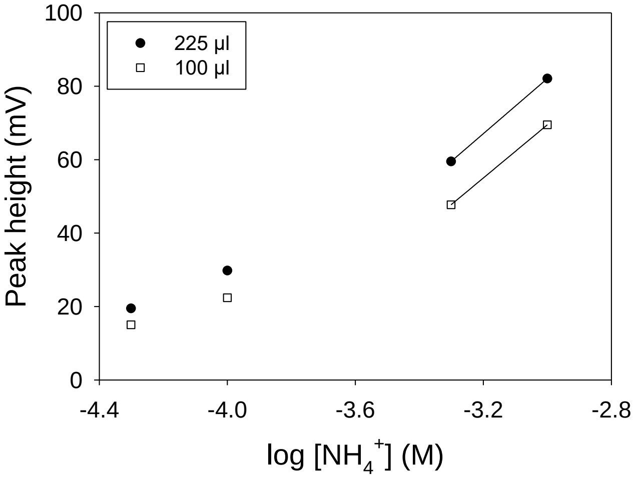

Fig. 4.32 Calibration curve obtained with PIII including M4 with an injection volume of 225 µ (black) and 100 µl (white).

Because further increasing the sample volume is undesirable for the application, an alternative strategy was to increase the time that the sample plug is in contact with the gas diffusion membrane. This can be done by two approaches: decreasing the flow rate or introducing a stop flow step.

Regarding the reduction in the flow rate, In *Fig. 4.33* it can be seen the signal recording of a 225 µl injection of a 100 µM $NH_4Cl$ standard solution at the previously optimized 650 µl/min flow rate and at a random lower flow rate of 300 µl/min. This data demonstrated that the reduction of the flow rate led to an increase of 35 % the signal height.

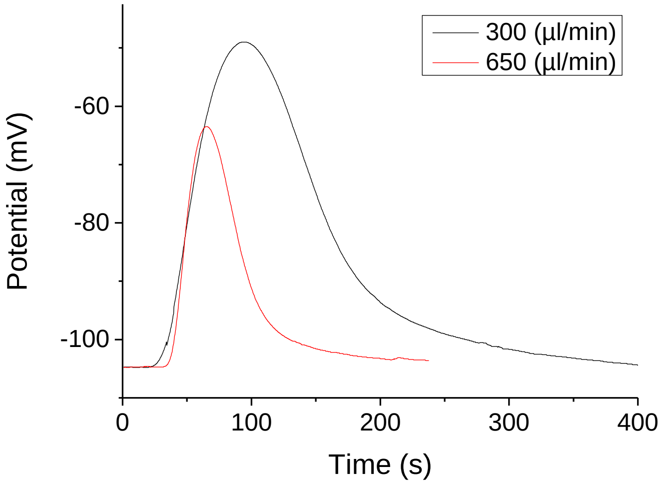

Fig. 4.33 Signal recordings obtained with a 225 µl injection of 100 µM $NH_4Cl$ at a flow rate of 650 µl/min (red) and of 300 µ/min (black) using PIII with M4.

A calibration curve obtained with a 300 µl/min flow rate and an a 225 µl injection volume can be seen in Fig. 4.34. The resulting linear regression was E = 54 (± 6) · log [NH4+] + 270 (± 20) and a $R^2$ of 0.999. Under these conditions the linear working range was from 50 to 1000 µM $NH_4Cl$ and the LD was 9.1 µM NH4Cl.

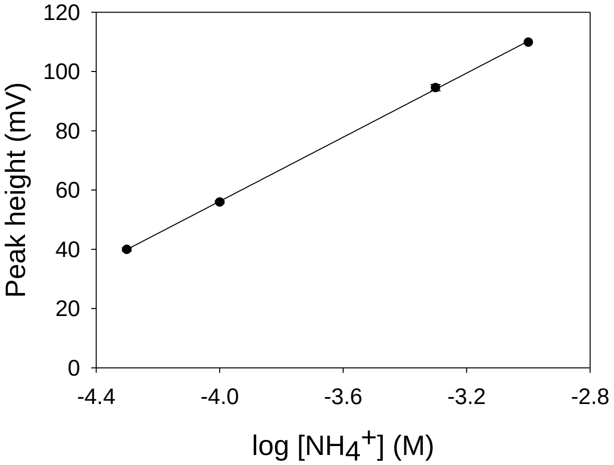

Fig. 4.34 Calibration curve obtained using a 300 µl/min flow rate and a 225 µl injection volume.

Hence, a reduction of the flow rate would be an acceptable approach to improve the analytical characteristics of PIII with M4. However, this also caused an obvious increase in the analysis time, as the signal takes longer to reach the baseline after the analysis: response time is of 150 s at 650 µl/min flow rate, but over 300 s at 300 µl/min flow rate.

The second approach for increasing the contact time between the sample and the gas diffusion membrane was to introduce a stop flow step. This step consists of stopping the flow of the solution carrying the sample for a determinate time when the sample plug is on the microchannels that are in direct contact with the protective membrane. This way, the time for the diffusion process of $NH_3$ across the gas diffusion membrane is increased. To evaluate and select the optimum duration for this stop flow step, 100 µl injections of a 1000 µM $NH_4Cl$ standard solution at 650 µl/min with different stop flow times (0 s, 45 s, 60 s and 90 s) were tested. Signal recordings obtained are shown in *Fig. 4.35*, and they indicate a clear increase in the peak heights when adding the stop flow step. The maximum peak height (121 mV) was achieved at a 60 s stop flow step and did not increase further with longer stop flow times. Therefore, 60 s was selected as the optimum, which provided an increase of 139 % with respect to the signal obtained without stop flow.

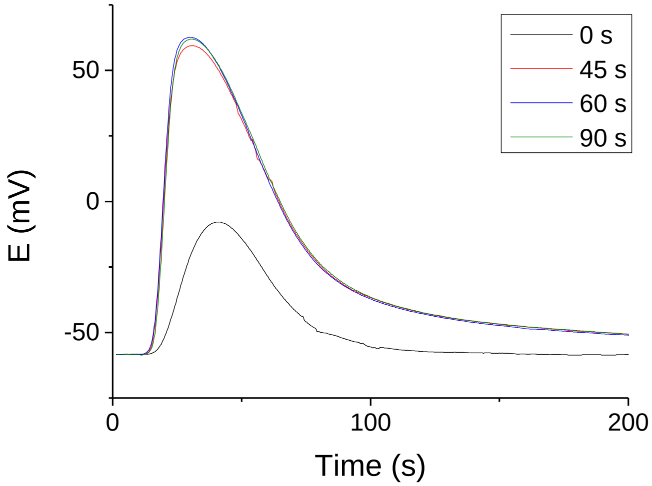

Fig. 4.35 Signal recordings of 100 µl injection of a 1000µM $NH_4Cl$ standard solution without stop flow (black) and different stop flow times: 45 s (red), 60 s (blue) and 90 s (green).

The increase of the analysis time using the stop-flow step was lower than when reducing the flow rate to 300 µl/min; because the analyte is, at the end, emptied from the detection chamber faster as the flow rate is maintained at 650 µl/min. For this reason, the introduction of the stop flow step was the method selected to achieve acceptable analytical characteristics with the protective membrane M4.

### 4.4.3. Analitical characteristics of PIII with M4

Applying the stop flow of 60 s, a 650 µl/min flow rate and an injection volume of 100 µl, it was obtained the signal recording of the calibration procedure (*Fig. 4.36*) and the calibration curve, which was E = 58 (± 2) · log $[NH_4^+]$ + 270 (± 9) and a $R^2$ of 0.9963, a linear working range from 30 µM to 1000 µM $NH_4Cl$ and a LD of 20.6 µM $NH_4Cl$.

As it can be seen, good analytical characteristics were achieved and even the use of a reduced injection volume to 100 µl was feasible. The protocol followed with PIII and M4 allowed achieving a linear working range suitable for the discrimination of healthy and pathological levels of $NH_4^+$.

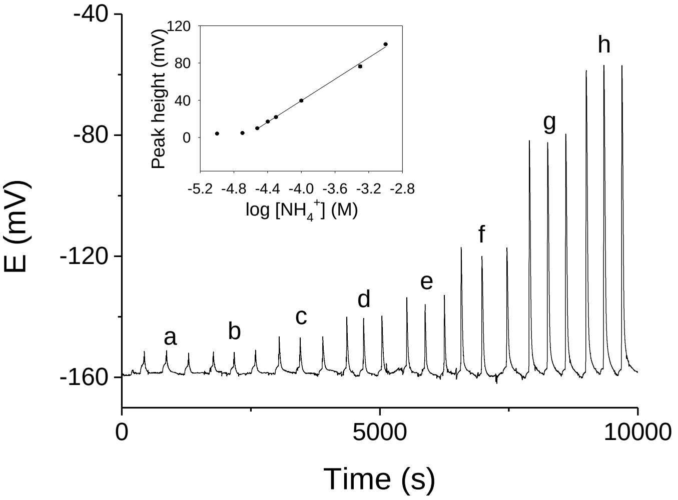

Fig. 4.36 Signal recording and calibration curve for PIII with M4 as protective membrane and a 60 s stop flow step using $NH_4Cl$ standard solutions of 10 µM (a), 20 µM (b), 30 µM (c), 40 µM (d), 50 µM (e) and 100 µM (f), 500 µM (g), and 1000 µM (h).

### 4.4.4. Analytical characteristics of PIII with M1

Using PIII and M1 with an injection volume of 100 µl and a 650 µl/min flow rate and the rest of the previously optimized variables, a calibration procedure was carried out and the signal recording is presented in *Fig. 4.37*. The following analytical characteristics were obtained: a linear regression of E = 62.8 (± 0.9) · log $[NH_4^+]$ + 297 (± 4) and a $R^2$ of 0.9993, a linear working range from 30 µM to 1000 µM $NH_4Cl$ and a LD of 18.6 µM $NH_4Cl$.

Both protective membranes M1 and M4 procured acceptable sensitivities with identical linear working ranges. However, due to the fact that the use of M1 gave a lower LD and did not require the addition of the stop flow protocol, M1 was finally chosen as the protective membrane for PIII.

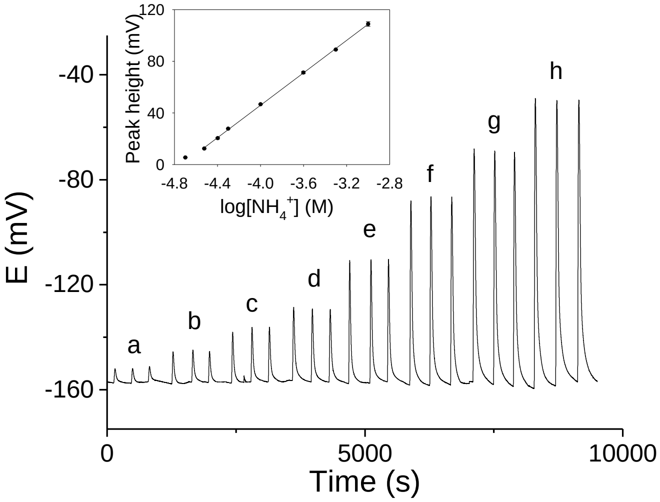

Fig. 4.37 Signal recording and calibration curve for PIII with M1 using $NH_4Cl$ standard solutions of 20 µM (a), 30 µM (b), 40 µM (c), 50 µM (d), 100 µM (e) and 250 µM (f), 500 µM (g) and 1000 µM $NH_4Cl$ (h).

### 4.4.5. Repeatability

Repeatability of the results obtained with PIII with the selected M1 was evaluated by 10 consecutive injections of $NH_4Cl$ standards of 30 µM $NH_4Cl$ (*Fig. 4.38A*), 100 µM $NH_4Cl$ (*Fig. 4.38B*) and 1000 µM $NH_4Cl$ (*Fig. 4.38C*), using the same conditions specified in the previous sections for the calibration procedure. RSD values obtained for each concentrations can be seen in *Table 4.X.*

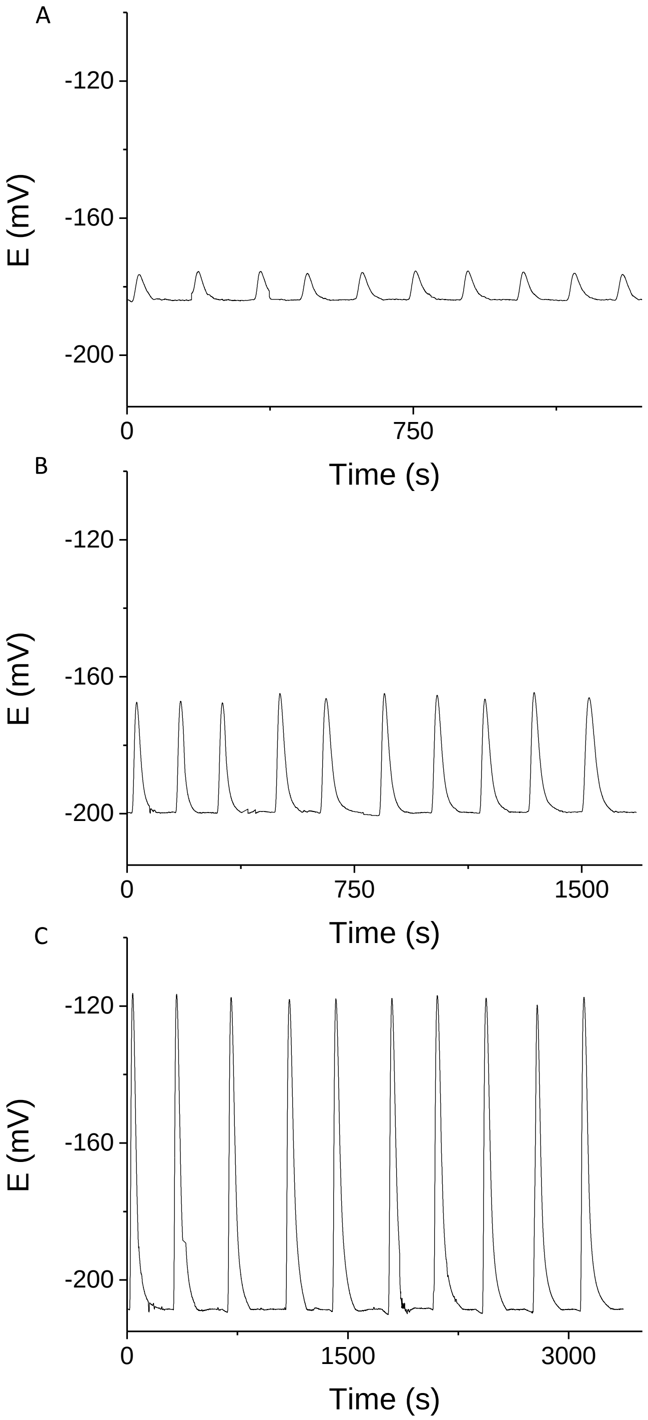

Fig. 4.38 Consecutive injections of standard solutions of 30 µM (A), 100 µM (B) and 1000 µM $NH_4Cl$ when using PIII with M1.

Table 4.X RSD values and signal peaks for consecutive analysis of 30 µM, 100 µM and 1000 µM $NH_4Cl$ using PIII with M1.

| $[NH_4Cl]$ | RSD (%) | E (mV) |
|---|---|---|
| **30** | 3 | 8.0 ± 0.3 |
| **100** | 3 | 34 ± 1 |
| **1000** | 1 | 92.6 ± 0.6 |

### 4.4.6. Analysis of plasma and blood samples

A total of 80 plasma and 26 blood samples were analysed in parallel using PIII with M1 and the reference method. Graphs in *Fig. 4.39* and *Fig. 4.40* display the comparison for plasma and blood samples, respectively.[13] Regarding the plasma analysis, results indicated that the inclusion of the protective M1 did not have a negative effect in the analysis of plasma samples, as there were not significant differences between both methods according to the paired t-test ($t_{calc}$ = 1.372, $t_{tab}$ = 2.000, $t_{calc} < t_{tab}$) and the graphical representation, which showed a regression equation of $y = 1.00 (\pm 0.02) \cdot \log [NH_4^+] + 3 (\pm 3)$ and a $R^2$ of 0.99 (N = 8; 95 % confidence).

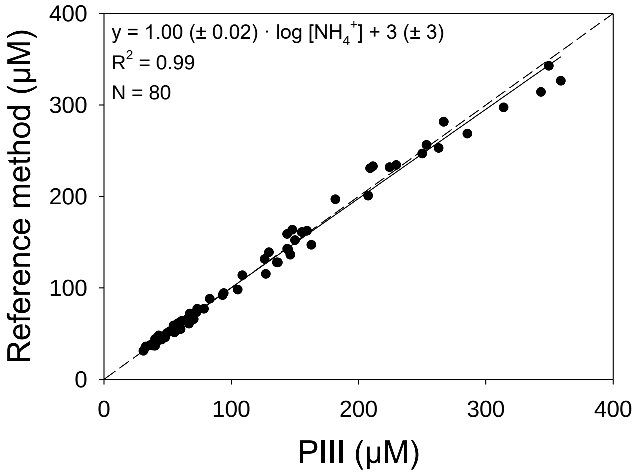

Fig. 4.39 Comparative study of the results for the analysis of plasma samples using PIII with M1 and the enzymatic reference method (n=80).

On the other hand, regarding the analysis of blood samples, the comparison of the results obtained with PIII with M1 and the reference method gave a regression equation of $y = 1.09 (\pm 0.05) \cdot \log [NH_4^+] + 1 (\pm 3)$ a $R^2$ of 0.9840 (N = 26; 95 % confidence). In this case, there was a systematic underestimation of 12 %. Therefore, it was necessary to apply a correction factor of 12 %, to the results obtained by the proposed potentiometric microanalyzer. Then, the resulting regression equation obtained was y = 0.97 (± 0.05) log [$NH_4^+$] + 1 (± 3), a $R^2$ of 0.9840 (N = 26; 95 % confidence). Statistical analysis by paired t-test revealed no significant differences between PIII with M1 and the reference method when this 12 % correction factor was applied ($t_{calc}$ = 1.152, $t_{tab}$ = 2.064, $t_{calc} < t_{tab}$). The application of a correction factor is an acceptable and common way to compare analytical data obtained with two different methods.[14]

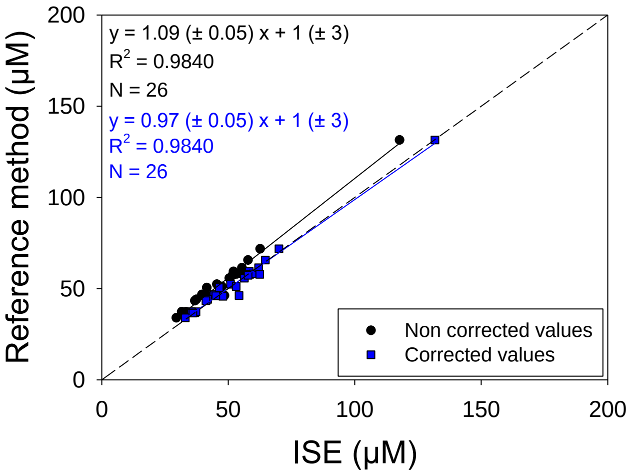

Fig. 4.40 Comparative study of the results for the analysis of blood samples using PIII with M1 and the enzymatic reference method (n=26) without (black) and with the correction factor applied (blue).

The need to use this correction factor of 12 % may arise for two different reasons: an increase of the $NH_4^+$ concentration in plasma samples analysed using the reference method due to the additional time for the centrifugation step and the process itself, or due to a different diffusion pattern between the aqueous standard solutions used for the calibration procedure and the blood samples, owing to the presence of a more complex matrix with a higher protein content.

To assess the effect of the centrifugation step in the increase of the $NH_4^+$ content, three blood samples were centrifuged to obtain the plasma and two different aliquots for every sample were analysed using PIII: one was analysed directly and the other was subjected to centrifugation and vortexed prior to analysis. Nevertheless, results showed a difference less than 5 % (*Table 4.XI*) between centrifuged and non-centrifuged blood samples, so it was concluded that the discrepancies between the two analytical methods did not arise as a consequence of the centrifugation process. Nonetheless, this discrepancy between these two types of sample is not surprising, as results obtained from the analysis of two very different matrixes are being compared.

Table 4.XI Error (%) between analysis of centrifuged and non-centrifuged blood samples obtained by PIII with M1.

| **Sample** | **[$NH_4^+$] PIII (µM) Centrifuged** | **[$NH_4^+$] PIII (µM) Non-centrifuged** | **Error (%)** |
|---|---|---|---|
| **1** | 41.1 | 42.8 | 4 |
| **2** | 40.8 | 39.7 | –3 |
| **3** | 44.1 | 43.3 | –2 |

It is also important to note that when extracting the blood sample from the patient, two different anti-coagulants can be used, EDTA and heparin. To assess if there were any differences between both anti-coagulants, three different samples were analysed by duplicate (one duplicate with each anti-coagulant) and results were compared to those obtained to the reference method. The average error for samples containing heparin was –3 % and for samples containing EDTA was –1 %. Therefore, it was proved that none of the anticoagulants negatively affected the analysis of blood samples.

Finally, the repeatability of PIII with M1 was evaluated by the analysis of a plasma sample and three blood samples by quintuplicate and results, which can be seen in *Table 4.XII,* showed acceptable RSD values in all cases.

Table 4.XII RSD values for consecutive analysis of real plasma and blood samples.

| **Sample** | **Type** | **[$NH_4^+$] (µM)** | **RSD (%)** |
|---|---|---|---|
| **1** | plasma | 108 ± 5 | 2 |
| **2** | blood | 44 ± 4 | 3 |
| **3** | blood | 66 ± 3 | 2 |
| **3** | blood | 68 ± 6 | 4 |

## 4.5. Conclusions

In this chapter the successful design, fabrication and evaluation of a prototype for the potentiometric determination of $NH_4^+$ by means of a ISEs is reported. An interference effect study carried out with PI showed that cations commonly found in blood ($K^+$ and $Na^+$) caused interference effects with the detection of $NH_4^+$. Consequently, PII was developed by the incorporation of a gas diffusion membrane to eliminate these interfering effects on the ISM. The optimization of the chemical and hydrodynamic parameters to obtain the best analytical characteristics was carried out. During this optimization the size of the detection chamber to be used was selected and it was demonstrated that the use of either TRIS or HEPES as buffer solution were feasible. Nevertheless, HEPES was selected for its better long term stability. Under the optimized conditions for PII, a Nernstian response, a low LD and a convenient linear working range. These results showed that PII was suitable for the discrimination of healthy and pathological levels of $NH_4^+$ in blood.

The following step was to use this PII for the analysis of plasma and blood samples provided by the HSJD and to compare the results with those of the reference method. Regarding the analysis of plasma samples, statistical studies revealed no significant differences between both methods, demonstrating the suitability of PII to be used in the determination of $NH_4^+$ for the diagnosis and monitoring of hyperammonemia in plasma samples. However, the final aim of this work was to be able to determine $NH_4^+$ in blood samples, thus avoiding the centrifugation step, shortening the analysis time and developing a simple analytical equipment that can be used by non-specialized personnel. Unfortunately, PII was not suitable for the analysis of blood samples because of fouling of the gas diffusion membrane with the blood matrix.

This led to the development of PIII, which included a protective membrane to avoid the clogging and consequent damaging of the gas diffusion membrane. Several different membrane candidates were evaluated and eventually two of them (M1 and M4) maintained acceptable analytical characteristics of sensitivity, linear working range and LD. However, as M1 does not require a stop-flow step, so this membrane was the one selected to be included in PIII. Plasma and blood samples were analysed using PIII with M1, which showed good protection capabilities and consequently, good analytical characteristics were obtained. By using PIII together with M1 there was an excellent correlation between the results obtained with PIII and the reference method for plasma samples, which demonstrated the viability of using the proposed microanalyzer for the management of hyperammonemia cases. Nevertheless, the analysis of blood samples revealed a systematic underestimation when using PIII in comparison to the reference method, which was not caused by the centrifugation step but was likely a consequence of unidentified factors differences related to matrix effects. The application of a correction factor of 12 % was proposed as a solution, because the underestimation was well stablished and controlled. After that, PIII constituted a reliable method for the determination of $NH_4^+$ in blood which is suitable for the discrimination of healthy and pathological levels and presented a good repeatability.

Further work must be focused on the analysis of a higher volume of samples to validate the described analytical system, the proposed correcting factor and the appropriateness of PIII to be used as a decisive tool for the diagnosis and management of hyperammonemia cases and the monitoring of UCDs.

Additionally, in order to be able to implement PIII in an hospital setting for the continued analysis of blood samples, it was necessary to fully automate the analytical system in order to ease its use and allow its operation by non-specialized personnel. This development is covered in *Chapter 5*.

## 4.6. References

(1) Ha, L. Y.; Chiu, W. W.; Davidson, J. S. Direct Urine Ammonium Measurement: Time to Discard Urine Anion and Osmolar Gaps. *Ann. Clin. Biochem. Int. J. Lab. Med.* **2012**, *49* (6), 606–608. https://doi.org/10.1258/acb.2012.012013.

(2) Cojocaru, K.-A.; Oprea, O. R.; Dobreanu, M. The Influence of Transport Condition and Processing Time on Plasma Ammonia Results. *Acta Marisiensis - Ser. Medica* **2022**, *68* (1), 24–27. https://doi.org/10.2478/amma-2022-0005.

(3) Sigma-Aldrich. *Biological Buffers Selection Guide*; 2019. https://www.sigmaaldrich.com/deepweb/assets/sigmaaldrich/marketing/global/documents/101/257/biological-buffers-selection-guide-ps3138en-ms.pdf.

(4) Häring, M.; Pérez-Madrigal, M.; Kühbeck, D.; Pettignano, A.;

Quignard, F.; Díaz, D. DNA-Catalyzed Henry Reaction in Pure Water and the Striking Influence of Organic Buffer Systems. *Molecules* **2015**, *20* (3), 4136–4147. https://doi.org/10.3390/molecules20034136.

(5) Fijorek, K.; Püsküllüoğlu, M.; Tomaszewska, D.; Tomaszewski, R.; Glinka, A.; Polak, S. Serum Potassium, Sodium and Calcium Levels in Healthy Individuals - Literature Review and Data Analysis. *Folia Med. Cracov.* **2014**, *54* (1), 53–70.

(6) Grandjean, E. M.; Aubry, J.-M. Lithium: Updated Human Knowledge Using an Evidence-Based Approach. *CNS Drugs* **2009**, *23* (4), 331–349. https://doi.org/10.2165/00023210-200923040-00005.

(7) Calvo-López, A.; Ymbern, O.; Puyol, M.; Casalta, J. M.; Alonso-Chamarro, J. Potentiometric Analytical Microsystem Based on the Integration of a Gas-Diffusion Step for on-Line Ammonium Determination in Water Recycling Processes in Manned Space Missions. *Anal. Chim. Acta* **2015**, *874*, 26–32. https://doi.org/10.1016/j.aca.2014.12.038.

(8) Calvo-López, A.; Ymbern, O.; Izquierdo, D.; Alonso-Chamarro, J. Low Cost and Compact Analytical Microsystem for Carbon Dioxide Determination in Production Processes of Wine and Beer. *Anal. Chim. Acta* **2016**, *931*, 64–69. https://doi.org/10.1016/j.aca.2016.05.010.

(9) Ymbern, O.; Sández, N.; Calvo-López, A.; Puyol, M.; Alonso-Chamarro, J. Gas Diffusion as a New Fluidic Unit Operation for Centrifugal Microfluidic Platforms. *Lab Chip* **2014**, *14* (5), 1014–1022. https://doi.org/10.1039/c3lc51114f.

(10) Olczyk, P.; Małyszczak, A.; Kusztal, M. Dialysis Membranes: A 2018 Update. *Polym. Med.* **2018**, *48* (1), 57–63. https://doi.org/10.17219/pim/102974.

(11) Kohlová, M.; Amorim, C. G.; Araújo, A.; Santos-Silva, A.; Solich, P.; Montenegro, M. C. B. S. M. The Biocompatibility and Bioactivity of Hemodialysis Membranes: Their Impact in End-Stage Renal Disease. *J. Artif. Organs* **2019**, *22* (1), 14–28. https://doi.org/10.1007/s10047-018-1059-9.

(12) Chen, Y. A.; Ou, S. M.; Lin, C. C. Influence of Dialysis Membranes on Clinical Outcomes: From History to Innovation. *Membranes (Basel).* **2022**, *12* (2), 152. https://doi.org/10.3390/membranes12020152.

(13) Calvo-López, A.; Rebollo-Calderon, B.; Ormazábal, A.; Artuch, R.; Rosell-Ferrer, J.; Alonso-Chamarro, J.; Puyol, M. Biomedical Point-of-Care Microanalyzer for Potentiometric Determination of Ammonium Ion in Plasma and Whole Blood. *Anal. Chim. Acta* **2022**, *1205*, 339782. https://doi.org/10.1016/j.aca.2022.339782.

(14) Barton, R.; Mackay, M.; Jones, G. R. D.; Badrick, T. The Management of Post Analytical Correction Factors. *Clin. Biochem. Rev.* **2017**, *38* (2), 101–103.

# Chapter 5

# Automation of prototype III

This section is focused on the automation of the previously developed PIII. This step was necessary to allow its implementation in any hospital laboratory or clinic. For this purpose, the IEB Group of the UPC collaborated with the GSB group in the design and construction of a fully automated computer-controlled multicommutation POC system based on the previously described PIII. Specifically, this automated POC system was able to carry out the preparation of the $NH_4Cl$ standard solutions, perform the calibration procedure and the analysis of a control solution, perform the analysis of the sample and finally, execute a cleaning protocol between samples to avoid any carry-over effect. Additionally, the IEB group also developed a labview software that controls this equipment and performs data acquisition and treatment in order to give as a result the $NH_4^+$ concentration for each sample. Thus, the developed automated POC carried out all of the steps of the analytical process without the need for specialized personnel.

The experimental set-up for PIII described previously in *Chapter 3* was re-designed to constitute an automated MCFA. MCFA systems include commutation devices that can be easily reprogrammed by the use of a software to re-configure the flow network. Consequently, the number of these commutation devices defines the level of versatility that can be achieved by a system.[1,2] MCFA systems are compatible with different modes of flow analysis (such as segmented flow, sequential injection, multisyringe FIA). But the system described in this chapter is a FIA system, where the commutation devices used were five 3-way injection valves (referred as $V_1$ – $V_5$). These injection valves can change between an ON and an OFF state, by the application of 12V, and were included to allow the injection of the control solution, the injection of the sample and dilution and injection of the $NH_4Cl$ stock solution for the calibration procedure and for the realization of priming protocols. Because the aspiration of reagents by a peristaltic pump may lead to the introduction of bubbles into the system a bubble trap was incorporated, to prevent air from reaching the detection chamber.

Most MCFA systems rely on a time-based injection of sample and reagents. Therefore, volume is defined by the activation time of the injection valves, which can be easily modified according to the desired analytical protocol. This leads to a reduction of the sample and reagents consumption, as they can be dispensed in a very precisely manner. Moreover, as the activation and deactivation of the valves is computer-controlled it is much more reproducible than if it was controlled by an operator, leading to a higher repeatability.[3]

Another very attractive characteristic of MCFA systems is their autonomy and ability to function unattended by any personnel. This trait is enhanced by the inclusion of real time data acquisition and feedback mechanism, allowing for autonomous manifold re-programming and self-optimization of the operating conditions according to a pre-stablished algorithm. [4]

All in all, these advantages have made MCFA systems an extremely useful tool for a wide range of analytical applications.

The development of an automated POC for hospital use is the culmination of the first objective detailed in *Chapter 2*. It represents the realization of a novel approach for $NH_4^+$ determination, which presents several advantages with respect to the current method such as low cost, ease of use, portability and short time of analysis. However, the most remarkable characteristic of the proposed POC is the possibility to analyse blood samples, instead of plasma which is the sample used for the current method employed at hospitals. Therefore, the centrifugation step to obtain the plasma is not needed and the overall analysis time is shortened. Also, the POC can be moved close to the patients to avoid the need for transporting the samples to the laboratory.

Nevertheless, the fact that there are not accepted methods for $NH_4^+$ determination in blood difficults the validation of the proposed POC, due to the impossibility to compare two methods that use the same sample matrix. Despite this, the GSB group has collaborated with the members of the laboratory of the HSJD to install and validate the automated POC by the analysis in parallel of a high number of blood samples.

## 5.1. Experimental

The selection of the calibration protocol and the evaluation of the multicommutation process was carried out by a calibration procedure consisting of the analysis of a series of $NH_4Cl$ standard solutions. Repeatability studies of the automated POC were carried out by 10 consecutive analysis of $NH_4Cl$ standards solutions to obtain the resulting RSD value.

The validation of the automated POC with real blood samples was done by analysis of spiked and non-spiked blood samples and their corresponding plasmas in parallel with the proposed method and the spectrophotometric enzymatic method used by the HSJD: the Architect ci8200 analyser from ABBOT (IL, US). The statistical analysis of the results was done using the Passing-bablok regression, the Band-Altman plot and the paired t-test.

## 5.2. Design of the automated calibration protocols

With the aim to reduce the time for the calibration procedure it was decided to perform a single analysis of only two $NH_4Cl$ standard solutions obtained by multicommutation from a stock solution of 1000 µM $NH_4Cl$. To select these two concentrations for the calibration procedure, the threshold value to discriminate healthy and pathological levels must be considered. This threshold has been defined in *Chapter 1* as 50 µM $NH_4^+$ for children and adults and 110 µM $NH_4^+$ for newborns.[5]

In order to select the two $NH_4Cl$ concentrations, a calibration procedure was carried out with duplicate analysis of different $NH_4Cl$ standard solutions under the conditions optimized in the previous chapter. In *Table 5.I* appear the analytical characteristics of the different calibration curves obtained with all the $NH_4Cl$ concentrations analysed and with different combinations of only two $NH_4Cl$ standard solutions. Although in all cases a Nernstian slope was achieved sensitivities are slightly different depending on the specific concentrations selected. Furthermore, in *Table 5.I* it can also be seen the error when interpolating the measured signal for each $NH_4Cl$ concentration into the different calibration curves. In all cases, errors for the lowest concentration, 30 µM $NH_4Cl$, were very high. This was understandable because this concentration falls outside the linear working range of the analytical system. Nevertheless, the aim was to obtain a good reliability for the measurement at the threshold level of $NH_4^+$ to discriminate between healthy and pathological levels, and 30 µM $NH_4Cl$ was well under that value. Therefore, errors at these low concentrations were considered acceptable.

Obviously, the overall errors for all concentrations were lower when interpolating in a calibration curve obtained with all the $NH_4Cl$ standard solutions, from 50 to 1000 µM. However, carrying out a calibration procedure with so many points is not feasible when using the automated POC, as it would take too much time and consume a high volume of reagents. For this reason, the errors assumed when using a calibration curve resulting from the analysis of only two $NH_4Cl$ concentrations were assessed. The aim was to achieve the smaller error for the 50 – 100 µM $NH_4Cl$ range, as lower and higher concentrations are clearly within a healthy or pathological $NH_4^+$ spectrum respectively. The lower errors for this $NH_4Cl$ range were obtained interpolating in the calibration curve resulting from the analysis of standard solutions of 50 and 100 µM $NH_4Cl$ and 100 and 500 µM $NH_4Cl$. Eventually, 50 and 100 µM $NH_4Cl$ were selected for the calibration procedure as the analysis of lower concentrations lead to a shorter analysis time.

Table 5.I Analytical characteristics of the calibration curves obtained with different combination of $NH_4Cl$ standard solutions and errors (%) of the interpolated values in these calibration curves.

| | | **Error (%)** | | | | | |
|---|---|---|---|---|---|---|---|
| | | **[$NH_4Cl$] (µM)** | | | | | |
| **Calibration curve (µM)** | **Slope** | **1000** | **500** | **200** | **100** | **50** | **30** |
| **50 to 1000** | 60.2 | 5 | –6 | 0.5 | –2 | 2 | 38 |
| **50 – 100** | 56.5 | 25 | 6 | 7 | 0.03 | –0.2 | 33 |
| **50 – 200** | 59.3 | 7 | –5 | –0.02 | –3 | –0.2 | 35 |
| **50 – 500** | 57.9 | 15 | 0.02 | 3 | –2 | –0.2 | 34 |
| **100 – 500** | 58.6 | 14 | 0.02 | 4 | 0.03 | 2 | 38 |

During the development of the automated POC system it was observed that analytical devices that were not being used often displayed a decreased sensitivity at lower concentrations for the first calibration procedure. However, for the second calibration this difference was corrected and both sensitivities at low and high concentrations were similar. This effect can be seen in the graphical representation in *Fig. 5.1* and in *Table 5.II*. Because concentrations of 50 µM and 100 µM $NH_4Cl$ were selected as the standard solutions for the calibration procedure, it is important to obtain a sensitivity in this range that is representative of the whole linear range. Even though this automated POC is meant to be employed for continued use, it is possible that the continuous flow of buffer combined with the long periods when there are no analysis taking place may have a negative effect in the sensitivity. For this reason, an initial injection of 1000 µM $NH_4Cl$ was implemented prior to the calibration procedure once a day.

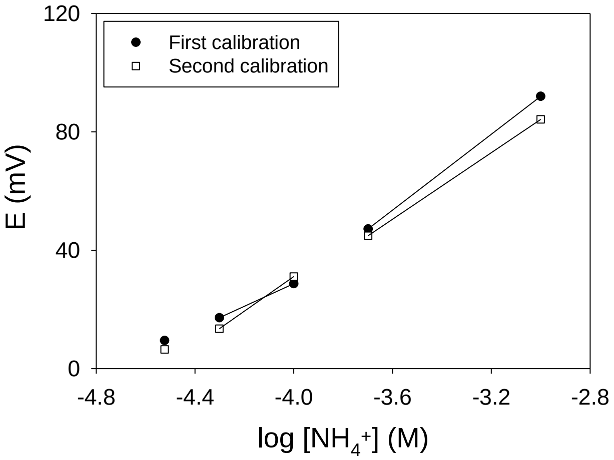

Fig. 5.1 First (black) and second calibration curves (white) obtained for the same analytical device using $NH_4Cl$ standard solutions of 30 µM, 50 µM, 100 µM, 200 µM and 1000 µM. N=1.

Table 5.II Analytical characteristics of the first and second calibration obtained with the same analytical device.

| Calibration curve | Order | Slope |
|---|---|---|
| **50 – 100 µM** | 1st calibration | 38.2 |
| | 2nd calibration | 64.1 |
| **200 – 1000 µM** | 1st calibration | 58.5 |
| | 2nd calibration | 56.2 |

When dealing with MCFA systems it is important to keep in mind that standard solutions and samples injections are not based on volume, but on time of injection. Thus, the final volume injected depends on both of the flow rate and the injection time.

As stablished in *Chapter 4*, an injection volume of 100 µl was enough to achieve the desired analytical characteristics for the proposed objective. Nevertheless, for this automated POC, it was decided to increase the sample volume in order to maintain sensitivity and linear working range even if the signal heights decrease with continued use of the detection module. A time of injection of 20 s was stablished, which translated into an injection volume of 215 µl at the previously selected flow rate of 650 µl/mL. For this time of injection, the dilution sequences using $V_2$ for the preparation of 50 µM and 100 µM $NH_4Cl$ from a 1000 µM $NH_4Cl$ stock solution are shown in *Table 5.III.*

Table 5.III Dilution sequences to obtain 50 µM and 100 µM $NH_4Cl$ from a stock solution of 1000 µM $NH_4Cl$ .The ON time and the OFF time refer to the time that the $V_2$ is allowing the flow of the stock solution and the water respectively.

| **[$NH_4Cl$] (µM)** | **Injection time (s)** | **ON time (s)** | **OFF time (s)** | **Cycles** | **Dilution Factor** |
|---|---|---|---|---|---|
| **50** | 20 | 0.5 | 9.5 | 2 | 20 |
| **100** | 20 | 0.5 | 4.5 | 4 | 10 |

## 5.3.Steps of the complete analytical process

The complete analytical process using this automated POC consists of several steps, and the schematic representation of the actuation of the different elements for each step is detailed in *Fig. 5.2.*

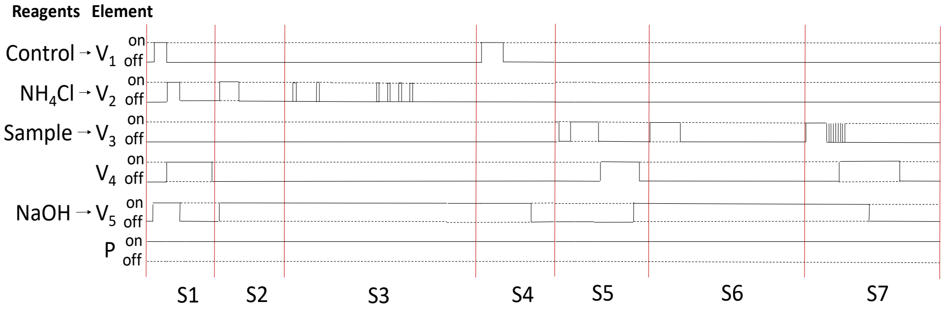

Fig. 5.2 Schematic representation of the ON/OFF state for the different elements of the automated set-up for steps 1 (S1), 2 (S2), 3 (S3), 4 (S4), 5 (S5), 6 (S6) and 7 (S7). V) 3-way injection valve and P) peristaltic pump

- Step 1 (*Fig. 5.3*): an initial priming process, which only takes place if any of the mixing, gas diffusion or detection modules has to be replaced by a new one. Valves $V_1$ and $V_2$ opened sequentially to let the control solution and the 1000 µM $NH_4Cl$ stock solution flow through the tubing up to the valves. Meanwhile, $V_4$ also activates to lead the excess that flow past the valves to the waste outlet. $V_5$ also opens to allow the priming of the 0.1M NaOH and $10^{-3}$ M EDTA solution.

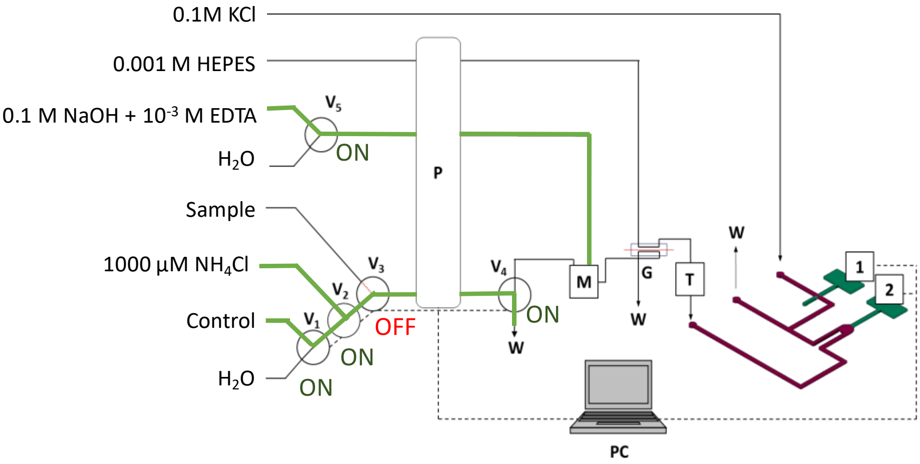

Fig. 5.3 Schematic representation of step 1. 1) reference electrode, 2) indicator electrode, T) bubble trap, V) 3-way injection valve, P) peristaltic pump, M) mixing module, G) gas diffusion module, PC) computer and W) waste.

- Step 2 (*Fig. 5.4*): an initial injection of 1000 µM $NH_4Cl$ (which is not taken into account for the calibration curve) is done before every calibration procedure. The $NH_4Cl$ stock solution enters through $V_2$ while $V_5$ stays in the ON position to allow the flow of the 0.1 M NaOH and $10^{-3}$ M EDTA solution. $V_4$ remains on the OFF position so the reagents reach the mixing module.

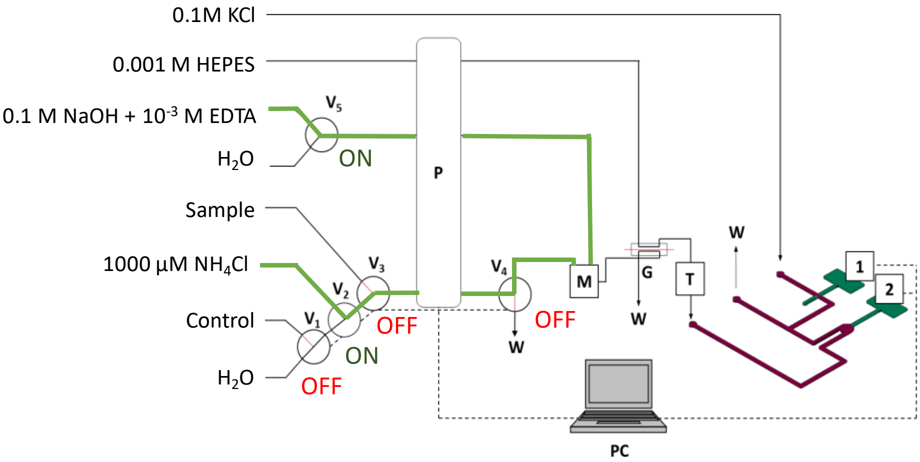

Fig. 5.4 Schematic representation of step 2. 1) reference electrode, 2) indicator electrode, T) bubble trap, V) 3-way injection valve, P) peristaltic pump, M) mixing module, G) gas diffusion module, PC) computer and W) waste.

- Step 3 (*Fig. 5.5*): a calibration procedure resulting from a single analysis of 50 and 100 µM $NH_4Cl$, which takes place once a day is done. These concentrations are obtained by a dilution sequence from the 1000 µM $NH_4Cl$ stock solution by action of $V_2$, while $V_5$ keeps the ON position. During this step $V_4$ remains on the OFF position so the reagents reach the mixing module.

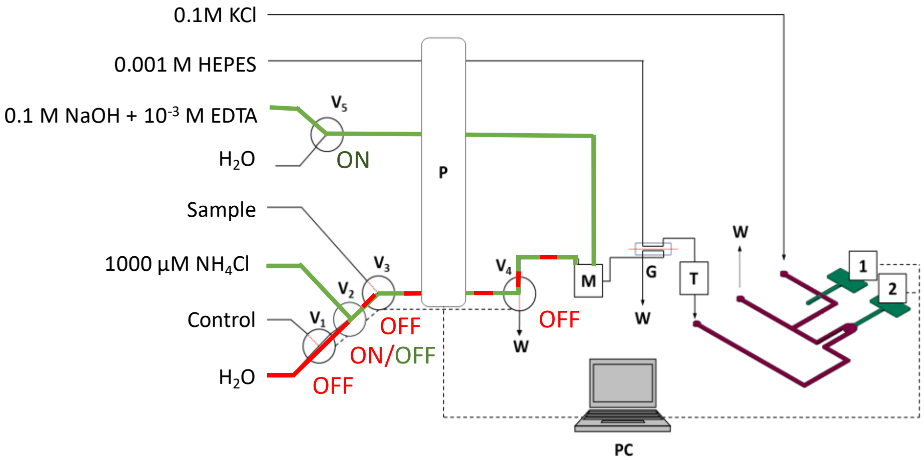

Fig. 5.5 Schematic representation of step 3. 1) reference electrode, 2) indicator electrode, T) bubble trap, V) 3-way injection valve, P) peristaltic pump, M) mixing module, G) gas diffusion module, PC) computer and W) waste.

- Step 4 (*Fig. 5.6*): a control solution analysis after the calibration and every 10 sample analysis is done. This serves a dual purpose: to monitor changes in signal heights (and correct the current calibration curve if needed) and to correct the initial calibration curve in order to be able to compare results to those obtained by the reference method. The control solution is injected through the activation of $V_1$ and consist of the same calibrator solution (293.5 µM $NH_4^+$) used by the spectrophotometric enzymatic method employed at the hospital. $V_4$ remains on the OFF position so the reagents reach the mixing module. $V_5$ de-activates after the measurement of the control solution. This way, if no sample analysis take place immediately after this step, water flows instead of the 0.1 M NaOH and $10^{-3}$ M EDTA solution.

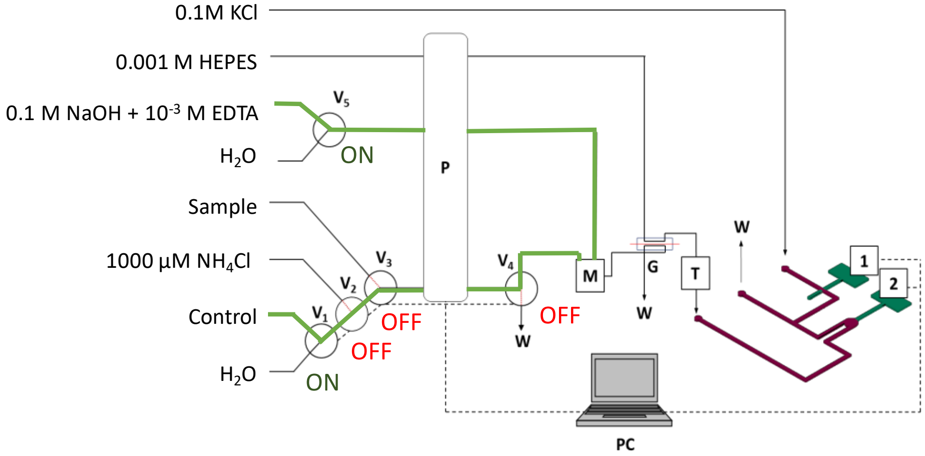

Fig. 5.6 Schematic representation of step 4. 1) reference electrode, 2) indicator electrode, T) bubble trap, V) 3-way injection valve, P) peristaltic pump, M) mixing module, G) gas diffusion module, PC) computer and W) waste.

- Step 5 (*Fig. 5.7*): a priming process for every sample analysis takes place. It starts with the introduction of an air plug (to avoid the contact with residues of previous samples) and the introduction of the sample in the tubing until reaching $V_3$. In parallel, $V_4$ activates temporally to lead any volume of sample that goes past $V_3$ to the waste outlet. When the sample is fully primed, $V_3$ deactivates and $H_2O$ flows to lead the excess of sample to the waste. The tubing leading to $V_3$ has been measured to contain exactly 215 µl of sample. So, after the priming, the vial of blood can be removed and no additional sample is wasted during the rest of the analysis protocol. $V_5$ activates to allow the flow of the 0.1 M NaOH and $10^{-3}$ M EDTA solution.

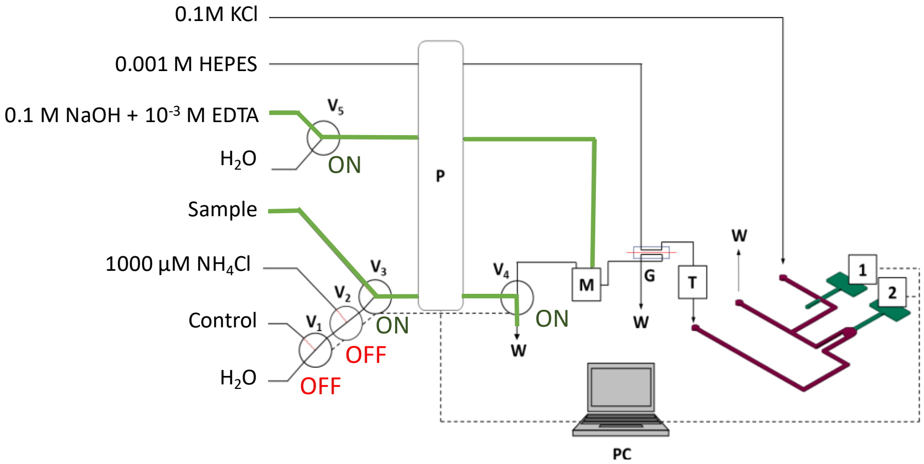

Fig. 5.7 Schematic representation of step 5. 1) reference electrode, 2) indicator electrode, T) bubble trap, V) 3-way injection valve, P) peristaltic pump, M) mixing module, G) gas diffusion module, PC) computer and W) waste.

- Step 6 (*Fig. 5.8*): an analysis protocol for every sample analysis is done. The sample is injected by the activation of $V_3$ and $V_5$ maintains its activated state to allow the flow of the 0.1 M NaOH and $10^{-3}$ M EDTA solution. $V_4$ remains on the OFF position so the reagents reach the mixing module.

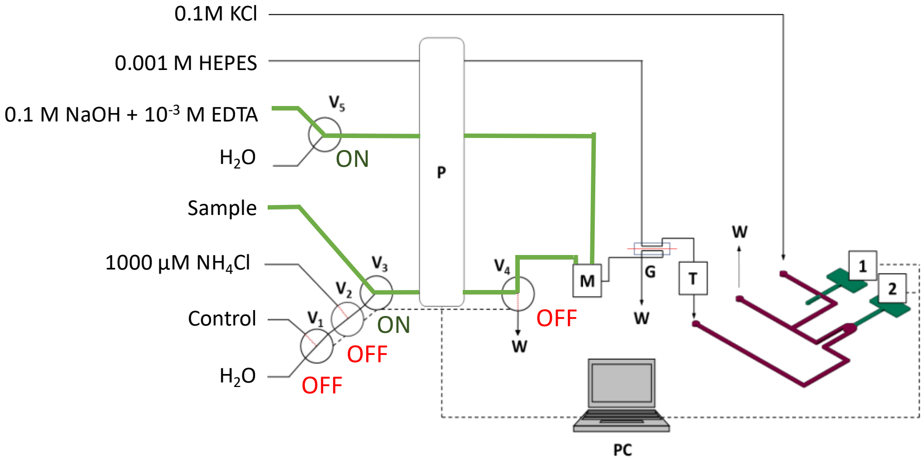

Fig. 5.8 Schematic representation of step 6. 1) reference electrode, 2) indicator electrode, T) bubble trap, V) 3-way injection valve, P) peristaltic pump, M) mixing module, G) gas diffusion module, PC) computer and W) waste.

- Step 7 (*Fig. 5.9*): a cleaning protocol after every sample analysis is done. It is based on the injection of water and the activation of $V_3$ to clean the inside of this valve. Like in step 5, $V_4$ activates to lead these residues to the waste outlet. Additionally, $V_5$ goes back to the OFF state, and water flows instead of the 0.1 M NaOH and $10^{-3}$ M EDTA solution.

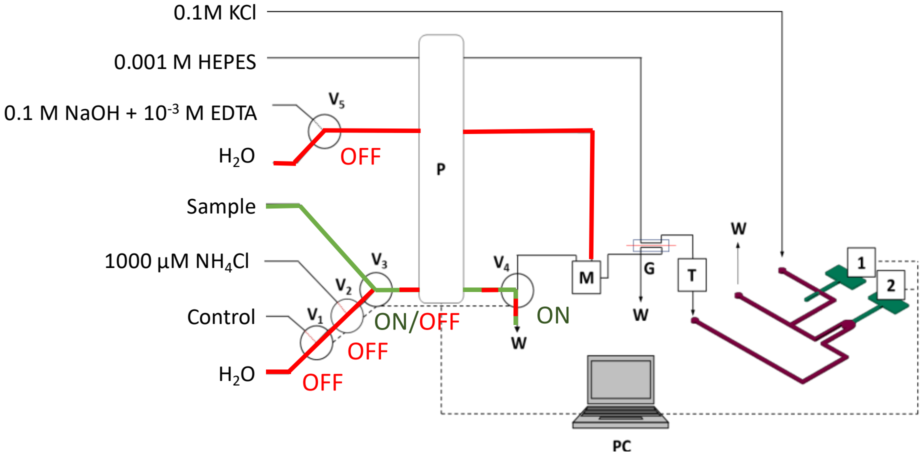

Fig. 5.9 Schematic representation of step 7. 1) reference electrode, 2) indicator electrode, T) bubble trap, V) 3-way injection valve, P) peristaltic pump, M) mixing module, G) gas diffusion module, PC) computer and W) waste.

- A stand-by state (*Fig. 5.10*) where the flow rate is reduced to 70 µl/mL when the POC is not being used.

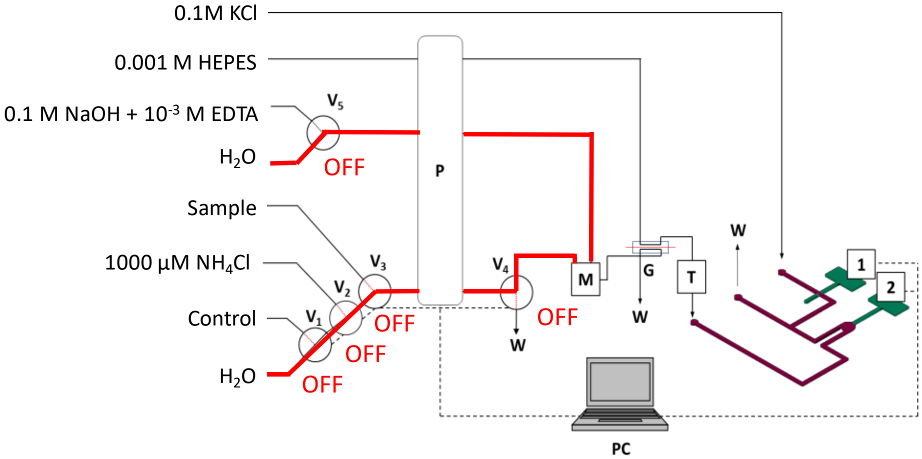

Fig. 5.10 Schematic representation of the stand by state. 1) reference electrode, 2) indicator electrode, T) bubble trap, V) 3-way injection valve, P) peristaltic pump, M) mixing module, G) gas diffusion module, PC) computer and W) waste.

Note that $V_5$ goes back to the OFF position at the end of steps 4 and 7. This way, in the event that the POC stays in the stand-by position after the analysis of the control solution or a sample, the NaOH solution would not be flowing. Therefore, reagents consumption is reduced.

This is a highly complex system that differs from the previous experimental set-ups for PII and PIII described in *Chapter 3*. The automated POC, as well as PII and PIII, all rely on a single peristaltic pump to propel the fluids in all channels. However, for PII and PIII there was one 6-way injection valve that was manually activated, and that was used for the injection of the $NH_4Cl$ standard solution, the control solution and the sample using the same channel. Hence, $V_1$, $V_2$ and $V_3$ were not necessary. Likewise, in PII and PIII, the NaOH solution was constantly flowing due to the lack of $V_5$. Moreover, the bubble-trap was also incorporated in the automated POC, but was not present in the PII and PIII experimental set-ups.

## 5.4. Valves repeatability

Even though the time of injection for all the valves was programmed to be the same, there can be slight variations in the injected volume due to the state of each particular valve. Each valve exerts a different resistance to the flow, that is a different pressure drop, leading to the aspiration of slightly different injection volumes (*Fig. 5.11*). These variations in resistance are caused either due to slight differences in fabrication or to deterioration of the valves caused to continued use.

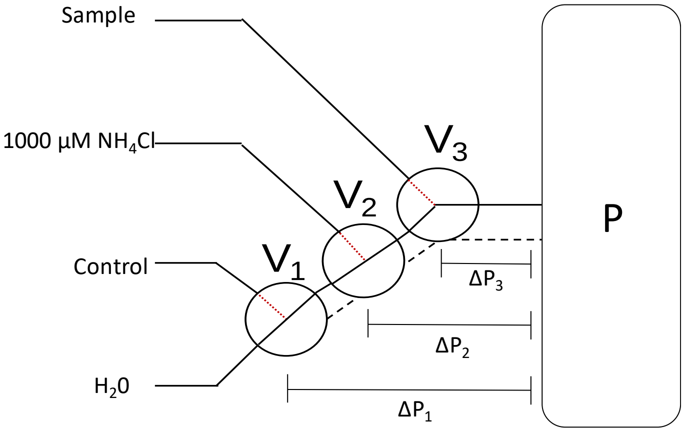

Fig. 5.11 Schematic representation of the different pressure differences for $V_1$ ($\Delta P_1$), $V_2$ ($\Delta P_2$) and $V_3$ ($\Delta P_3$).

The repeatability of each valve were assessed by 10 consecutive injections of a 100 µM $NH_4Cl$ hand-prepared standard solution. In all cases there is an acceptable repeatability, with RSD values lower than 3 % for all valves.

For the assessment of the effect of the multicommutation process, two calibration procedures were performed from triplicates of $NH_4Cl$ standard solutions obtained both by multicommutation and by hand-preparation under the previously optimized parameters. These calibration curves can be seen in *Fig. 5.12* and its analytical characteristics are shown in *Table 5.IV.* In both cases Nernstian sensitivities and similar LD are obtained. However, the sensitivity and the Y-intercept were slightly lower for the calibration curve obtained by multicommutation because of the action of the valves. The use of the multicommutation is also linked to a lower repeatability.

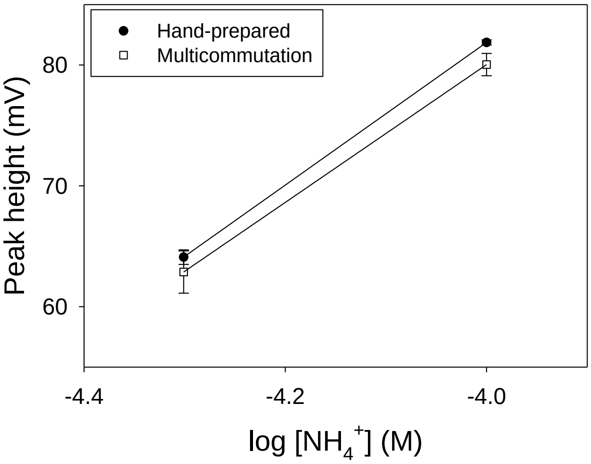

Fig. 5.12 Calibration curves for the automated POC using $NH_4Cl$ standard solutions of 50 µM and 100 µM obtained by hand (black) and by multicommutation (white). N = 3.

Table 5.IV Analytical characteristics corresponding to calibration curves using $NH_4Cl$ standard solutions obtained by multicommutation and hand-preparation.

| **Calibration curve** | **Slope** | **Linear range (µM)** | **LD (µM)** | **$R^2$** |
|---|---|---|---|---|
| **Hand-prepared** | 59 ± 5 | 50 – 100 | 4.1 | 0.998 |
| **Multicommutation** | 60 ± 20 | 50 – 100 | 3.9 | 0.990 |

Indeed, the resulting RSD values for 10 injections of a 100 µM $NH_4Cl$ standard solution obtained by hand-preparation and by multicommutation are shown in *Table 5.V*. Even though in both cases the RSD was lower than 5 %, it was slightly higher when multicommutation was employed. So, it can be concluded that the use of a 3-way injection valves during the multicommutation process involves a certain degree of acceptable variability.

Table 5.V RSD (%) values obtained for consecutive injections of 100 µM $NH_4Cl$ solutions obtained by multicommutation and hand-prepared.

| [$NH_4Cl$] (µM) | | RSD (%) |
|---|---|---|
| **100** | Multicommutation | 3 |
| **100** | Hand-prepared | 1 |

## 5.5. Improvement of the gas diffusion module configuration

When using the non-automated set-up for PIII used for the previous *Chapter 4*, the diffusion and the protective membranes were substituted for new ones as needed. It was easy to identify the time for replacement, as the signal baseline increased dramatically due to the NaOH solution entering the detection module because of the membrane fouling. However, the useful lifetime of the gas diffusion and protective membranes with this automatic POC was less than a day when analysing blood samples. Keeping in mind that the final microanalytical device is meant to be a monolithic device that includes the mixing, the gas diffusion and the detection module, it was imperative to identify and solve the problem causing this issue.

In *Fig. 5.13* it can be seen a real image of a damaged gas diffusion membrane, where it was clear that the deterioration of the membrane was focused at the inlet of the carrier and 0.1 M NaOH and $10^{-3}$ M EDTA solutions, referred to as the donor side. Hence, the damage was most likely to be caused due to the high pressure at this inlet point, where solutions pass from a 0.8 mm diameter Teflon tubes to a 100 µm x 1 mm section channel in the gas diffusion module. Moreover, on the acceptor side (where HEPES is flowing) no damage was visible. This can be explained by two main reasons. The first one is that the buffer flow rate at the acceptor side is half of the flow rate at the donor side. The second reason is that the blood sample passes through the gas diffusion module at the donor side and this complex matrix contains proteins that may foul the membrane at such high pressure conditions. Indeed, when analysing plasma samples, the membrane deterioration was not as quick and several consecutive analyses could be carried out. Therefore, an alternative configuration of the gas diffusion module was designed, fabricated and evaluated to reduce the pressure at the donor side inlet point.

This alternative configuration was already described in *Chapter 3* and relies on tiered-like inlets. This way, the highest pressure point is located on top of the gas diffusion module structure instead of on the gas diffusion and protective membrane themselves. This new configuration also had a 200 µm depth instead of 100 µm, which also helps reducing the pressure. This new configuration extended the useful lifetime of the gas diffusion and protective membranes up to 14 days of use and the analysis of over 100 blood samples.

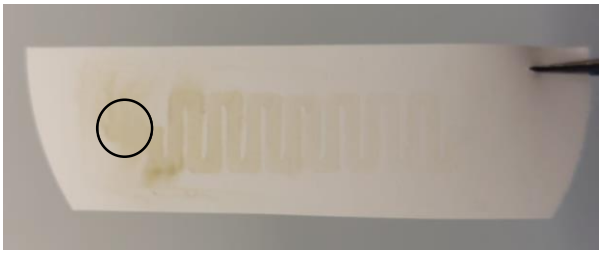

Fig. 5.13 Real image of the damaged gas diffusion membrane. Donor side inlet indicated by a black circle.

## 5.6. Validation of the automatic POC in a hospital setting

The developed automated POC was installed in the laboratory of the HSJD, for its validation under continued use during a two-month period. A total of 238 blood samples, both spiked and non-spiked, were analysed in parallel with both the automated POC and the enzymatic spectrophotometric method. Because blood samples analysed were obtained from routine blood extractions done at the hospitals, most of them had healthy levels of $NH_4^+$. Consequently, some samples were spiked in an attempt to analyse samples that covered all the pathophysiological range for $NH_4^+$.

To compare both analytical methods, the Passing-Bablok regression was applied. It is represented in *Fig. 5.14,* and the corresponding values for the slope and Y-intercept are summarized in *Table 5.VI*. As the interval of confidence (IC) (confidence 95 %) includes the 0 value for the Y-intercept, and the 1 value for the slope, it can be concluded that both methods are comparable in the evaluated concentration range.

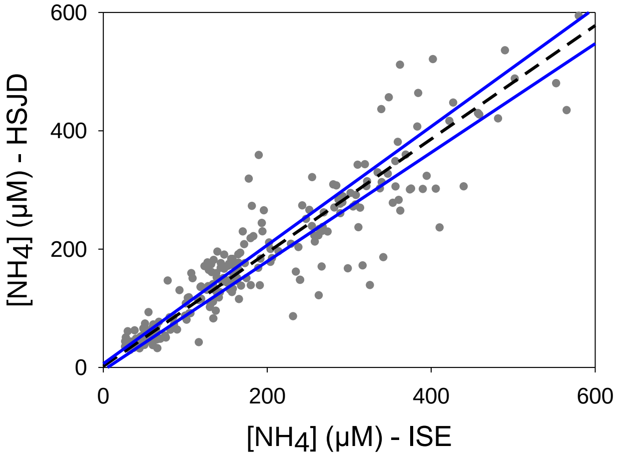

Fig. 5.14 Passing-Bablok regression (dashed line) and the upper and lower values of the IC (blue). N = 238.

A Bland-Altman plot for the methods comparison was also done because it allows the visualization of the agreement between two methods and any systematic bias or random error. It consists of the representation of the difference between the two measurements versus the average of the two measurements. The graphical representation can be seen in *Fig. 5.15* and the resulting bias and the limits of the IC (confidence 95 %) are specified in *Table 5.VI.* As can be observed from these results, there was a small positive bias (of 6.2 µM) when using the proposed automated POC, indicating a negligible systematic error.

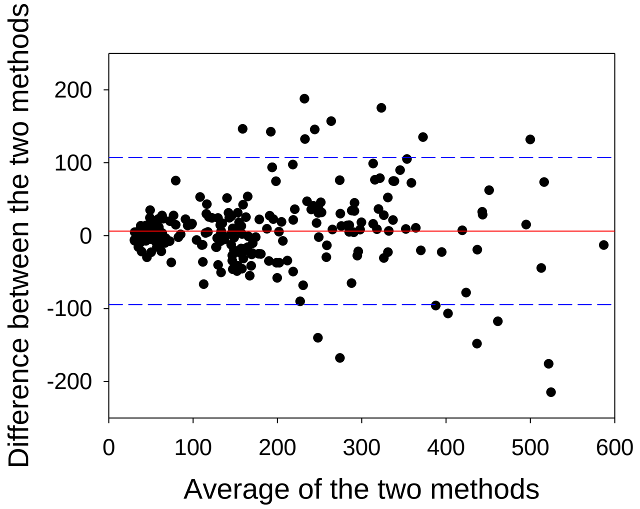

Fig. 5.15 Bland-Altman plot for the comparison of the automated POC and the hospital method. N = 238.

Table 5.VI Slope and Y-intercept values (95 %) for the Passing-Bablok regression and the Bias and IC (95 %) for the Band-Altman plots.

| **Passing-Bablok** | |
|---|---|
| **Slope** | **Y-intercept** |
| 1.0 (0.9 – 1.0) | 2 [(–5) – (6)] |
| **Bland-Altman** | |
| **Bias** | **IC** |
| 6.2 | [(–95) – (107)] |

On the other hand, despite the high variability of errors between both methods, only 16 samples from 238 (less than 7 % of the total) fall outside the IC according to the Band-Altman plot. All these 16 samples correspond to samples of a $NH_4^+$ concentration higher than 150 µM well above the threshold for hyperammonemia diagnosis.

The paired t-test ($t_{calc}$ = 1.87, $t_{tab}$ = 1.98, $t_{calc} < t_{tab}$) also supported the agreement and comparability of the two methods, as it showed that there were not significant differences between them.

Moreover, the repeatability of the system was assessed by 8 consecutive analysis of the same blood sample. The resulting RSD was of 5 %. Similarly, the repeatability of the system was also evaluated by two sets of 10 consecutive analyses of the control solution carried out with a month of difference. For both cases, the resulting RSD was of 3 %.

These results indicate that both the proposed automated POC and the reference method employed by the hospital are comparable, and the errors are randomly distributed. Therefore, it was not necessary to use the 12 % correction factor that was applied for the analysis of blood samples with the non-automated set-up for PIII as seen in *Chapter 4.*

## 5.7. Conclusions

This chapter is the culmination of one of the objectives of this thesis, which was the development of an automatic POC for hospital measurement of $NH_4^+$. It includes features not yet achieved by other analyzers, such as portability, ease of use, reduced consumption of reagents and samples, and its direct use on whole blood with high reliability.

In this chapter it was described the development of the automated version of PIII for the POC determination of $NH_4^+$ in blood to be used in a hospital setting. During this process it was clear that the limiting element to obtain a long lifetime for the automated use of the analytical system was the integrity of the gas diffusion membrane and the protective membrane. In this sense, a novel configuration was evaluated and it could achieve a membrane life time of 14 days of use and the analysis of over 100 blood samples.

A prototype of this automated POC was installed in the laboratory of the HSJD for a two-month evaluation under continued use and its validation through the analysis of real blood samples. Despite the problems derived from the validation with a reference method that does not allow measurement in blood (only in plasma), as well as the difficulty of measuring $NH_4^+$, due to its marked increase in samples over time, excellent results were obtained. The comparison of the results between the proposed automated POC and the current method employed at the hospital demonstrate that both methods are comparable. Therefore, the proposed automated POC is a promising reliable alternative for the monitoring of blood $NH_4^+$ in clinics and hospitals.

## 5.8.References

(1) Llorent-Martinez, E.; Barrales, P.; Fernandez-de Cordova, M.; Ruiz-Medina, A. Multicommutation in Flow Systems: A Useful Tool for Pharmaceutical and Clinical Analysis. *Curr. Pharm. Anal.* **2010**, *6* (1), 53–65. https://doi.org/10.2174/157341210790780195.

(2) Rocha, F. R. .; Reis, B. F.; Zagatto, E. A. G.; Lima, J. L. F. C.; Lapa, R. A. .; Santos, J. L. M. Multicommutation in Flow Analysis: Concepts, Applications and Trends. *Anal. Chim. Acta* **2002**, *468* (1), 119–131. https://doi.org/10.1016/S0003-2670(02)00628-1.

(3) Catalá Icardo, M.; García Mateo, J. V.; Martínez Calatayud, J. Multicommutation as a Powerful New Analytical Tool. *TrAC - Trends Anal. Chem.* **2002**, *21* (5), 366–378. https://doi.org/10.1016/S0165-9936(02)00505-8.

(4) Zagatto, E. A. G.; Rocha, F. R. P. Large-Scale Flow Analysis: From Repetitive Assays to Expert Analyzers. *Talanta* **2021**, *233*, 122479. https://doi.org/10.1016/J.TALANTA.2021.122479.

(5) Maines, E.; Piccoli, G.; Pascarella, A.; Colucci, F.; Burlina, A. B.

Inherited Hyperammonemias: A Contemporary View on Pathogenesis and Diagnosis. *Expert Opin. Orphan Drugs* **2018**, *6* (2), 105–116. https://doi.org/10.1080/21678707.2018.1409108.

# Chapter 6

# Disposable prototypes for the detection of ammonium ion and other metabolites in blood at home

Hitherto, it has been discussed the development of a microfluidic FIA system to be used as a POC device in an hospital setting for the detection of $NH_4^+$ in blood. However, cases of acute hyperammonemia states require a fast and early diagnosis and treatment to avoid long-lasting health complications and even death. To achieve this immediate intervention, it is necessary for the patients to be able to have a close control of their $NH_4^+$ levels in blood routinely. In order to tackle this issue, the conceptual approach for $NH_4^+$ determination needed to be modified and new analytical instrumentation had to be explored. Besides reliable, this new instrumentation must also be disposable, low cost, suitable for use at home and user-friendly.

Consequently, this chapter focuses on the development and optimization of a disposable microanalytical device for detection of $NH_4^+$ in blood at home. This disposable microanalyzer was designed resembling the glucometer concept: a portable reader used together with single-use reactive strips which can be used in a user-friendly manner. Nevertheless, for this proposed microanalyzer, strips are made of COC and integrate two $NH_4^+$ ISE for the potentiometric determination of the analyte. Because these strips must be disposable it is compulsory to reduce the cost as much as possible. Additionally, the portable reader could connect via Bluetooth to the patient's smartphone and send results to the patient's doctor.

Despite some similarities with amperometric glucometers, these potentiometric devices cannot rely on factory calibration due to the low reproducibility between them. Therefore, it was necessary to develop a strategy for the auto-calibration procedure prior to use, which was already described in *Chapter 1*.[1,2] This way, a reliable quantification of the analyte is obtained, even if the reproducibility between devices is low. After the auto-calibration step, the analysis of $NH_4^+$ is similar to that of PII: $NH_4^+$ from the sample converts to volatile $NH_3$ at one side of a PVDF gas diffusion membrane under basic conditions. Then, $NH_3$ diffuses to the other side of the membrane, where there is a buffer at a neutral pH, and $NH_3$ is converted back to $NH_4^+$ to be detected by the ISE.

Because these disposable microanalyzers were designed for the analysis of capillary blood, they can circumvent the issue of the poor stability of the $NH_4^+$ levels in blood samples, which increase quickly with time if these samples are not analysed as fast as possible.[3] Moreover, they do not require the use of a protective membrane as they are meant for one analysis only.

In addition, this chapter also focuses on the explotation of another characteristic of these disposable devices: their great versatility. Devices for determination of $NH_4^+$ at home (which will be referred as N-DP in this work) can be easily customised for the indirect determination of other analytes or biomarkers by the introduction of an enzyme that catalyses the production of $NH_4^+$, facilitating the monitoring of other IEMs at home. To prove the potential of this conceptual approach, this enzymatic indirect determination was first validated using urease as a model enzyme (with the U-DP) due to the low cost and availability of this enzyme. Afterwards, this concept was applied for the indirect determination of Phe (with the P-DP). The close monitoring of PKU patients is of upmost importance. Acute hyperphenylalaninemia may not present symptoms as noticeable and deadly as those linked to hyperammonemia. Hence, decompensation states can be harder to identify. However, sustained high Phe levels do have a severe neurological impact and lead to intellectual impairment. This disposable device will allow these patients to monitor their Phe levels from home periodically and easily detect these acute hyperphenylalaninemia states that could be otherwise undetected.

## 6.1. Experimental

Calibration curves shown in this work were obtained using both the batch and the dual set-ups described in *Chapter 3*. Unlike the FIA systems of PI, PII and PIII used in the previous chapters (which gave a transient signal as the standard solution or sample plug passed through the detection chamber), calibration procedures here described were carried out by micropippeting a given volume of a $NH_4Cl$ standard solution either in the beaker (for the batch set-up) or on top of the gas diffusion membrane located over the indicator electrode (for the dual set-up). After each addition, the potential reaches a stable signal before continuing the procedure with the following addition. At the end of the calibration procedure the detection chambers were emptied and cleaned. As a consequence, replicates corresponded to calibration procedures carried out with different devices under the same experimental conditions.

The analyte concentrations used for the construction of the calibration curves depended on the physiopathological range of each analyte.

In the case of the $NH_4^+$ determination using N-DP in a batch set-up, the concentration used ranged from 1 to 2176 µM $NH_4Cl$ with a time between additions of 1 minute, under stirring and without the gas diffusion module. This set-up was used for the optimization of the ISM composition. When using the dual set-up for the optimization of the chemical parameters for $NH_4^+$ determination, the concentrations used were from 50 µM to 1000 µM $NH_4Cl$ and the platform used contained the 3.5 mm diameter ISEs, which required a 5 µL buffer volume inside each ISE chamber. For the conversion of $NH_4^+$ into $NH_3$, 5 µL of a 0.1 M NaOH was used on top of the gas diffusion membrane. Additionally, a motor was used to mimic the solution stirring in the batch set-up.

Regarding the determination of urea with U-DP, calibration curves in the batch set-up were obtained using urea concentrations from 1 mM to 33 mM with a time between additions of 1 minute, under stirring conditions and without the gas diffusion module. For the dual-set-up, a DP platform containing 1.8 mm diameter ISEs was used, with a volume of 1.5 µl in the each ISE chamber and calibrations procedures were performed without the presence of a vibrating motor. For the conversion of urea into $NH_3$, 3 µl of a buffer solution containing urease was deposited on top of the gas diffusion membrane. Urea concentrations analysed with the U-DP dual set-up were the same as with the batch set-up.

Regarding the determination of Phe using P-DP, the entire optimization was carried out with the dual-set up with the analytical platform containing the 3.5 mm diameter ISEs and the motor-induced agitation. Calibration curves were obtained by the consecutive analysis of concentrations ranging from 120 µM to 1600 µM Phe. For the conversion of Phe into $NH_3$, 5 µl of a solution containing PAL enzyme was deposited on top of the gas diffusion membrane.

In the case of the dual set-up, with every addition of standard solutions, there was a substantial change in the ionic strength of the small volume on top of the detection chamber. Under these conditions, it is not possible to equate the ionic concentration to the ionic activity. Thus, graphs displaying calibration curves in this chapter show the potential versus the logarithmic value of the ionic activity.

When using the batch set-up, results show the calibrations of a total of 4 or 8 different ISEs. In the case of the dual set-up, optimizations of the chemical variables were carried out by 3 replicates of each condition (which correspond to calibrations of 3 different devices) for N-DP and P-DP. Regarding the use of U-DP with urease as model enzyme, the optimization results were obtained from a single calibration with each condition. Calibration curves obtained with the optimized parameters have been carried out with 5 individual devices for all analytes.

It is important to remark that, despite the fact that this analytical devices are meant for one use only, the optimization processes were carried out re-using the detection and gas diffusion modules. This may lead to a decrease singal heights and repeatability, due to the continued use.

## 6.2. Disposable prototype for ammonium ion detection in blood

The chemical basis for this new conceptual approach using N-DP is schematically shown in *Fig. 6.1.* As in the previous chapters, the detection of $NH_4^+$ by an ISE takes place after the diffusion of the analyte through a PDVF gas diffusion membrane. This allows the separation of the $NH_4^+$ from the blood matrix, thus, avoiding interferences. The blood sample is situated on top of the gas diffusion membrane in the presence of a 0.1M NaOH solution. Thus, the $NH_4^+$ converts into volatile $NH_3$ and crosses the gas diffusion membrane. On the other side, $NH_3$ converts back to $NH_4^+$ in the presence of a buffer solution at a neutral pH. Underneath the gas diffusion membrane there is one of the ISEs of the microanalytical device, the one that acts as an indicator electrode. The $NH_4^+$ ions reach this indicator electrode first, but do not diffuse to the other ISE (the one acting as reference electrode) during the time of the analysis. Therefore, the potential of this reference electrode is kept stable during the measurement. In this instance, the blood sample fouls the gas diffusion membrane, which is rendered it unusable for more analysis. However, a protective membrane is not needed as these microanalytical devices are meant to be for one use only.

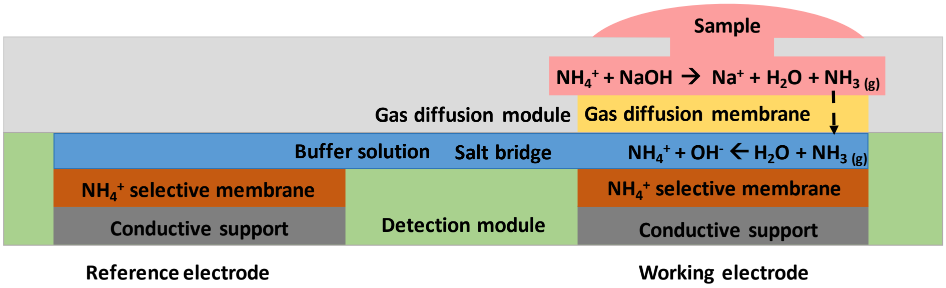

Fig. 6.1 Schematic representation for the detection of $NH_4^+$ using N-DP.

### 6.2.1. Optimization of the ISM composition

The evaluation of the composition of the ISM in order to adapt them for this disposable concept was carried out using the batch set-up and the N-DP without the gas diffusion membrane. The composition of the ISM evaluated are specified in *Table 6.I.*

Table 6.I Chemical composition of the two ISM evaluated.

| | Original membrane | | Alternative membrane | |
|---|---|---|---|---|
| **Component** | Reactive | % | Reactive | % |
| **Ionophore** | Nonactin | 1 | Nonactin | 2 |
| **Additive** | – | – | Potassium tetrakis(4-chlorophenyl) borate | 0.5 – 1 |
| **Plasticizer** | BBPA | 65.5 | PBSP | 84 |
| **Polymer** | PVC | 33.5 | PVC | 13.5 |

Traditionally, the $NH_4^+$ selective electrodes employed by the GSB group consist of a ISM containing BBPA as plasticizer. With the aim to improve the analytical characteristics, the performances of two ISM compositions were evaluated. The ISM containing BBPA will be referred as original membrane, and the new ISM composition will be referred as alternative membrane. This alternative ISM composition contains PBSP as plasticizer instead of BBPA, as it has been previously reported to extend the lifetime of $K^+$ ISEs. [4,5]

This evaluation was done using the batch set-up, using a buffer solution of 0.001 M HEPES at pH 7. The resulting calibration curves for 8 ISEs containing the original membrane composition and 8 ISEs containing the alternative membrane composition (with 0.5 % additive) can be seen in *Fig. 6.2.* The corresponding analytical characteristics with these membrane formulations are specified in *Table 6.II*. From this table, it can be seen that both compositions show a satisfactory sensitivity and LD. However, with the alternative ISM composition, the linear working range reached slightly lower $NH_4^+$ concentrations (1 µM $NH_4Cl$) than the original ISM composition (7 µM $NH_4Cl$).

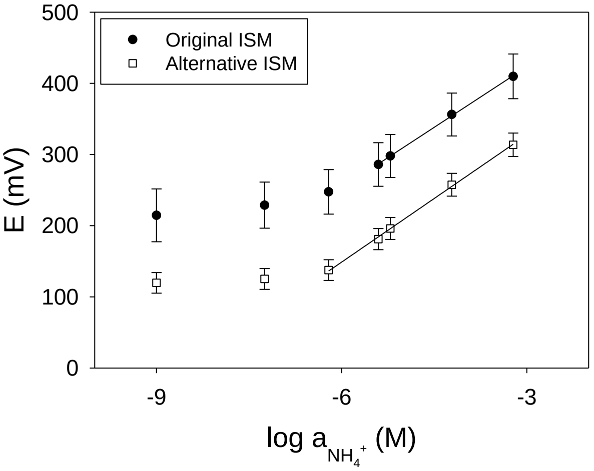

Fig. 6.2 Optimization of the ISM composition for N-DP: original ISM (black) and alternative ISM compositions (white). N = 8.

Table 6.II Average values of the analytical characteristics for the original and alternative membranes compositions for the N-DP.

| Membrane | Slope | Linear range (µM) | LD (µM) | $R^2$ |
|---|---|---|---|---|
| **Original** | 57 ± 9 | 7 – 2176 | 0.3 ± 0.5 | 0.9993 |
| **Alternative** | 60 ± 3 | 1 – 2176 | 0.3 ± 0.1 | 0.9984 |

Additionally, this alternative ISM composition does not require a conditioning step, so the fabrication process is shortened. Given this results, the alternative ISM composition was selected for the disposable microanalytical devices.

Afterwards, the effect of different percentage of the additive, Potassium tetrakis(4-chlorophenyl) borate, was evaluated using the batch set-up. The presence of the additive in the alterative ISM composition comes from previous experience in the group regarding the use of membranes containing PBSP as plasticizer in devices used for batch analysis.[5] Specifically, 4 calibration procedure were carried out for each percentage of additive tested: 0.5 % and 1 % of additive (*Fig. 6.3*). The corresponding analytical characteristics can be seen in *Table 6.III*. With 1 % of additive sensitivity is high, even reaching supernernstian values. Moreover, a percentage of 0.5 % is enough to obtain a good sensitivity and a Nernstian behavior, a linear working range from 1 µM to 2176 µM $NH_4^+$ and a very low LD. Consequently, 0.5 % of additive was chosen for this microanalytical platform.

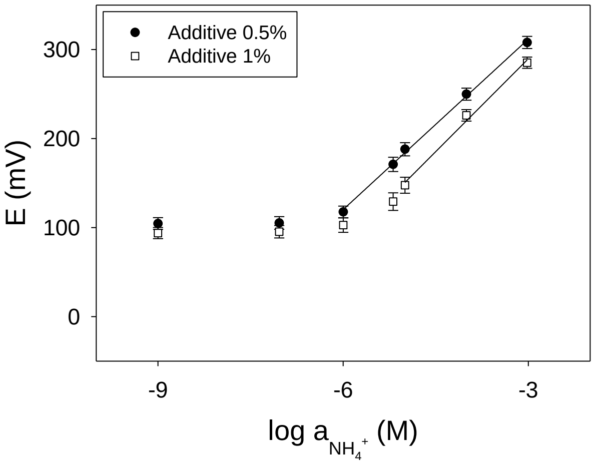

Fig. 6.3 Additive percentage optimization for N-DP: 0.5 % (black) and 1 % (white). N = 4.

Table 6.III Analytical characteristics for ISEs containing the alternative ISM composition with different percentage of additive for N-DP.

| Additive (%) | Slope | Linear range (µm) | LD (µm) | $R^2$ |
|---|---|---|---|---|
| **0.5** | 63 ± 2 | 1 – 2176 | 0.5 ± 0.2 | 0.9984 |
| **1** | 70 ± 6 | 7 – 2176 | 2 ± 1 | 0.9948 |

### 6.2.2. Optimization of chemical variables of N-DP

Once the chemical composition of the ISM was optimized, the next step was to optimize the chemical variables involved in the analytical reaction. The variables optimized for the determination of $NH_4^+$ were the concentration and pH of the buffer solution and the analysis time (*Table 6.IV*). These experiments were done using the dual set-up.

Table 6.IV Optimization of the chemical variables for N-DP.

| Variable optimized | [HEPES] (M) | HEPES pH | Time (min) | Optimized value |
|---|---|---|---|---|
| **[Buffer]** | 0.001 – 0.05 | 7 | 4 | 0.01 |
| **Buffer pH** | 0.01 | 6.5 – 7 | 4 | 6.5 |
| **Time of analysis** | 0.01 | 6.5 | 4 – 5 | 5 |

HEPES was selected as a buffer, and three different concentrations were evaluated: 0.001 M, 0.01 M and 0.05 M (*Fig. 6.4*). All buffers had pH 7 and the time of analysis between additions of $NH_4Cl$ standard solutions was of 4 minutes. The analytical characteristics for the calibration curves with each buffer concentration are specified in *Table 6.V.* Sensitivities were low with all conditions. So, a buffer concentration of 0.01M was selected to correctly maintain the pH value underneath the gas diffusion membrane and achieve the fast and complete conversion of $NH_3$ back into $NH_4^+$.

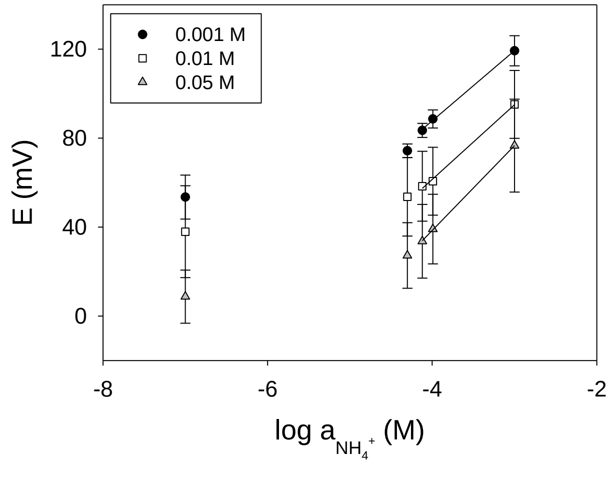

Fig. 6.4 Buffer optimization for N-DP: 0.001M (black), 0.01M (white) and 0.05M (grey). N = 3.

Table 6.V Analytical characteristics of calibration curves obtained with different buffer concentrations for N-DP.

| [HEPES] (M) | Slope | Linear range (µm) | LD (µm) | $R^2$ |
|---|---|---|---|---|
| **0.001** | 30 ± 20 | 76 – 1000 | 10 ± 20 | 0.9991 |
| **0.01** | 30 ± 20 | 76 – 1000 | 20 ± 20 | 0.9960 |
| **0.05** | 30 ± 10 | 76 – 1000 | 10 ± 10 | 0.9966 |

Next, the effect of buffer pH was tested. Values close to the lower end of the useful pH range for HEPES were evaluated, as a more acidic pH promotes the conversion of $NH_3$ to $NH_4^+$. Taking into account the HEPES $pK_a$ value of 7.48 (at 25 °C), this buffer has a useful pH range from 6.8 to 8.2.[6] Hence, calibration curves with HEPES 0.01 M at pH 6.5 and 7 were obtained, which can be seen in *Fig. 6.5*. The analytical characteristics compiled in *Table 6.VI* show that the sensitivity was significantly improved when using a lower pH. Therefore, a more acidic pH of 6.5 was selected as optimized value because it ensured the conversion of all the diffused $NH_3$ back into $NH_4^+$.

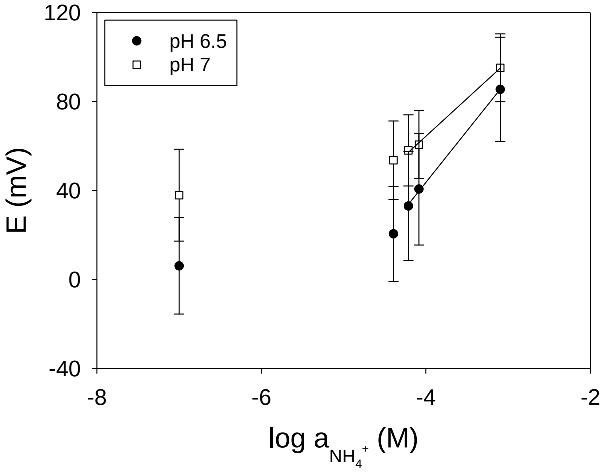

Fig. 6.5 Buffer pH optimization for N-DP: 6.5 (A) and 7 (B). N = 3.

Table 6.VI Analytical characteristics of calibration curves obtained with different buffer pH for the N-DP.

| HEPES pH | Slope | Linear range (µm) | LD (µm) | $R^2$ |
|---|---|---|---|---|
| **6.5** | 50 ± 10 | 76 – 1000 | 20 ± 30 | 0.9978 |
| **7** | 30 ±20 | 76 – 1000 | 20 ± 20 | 0.9960 |

As the desired sensitivity was not yet achieved with the current optimized values, a longer time between $NH_4Cl$ additions was assessed. The resulting graphs can be seen in *Fig. 6.6*, and the corresponding analytical characteristics appear in *Table 6.VII.* At longer times of analysis more $NH_3$ diffuses through the gas diffusion membrane. At 5 minutes, which was a reasonable time for analytical device to use at home, the sensitivities obtained were adequate and the linear working range was from 50 µM to 1000 µM $NH_4^+$.

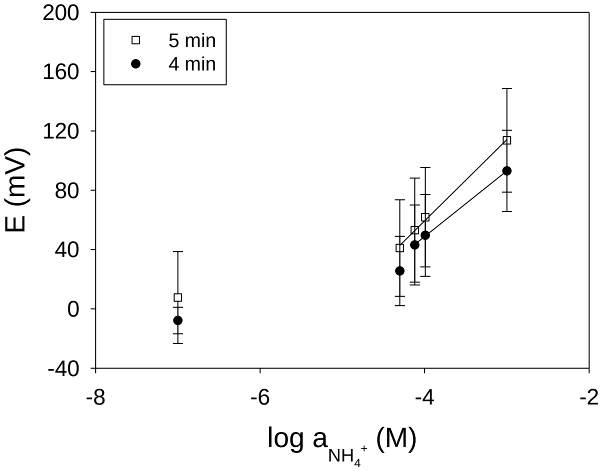

Fig. 6.6 Analysis time optimization for N-DP: 4min (black) and 5 min (white). N = 3.

Table 6.VII Analytical characteristics of calibration curves obtained with different time of analysis for N-DP.

| Time (min) | Slope | Linear range (µm) | LD (µm) | $R^2$ |
|---|---|---|---|---|
| **4** | 44 ± 7 | 76 – 1000 | 10 ± 50 | 0.9997 |
| **5** | 55 ± 9 | 50 – 1000 | 10 ± 20 | 0.9969 |

### 6.2.3. Analytical features of N-DP

With the optimized parameters of the alternative ISM composition with 0.5 % additive, a buffer solution of 0.01 M HEPES at pH 6.5 and a time of analysis of 5 minutes, the calibration curves for 5 different devices were obtained and can be seen in *Fig. 6.7*. The analytical characteristics for all these devices, as well as for their average value are shown in *Table 6.VIII*.

The calibration curves obtained revealed a satisfactory Nernstian sensitivity for a linear working range from 50 µM to 1000 µM $NH_4Cl$. Hyperammonemia was defined in chapter one as being $NH_4^+$ levels higher than 50 µM $NH_4Cl$ in blood in children and adults.[7] So this working range was acceptable to discriminate a pathological concentration of this analyte in blood and allowing the patients to keep a close control of their pathology.

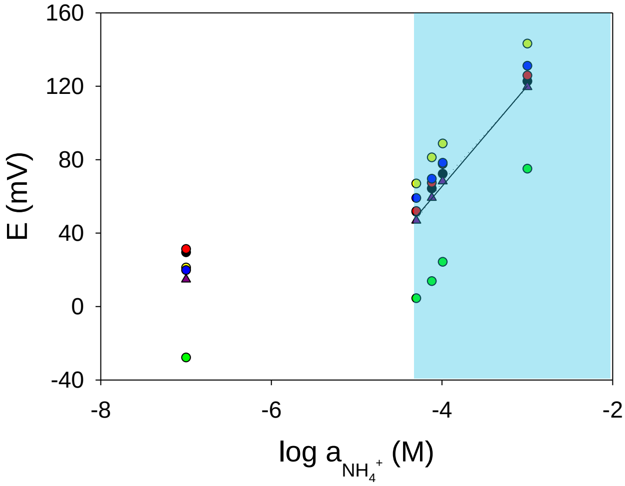

Fig. 6.7 Calibration curves obtained with optimized parameters for 5 different N-DP. The average values and their linear regression appear as purple triangles and as a purple line respectively. The pathological range for $NH_4^+$ concentrations in blood is indicated in blue.

Table 6.VIII Analytical characteristics of the calibration curves obtained with the optimized chemical parameters for the N-DP.

| Calibration curves | Slope | Y-intercept | Linear range (µm) | LD (µm) | $R^2$ |
|---|---|---|---|---|---|
| **1** | 53.3 | 277.6 | 50 – 1000 | 22.4 | 0.9967 |
| **2** | 54.3 | 290.1 | 50 – 1000 | 17.3 | 0.9865 |
| **3** | 53.4 | 237.3 | 50 – 1000 | 12.2 | 0.9974 |
| **4** | 57.1 | 315.0 | 50 – 1000 | 7.1 | 0.9967 |
| **5** | 54.9 | 296.1 | 50 – 1000 | 9.3 | 0.9991 |
| **Average** | 55 ± 4 | 280 ± 80 | 50 – 1000 | 10 ± 17 | 0.9953 ± 0.01 |

## 6.3. Disposable prototype integrating an enzyme for the indirect detection of other metabolites: urease as model enzyme

As stated before, one great advantage of this proposed disposable platform is its potential versatility to be applied for the indirect determination of other biologically relevant biomarkers. Any enzyme that can convert a biomarker of interest into $NH_3$ can be included into the DP platform, on top of the gas diffusion membrane. This way, the $NH_3$ generated correlates to the concentration of the biomarker of interest present in the blood sample. The $NH_3$ diffuses through the gas diffusion membrane to reach the ISE located at the other side and the potentiometric detection occurs in the same way as in the case of the direct determination of $NH_4^+$. To validate this enzymatic DP concept, urease was selected as model enzyme due to its low cost and availability. The catalysed reaction is shown here:

$$\mathrm{Urea} + \mathrm{H_2O} \xrightarrow{\mathrm{Urease}} \mathrm{CO_2} + 2\ \mathrm{NH_3}$$

In *Fig. 6.8* appears a schematic diagram of the analysis process for the indirect detection of urea with the proposed U-DP. Urea levels are monitored as a biomarker of renal function. In healthy adults, normal levels range from 2 mM to 7 mM but increase in patients that present chronic kidney disease to levels that can be 10 times or more higher.[8] Therefore, the linear working range that must be achieved with the U-DP is much higher than that obtained with the N-DP. For this reason, for the use of the U-DP, the motor induced agitation was not included and an analytical platform with a smaller detection chamber diameter (1.8 mm instead of 3.5 mm) was used in order to reduce the volume of reagents and sample.

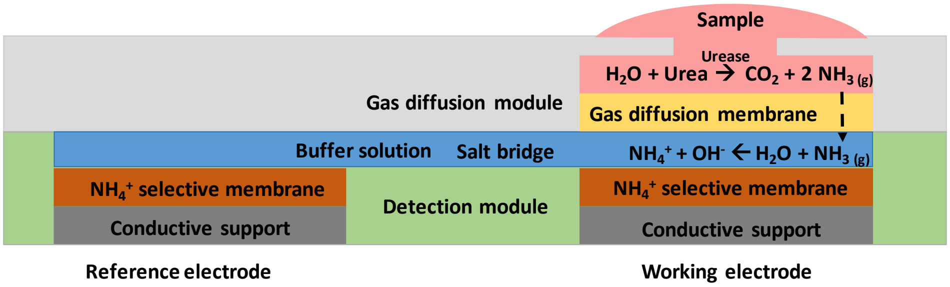

Fig. 6.8 Schematic representation for the indirect detection of urea using U-DP.

### 6.3.1. Optimization of the chemical variables of U-DP

A summary of the optimization process for the U-DP can be seen in *Table 6.IX.*

Table 6.IX Optimization of the chemical variables for U-DP.

| Variable optimized | [HEPES] (M) | [Urease] (U·ml$^{-1}$) | Time (min) | Optimized value |
|---|---|---|---|---|
| **[HEPES]** | 0.001 – 0.1 | 2 | 1 | 0.1 |
| **[Urease]** | 0.1 | 30 – 50 | 5 | 30 |
| **Time (min)** | 0.1 | 30 | 5 – 10 | 10 |

The first steps of the optimization process were carried out using the batch set-up. Due to the increase of the desired linear range for the determination of urea up to 33 mM (as opposed to 1000 µM for $NH_4^+$) it was necessary to re-evaluate the buffer concentration. At such high urea concentrations, the amount of $NH_3$ reaching the buffer of top of the ISE could lead to its alkalinization if the buffer capacity is not high enough. In fact, this is what was demonstrated when measuring the final pH of the buffer solution after carrying out calibration procedures using HEPES concentrations of 0.001 M, 0.01 M and 0.1 M at an initial pH 7. An arbitrary urease concentration of 2 U·ml$^{-1}$ was used. Only when using 0.1 M HEPES the pH was not altered, so this concentration was selected to be used for the buffer solution on top of the ISEs. With lower concentrated buffer solutions, the final measured pH was more basic than prior to the calibration (*Table 6.X*).

Table 6.X Measured HEPES pH after the calibration procedure using different HEPES concentrations.

| | [HEPES] (M) | | |
|---|---|---|---|
| | **0.001** | **0.01** | **0.1** |
| **pH post-calibration** | 9 | 8 | 7 |

After the evaluation of the HEPES concentration, the time of analysis necessary to obtain the conversion of urea into $NH_3$ was appraised. This was done using 0.1 M HEPES at pH 7 and a urease concentration of 2 U·ml$^{-1}$ using the batch set-up. This evaluation was carried out using a low, medium and high urea concentrations: 9 mM, 17 mM and 33 mM urea. According to *Fig. 6.9*, the total degradation of urea into $NH_3$ was achieved at 25 min, 35 min and 50 min respectively; times which are too long for a POC device. Nevertheless, at shorter times it was possible to stablish a linear relation between these concentrations, even if not all the urea present underwent enzymatic catalysis. Therefore, a short time of 5 minutes (300 s) was selected to continue the optimization of the rest of the parameters.

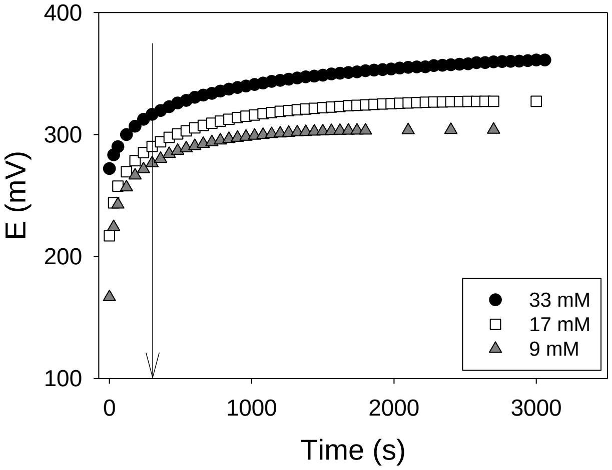

Fig. 6.9 Monitoring of the enzymatic degradation time for 9 mM (grey), 17 mM (white) and 33 mM urea (black) using 2 U·ml$^{-1}$ urease for U-DP. Arrow indicates values at 5 min.

The following optimization steps were carried out using the dual set-up: the selection of the urease concentration and the time of analysis. Regarding the former, two different concentrations were evaluated: 30 and 50 U·ml$^{-1}$ using a 0.1 M HEPES solution at pH 7 and a 5-minute analysis. The resulting calibration curves and analytical characteristics are shown in *Fig. 6.10* and *Table 6.XI*. The 30 U·ml$^{-1}$ urease concentration gave an almost Nernstian response, and the following optimization of the time of analysis is expected to further increase this sensitivity by increasing the time of analysis. Therefore, this concentration was selected to continue the optimization process, to avoid using an even higher urease concentration.

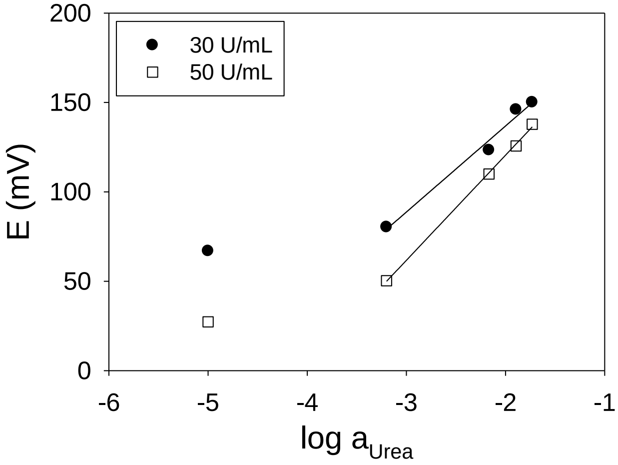

Fig. 6.10 Urease concentrations optimization for U-DP: 30 U·ml$^{-1}$ (black) and 50 U·ml$^{-1}$ (white). N = 1.

Table 6.XI Analytical characteristics of calibration curves obtained with different urease concentrations for U-DP.

| [Urease] (U·ml$^{-1}$) | Slope | Linear range (mM) | LD (µm) | R$^2$ |
|---|---|---|---|---|
| **30** | 48 | 1 – 33 | 276 | 0.9843 |
| **50** | 59 | 1 – 33 | 338 | 0.9991 |

Indeed, when times of analysis were assessed (5, 7 and 10 minutes) it was clear that a Nernstian sensitivity was achieved when using the longest time of analysis, and this was the selected value. All calibration curves are depicted in *Fig. 6.11*. From the resulting analytical characteristics seen in *Table 6.XII*.

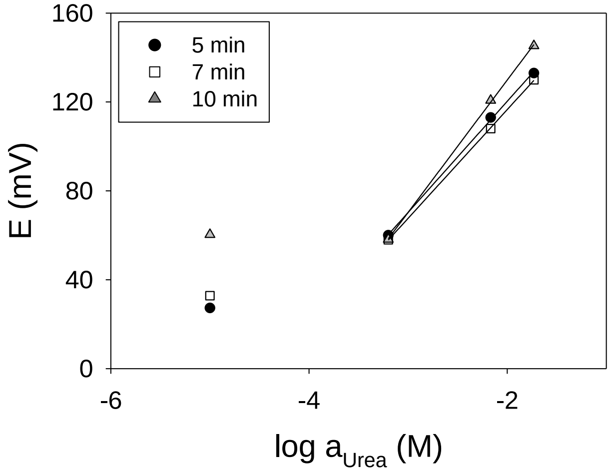

Fig. 6.11 Analysis time optimization for U-DP: 5 (black), 7 (white) and 10 minutes (grey). N = 1.

Table 6.XII Analytical characteristics of calibration curves obtained with different times of analysis for the U-DP.

| Time (min) | Slope | Linear range (mM) | LD (µm) | $R^2$ |
|---|---|---|---|---|
| **5** | 49 | 1 - 33 | 260 | 0.9991 |
| **7** | 50 | 1 - 33 | 632 | 0.9994 |
| **10** | 59 | 1 - 33 | 234 | 0.9998 |

### 6.3.2. Analytical features of U-DP

After the optimization of all the chemical and kinetic variables, the calibrations of 5 individual devices were obtained, which appear in *Fig. 6.12*. The analytical characteristics of these calibrations curves as well as those from the average values are specified in *Table 6.XIII.* All these calibration curves give satisfactory sensitivities, the same linear range from 1 mM to 33 mM urea and low LD.

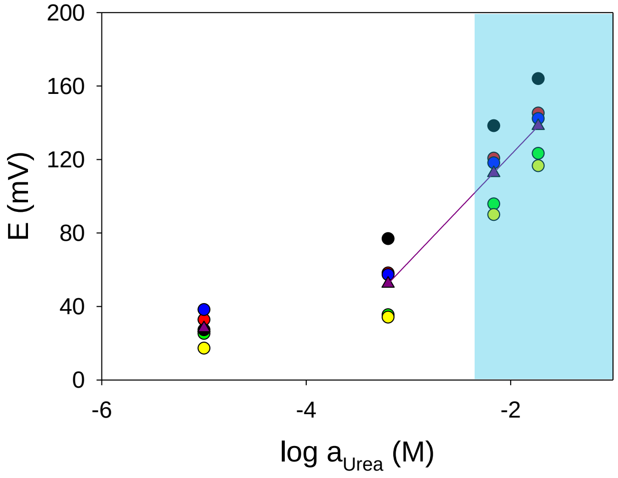

Fig. 6.12 Calibration curves obtained with the optimized parameters for 5 different U-DP devices. The average values and their linear regression appear as purple triangles and as a purple line respectively. The pathological range for urea concentrations in blood is indicated in blue.

Table 6.XIII Analytical characteristics of the calibration curves obtained with the optimized chemical parameters for U-DP.

| Calibration curves | Slope | Y-intercept | Linear range (mM) | LD (mM) | $R^2$ |
|---|---|---|---|---|---|
| **1** | 59.5 | 248.8 | 1 – 33 | 0.2 | 0.9998 |
| **2** | 59.5 | 225.6 | 1 – 33 | 0.4 | 0.9997 |
| **3** | 59.3 | 266.8 | 1 – 33 | 0.1 | 1.0000 |
| **4** | 58.1 | 243.3 | 1 – 33 | 0.3 | 0.9998 |
| **5** | 55.7 | 212.1 | 1 – 33 | 0.3 | 0.9992 |
| **Average** | 58 ± 4 | 240 ± 60 | 1 – 33 | 0.3 ± 0.3 | 0.9997 |

## 6.4. Disposable prototype integrating an enzyme for the indirect detection of phenylalanine

Once that the indirect determination of other analytes of interest by means of an enzymatic reaction was demonstrated by the use of a model enzyme, the determination of Phe could be explored. This was done by means of the use of the PAL enzyme, according to the following reaction:

$$\text{L-Phenylalanine} \xrightarrow{\text{PAL}} \text{Trans-cinnamate} + \text{NH}_3$$

In *Fig. 6.15* there is a schematic representation of P-DP, which is very similar to that of the U-DP, but using PAL instead of urease on top of the gas diffusion membrane.

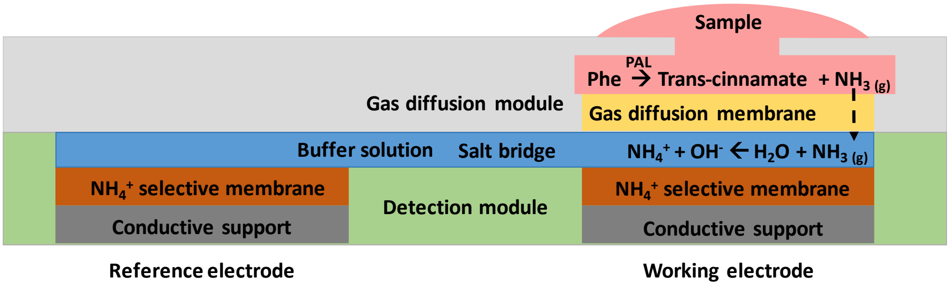

Fig. 6.13 Schematic representation for the indirect detection of P-DP.

### 6.4.1. Optimization of the chemical variables of P-DP

The pathological range of Phe is 120 – 1200 µM,[9] which is higher than the pathological range associated with hyperammonemia. Therefore, for optimization of the chemical variables for Phe determination, slightly different initial conditions were selected with respect to the previous section: the time of analysis was set to 3 minutes and the HEPES concentration was increased to 0.1 M because a higher concentration may be needed to maintain the ionic strength at higher $NH_3$ concentrations. A summary of the optimization process to achieve optimum analytical characteristics for P-DP is displayed in *Table 6.XIV.* All optimizations were carried out using the dual set-up and the 3.5 mm diameter ISEs platform.

Table 6.XIV Optimization of the chemical variables for the P-DP.

| Variable optimized | Enzyme solution pH | [PAL] (mg·ml$^{-1}$) | [HEPES] (M) | Time (min) | Optimized value |
|---|---|---|---|---|---|
| **With PBS as enzyme solution** | | | | | |
| **Enzyme solution pH** | 7 – 10.5 | 3.5 | 0.1 | 3 | 9 |
| **[PAL] (mg·ml$^{-1}$)** | 9 | 3.5 – 28 | 0.1 | 3 | 14 |
| **With water as enzyme solution** | | | | | |
| **[HEPES] (M)** | 7.4 | 7 | 0.1 – 0.01 | 3 | 0.1 |
| **Time of analysis** | 7.4 | 7 | 0.1 | 2 – 4 | 3 |

First, it was evaluated if the motor induced stirring is needed to achieve an acceptable sensitivity at the desired linear range. For this, DP in a dual set-up was used without enzyme, and 3 calibration procedures for $NH_4^+$ determination were performed with and without the presence of the vibrating motor (*Fig. 6.14*). The corresponding analytical characteristics can be seen in *Table 6.XV*. It is clear that a Nernstian sensitivity at a 120 – 1600 µM $NH_4^+$ linear range was only obtained when the motor was used. Additionally, the reproducibility between devices was also improved by the use of the motor. Thus, the use of the vibrating motor was maintained to induce stirring for the subsequent optimizations.

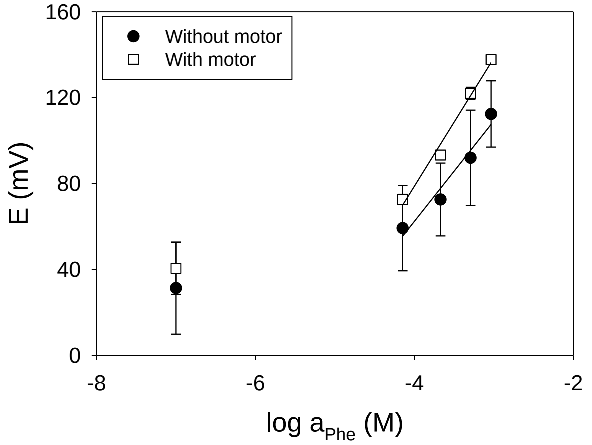

Fig. 6.14 Calibration curves obtained without (black) and with a motor induced stirring (white) for P-DP. N = 3.

Table 6.XV Analytical characteristics of calibration curves obtained with and without motor induced agitation.

| **Motor** | **Slope** | **Linear range (µM)** | **LD (µM)** | **$R^2$** |
|---|---|---|---|---|
| **No** | 47 ± 7 | 120 – 1600 | 22 ± 4 | 0.9522 |
| **Yes** | 59 ± 1 | 120 – 1600 | 18 ± 5 | 0.9857 |

Afterwards, the PAL enzyme was included in the DP platform and the calibration curves were obtained using Phe standard solutions. The first step was to optimize the variables related to those of the donor solution, which contains the enzyme: its composition, concentration and pH. The PAL enzyme was purchased lyophilized in PBS at a pH 7.4. Hence, PAL was first reconstituted in a PBS buffer containing phosphate buffer 10 mM and NaCl 137 mM. Calibration curves for 3 different devices were obtained, using a PAL concentration of 3.5 mg·ml$^{-1}$, for three different pH values: 7.4, 9.0 and 10.5. The resulting calibration curves are shown in *Fig. 6.15*, and the analytical characteristics appear in *Table 6.XVI*.

With all three pH evaluated the same linear range of 120 to 1600 µM Phe was obtained. Even though there was a higher sensitivity with pH 9.0, this sensitivity was still too low compared to the expected Nernsitan sensitivity.

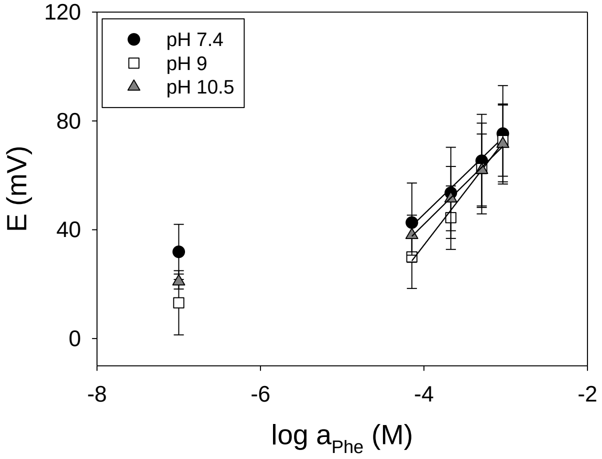

Fig. 6.15 Optimization of the PBS pH for P-DP: 7.4 (black), 9 (white) and 10.5 (grey). N = 3.

Table 6.XVI Analytical characteristics of calibration curves obtained with different pH for the PBS buffer for P-DP.

| pH | Slope | Linear range (µM) | LD (µM) | R$^2$ |
|---|---|---|---|---|
| **7.4** | 30 ± 6 | 120 – 1600 | 11 ± 5 | 0.9873 |
| **9** | 40 ± 7 | 120 – 1600 | 29 ± 5 | 0.9904 |
| **10.5** | 30 ± 20 | 120 – 1600 | 20 ± 6 | 0.9967 |

In order to increase the sensitivity of the proposed P-DP, the concentration of the enzyme was assessed next. The calibration curves obtained using enzyme concentrations of 3.5, 7, 14 and 28 mg·ml$^{-1}$ PAL are shown in *Fig. 6.16*. From the information in *Table 6.XVII* it is evident that the enzyme concentration that displayed the best analytical characteristics was 14 mg·ml$^{-1}$ PAL. This behaviour goes against of what would be expected, that is, better sensitivities with higher PAL concentrations. Furthermore, when carrying out this optimization process it was observed that the activity of PAL was not stable. When carrying out a calibration procedure with a newly prepared donor solution containing the enzyme, the sensitivities where higher than for subsequent calibrations performed with the same donor solution under the same conditions. Signals, as well as the sensitivities, for following calibrations decreased and then, stabilized. This behaviour was attributed to the enzyme unstability, leading to a loss of enzymatic activity.

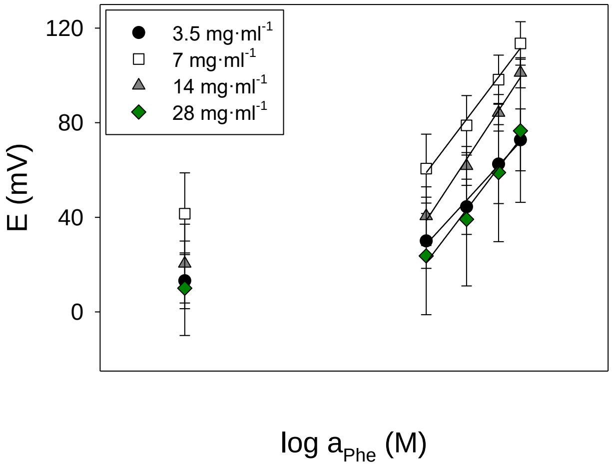

Fig. 6.16 PAL concentration optimization for P-DP: 3.5 (black), 7 (white), 14 (grey) and 28 mg·ml$^{-1}$ PAL (green). N = 3.

Table 6.XVII Analytical characteristics of calibration curves obtained with different PAL concentrations for P-DP.

| [Enzyme] (mg·ml$^{-1}$) | Slope | Linear range (µM) | LD (µM) | $R^2$ |
|---|---|---|---|---|
| **3.5** | 40 ± 7 | 120 – 1600 | 29 ± 5 | 0.9904 |
| **7** | 50 ± 10 | 120 – 1600 | 50 ± 60 | 0.9908 |
| **14** | 58 ± 9 | 120 – 1600 | 40 ± 40 | 0.9922 |
| **28** | 50 ± 10 | 120 – 1600 | 40 ± 20 | 0.9745 |

In an effort to increase the enzyme stability, PAL was reconstituted using water (instead of PBS) at pH 7.4 to fix the pH to the one indicated by the manufacturer. An enzyme concentration of 7 mg·ml$^{-1}$ was used to obtain the calibration curves shown in *Fig. 6.17*. This graph shows that there was an improvement of the enzymatic stability, as a good sensitivity was obtained with a lower enzyme concentration.

Reproducibility between calibrations was better and signals obtained were maintained for later calibrations. Furthermore, this PAL concentration was enough to achieve a Nernstian sensitivity at a linear range from 120 µM to 1600 µM Phe and a low LD (*Table 6.XVIII*).

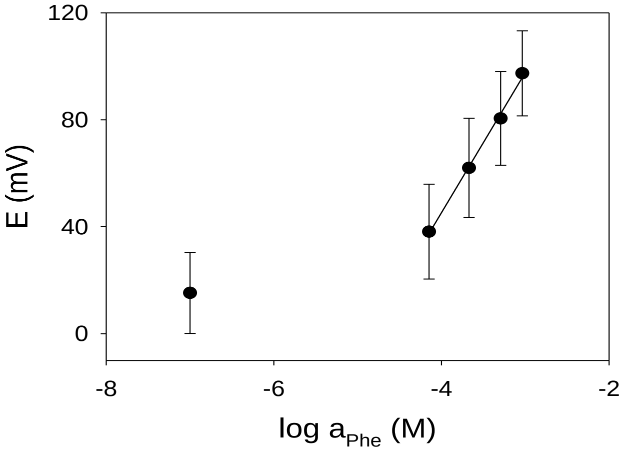

Fig. 6.17 Calibration curves obtained with a 7 mg·ml$^{-1}$ PAL reconstituted in water for P-DP. N = 3.

Table 6.XVIII Analytical characteristics of calibration curves obtained with 7 mg·ml$^{-1}$ PAL reconstituted in water for the P-DP-

| **[Enzyme] (mg·ml$^{-1}$)** | **Slope** | **Linear range (µM)** | **LD (µM)** | **R$^2$** |
|---|---|---|---|---|
| **7** | 53 ± 4 | 120 – 1600 | 30 ± 10 | 0.9967 |

Then, the optimization of the buffer solution on top of the ISE was also evaluated, by means of calibration procedures carried out with 3 different devices with HEPES concentrations of 0.1 M and 0.01 M both at pH 7. From the calibration curves seen in *Fig. 6.18* and the analytical characteristics in *Table 6.XIX* it is clear that a concentration of 0.1 M was necessary to maintain a suitable sensitivity at the desired linear range.

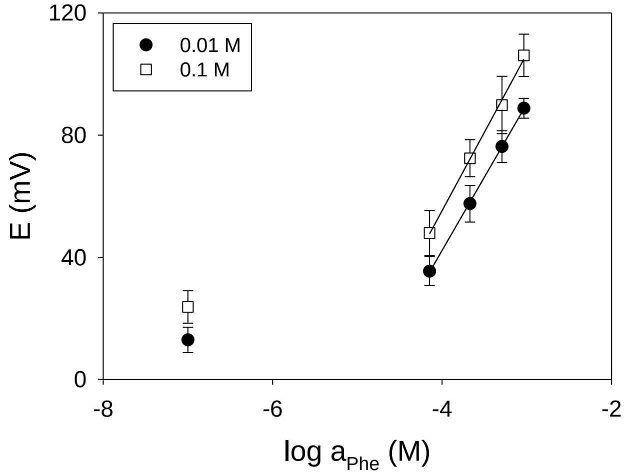

Fig. 6.18 HEPES concentration optimization for P-DP: 0.01 M (black) and 0.1 M (white). N = 3.

Table 6.XIX Analytical characteristics of calibration curves obtained with different buffer concentrations for P-DP.

| [HEPES] (M) | Slope | Linear range (µM) | LD (µM) | $R^2$ |
|---|---|---|---|---|
| **0.01** | 48 ± 3 | 120 – 1600 | 25 ± 5 | 0.9998 |
| **0.1** | 52 ± 2 | 120 – 1600 | 24 ± 4 | 0.9975 |

Finally, different analysis times were evaluated: 2, 3 and 4 minutes. The resulting calibration curves and analytical characteristics are shown in *Fig. 6.19* and *Table 6.XX* respectively. From these results it can be seen that 3 minutes was long enough to obtain a good sensitivity in the desired linear range of 120 µM to 1600 µM Phe and a low LD of 24 µM Phe. This allowed us to select a low time of analysis of 3 minutes. It would be even possible to increase this time to 4 minutes if the enzyme concentration needed to be reduced in order to lower the price of the final analytical device.

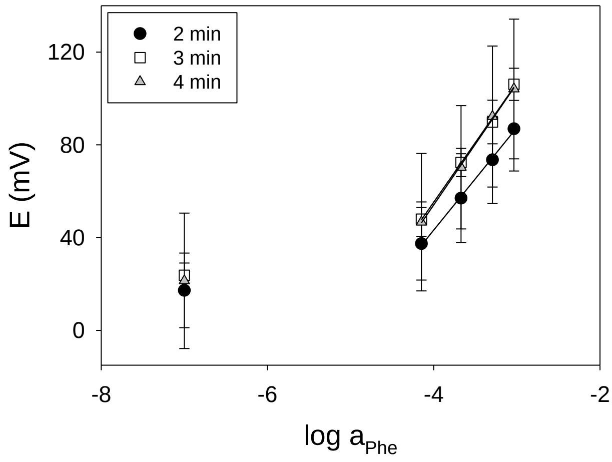

Fig. 6.19 Analysis time optimization for P-DP: 2 min (black), 3 min (white) and 4 min (grey). N = 3.

Table 6.XX Analytical characteristics of calibration curves obtained at different times of analysis for P-DP.

| **Time (min)** | **Slope** | **Linear range (µM)** | **LD (µM)** | **$R^2$** |
|---|---|---|---|---|
| **2** | 44 ± 9 | 120 – 1600 | 30 ± 20 | 0.9978 |
| **3** | 52 ± 2 | 120 – 1600 | 24 ± 4 | 0.9975 |
| **4** | 52 ± 3 | 120 – 1600 | 24 ± 3 | 0.9987 |

### 6.4.2. Analytical features of P-DP

With all the previously optimized parameters, calibration curves for 5 different devices were obtained and can be seen in *Fig. 6.20*, alongside the average values. The analytical characteristics resulting from these calibration are displayed in *Table 6.XXI* and show an acceptable Nernstian sensitivity, a LD of 30 µM Phe and a linear range from 120 µM to 1600 µM Phe, which is suitable for the discrimination of healthy and pathological levels of Phe in blood.

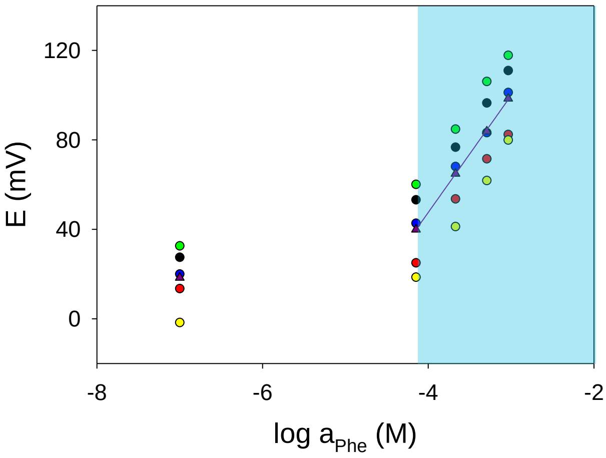

Fig. 6.20 Calibration curves obtained with the optimized parameters for 5 different P-DP devices. The average values and their linear regression appear as purple triangles and as a purple line respectively. The pathological range for Phe concentrations in blood is indicated in blue.

Table 6.XXI Analytical characteristics of the calibration curves obtained with the optimized parameters for P-DP.

| Calibration curves | Slope | Y-intercept | Linear range (µM) | LD (µM) | $R^2$ |
|---|---|---|---|---|---|
| **1** | 51.8 | 267.5 | 120 – 1600 | 23.2 | 0.9993 |
| **2** | 51.6 | 240.8 | 120 – 1600 | 39.8 | 0.9939 |
| **3** | 52.4 | 277.6 | 120 – 1600 | 21.2 | 0.9990 |
| **4** | 54.4 | 242.9 | 120 – 1600 | 32.1 | 0.9933 |
| **5** | 50.9 | 254.1 | 120 – 1600 | 25.6 | 0.9925 |
| **Average** | 52 ± 3 | 260 ± 30 | 120 – 1600 | 30 ± 20 | 0.995 ± 0.007 |

## 6.5. Conclusions

Work shown in this chapter demonstrated that a disposable platform for the potentiometric determination of $NH_4^+$ was successfully designed, fabricated and evaluated showing satisfactory results. The composition of the ISM, as well as the chemical parameters for its use were optimized to obtain the best desired sensitivity, linear working range and LD. Indeed, the analytical characteristics obtained for the N-DP allow its use to discriminate between healthy and pathological levels of $NH_4^+$ in few minutes and has a great potential to be used as disposable $NH_4^+$ POC for home use.

The versatility of this analytical platform was also demonstrated by the incorporation of urease as a model enzyme for the indirect determination of other metabolites. Indeed, the chemical and kinetic parameters for the use of U-DP were optimized to determinate levels of urea at the physio-pathological range.

This enzymatic concept for the DP was applied for the monitoring of an IEM of interest, PKU, by the use of the PAL enzyme for the indirect determination of Phe by its conversion into $NH_3$. The chemical and kinetic variables were optimized to achieve the best analytical characteristics for the determination of healthy and pathological levels of Phe. This demonstrated the viability of using these type of analytical devices for monitoring of Phe levels at home.

Results obtained regarding P-DP are of great relevance because demonstrate the versatility of the proposed disposable analytical sensors to be aimed at the detection of a wide range of biomarkers. Depending on whether the limiting step is the time of analysis or the cost of the enzyme, these two parameters can be tailored to obtain the conditions that better suit the needs of the situation. A higher enzyme concentration would lead to shorter times of analysis, but if the cost is too high, the enzyme concentration could be decreased maintaining the analytical characteristics unaltered if the time of analysis is increased.

As future prospective, the DP described in this chapter could be used together with the miniaturized potentiometric reader developed by the IEB group, previously shown in *Chapter 3*. This potentiometer could incorporate a small piezoelectric system to provide vibration and enhance the $NH_3$ diffusion and can also send results by Bluetooth to the patients' smartphone. In this way, a cheap and easy to use system for the monitoring of metabolic diseases at home would be realized, similar to those already existing for the monitoring of glucose level for diabetic patients.

In order to achieve this final objective, DP devices must be fabricated at a mid-scale to validate the auto-calibration step and a way to encapsulate the enzyme onto the gas diffusion membrane must be optimized. Finally, the analysis of real blood samples must be performed to validate the proposed microanalyzers with the reference methods currently used in the hospital laboratories for the determination of $NH_4^+$ and Phe.

## 6.6. References

(1) Carretero, L. G. Dispositiu Point of Care (POC) per a La Determinació de Clorur En Suor per Al Diagnòstic de Fibrosi Quística. Bachelor's Thesis, Universitat Autònoma de Barcelona, Spain, 2022.

(2) Calvo-Lopez, A.; Puyol, M.; Alonso-Chamarro, J. New Strategy of Autocalibration for Disposable Potentiometric Point-of-Care Analyzers. In *XXII Transfront. Meet. Sensors Biosensors. Barcelona, Spain* 2018.

(3) Cojocaru, K.-A.; Oprea, O. R.; Dobreanu, M. The Influence of Transport Condition and Processing Time on Plasma Ammonia Results. *Acta Marisiensis - Ser. Medica* **2022**, *68* (1), 24–27. https://doi.org/10.2478/amma-2022-0005.

(4) Zahran, E. M.; New, A.; Gavalas, V.; Bachas, L. G. Polymeric Plasticizer Extends the Lifetime of PVC-Membrane Ion-Selective Electrodes. *Analyst* **2014**, *139* (4), 757–763. https://doi.org/10.1039/C3AN01963B.

(5) Calvo-López, A.; Arasa-Puig, E.; Alonso-Chamarro, J.; Puyol, M. Serum/Plasma Potassium Monitoring Using Potentiometric Point-of-Care Microanalyzers with Improved Ion Selective Electrodes. *Talanta* **2023**, *253*, 124100. https://doi.org/10.1016/j.talanta.2022.124100.

(6) Sigma-Aldrich. *Biological Buffers Selection Guide*; 2019. https://www.sigmaaldrich.com/deepweb/assets/sigmaaldrich/marketing/global/documents/101/257/biological-buffers-selection-guide-ps3138en-ms.pdf.

(7) Maines, E.; Piccoli, G.; Pascarella, A.; Colucci, F.; Burlina, A. B. Inherited Hyperammonemias: A Contemporary View on Pathogenesis and Diagnosis. *Expert Opin. Orphan Drugs* **2018**, *6* (2), 105–116. https://doi.org/10.1080/21678707.2018.1409108.

(8) Vanholder, R.; Gryp, T.; Glorieux, G. Urea and Chronic Kidney Disease: The Comeback of the Century? (In Uraemia Research). *Nephrol. Dial. Transplant.* **2018**, *33* (1), 4–12. https://doi.org/10.1093/ndt/gfx039.

(9) Cleary, M. A. Phenylketonuria. *Paediatr. Child Health (Oxford).* **2015**, *25* (3), 108–112. https://doi.org/10.1016/j.paed.2014.10.006.

# Chapter 7

# General conclusions and future perspectives

Throughout the last three chapters, some partial conclusions have already been discussed about the work described in this thesis. As general conclusions, it can be summarised that several analytical platforms arising from the combined use of microfabrication technologies, to develop polymeric microfluidic platforms, and potentiometric detectors, which can be integrated in this structures, were presented in this work. The optimum configurations and work conditions for all these analytical platforms were stablished to obtain the desired analytical characteristics of sensitivity and lineal range required for each intended purpose.

A reusable FIA microanalyzer for the fast and automated high-throughput analysis of $NH_4^+$ in blood was designed, fabricated, optimized and validated by the direct analysis of blood samples. Owing to its outstanding analytical characteristics and low errors when compared to the reference method, it was concluded that the proposed analytical system was a suitable candidate to be used as a robust and reliable POC device in an hospital or a clinic, for the monitoring and management of hyperammonemia presenting diseases such as UCDs. A particularly important characteristic of this system was the high level of automation achieved, which resulted in ease of use by non-specialized personnel, and the improvements aimed to greatly increase the lifetime of the microsystem, thus reducing upkeep, maintenance requirements and overall costs.

In parallel, great effort was undertaken regarding the development of an auto-calibrating and disposable analytical devices, which is meant to be used by the patients themselves at their own homes. This proposed disposable device allowed the direct determination of $NH_4^+$ levels in capillary blood. Moreover, it is an exceedingly versatile platform, which also permits the indirect determination of other analytes of interest by the addition of an enzyme. Thus, it can be a remarkably useful tool for the management of several IEMs. Indeed, two different analytical platforms for the determination of $NH_4^+$ and Phe were fabricated and optimized, and the resulting analytical characteristics demonstrated the potential of their use as POC devices for the reliable determination of these two biomarkers within their physio-pathological ranges.

Further work continuing these research topics should focus on:

1) The validation of the automated POC system for $NH_4^+$ determination in blood by means of a larger amount of blood samples and the comparison of results to the reference method.

2) The evaluation of the auto-calibrating step for the DP platform. Fabrication of a set of devices at mid-scale to validate the approach.

3) The validation of the N-DP and P-DP devices by analysis of blood samples and the comparison of the results to the reference methods for determination of $NH_4^+$ and Phe respectively.

4) Study of the enzyme encapsulation in the P-DP and evaluation of lifetime and storing conditions for both N-DP and P-DP regarding future high-scale manufacturing and commercialization.

5) The development of a user friendly and smartphone-compatible software for data acquisition and monitoring of the results obtained by N-DP and P-DP, and the accessibility of these results by the healthcare professionals to improve medical monitoring.